Controlling the Microstructure of the Porous Nickel Electrodes in Alkaline Electrolysers

Gulcan Serdaroglu, MSc, BSc

Thesis submitted to the University of Nottingham for the degree of

Doctor of Philosophy

January 2018

Abstract

Ni-based electrodes have been extensively studied for hydrogen evolution reaction (HER) in alkaline electrolysers in an attempt to improve its electrocatalytic activity through alloying it with other metals and/or increasing the surface area. However, the role of microstructure on the electrochemical performance has received little attention. In this study, Ni-based catalysts have been prepared by a powder metallurgy technique including compaction and sintering of a mixture of Ni, starting alloy (consisting of Al_3Ni and Al_3Ni_2) and binder. As-sintered samples were then treated in concentrated alkaline solution for leaching of Al. The microstructural properties are controlled by changing the parameters of the preparation process; i.e. sintering temperature, starting alloy to Ni ratio, leaching temperature and binder properties (concentration and particle size).

Increasing the sintering temperature from 625 to 900 ºC improved the mechanical strength but also increased the diffusion of Al from Al-rich phases into Ni, resulting in reduced Al-rich phases available after sintering. Since Al can only be leached from Al-rich phases, the specific surface area of micro- and mesopores (with the latter having a size range of 2-14 nm) created during the leaching reduced by almost 90 % from 625 to 900 ºC sintering temperature. Although there was a *ca.* 15 times increase in the specific surface area by increasing the starting alloy concentration from 0 to 60 wt.%, the robustness of catalysts reduced since the compressibility of alloy powder is lower than that of Ni, resulting in increased macroporosity. This suggests that the starting alloy concentration should be in the range of 20-40 wt.% in order to achieve relatively robust and inexpensive porous catalysts without compromising too much the surface area.

N_2 sorption isotherms showed that leaching at 30 and 50 ºC resulted in pores with a slit shape, whilst leaching at 60, 70 and 80 ºC lead to ink-bottle pores. This was attributed to increasing leaching rate with higher leaching temperatures in comparison to speed of atomic rearrangement at the surface. Increasing the leaching temperature from 30 to 60 °C improved the specific surface area by almost 4 times, whilst leaching at 60, 70 and 80 ºC gave similar surface areas.

Greater binder concentrations led to increased macroporosity and surface roughness as well as greater numbers of windows between the adjacent cavities. Consequently, the mechanical strength of porous catalysts reduced due to the decrease in the wall thickness. It was also found that the size of the binder particles influences the robustness of the porous catalysts, with the smaller the binder size the greater the robustness.

The comparison of trends in alkaline electrolyser cell voltage and compositional and microstructural properties showed that the surface area has a dominant effect on the electrocatalytic activity for HER in comparison to the composition of Ni-based electrodes. Despite greater Al contents, the cell voltage still decreased with increasing surface areas (with micropores accounting for *ca.* 80 %). However, it was found that the effective use of micro- and mesopores depends on the pore morphology, with slit-shaped pores being more effectively used during HER in comparison to ink-bottle pores which can be more subject to mass transport limitation. It was shown that H_2 bubbles cannot form inside the micro- and mesopores, therefore generated H_2 can only leave the pores through diffusion which appears to be favoured by a slit shape in comparison to ink-bottles. It was also found that increasing the amount of large macropores (> 15 µm) is not advantageous to the production of electrodes for alkaline electrolysers as it results in increased electrode thickness and reduced mechanical strength with no measureable improvement in electrochemical performance.

Publications and Presentations

Publications:

Serdaroglu, G., Khzouz, M., Gillott, M., Shields, A. and Walker, G.S., 2015. The effect of environmental conditions on the operation of a hydrogen refuelling station. *International Journal of Hydrogen Energy*, *40*(47), pp.17153-17162.

Symes, D., Maillard, J.G., Courtney, J., Watton, J., Meadowcroft, A., Chandan, A.S., Gurley, L., Priestly, R. and Serdaroglu, G., 2014. Development of a hydrogen fuelling infrastructure in the Northeast USA. *International Journal of Hydrogen Energy*, *39*(14), pp.7460-7466.

Oral Presentations:

Gulcan Serdaroglu, Ming Li, Nick Van Dijk and Gavin S Walker. “Effect of microstructure on the performance of porous nickel electrodes for alkaline electrolysers.” Fuel Cell and Hydrogen Technical Conference, Birmingham, UK (2016).

Gulcan Serdaroglu, Ming Li, Nick Van Dijk and Gavin S Walker. “Effect of microstructure on the performance of porous nickel electrodes for alkaline electrolysers.” H2FC SUPERGEN Researcher Conference, Bath, UK (2015).

Poster Presentation:

Gulcan Serdaroglu, Martin Khzouz, Mark Gillott, Alex Shields, and Gavin S Walker. “The effect of environmental conditions on the operation of a hydrogen refuelling station.” Awarded with the best poster prize in International Conference in Hydrogen Storage and Embrittlement Applications, Rio De Janeiro, Brazil (2014).

Acknowledgements

This thesis is dedicated to my parents, Mehmet Serdaroglu and Perihan Serdaroglu.

I would like to express my deepest gratitude to my supervisors, Prof. Gavin S Walker, Dr Ming Li and Prof. Mark Gillott for their endless support and guidance during my PhD studies. I also would like to thank my industrial supervisor, Dr Nick Van Dijk for his invaluable discussions and help. Thanks to everyone in ITM Power for their contributions and support.

Thank you also to Dr Lee Stevens for his assistance with porosity characterisation techniques; Dr Nigel Neate for his help with Rietveld refinement method; Dr Martin Corfield for his support in three-dimensional image analysis.

I would also like to thank my colleagues in the hydrogen research group who have been very friendly and supportive. In particular I would like to thank Prof. David Grant, Dr Priyen Mistry, Dr Alastair Stuart and William Boardman for their continued help.

A massive thank to my friends in UK for their support, caring and ability to brighten my mood when in need of a break and for the many great moments we shared together.

Finally, my sincerest thanks to all my family; Zafer, Ihsan, Mehmet, Perihan, Neslihan, Aslihan, Murat, Ismail and Serap for their great love, support, caring, encouragement and understanding. Thanks for always being there for me and giving me strength to achieve my goals.

This research was undertaken as a part of the EPSRC Centre for Doctoral Training in Fuel Cells and their Fuels and also supported by ITM Power.

List of Abbreviations

HER	Hydrogen evolution reaction
SMR	Steam methane reforming
PEM	Polymer electrolyte membrane
SO	Solid oxide
PFSA	Perfluorosulfonic acid
YSZ	Yttria-stabilized zirconia
RDS	Rate determining step
RT	Room temperature
CV	Cyclic voltammetry
EIS	Electrochemical impedance spectroscopy
FRA	Frequency response analyser
AC	Alternating current
DC	Direct current
SEM	Scanning electron microscopy
AAS	Atomic absorption spectroscopy
BET	Brunauer, Emmett and Teller
EPMA	Electron probe X-ray microanalysis
EDX	Energy dispersive analysis of X-rays
ICP	Inductively coupled plasma
XRD	X-ray diffraction
ASTM	American Society for Testing and Materials
BSI	British Standards Institute
SS	Stainless steel

WE	Working electrode
CE	Counter electrode
RE	Reference electrode
SE	Sense electrode
CP	ChronoPotentiometry
IUPAC	International Union of Pure and Applied Chemistry
BJH	Barrett-Joyner-Halenda
D-A	Dubinin-Astakhov
MIP	Mercury intrusion porosimetry
PXD	Powder X-ray diffraction
ICSD	International Crystal Structure Database
FWHM	Full widths at half maximum
GSAS	General Structure Analysis System
SE	Secondary electron
BSE	Back scattered electron
ICP-MS	Inductively coupled plasma mass spectrometry
ICP-OES	Inductively coupled plasma optical emission spectrometry
CT	Computed tomography
3D	Three-dimensional
TGA	Thermogravimetric analysis

Contents

1. Introduction

1.1. Path to a Sustainable Energy Future

The growing world energy demand has led to significant challenges related to intensive fossil fuel consumption. Greenhouse gas emissions, especially carbon dioxide (CO_2) emissions have reached critical levels resulting in visibly adverse effects of climate change throughout the world. Energy-related CO_2 emissions are projected to rise by one-fifth by 2040 [1]. The air pollution has also become a serious problem especially in highly populated areas taking a growing toll on human health and the environment [1]. In addition, the limited sources of fossil fuels with regard to the increasing energy demand have raised concerns about energy security and economic dependency. The world energy demand is anticipated to increase by 37 % by 2040 [2], whilst the total consumption of oil, natural gas and coal is projected to take place by 2050, in 70-100 years and in the next few centuries respectively [3]. Consequently, the urgent need for sustainable and clean energy solutions has become inevitable in order to secure the world energy demand and overcome environmental issues.

In an attempt to mitigate climate change, several countries have agreed to the Kyoto Protocol and are committed to the promotion of low-carbon economy through internationally binding emission reduction targets. The first legally binding target has been set by the UK aiming to cut carbon emissions by 34 % by 2020 and at least 80 % by 2050 from 1990 levels [4]. The European Union (EU) have set an overall goal of 20 % reduction in green gas emissions by 2020 and to achieve this target the share of renewable energy sources will be promoted to 20 % of the EU energy consumption with a specific target of 10 % share in the transport sector (both measured in terms of gross final energy consumption) by 2020 [5]. At the Paris climate conference (COP21) in 2015, 195 countries have agreed to limit the increase in global average temperature to well below 2 ºC to reduce the risks and the effects of climate change [6].

Renewable energies such as hydroelectricity, biofuels, solar, wind, tidal and geothermal energies offer potential solutions to climate change and energy security. Despite the abundance of renewables, they cannot provide a continuous energy flow due to their intermittent nature. Consequently, there remain challenges that require addressing such as mismatches between the supply and demand, storage and utilization of surplus energy, management of decentralised production and integration of renewable energy with the transport sector. All these challenges underline the necessity for the deployment of effective energy storage technologies.

Currently, a variety of methods are used to store renewable energy such as pumped hydroelectricity, compressed air, batteries, super-capacitors and thermal storage [7, 8]. Alternatively, hydrogen, as a versatile energy carrier, has a potential to facilitate energy storage and distribution from renewables reducing the dependence on fossil fuels.

1.2. Why Hydrogen?

Hydrogen offers several benefits as a promising energy carrier. First, it has the highest energy content per unit mass (141.6 $MJ.kg^{-1}$) amongst any fuels [9]. For instance, the gravimetric energy content of hydrogen is *ca.* 3 times more than that of petrol [10]. Secondly, utilization of hydrogen as a fuel can avoid air pollution and the release of greenhouse gas emissions as the combustion and electrochemical oxidation of hydrogen produce water only. This is particularly important for the transport sector which accounted for *ca.* 26 % of the world total energy consumption [11] and *ca.* 23 % of the global CO_2 emissions in 2014 [12]. The internal combustion of hydrogen to run a vehicle has an efficiency of *ca.* 25 % [13], whilst electrochemical oxidation of hydrogen through a fuel cell system, that converts the chemical energy of hydrogen directly into electricity, offers energy conversion efficiencies up to *ca.* 60 % [9].

Lastly, hydrogen is the most abundant element in the universe and can be produced from a variety of resources including water, biomass and hydrocarbons making it attractive towards a sustainable energy future [14].

1.3. Hydrogen Production

A wide range of techniques can be used to produce hydrogen from different resources such as thermochemical, electrochemical and biological processes (Figure 1.1). Amongst different techniques, the steam methane reforming (SMR) is the most commonly used method due to its maturity, relatively low cost and suitability for large-scale production [15]. Currently, approximately 50 % of the global hydrogen is met by SMR followed by oil reforming and coal gasification techniques with the shares of *ca.* 30 and 18 % respectively [16]. However, utilization of fossil fuels to generate hydrogen leads to CO_2 emissions and is not sustainable since fossil fuels are subject to depletion. Although CO_2 emissions can be captured and stored in depleted natural gas and oil wells or in geological formations, carbon capture and storage is not yet technically and commercially proven and it increases the system complexity and costs [10, 17].

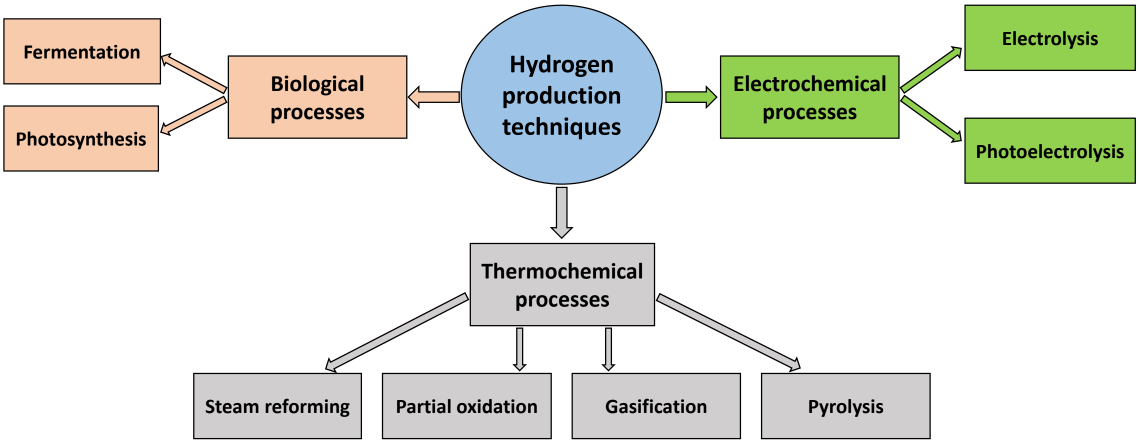

Figure 1.1. The main hydrogen production techniques [18, 19].

Biomass can be a substitute for fossil fuels and comes from a variety of sources including energy crops, residues from agriculture, forestry, industrial and municipal wastes which can be used as a feedstock to produce hydrogen via steam reforming, gasification, pyrolysis and fermentation [20]. Although these processes can contribute to sustainable hydrogen supply, hydrogen production from biomass is still uneconomical due to low yields and additional treatment steps required such as drying of wet biomass before the gasification process [21]. For example, the cost of direct gasification of lignocellulosic biomass is *ca.* 3 times greater than that of SMR [21]. Other concerns are the local availability and cost of biomass feedstocks. Transportation of feedstocks from distant locations to the point-of-use could be costly and lead to significant greenhouse gas emissions especially for large scale applications.

Alternatively, water, as the most abundant hydrogen resource, can be split into hydrogen and oxygen through electrolysis, photo-electrolysis, thermo-chemical decomposition and photo-biological splitting [10]. Photo-electrolysis and photo-biological processes have low efficiencies (*ca.* 10 %) and are still at an early stage of development and further away from commercialization [22, 23]. Thermo-chemical decomposition requires further development of materials with the focus on high-temperature membranes and heat exchangers [17]. Amongst these processes, electrochemical splitting of water is the most promising method for sustainable hydrogen production as it is a proven technology and can be readily integrated with existing water and electricity infrastructures. Due to the compact design and modularity of water electrolysers, the production rate can be tuned to meet a certain hydrogen demand [24]. Furthermore, they can be coupled with renewables such as solar, wind, wave and tidal power which will not only provide green and sustainable hydrogen fuel for mobile and stationary applications, but will also offer a means of energy storage tackling the issues related to intermittency of renewable power sources.

1.4. Water Electrolysis Technologies

Water electrolysis is an electrochemical process in which water is decomposed into hydrogen and oxygen through the application of a direct electric current between two electron conductive electrodes; i.e. anode and cathode separated by an ion conductive substance called electrolyte [17]. Depending on the nature of the electrolyte material used there are three main types of electrolyser technologies; i.e. alkaline, polymer electrolyte membrane (PEM) and solid oxide (SO) electrolysers.

Table 1.1 compares the typical characteristics of main water electrolyser technologies. In alkaline electrolysers, the electrolyte is an aqueous solution of potassium hydroxide (KOH) or sodium hydroxide (NaOH) with a typical concentration range of 20-30 wt.% for commercial applications, while PEM electrolysers use a polymeric membrane electrolyte with perfluorosulfonic acid (PFSA) being the most commonly used material [25]. Alkaline and PEM electrolysers are considered as low temperature electrolysers as they operate at temperatures typically less than 80 ºC. Whereas for SO electrolysers the operating temperature is usually greater than 800 ºC and yttria-stabilized zirconia (YSZ) is generally employed as an electrolyte material [26]. Although high operating temperature facilitates elevated electricity-to-hydrogen conversion efficiencies (exceeding 95 %) [22], it leads to critical challenges related to material dilatation, stability and corrosion [27].

Table 1.1. Typical characteristics of main water electrolysis technologies [25-29].

Parameter	Alkaline	PEM	SO
Technology status	Mature	Mature	Lab scale/Research and development
Electrolyte	KOH or NaOH aqueous solution	Solid polymer membrane	YSZ
Mobile species	OH^-	H^+	O^{-2}
Anode reaction	$2OH^- \rightarrow 0.5O_2+H_2O+2e^-$	$H_2O \rightarrow 2H^++2e^- +0.5O_2$	$O^{-2} \rightarrow 0.5O_2+2e^-$
Cathode reaction	$2H_2O+2e^- \rightarrow H_2+2OH^-$	$2H^++ 2e^- \rightarrow H_2$	$H_2O+2e^- \rightarrow H_2+ O^{-2}$
Anode catalyst	Ni or Cu	Ir/Ru oxide	$(La,Sr)(Mn,Co,Fe)O_3$
Cathode catalyst	Ni	Pt	Ni-YSZ
Operating temperature (ºC)	ambient-120	ambient-80	800-1000
Current density (A/cm^2)	0.1-0.4	0.6-2.0	0.3-1.0
Cell voltage (V)	1.8-2.4	1.8-2.2	0.95-1.3
Capacity (Nm^3/h)	Up to ~ 670	1-230	1
Lifetime (h)	Up to 100,000	10,000-50,000	500-2,000

Low temperature electrolysers have the greatest potential to couple with renewables as their start-up time is shorter (few seconds or minutes) and they can potentially cope with intermittent power supply as opposed to high temperature electrolysers for which the start-up time can be as long as *ca.* 12 h [27]. PEM electrolysers can offer higher current densities up to 2 A/cm^2 while still operating at lower cell voltages compared to conventional alkaline electrolysers which typically operate at current densities up to 0.4 A/cm^2 (Table 1.1). The greater power density and more compact design make PEM electrolysers more attractive for a wide range of applications. However, the highly acidic electrolyte demands the use of noble metals as catalyst materials, e.g. platinum (Pt), ruthenium (Ru) and iridium (Ir) [26]. Although these noble metals can offer better electrocatalytic activities than non-noble catalysts, they increase the capital costs significantly. For instance, the price of Pt nanopowder is *ca.* £1620/g, whereas Ni nanopowder costs *ca.* £7/g [30, 31]. In addition to noble-metals, utilization of polymer membrane and expensive materials for other cell components such as Titanium (Ti) make PEM electrolysers costly [26].

Currently, alkaline electrolysers are the most commonly used technique for the electrochemical water splitting for industrial applications with a typical production rate in the range of 5-500 Nm^3 H_2/h [26]. This is because they are a well-established technology and offer a lower cost solution with relatively longer lifetimes. Utilization of non-noble metals such as Ni as an electrode catalyst reduces the capital costs. However, the electrochemical activity of non-noble metals is lower than that of noble metals resulting in greater electricity consumption to generate the same amount of H_2 [29].

There is still room to improve the performance of alkaline electrolysers by enhanced electrocatalytic activity and advanced cell designs which can reduce the cell voltages and increase the operating current densities. A more detailed review on alkaline electrolysers with particular attention to electrocatalytic activity of Ni-based cathodes is provided in Chapter 2.

1.5. Aims and Scope of the Research

Research carried out from this work has aimed to investigate the effects of porous electrode preparation conditions on the microstructural properties with a view to establishing a relationship between the microstructure and electrochemical performance of these electrodes in alkaline electrolysers. The microstructure of porous electrodes is controlled by changing the following parameters of the preparation process;

- sintering temperature
- starting Ni-Al alloy to Ni ratio
- leaching temperature
- binder properties (concentration and particle size).

The main objectives of this work are to

- Control the porosity characteristics of Ni electrodes through modifying the preparation conditions
- Characterize the physical and chemical properties of electrodes prepared at different conditions with the main focus on the microstructure
- Determine the effect of different parameters of preparation process on the microstructure
- Evaluate the electrochemical performance of electrodes with differing porosity characteristics in an alkaline electrolyser cell
- Establish a relationship between the microstructural properties and electrochemical activity of porous electrodes.

1.6. Thesis Overview

Chapter 2 provides a critical review of published literature on the performance of Ni-based electrodes in alkaline electrolysers with the focus on the cathodic activity. This chapter first describes the thermodynamics of water electrolysis and principles of alkaline electrolysers. Then, the literature review covers two main approaches used to improve the electrocatalytic activity of Ni-based cathodes, i.e. alloying Ni with other metals and increasing the surface area.

Chapter 3 describes in detail the materials, equipment and methods used to manufacture and characterize the porous electrodes including a detailed description of principles of the characterization techniques.

Chapter 4 presents the results of physical, chemical and electrochemical characteristics of porous electrodes manufactured in different conditions.

Chapter 5 discusses the results presented in Chapter 4 while explaining how different preparation conditions influence the physical and chemical characteristics of electrodes with the main focus on the microstructural properties and how this correlates with the electrochemical performance in alkaline electrolysers.

Finally, Chapter 6 summarizes conclusions that are made from this work while future investigations are suggested in Chapter 7.

2.Literature Review

2.1. Introduction

This chapter gives an overview of Ni-based electrocatalyts developed for hydrogen evolution reaction (HER) in alkaline electrolysers. Section 2.2 describes the thermodynamics of water electrolysis, followed by principles of alkaline electrolysers and kinetics of HER explained in Section 2.3 and 2.4 respectively. Section 2.5 provides a general background on electrocatalyts for HER in an alkaline medium. In Section 2.6, a detailed review on various Ni alloys for HER is described, while Section 2.7 provides the relevant literature on porous Ni electrodes prepared by different techniques.

2.2. Thermodynamics of Water Electrolysis

The total energy required to dissociate water into H_2 and O_2 is equal to the enthalpy change (ΔH) associated with the overall reaction;

$$\Delta H = \Delta G + T\Delta S \tag{2.1}$$

where ΔG is the change in Gibbs free energy; T is the temperature and ΔS is the entropy change. Electrolytic splitting of water demands ΔG of electrical energy over the available thermal energy, $T\Delta S$ [32]. The minimum electrical potential required to start the water electrolysis under standard ambient conditions (25 ºC and 101.325 kPa) is called the standard thermodynamic or reversible potential ($E^0{}_{td}$);

$$E^0{}_{td} = \frac{\Delta G^0}{nF} \tag{2.2}$$

Where n is 2, number of electrons exchanged during the reaction, F is the Faraday constant, 96845 C/mol and ΔG^0 is the change in Gibbs free energy under standard conditions, 237.178 kJ/mol [32]. The temperature and pressure dependence of the thermodynamic cell potential (E_{td}) can be defined by the Nernst equation [26];

$$E_{td} = E_{td}^0 + \frac{RT}{nF} ln\left(\frac{P_{H_2} {P_{O_2}}^{1/2}}{\alpha_{H_2O}}\right) \tag{2.3}$$

where P_{H2} and P_{O2} are the partial pressures of the H_2 and O_2 respectively and α_{H2O} is the activity of water in the electrolyte (close to unity in a first approximation) [26]. According to Equation 2.3, an increase in the operating pressure results in an increase in the potential. However, the temperature dependency of the E_{td} is governed by the temperature dependence of the ΔG^0, which decreases significantly with increasing temperatures [32].

While E_{td} represents the minimum potential required for the electrical energy demand, the thermoneutral potential (E_{tn}) also considers the heat demand of the reaction [26];

$$E_{tn} = \frac{\Delta H}{nF} \tag{2.4}$$

If E, the cell equilibrium potential, is between E_{td} and E_{tn}, which are *ca.* 1.23 and 1.48 V respectively under standard ambient conditions, the reaction takes place, however absorbs heat from the environment. At $E = E_{tn}$, the reaction carries on adiabatically with no net heat exchange between the electrolyser cell and its surroundings. Finally, heat is released to the environment when $E > E_{tn}$ [26].

2.2.1. Cell Overpotentials

The cell potential required to drive the water electrolysis reaction at a practical rate must be significantly higher than the thermodynamic voltage considering various resistances within the cell. Equation 2.5 [26] shows the contribution of different overpotentials to the cell voltage (U);

$$U = E_{td} + \eta_a + \eta_c + U_{\Omega} + U_{conc} \tag{2.5}$$

where η_a and η_c are the activation or charge transfer overpotentials between the anode/electrolyte and cathode/electrolyte interfaces respectively, U_{Ω} is the ohmic overpotential and U_{conc} is the concentration overpotential.

Figure 2.1 demonstrates a typical cell voltage-current density curve of a conventional alkaline electrolyser, where the contributions of different overpotentials are separated. Typically, the operating current densities are in the range of 0.4-0.5 A/cm^2 for the industrial processes [26, 33]. At this current density range, the anodic and cathodic overpotentials as well as ohmic drop across the electrolyte have similar contributions to the overall cell voltage.

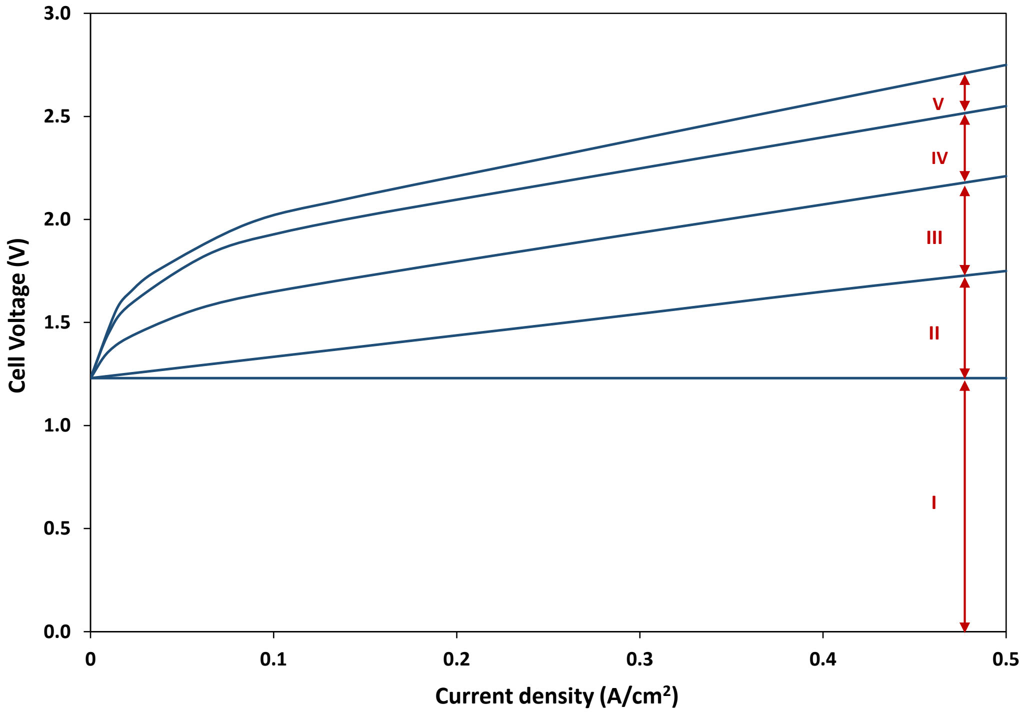

Figure 2.1. Electrochemical performance of a conventional alkaline electrolyser cell, where I is the thermodynamic voltage (E_{td}); II is the ohmic drop in the electrolyte; III is the anodic overpotential; IV is the cathodic overpotential; V is the ohmic drop in the main power line, reproduced from [34].

2.2.1.1. Activation Overpotential

Activation overpotentials are inherent energy barriers due to the surplus electrical energy required to overcome the activation energies of the electrode reactions [35]. They are dependent on the reaction kinetics, the electrocatalytic properties and surface characteristics of the electrode materials, as well as operating conditions, e.g. temperature, pressure and current density [36]. The Butler-Volmer equation [37] shows the relationship between the current density (i) and activation overpotential (η) for an electrochemical reaction on an electrode;

$$i = i_0 \left\{ exp\left[-\frac{\alpha_{Rd} nF\eta}{RT} \right] - exp\left[\frac{\alpha_{Ox} nF\eta}{RT} \right] \right\} \tag{2.6}$$

where i_0 is the exchange current density; α_{Rd} and α_{Ox} are the charge transfer coefficients for the reduction and oxidation respectively; n is the number of electrons exchanged during the reaction; F is the Faraday constant, 96845 C/mol; R is the universal gas constant and T is the temperature.

The exchange current density demonstrates the electrode’s readiness to proceed with an electrochemical reaction. It depends on the electrocatalytic properties and electroactive surface area of the electrodes, as well as operating temperature and pressure. The lower the exchange current density, the higher the energy barrier that the charge must overcome moving from the electrode surface to the electrolyte and vice versa [36].

Charge transfer coefficient defines the relative response of the respective partial current densities towards a change in overpotential [38]. For an electrochemical reaction involving more than one step and more than one electron transfer;

$$\alpha_{Rd} + \alpha_{Ox} = v_e \tag{2.7}$$

where v_e is the stoichiometric number of the electrons of the rate-determining electrode step [38].

Equation 2.6 can be rearranged to define the activation overpotentials on the cathode and anode sides of the electrolyser cell where only reduction and oxidation currents are predominant respectively;

$$\eta_c = \frac{RT}{\alpha_c nF} In\left(\frac{i}{i_o,c}\right) \tag{2.8}$$

$$\eta_a = \frac{RT}{\alpha_a nF} In\left(\frac{i}{i_o,a}\right) \tag{2.9}$$

where α_c and α_a are the charge transfer coefficients of the cathode and anode respectively and $i_{0,c}$ and $i_{0,a}$ are cathodic and anodic exchange current densities respectively [36].

A simplified way to express the activation overpotential (η_{act}) is the Tafel empirical equation [37];

$$\eta_{act} = a + b\log(i) \tag{2.10}$$

where

$$a = -2.3\frac{RT}{\alpha F}log(i_0) \tag{2.11}$$

$$b = 2.3\frac{RT}{\alpha F} \tag{2.12}$$

So-called Tafel plots (Figure 2.2), where η_{act} is plotted against the *log(i)*, are often used to compare the electrocatalytic properties of different electrode materials. The Tafel slope, *b*, is also an indicator of the electrochemical performance. An enhancement in the performance of an electrode can be achieved by increasing the exchange current density or reducing the Tafel slope or accomplishing both objectives if possible [32].

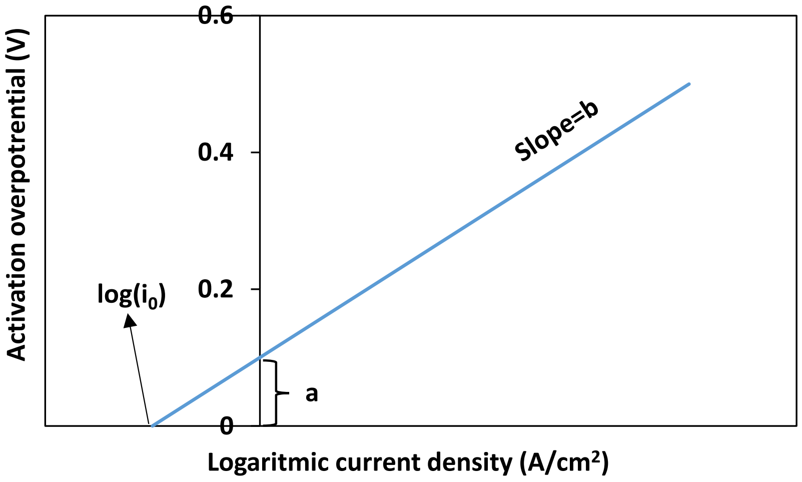

Figure 2.2. Demonstration of a hypothetical Tafel plot, reproduced from [36].

2.2.1.2. Ohmic Overpotential

Ohmic overpotentials are due to the resistance to the transfer of ions in the electrolyte and resistance to the flow of electrons through the electrically conductive components of the electrolyser [36]. These overpotentials can be defined by Ohm's law [36];

$$\mathrm{U}_{\Omega} = iR_i \tag{2.13}$$

where i is the current density and R_i is the total cell internal resistance, which is the sum of ionic, electronic and contact resistances.

The ionic resistance is related to the conductivity of the electrolyte, which depends on the electrolyte concentration for alkaline electrolysers, as well as the membrane characteristics and the distance between the electrodes [39]. The smaller the distance between cathode and anode, the smaller the ohmic resistance is. Presence of bubbles in the electrolyte could also lead to additional resistances to the flow of ions [39].

Electronic and contact resistances depend on electron conductivity and dimensions of the circuit components including wires, connectors and electrodes. These resistances can be minimized by reducing the length of the wires, increasing the cross-sectional area and using more conductive materials [39].

2.2.1.3. Concentration Overpotential

Once an electrochemical reaction starts, the concentration of reactants will be lower at the electrode/electrolyte interface than the bulk concentration leading to a concentration gradient which determines the rate of mass transfer towards an electrode. The diffusion rate of reactants (N) can be expressed by Fick's Law [36];

$$N = \frac{D(C_B - C_S)}{\delta} A \tag{2.14}$$

where D is the diffusion coefficient of the reactants, C_B and C_S are the bulk concentration of the reactant and reactant concentration at the surface of the electrode respectively, A is the electrode active area and δ is the diffusion distance.

In steady state, the diffusion rate is equivalent to the rate at which the reactants are consumed in the electrochemical reaction [36];

$$N = \frac{I}{nF} \tag{2.15}$$

where I is the current, n is the number of electrons exchanged during the reaction and F is the Faraday constant. By combining Equation 2.14 and 2.15, the dependence of reactant concentration on the current density (i) can be obtained;

$$i = \frac{nFD(C_B - C_S)}{\delta} \tag{2.16}$$

As Equation 2.16 suggests, the surface concentration on the electrode decreases with increasing current densities. If the consumption rate of reactants is faster than the diffusion rate to the surface, the surface concentration reaches zero. This occurs at a current density called limiting current density (i_L);

$$i_L = \frac{nFDC_B}{\delta} \tag{2.17}$$

Since the potential of electrochemical reaction changes with the concentration of reactant via Nernst equation, the concentration overpotential (U_{conc}) can be expressed as;

$$U_{conc} = \frac{RT}{nF} ln\left(\frac{i_L}{i_L - i}\right) \tag{2.18}$$

2.3. Principles of Alkaline Electrolysers

The water electrolysis in an alkaline electrolyte can be described by the following half reactions;

Cathode (-): $2H_2O + 2e^- \rightarrow H_2 + 2OH^-$ (2.19)

Anode (+): $2\ OH^- \rightarrow H_2O + ½O_2 + 2e^-$ (2.20)

which gives an overall reaction of;

Full reaction: $H_2O \rightarrow H_2 + ½O_2$ (2.21)

As shown in Figure 2.3, two electron conductive electrodes are immersed in an aqueous solution of KOH or NaOH. The water is consumed at the cathode side, where it is reduced to generate H_2 and OH^- ions. The standard electrode potential for water reduction, E_C^0, is *ca.* -0.83 V (at 25 ºC and 101.325 kPa) [40]. Although K^+ or Na^+ cations are also present in the aqueous solution, the reduction of these cations is hindered by high standard reduction potentials required, i.e. -2.92 and -2.71 V (at 25 ºC and 101.325 kPa) for K^+ or Na^+ respectively [40].

At the anode side, OH^- ions lose their electrons and generate O_2 and H_2O with a standard electrode potential, E_A^0, of 0.40 V [26]. A separator is placed between the two electrodes to prevent the spontaneous recombination of H_2 and O_2 during the electrolysis. The separator, which is also called the diaphragm or membrane, can be an inert porous material, impregnated with the liquid electrolyte [26]. Asbestos has been widely employed as a separator for several decades, because of its properties such as wettability and its chemical resistance to the alkaline solution. However, due to its toxic nature, it has been banned by the European Union leading to an increasing use of ion-conducting polymers as an alternative solution [33].

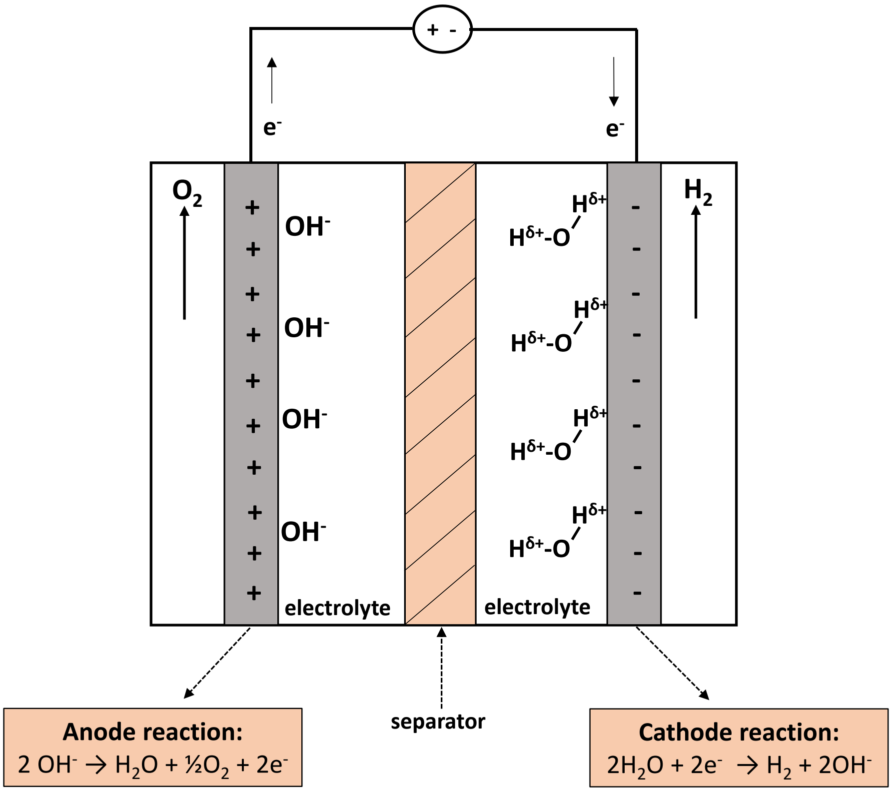

Figure 2.3. Schematic diagram of an alkaline electrolyser cell, reproduced from [26].

Conventional alkaline electrolysers are designed based on the gap cell configuration (Figure 2.4 (a)), where there is a certain electrolyte gap between the planar electrodes and the separator where H_2 and O_2 gases are evolved. The ohmic overpotential increases linearly with the distance between the electrodes [41]. In this cell configuration, the operating current density is limited up to a few 100 mA/cm^2 [33] mostly due to the accumulation of gas bubbles at the surface of electrodes at higher current densities which increases the electrolyte resistance and reduces the electrochemically active surface area of electrodes [42].

A more efficient electrolyser performance can be achieved by using a zero-gap cell configuration (Figure 2.4 (b)), where two electrodes are porous and pressed against a separator/membrane. The distance between the electrodes is minimised and gases are evolved at the back of the electrodes facilitating operations at higher current densities compared to those with the gap cell configuration [33].

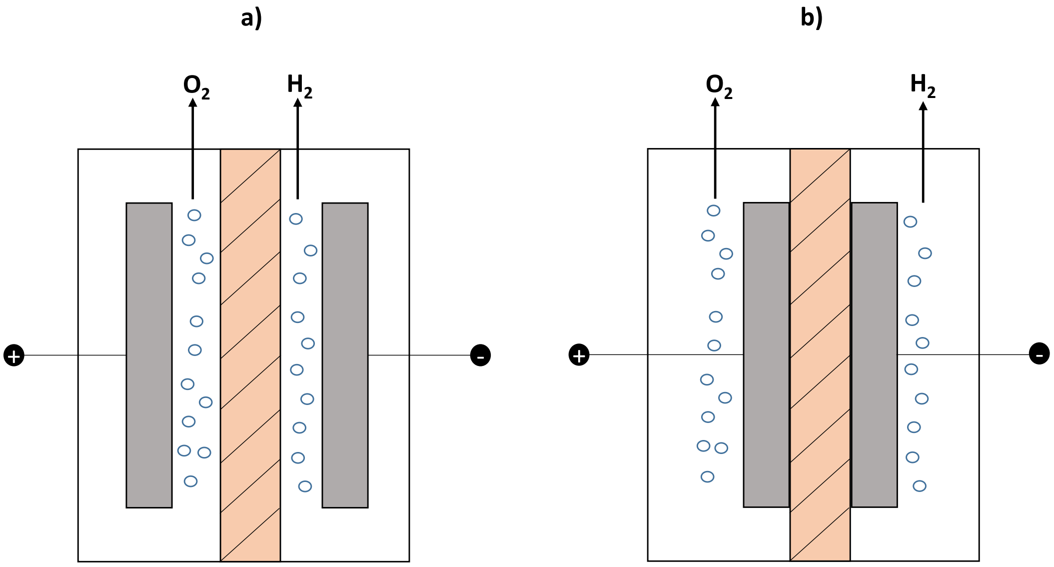

Figure 2.4. Schematic diagram of a gap cell (a) and zero-gap cell (b), reproduced from [33].

2.4. Kinetics of Hydrogen Evolution Reaction

Catalytically enhanced cathodic hydrogen evolution reaction on a metal (M) in an alkaline media proceeds through three reactions [37];

I. $M + H_2O + e^- \leftrightarrow MH_{ads} + OH^-$ (Volmer reaction) (2.22)

II. $MH_{ads} + H_2O + e^- \leftrightarrow M + H_2 + OH^-$ (Heyrovsky reaction) (2.23)

III. $2MH_{ads} \leftrightarrow 2M + H_2$ (Tafel reaction) (2.24)

The first step involves the electro-reduction of water with hydrogen atomic adsorption and is followed by either electrochemical (Heyrovsky reaction) or chemical desorption (Tafel reaction). The rate determining step (RDS) depends on the nature of the cathode material as well as the operating conditions, e.g. applied potential range [37]. If the applied potential is low, hydrogen adsorption will be the RDS as the electron transfer will be slower than desorption of hydrogen [39]. If the potential is high enough, RDS will be hydrogen desorption. An alternative explanation is the increased H_2 release rate at high voltages which can lead to a surface blockage if generated H_2 is not being transported away from the electrode surface fast enough.

For cathode materials with a low catalytic activity, the electro-reduction of water is likely to be the RDS, whereas the removal of H_2 from the electrode surface could be the slow stage for cathode materials with a high catalytic activity [37]. In the case of hydrogen adsorption being the limiting step, the electron transfer might be favoured by using electrode materials with more edges and cavities on their surface structure creating more centres for hydrogen adsorption. Similarly, surface roughness or porosity might improve the electron transfer by increasing the reaction area [39].

2.5. Electrocatalysts for the HER

The charge transfer or chemical reaction occurs on the surface of the electrocatalysts whose role is to reduce the activation energy of the electrochemical reaction, either by facilitating a more convenient sequence of reaction steps or by forming more favourable adsorption bonds [32]. As explained in Section 2.2.1.1, the reaction rate, hence the activation overpotential is defined by the properties of electrocatalyst material.

The electrocatalysis of HER is typically observed on platinum (Pt) group metals; ruthenium (Ru), rhodium (Rh), palladium (Pd), osmium (Os), iridium (Ir) and Pt, and Group VIII elements particularly transition metals, such as iron (Fe), cobalt (Co) and nickel (Ni). Volcano curves (Figure 2.5), where the exchange current densities are plotted against the metal-hydrogen (M-H) bond strength (the enthalpy of hydrogen adsorption on a metal), are used to evaluate the electrocatalaytic properties of metals for HER. A cathode material with an intermediate M-H bond strength is favourable to achieve the desirable adsorption without hindering the electrochemical or chemical desorption [38]. Pt optimally fulfils these conditions as the best catalyst known for HER [43].

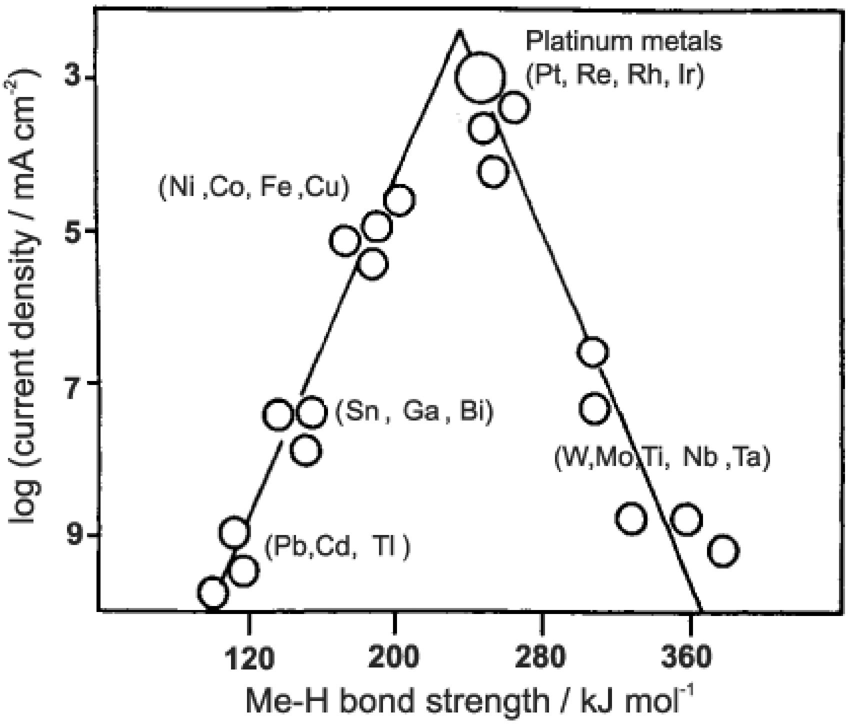

Figure 2.5. Variation of exchange current density as a function of metal-hydrogen bond strength with several cathode metals [38].

Although the selection of cathode material is based on the electrocatalytic properties, there are other criteria that should be met in order for the cathode material to be of technological interest including large electroactive surface area, good electronic conductivity, enhanced selectivity, long-term stability, good mechanical properties, minimized gas bubble issues, low cost, health and safety and widely availability [32, 39, 44, 45]. Therefore, Pt is not the common cathode material used for the alkaline electrolysers despite its desirable electrocatalytic performance. This is because of its high cost, limited availability and at least 2 orders of magnitude higher exchange current densities for HER in an acid media compared to those in an alkaline electrolyte [29, 39, 43].

The most widely used electrocatalyst for HER in an alkaline media is Ni due to its relatively low cost, easy availability and high corrosion stability in concentrated alkaline solutions [29, 46]. The mechanism and kinetics of HER on Ni cathodes in the forms of disk, rod, wire or foam have been extensively studied in order to understand the cathodic behaviour of Ni in alkaline solutions [47-52]. Although there has been no common agreement on the reaction mechanism, the most frequently cited mechanism of HER on Ni electrodes has been slow Volmer reaction (Equation 2.22) followed by a rapid Tafel reaction (Equation 2.24), with the Volmer step being rate determining [48-50, 53].

Ni has a lower electrocatalytic activity compared to precious metals resulting in a higher electricity consumption to generate the same amount of H_2 [54, 55]. To achieve the same current density, which defines the hydrogen generation rate, a higher cell voltage is needed when using Ni electrodes in comparison to noble metals due to the increase in the activation overpotential (Equation 2.8). In an attempt to improve the electrocatalytic activity of Ni-based electrodes for alkaline electrolysers, there have been two main approaches in the literature;

- alloying Ni with a different metal or metals to benefit from the synergistic effects of different metals
- increasing the surface area of Ni by introducing further porosity in the structure.

The electrochemical performance of these Ni-based electrodes has been tested for HER in a conventional 3-electrode cell (half-cell) configuration, an ex-situ test where the overpotential of the electrode is measured against a counter electrode (usually Ni or Pt plate) in an alkaline electrolyte media (aqueous KOH or NaOH solution with a concentration range of 0.1-10 M). Different electrolysis temperatures have been chosen by different researchers from room temperature (RT) up to 100 ºC with the RT being the most common one. Current-potential (polarization) curves have been recorded using a potentiostat either by controlling the current or voltage values. In addition to current-voltage curves, most of the studies have used the kinetic parameters for HER, i.e. exchange current density and Tafel slopes to compare the electrocatalytic properties of different combinations. These parameters have been calculated using the Tafel equation (Equation 2.10). Although less common, cyclic voltammetry (CV), where the voltage has been swept between two values at a fixed rate, has also been used to compare electrode activities and investigate hydrogen desorption properties. Lastly, some researchers have employed electrochemical impedance spectroscopy (EIS) where a frequency response analyser (FRA) is used to apply a small amplitude alternating current (AC) at a chosen frequency range and analyse the response of the electrode. Through equivalent circuit modelling of EIS data, charge transfer resistance (R_{ct}) which is the resistance to the charge transfer process at the electrode surface and double layer capacitance (C_{dl}) are determined. The latter, which is a measure of active surface area, has also been used to calculate the roughness factor (R) of some electrodes;

$$R = \frac{C_{dl}\, of\ rough\ electrode}{C_{dl}\, of\ smooth\ surface} \tag{2.25}$$

where C_{dl} is often assumed to be 20 μF/cm^2 for Ni smooth surface [56].

Section 2.6 reports the findings for Ni alloys for HER, whilst Section 2.7 covers the porous Ni cathodes.

2.6. Ni Alloys for HER

In principle, alloying Ni, a metal belonging to the left-hand branch of the Volcano curve (Figure 2.5) with a metal lying on the right-hand side should result in an improved electrocatalytic activity compared to the pure metals [45]. There has been a significant amount of research dedicated to improving the electrocatalytic activity of Ni cathodes by alloying it with a different metal or metals to benefit from the synergistic effects of different metals and/or obtain optimised H-adsorption characteristics. Several Ni-based binary and ternary alloys have been investigated for HER including Ni-Co [44, 57-59], Ni-molybdenum (Mo) [58, 60-65], Ni-Co-Mo [58, 66], Ni-Mo-vanadium (V) [64], Ni-tungsten (W) [59, 62, 67], Ni-zinc (Zn) [68], Ni-titanium (Ti) [56, 69, 70], Ni-Fe [59], Ni-Co-Fe [71], Ni-Co-R (R= yttrium (Y), cerium (Ce), praseodymium (Pr), erbium (Er)) [72], Ni-zirconium (Zr) [73], Ni-chromium (Cr) [59], Ni-lanthanum (La) [74, 75] and Ni-Ce [74]. Different preparation techniques have been utilised such as mechanical alloying, melting, annealing, sputter-deposition and polyol method, although the electro-deposition is the most common.

The combination of Ni-Co has been one of the commonly studied alloys for HER. Lupi *et al.* [44] investigated electro-deposited Ni-Co alloys prepared with varying Co compositions. Although there was no consistent trend in the electrochemical performance with respect to Co composition, an improved electrocatalytic activity with alloys containing *ca.* 40 to 60 wt.% Co was reported in comparison to a Ni electrode. This was attributed to the synergism among Ni (with low hydrogen overpotential) and Co (with high hydrogen adsorption) being best recognized in this range. However, volcano curves for HER in alkaline solutions reported by different studies have shown that Ni and Co are in the same branch of volcano curve and have similar hydrogen binding characteristics and electrochemical activities [76-78]. In addition, the performance data for the Ni electrode, that was used to compare with the performance of Ni-Co alloys, was taken from another study without any clarification on the test and preparation conditions as well as surface characteristics of Ni; whether it was smooth or porous. It is highly likely that the change in electrocatalytic activity can be explained by the microstructural properties.

Dominguez-Crespo *et al.* [58] observed a slightly improved electrocatalytic activity with $Ni_{0.7}Co_{0.3}$ alloy, which gave a *ca.* 14 % higher current density at an overpotential of 1.5 V, in comparison to Ni. They also investigated the combinations of $Ni_{0.3}Co_{0.7}$, $Ni_{0.3}Mo_{0.7}$ and $Co_{0.1}Ni_{0.2}Mo_{0.7}$ and reported an increase in exchange current density in the following order; $Ni_{0.7}Co_{0.3}$ > Ni > $Ni_{0.3}Mo_{0.7}$ > $Co_{0.1}Ni_{0.2}Mo_{0.7}$ whose grain sizes were *ca.* 9.8, 11.3, 10.3, 15.2 nm respectively based on X-ray diffraction (XRD) results. They related this improvement to the synergetic effects as well as increased surface area achieved by reducing the grain size during mechanical alloying. Therefore, it was not possible to conclude whether the surface area or alloy chemistry was the main reason for the change in the electrochemical performance. They also did not investigate the porosity characteristic of their samples.

Ni-Mo alloys have received a great attention for HER in alkaline electrolysers. Jaksic *et al.* [60] investigated Ni-Mo metallic compounds prepared by melting Ni and Mo powders. They mechanically polished the electrodes before the electrochemical test in an attempt to minimize the surface area effects. As shown in Figure 2.6, all Ni-Mo alloys gave better catalytic activities than Ni or Mo with the combination of NiMo having the highest activity towards HER. The study in HER mechanisms on Ni, Mo and NiMo revealed that at low overpotentials ($|\eta| < 0.15$ V) the reaction proceeded through Volmer, Heyrovsky and Tafel steps (Equations 2.22, 2.23 and 2.24), where the Heyrovsky step was more significant than the Tafel step on Ni and vice versa on Mo. On NiMo alloy, however, Heyrovsky and Tafel steps gave similar rates. At high overpotentials ($|\eta| > 0.25$ V) HER proceeded through Volmer and Heyrovsky steps with Heyrovsky being the RDS regardless of the composition. Evaluated C_{dl} values were similar for all electrodes suggesting the improvement in the electrocatalytic performance was due to change in the intrinsic catalytic properties.

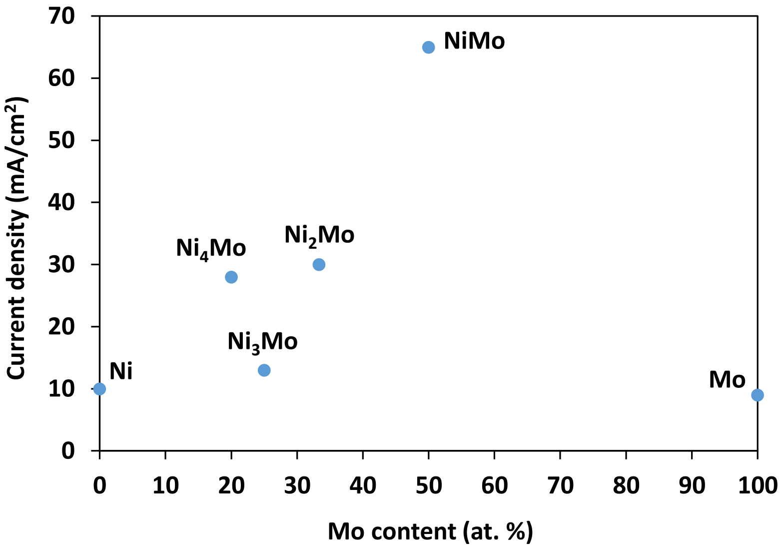

Figure 2.6. The effect of Mo content of Ni-Mo alloys on the current density for HER at an overpotential of -0.4 V in 1 M NaOH solution at 25 ºC, reproduced from [60].

Similarly, Chialvo *et al.* [61] studied HER on smooth Ni-Mo alloys up to 25 at.% Mo concentration. Alloys with 1 and 5 at.% Mo compositions gave similar electrocatalytic activities to that of a Ni electrode, whereas at low overpotentials ($|\eta| < 0.17$ V) alloys with 3, 10, 20 and 25 at.% Mo compositions gave a slightly improved electrocatalytic activity compared to Ni with the order of; 3 at.% Mo ≈ 25 at.% Mo > 10 at.% Mo ≈ 20 at.% Mo. Analogous performance was observed with all electrodes regardless of the Mo content at high overpotentials ($|\eta| > 0.27$ V). They excluded the results from 3 at.% Mo alloy and concluded alloying Ni with Mo could improve the kinetic properties. They related this improvement to a possible synergistic effect resulting from different electronic configurations of the elements on the basis of the Brewer-Engel valence-bond theory. Based on this intermetallic bonding model, alloying transition metals on the left half of the series (e.g. Mo, W, Ti, Zr) having empty or half-filled vacant d-orbitals with a transition metal on the right half of the series (e.g. Ni, Co, Fe), which possesses internally paired non-bonding d-orbitals results in a synergism in the electrocatalysis for the HER [79]. Therefore, alloying Ni, a group VIII metal, with Mo, a VI group metal having less-filled d-orbitals, could improve the electrode performance. However, there was no direct relationship between the electrocatalytic activity and lattice parameters determined for the corresponding alloys.

Kawashima *et al.* [62] investigated various compositions of Ni-Mo and Ni-W alloys prepared by sputter-deposition technique. Figure 2.7 demonstrates the effects of composition on the electrochemical performance. All alloys showed enhanced electrocatalytic activities towards HER compared to Ni and Mo electrodes. The best performance was achieved by the 15 at.% Mo alloy with an overpotential less than a quarter of that of the Ni electrode at 0.1 A/cm^2, which was even lower than that of smooth Pt (Figure 2.7). The estimated exchange current density for this alloy was more than two orders of magnitude higher than that for bulk Ni. They also attributed the high catalytic activity of Ni-Mo alloys to the synergism raised from their electronic configurations. For the Ni-W alloys, however, the effect of W content on the electrode activity was not significant.

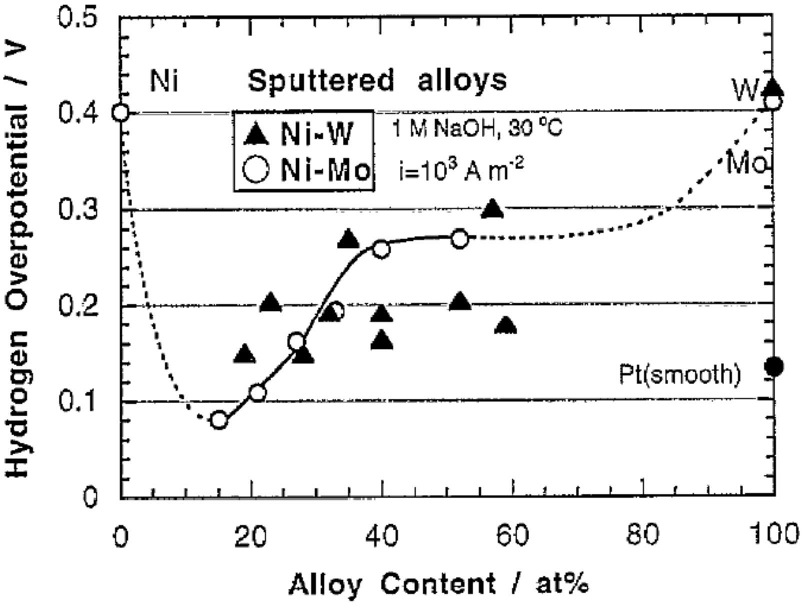

Figure 2.7. Change in the electrode overpotential with respect to Mo and W contents in Ni-Mo and Ni-W alloys respectively [62].

Raj and Vasu [59] compared the electrocatalytic activities of various Ni-based alloys prepared by electro-deposition on steel strips. The electrochemical activities of electrodes were in the following order; Ni-Mo > Ni-Co > Ni-W > Ni-Fe > Ni-Cr > Ni plated steel. They also calculated the activation energies for HER on the alloy deposits using Arrhenius plots (Table 2.1). Lower activation energies achieved by Ni-Mo and Ni-W could be explained by the fact that they lie on the right-hand branch of the Volcano curve (Figure 2.5) where the strengths of M-H bond are higher than those of the left-hand branch containing metals like Ni, Co, Fe and Cr. It must be noted that the effect of different compositions of the alloy coatings was not considered in this study. A more fair comparison could be made if all Ni alloys had the same composition.

Table 2.1. Chemical composition and electrochemical parameters of Ni-based alloys, reproduced from [59].

Alloy deposited on steel	Chemical composition of the alloy coatings (at.%)	Overpotential (|η|) at 300 mA/cm^2 at 80 ºC (mV)	The apparent energy of activation for the HER (kJ/mol)
Ni-Mo	75 % Ni 20 % Mo	150	2.00
Ni-Co	54 % Ni 45 % Co	250	24.22
Ni-W	73 % Ni 25 % W	270	7.66
Ni-Fe	80 % Ni 18 % Fe	300	17.06
Ni-Cr	90 % Ni 7 % Cr	420	19.49
Ni	-	490	-

Divisek and Schmitz [64] investigated the different preparation techniques for Ni-Mo alloys. They did not observe an improvement in the electrode activity with electro-deposited Ni-Mo and Ni-Mo-V alloys with respect to perforated Ni sheet which was used as the supporting material. This was attributed to the low effective surface area of these electrodes although it was not quantified.

Panek *et al.* [56] reported improved electrocatalytic activity with electro-deposited Ni-Ti alloys. The exchange current densities of alloys with 24 and 49 at.% Ti compositions were *ca.* 4 and 9 times higher than that of Ni electrode with a smooth surface. This improvement was explained by developed electrode surface as a result of incorporation of Ti powder into the Ni matrix. The roughness factor increased from 26 to 287 by increasing the Ti concentration from 21 to 49 at.% (Table 2.2). They also examined a Ni-Ti alloy with 24 at.% Ti concentration using coarser Ti grains with an approximate diameter of 150 µm. Its roughness factor was similar to that of alloy with 21 at.% Ti with a smaller grain size. However, R_{ct} decreased from 26 to 2.7 Ωcm^2 by switching the Ti grain size from 150 to 45 µm. This was explained by two possible effects; i.e. presence of non-stoichiometric Ti oxides and pore structure on the surface layer. They suggested that coarser Ti grains resulting in longer and narrower pores could be more beneficial for HER than smaller Ti grains with shorter and wider pores. In addition to this, different ratios of non-stoichiometric Ti oxides on the embedded Ti grains in both layers was proposed as a possible reason for the enhanced activity, as Ti oxides might participate in HER through the following steps;

I. $Ti_4O_3 + 3H_2O + 3e^- \leftrightarrow Ti_4O_3.H_3 + 3OH^-$ (2.26)

II. $Ti_4O_3.H_3 + 3H_2O + 3e^- \leftrightarrow Ti_4O_3 + 3H_2 + 3OH^-$ (2.27)

Table 2.2. Comparison of Ni-Ti alloys with different compositions and Ti grain sizes [56].

Ti composition (at.%)	Ti grain size (µm)	Roughness factor	R_{ct} (Ωcm^2)
21	~45	26	26.0
24	~150	23	2.7
49	~45	287	11.0

Fan *et al.* [67] studied the effect of roughness factor on HER overpotential of electrodeposited binary alloys; $Ni_{8.6}Mo$ (16 wt.% Mo), $Co_{3.7}Mo$ (30.6 wt.% Mo), $Ni_{14.3}W$ (18.1 wt.% W) and $Co_{10.7}W$ (22.6 wt.% W) and compared the results with Ni and Co deposits (Figure 2.8). A linear relationship was recognized where the overpotential decreased with increasing electrode surface area regardless of the composition. For similar roughness factors, Ni-W gave a better performance than Ni with a *ca.* 10 % reduction in the overpotential. Alloys containing Mo gave much higher surface areas than Ni and Co under the deposition conditions. Therefore, the results for Mo-containing alloys were compared with the extrapolated data for Ni and Co deposits, which demonstrated significant performance improvement.

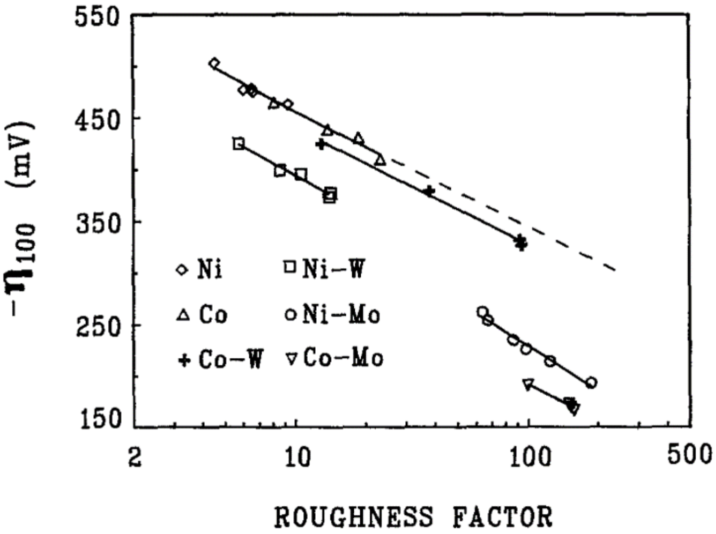

Figure 2.8. Change in HER overpotential (at 100 mA/cm^2) with respect to roughness factor and alloy composition [67].

Improved electrocatalytic activities were also reported for ternary Ni alloys such as Ni-Co-Fe [71], Ni-Co-R (R=Y, Ce, Pr and Er)[72] and Ni-Mo-Cd [80] which were related to synergetic effects as well as increased active surface areas.

2.7. Porous Ni Electrodes for HER

In general, the chemical nature of an electrocatalyst dictates the activity of an electrode. That is why many attempts have been made to improve the electrocatalytic activity of Ni electrodes for HER through the synergistic benefits of alloying it with different metals of interest. However, the physical characteristics/texture of an electrocatalyst are also of importance, since they define the specific activity, accessible surface to the reactants as well as the mass transport dynamics and electrode robustness [81, 82]. Therefore, porous Ni electrodes with increased surface areas have been investigated with a attempt to improve the performance of Ni electrodes for HER.

The most commonly used method to create porous/skeleton/sponge Ni, which is also referred to Raney Ni, was proposed by Murray Raney [83] in 1924 to prepare Ni catalysts for hydrogenation reactions. This technique requires an alloy of Ni and a more reactive metal such as aluminium (Al), which can be dissolved by a solvent without attacking the catalytic properties of Ni [83]. The reactive metal is leached out from the alloy by reacting it with an alkaline aqueous solution under controlled conditions to achieve a porous Ni catalyst with a high surface area. Combinations of Ni-Al and Ni-Zn are often used as starting alloys with a Ni-Al alloy mixture containing Al_3Ni and Al_3Ni_2 with an overall Ni composition of 50 wt.% being the most common option [84, 85].

2.7.1. Preparation Methods for Precursors

Different techniques have been used to obtain a precursor alloy or mixture for porous Ni electrodes for HER;

- electro-deposition of Ni-Zn alloys [86-89],

- electro-codeposition (composite coating) of Ni-Al alloy with deposited Ni [90-94],
- vacuum [95-98] and atmospheric plasma [99] spraying of Ni-Al alloys,
- chemical coating of Al powders [100] or gas-phase coating of Zn [54] on Ni,
- sintering [101] or melting [102-104] the powder mixtures of Ni + Al, Ni-Al alloy + Ni or just Ni-Al alloy,
- pressing and heating [97, 105, 106] or just pressing [105, 107, 108] metallic powders of Ni + Al or Zn, Ni-Mo alloy + Al.

Ni-Zn alloys were often obtained through an electro-deposition in an acidic plating bath containing dissolved Ni and Zn components in the forms of chlorides or sulphates [86-88]. The final composition of the alloy varied according to the initial Ni and Zn contents in the plating bath as well as the deposition current and duration of the electro-deposition [86, 109]. Various deposition currents were reported from 3.6 x 10^{-3} A/cm^2 [89] to 4 x 10^{-2} A/cm^2 [87]. Electro-deposition duration was mostly between 15 and 45 min, although a plating time of up to 24 h [89] was also studied.

Composite coated electrodes were also prepared by electro-codeposition of Ni-Al alloy powder with Ni. A commercially available Ni-Al alloy with a common Ni composition of 50 wt.%, homogenously dispersed in the plating bath, was codeposited on a variety of substrates with deposited Ni [90, 91]. Figure 2.9 demonstrates the cross section of Raney Ni composite-coated electrode. It was suggested that the homogeneity of the alloy particles in the plating bath as well as its particle size were important parameters defining the amount of the codeposited alloy as well as morphology and mechanical strength of the codeposited layer [91].

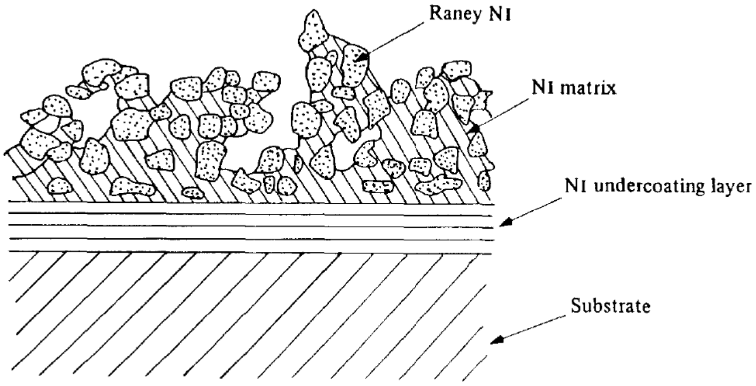

Figure 2.9. Cross-sectional schematic demonstration of Raney Ni composite-coated electrode [90].

Vacuum or atmospheric plasma spraying technique was also used to deposit Ni-Al alloys on a substrate, e.g. perforated Ni sheet. In plasma spraying technique, powdered alloy is introduced into the plasma jet where particles are melted and propelled towards the substrate [110]. Some of authors also used a Ni-Al-Mo ternary alloy or a mixture of Ni-Al alloy and Mo powders as a precursor to improve the electrocatalytic properties of the coatings [95-97].

Tanaka *et al.* [100] coated Al and Sn powders on a Ni wire substrate. Ni wire was painted with the coating suspension containing dissolved polymethyl methacrylate (PMMA) in chloroform together with dispersed Al and Sn powders. Once it was dried under air at room temperature, it was heated at 460 ºC for 30 min then at 660 ºC for 1 h in a vacuum furnace.

In one study, a mixture of Ni powder, Ni oxalate and methyl cellulose suspended in the water was spray-coated onto a Ni wire mesh [89]. Once the coated sample was dried, it was sintered at 900-1000 ºC for about half an hour in a reducing H_2 atmosphere. Methyl cellulose and Ni oxalate were added as a filler and a source of fine Ni powder respectively. Rausch and Wendt [54], on the other hand, used a gas-phase coating technique, where a Ni plate electrode was sherardized at 390 ºC (corresponding to *ca.* 10 Pa of Zn vapour pressure) under a N_2 atmosphere for 8 h.

Alternatively, starting alloys for porous Ni electrodes were prepared through sintering or melting the powder mixtures of Ni + Al, Ni-Al alloy + Ni or just Ni-Al alloy powder. Martinez *et al.* [102] mixed Ni and Al powders by 50-50 wt.% and melted the mixture at 1600 ºC in an induction oven under an Argon (Ar) inert atmosphere. The melted alloy was transferred to a melting pot with a desirable shape where it was cooled down to room temperature. Then, it was sintered at 700 ºC for 24 h under an Ar atmosphere. Hu *et al.* [104] also melted the mixtures of Ni + Al powders with various compositions at 1300 ºC in a vacuum induction furnace. They rapidly quenched the molten samples by spraying them onto a rotation wheel with a cooling rate of 10 ºC/s. Then, they milled the samples to pulverize to different particles sizes.

Rami and Lasia [101] sintered a commercial Ni-Al alloy powder consisting of Al_3Ni and Al_3Ni_2 (with an overall Ni composition of 50 wt.%) at 1400 ºC under high pressure (*c*a. 101.3 MPa) and an Ar atmosphere which gave hard and brittle electrodes. The duration time for sintering, however, was not reported. Los *et al.* [103] heated the same commercial Ni-Al alloy on its own as well as its mixtures with Ni powder at 1600 ºC for 1 h. Commercial Ni-Al alloys, which typically consist of Al_3Ni and Al_3Ni_2, are not ductile or malleable and show slight tensile or compressive strength as well as being friable and easily crumbled [83]. Therefore, Ni powder was added to improve the mechanical robustness of the electrodes. However, the compositions of intermetallic phases formed during sintering of commercial starting alloy and Ni powders were not determined.

Chen and Lasia [105] first mixed Ni and Al powders by 50-50 wt.% and then pressed them under 4250 kg/cm^2 for 5 min at room temperature. They either heated the pressed powder mixtures at 400 ºC or 700 ºC for 18 h under a nitrogen (N_2) atmosphere or leached them directly after they were pressed. Birry and Lasia [97] pressed and then heated powder mixtures of Ni + Al and Ni-Mo alloy + Al at 700 ºC for 12 h under a nitrogen (N_2) atmosphere. The pressing conditions were not reported. Brennecke and Ewe [106] pressed the powder mixture of Ni, Ni-Al alloy, a transition metal and a salt filler at 0.32 t/cm^2 at room temperature followed by heating to 400 ºC and finally hot-pressed them at 0.8 t/cm^2. They did not state the duration for the heating nor pressing. Lastly, Ni + Zn powder mixtures pressed at 19 t/cm^2 for 5 min and at 6 t/cm^2 for 10 min were also used as precursors to create porous Ni electrodes [107, 108].

2.7.2. Leaching Conditions

The selective removal of a reactive metal from an alloy or powder mixture is often carried out in a strong alkaline aqueous solution of potassium hydroxide (KOH) or sodium hydroxide (NaOH). Al remains the most popular choice of a reactive metal due to its relatively higher activity [111]. The leaching reaction for Al proceeds as follows [84];

$$2Al_{(s)} + 2OH^-_{(aq)} + 6H_2O\ (l) \rightarrow 2Al(OH)_4^-{}_{(aq)} + 3H_{2(g)} \qquad (2.28)$$

The reason for using an excess of concentrated alkaline solution is to prevent aluminate ($Al(OH)_4^-$) from precipitating [82, 84, 112]. Aluminates have a tendency to hydrolyse, if the pH falls, forming alumina [84];

$$2\ Al(OH)_4^- + 2H_2O \rightarrow Al_2O_3.3H_2O + 4OH^- \qquad (2.29)$$

Formation of alumina is not desirable as it could block the pores and cover the Ni catalyst surface [84, 102, 112]. Therefore, high concentrations (20-40 wt.%) of aqueous NaOH or KOH solutions are suggested as a leaching solution [84].

Various leaching conditions (Table 2.3) have been used to dissolve Al or Zn in an attempt to create porous Ni electrodes with a high surface area for HER. Leaching temperature varied from room temperature up to 100 ºC, with 70 ºC being the most common option. Similarly, different durations were chosen starting from as low as 30 min to as high as 92 h. A few authors also added K-Na tartrate-tetrahydrate to an aqueous KOH solution, which is a complex builder, as a further action to prevent the precipitation of alumina in the pores [95, 96].

Based on the literature in the corrosion of metals and alloys the etching process in aqueous solutions can result in pitting corrosion [113-115]. As shown in Figure 2.10, pitting corrosion creates pores with different shapes, sizes and depths depending on the precursor properties, the medium and conditions [116]. This implies that the leaching conditions used to prepare porous Ni electrodes can have an influence on the pore morphology created during the leaching of Al. However, the effect that this has on the electrochemical performance for HER in alkaline electrolysers has not been reported.

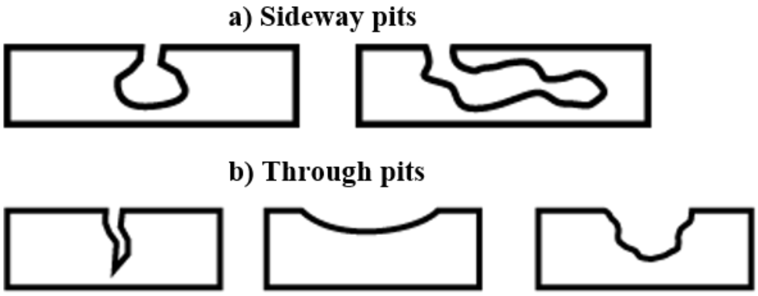

Figure 2.10. Examples of pores/cavities created during the pitting corrosion where (a) sideway pits and (b) through pits [117].

Table 2.3. Summary of leaching conditions used to create porous Ni for HER.

Metal leached	Leaching Temperature	Leaching Solution	Duration	Reference
Al	20-60 ºC	0.2310-0.6931 M NaOH	Not mentioned	[104]
	25-75 ºC	0.51 M- 9.14 M NaOH	100 s-92 h	[94]
	70 ºC	30 wt.% NaOH	24 h	[105, 107]
			18 h	[93]
			1 h or 2 h	[101, 103]
		6.25 M NaOH	1 h	[91]
		6 M NaOH	30 min or 3 h	[102]
		1.04 M NaOH	18 h	[92]
		30 wt.% KOH containing 10 wt.% of K-Na tartrate	24 h	[97]
		6 M KOH	1 h	[118]
	80 ºC	30 wt.% KOH containing 10 wt.% of K-Na tartrate	24 h	[96, 99]
		6 M KOH	24 h	[106]
		25 wt.% KOH containing 10 wt.% of K-Na tartrate	24 h	[95]
	90 ºC	35 wt.% NaOH	1 h	[90]
		6 M NaOH	Until no more H_2 gas evolved	[100]
	100 ºC	20 wt.% NaOH	Not mentioned	[119]
		30 wt.% NaOH	5 h	[120]
Zn	room temperature	10 M KOH	8 h	[87]
		28 wt.% KOH	10 h	[121]
	70 ºC	30 wt.% NaOH	24 h	[107, 108]
			4 h	[88]
		28 wt.% KOH	24 h	[86]
	~75 ºC	30-40 wt.% KOH	Not mentioned	[89]
	boiling point	40 wt.% KOH	10 h	[54]

2.7.3. Storage and Handling

After leaching, the electrocatalysts exhibit pyrophoric behaviour due to the hydrogen chemisorbed/trapped on the inner surface of porous Ni [106] and/or small metal crystallites formed during leaching [84]. If the catalyst is dried in air, the rapid oxidation of metal particles can produce large amounts of heat which could lead to combustion [84]. Consequently, they must be stored in a liquid. However, they can passivated through the controlled oxidation of electrodes when dried material is required [81].

The majority of the researchers did not mention about their procedures for rinsing, storing and oxidizing the electrodes prepared for HER after they were leached. Sheela *et al.* [87] treated the electrodes in boiling water for 4 h after leaching in a attempt to remove the products left on the surface. Devred *et al.* [112] washed the catalysts six times in distilled water with a maximum rinsing duration of 5 min. They observed hydrogen evolution during rinsing, which took place in less than 5 min.

Sheela *et al.* [87] and Schiller *et al.* [95] stored the electrodes in distilled water at room temperature after leaching, whereas Song *et al.* [119] used ethanol at room temperature as a storage liquid. Alternatively, Choquette *et al.* [94] and Martinez *et al.* [102] stored the electrodes under an inert Ar atmosphere.

Choquette *et al.* [94] oxidized the electrodes by immersing them in distilled water saturated by dissolved O_2 for about 2 h, whilst Martinez *et al.* [102] let leached electrodes oxidize slowly in deionizer water for 24 h. Schiller *et al.* [95] and Brennecke *et al.* [106] also slowly oxidized the leached layers through a controlled introduction of a low concentration of O_2. Needes [122] suggested another chemical treatment method to eliminate the pyrophoricity of porous Ni after leaching. The procedure involved immersing it for 1-4 h in a dilute aqueous solution, e.g. 3 wt.% $NaNO_3$, 3 wt.% $K_2Cr_2O_7$ or 3 wt.% $NaClO_3$+ 10 wt.% NaOH.

2.7.4. Electrochemical Performance

Electro-deposited electrodes

In general, improved electrocatalytic activities for HER were reported with porous Ni-based electrodes obtained from leaching Zn from electro-deposited Ni-Zn alloys. Santos *et al.* [86] reported *ca.* 20 % less electrode overpotentials with a Ni (Zn) porous electrode initially containing *ca.* 30 at.% Zn compared to that of only Ni electrodeposited electrode (tested in 28 wt.% KOH electrolyte solution at 70 ºC). However, they did not investigate the surface characteristics of these electrodes. Chen and Lasia [88] prepared Ni-Zn electrodes with different initial Zn compositions from 30 to 72 wt.% by varying the deposition voltage. After leaching Zn, HER overpotential showed a downward trend with increasing initial Zn content, with the electrode containing 72 wt.% Zn before leaching giving the lowest overpotential (Figure 2.11). They explained this improvement with increased electrode surface area through an increase in the porosity. This was confirmed by the scanning electron microscopy (SEM) images showing more small cracks on electrodes with increasing Zn content (Figure 2.12). However, the change in the porosity and corresponding increase in the surface area were not quantified and the characteristics of micropores (< 2 nm) and mesopores (2-50 nm) were not investigated. In addition, the final compositions of electrodes after leaching were not reported. Estimated roughness factors for the electrodes with 30 and 72 wt.% Zn contents were almost 60 and 600 times higher than that of a polycrystalline Ni electrode respectively. They also corrected the experimental exchange current densities (based on geometric surface area) of each electrode by dividing them with the surface roughness. The corrected values were slightly lower than that of a smooth Ni suggesting only the increase in the surface area was responsible for improved activity towards HER.

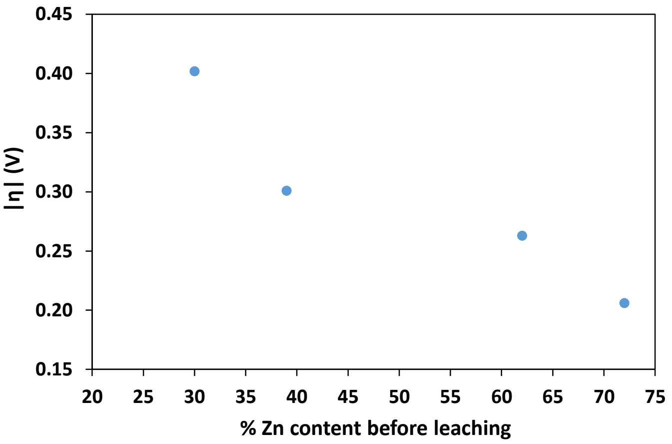

Figure 2.11. HER overpotentials measured at a current density of 250 mA/cm^2 in 1 M NaOH at 25 ˚C with respect to Zn content after deposition, reproduced from [88].

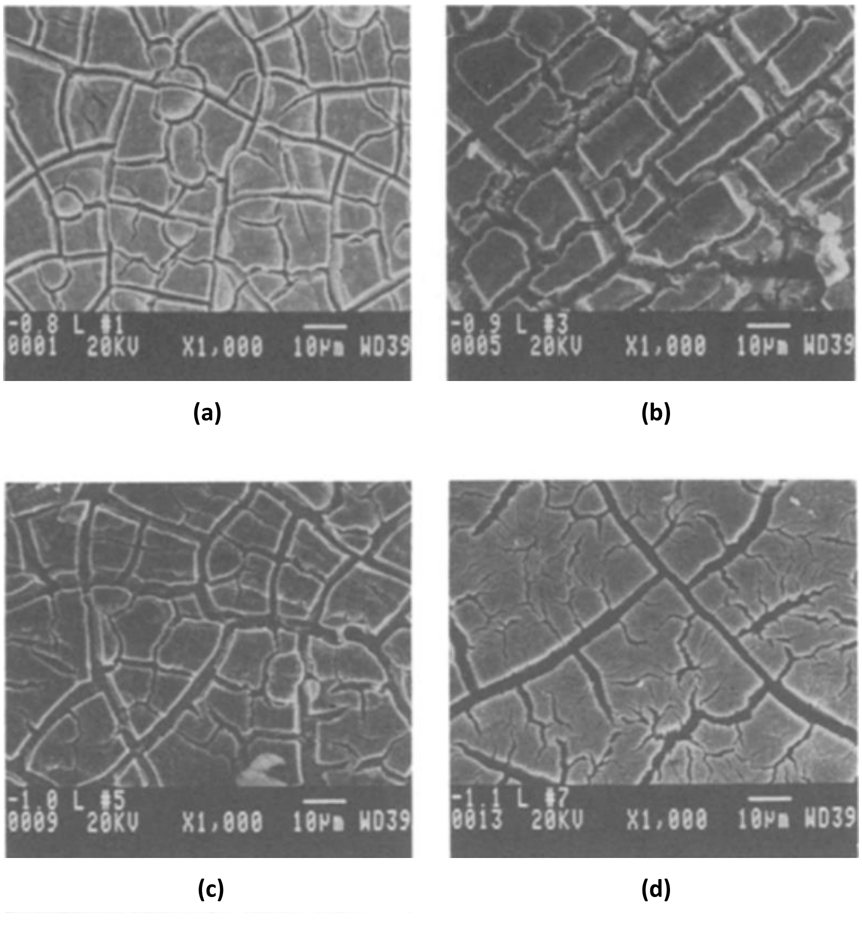

Figure 2.12. SEM images of Ni-Zn electrodes after leaching Zn in 30 wt.% KOH at 70 ºC for 4 h where the electrodes prepared from a Zn composition of (a) 30 wt.%; (b) 39 wt.%; (c) 62 wt.%; (d) 72 wt.% [88].

Similarly, Sheela *et al.* [87] also investigated the performance of electro-deposited Ni-Zn electrodes with different compositions, however they reported an opposite trend in the overpotential (Figure 2.13). Apart from the alloy with 25 wt.% Zn present, overpotential rose with increasing Zn content. The highest activity was recorded for the alloy with a 50 wt.% Zn composition which contained the phases of Ni_3Zn_{22}, Ni_5Zn_{21} and NiZn after the electro-deposition. Only Ni_3Zn_{22} was detected for the alloy consisting of 85 wt.% Zn before leaching. They analysed the alkaline solutions after leaching via an atomic absorption spectroscopy (AAS) to identity the amounts of Zn and Ni dissolved. As shown in Table 2.4, leaching was inefficient with the alloy containing 25 wt.% Zn, which explained its similar electrochemical performance to the Ni electrode. The leaching efficiency of Zn was 88 ± 2 % for the alloys containing ≥ 50 wt.% Zn content. Improved activities were attributed to the formation of small cracks (confirmed by the SEM images) which could provide a greater surface area for the reaction and shorter diffusion paths for H_2 gas release. However, the size of these cracks were not clarified nor the pore size distribution. Lower overpotentials with increasing Ni content up to 50 wt.% was explained by increasing Ni surface area. They concluded that the remaining Ni was not sufficient enough after leaching alloys with 85 and 75 wt.% Zn to form a continuous porous structure with smaller cracks. It is likely that the remaining Zn on the surface might be reducing the catalytic activity of the electrodes.

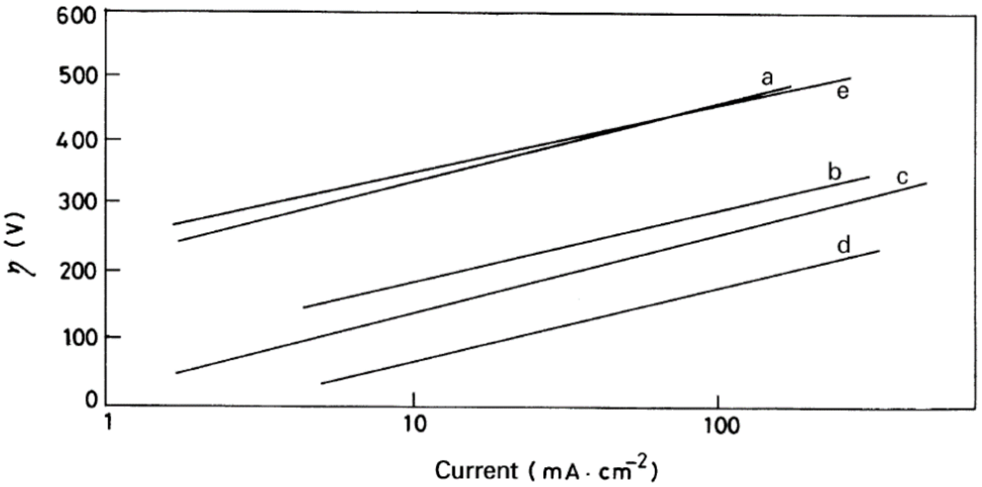

Figure 2.13. Overpotential-current density curves in 6.25 M NaOH at room temperature for alloys after leaching, where the compositions of electrodes before leaching were (a) Ni; (b) 15 wt.% Ni-85 wt.% Zn; (c) 25 wt.% Ni-75 wt.% Zn; (d) 50 wt.% Ni-50 wt.% Zn and (e) 75 wt.% Ni-25 wt.% Zn [87].

Table 2.4. Change in the compositions of electrode-deposited Ni-Zn alloys after leaching, reproduced from [87].

Electrode composition after deposition	wt.% Zn dissolved	wt.% Ni dissolved	Zn composition after leaching (~wt.%)
15 wt.% Ni-85 wt.% Zn	90.7	27.6	42
25 wt.% Ni-75 wt.% Zn	87.8	26.6	30
50 wt.% Ni-50 wt.% Zn	86.3	24.9	15
75 wt.% Ni-25 wt.% Zn	5.8	1.2	24

Ragunathan *et al.* [89] compared the characteristics of an electro-deposited Ni-Zn electrode to those of a porous Ni electrode prepared by spray-coating a mixture of Ni powder, Ni oxalate and methyl cellulose suspended in the water onto a Ni wire mesh followed by sintering at 900-1000 ºC for about half an hour in a reducing H_2 atmosphere. After leaching, electro-deposited electrodes showed widespread cracks and channels, and very fine deposit grains. An aggregate of sintered particles with high porosity and open structure was observed with the sintered electrodes. Electrodes prepared by both methods showed good adherence and had a porosity and surface area in the ranges of 65-75 % and 3-5 m^2/g respectively. They concluded that powder methodology is easier and more economical than electro-deposition for large scale applications. Similarly, Wendt *et al.* [123] and Rausch and Wendt [54] also highlighted the challenge with the electro-deposition technique. Since the Zn content of the deposited electrodes are highly sensitive to electrodeposition conditions, such as the Ni to Zn ratio in the solution, the deposition current, temperature and mass transfer limitations, a precise control of these parameters is necessary to achieve and reproduce an alloy with an exact Zn content.

Composite-coated electrodes

Porous Ni electrodes prepared by the electro-codeposition (composite coating) of a commercial Ni-Al alloy (with 50 wt.% Ni composition) with a deposited Ni layer followed by leaching of Al also yielded improved electrocatalytic activities. Figure 2.14 demonstrates the performance improvement reported by Endoh *et al.* [90] on a porous Ni electrode in comparison to untreated and sandblasted Ni. They attributed this significant improvement to the increase in the surface area. They suggested that not all small pores might be effectively used during HER due to mass transport limitations and they intended to prove this by estimating the electrochemically active surface area from the C_{dl} measurement. However, due to the highly porous structure of composite-coated electrodes they found this technique to be invalid as measured C_{dl} did not linearly correlate with the electrochemical active surface area. It must be noted that the composition and porosity characteristics of the final catalyst were not investigated.

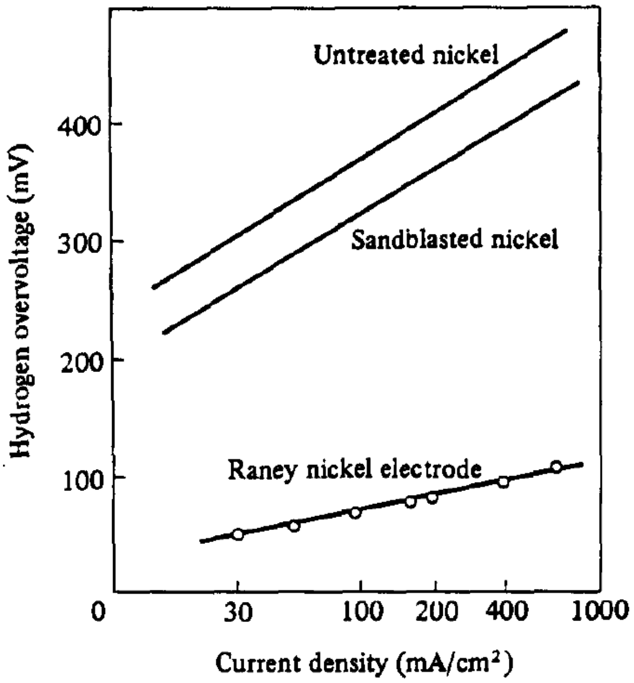

Figure 2.14. HER overpotentials for Ni and porous Ni electrodes in 35 wt.% NaOH at 90 °C [90].

Choquette *et al.* [91] studied the effect of the amount of codeposited Ni-Al alloy (with an overall Ni composition of 50 wt.%) on the electrodeposited Ni. As shown in Table 2.5, adding 31.7 wt.% alloy reduced the electrode overpotential by more than 2 times, which was attributed to the increased porosity created during leaching. The Brunauer, Emmett and Teller (BET) surface area was *ca.* 8 m^2/g which was *ca.* 2100 times higher than the geometric surface area. However, the characteristics of pores were not investigated. Increasing the alloy ratio from 31.7 to 43.1 wt.% only gave a slight improvement. It must be noted that the margin of error was not reported, compositions of phases present before and after leaching were not determined and it was assumed that all Al was dissolved during leaching. They also investigated the effect of particle size and codeposition time. The electrodes prepared from the alloy particle sizes of $\leq$ 38 µm and in the range of 53-74 µm gave similar electrochemical performance. However, the coarser electrodes showed more disintegrations during leaching resulting in more fragile electrodes, whereas disintegration was not observed when the alloy particle size was less than *ca.* 38 µm. Increasing the codeposition time improved the electrochemical performance up to 30 min, above which overpotential rose with increasing duration.

Table 2.5. Change in the electrochemical performance with respect to amount of composite-coated alloy, reproduced from [91].

Ni-Al content after composite-coating (wt.%)	0	31.7	35.9	36.9	42.5	43.1
Overpotential measured at 250 mA/cm^2 in 1 M KOH at 25 ºC (V)	0.528	0.223	0.226	0.206	0.202	0.203

Choquette and Brossard [94] investigated the effect of leaching conditions in the morphology and composition of composite-coated electrodes by using the techniques of SEM, XRD, electron probe X-ray microanalysis (EPMA), energy dispersive X-ray microanalysis (EDX) and inductively coupled plasma atomic emission spectroscopy (ICP-AES). They observed that 50 wt.% of Al initially present in the electrodes, consisting of 20 wt.% Al_3Ni and 80 wt.% Al_3Ni_2, was leached after 10000 s creating holes in the structure. After this duration, SEM images showed similar morphology regardless of the leaching time despite continuum Al dissolution which reached to 85-95 wt.% after 18 h of leaching. Based on the XRD results, they concluded that Al was first dissolved from Al_3Ni transforming it into Al_3Ni_2. After 1000 s of leaching they did not detect a peak associated with Al_3Ni, while a maximum peak height was reached for Al_3Ni_2. After this point, the peak height of the Al_3Ni_2 phase started to reduce and disappeared after 10000 s of leaching. They also detected small peaks associated to $Al(OH)_3$ after leaching for 10000 s. Leaching duration of 18 and 92 h gave only Ni phase in the XRD spectrum. They suggested that $Al(OH)_3$ might transform into $Al_2O_3.3H_2O$ as the leaching duration was increased. Regardless of the leaching duration and different intensities of phases detected by XRD, all electrodes gave similar electrochemical activities towards the HER. They attributed this to the dominant effect of electrodeposited Ni on the hydrogen discharge. They suggested that H_2 bubbles formed inside pores of leached Ni-Al alloy particles might prevent the electrolyte solution from penetrating inside the pores. They also discussed about possible pore blocking due to solid product(s) accumulating during the leaching process.

Choquette and Brossard [94] also studied the effect of leaching conditions. They reported increased reaction rates with increasing leaching temperatures from 25 to 55 ºC in 1.04 M NaOH. They also compared the leaching rate of their composite-coated electrodes with the results obtained from leaching a Ni-Al alloy powder. The slower leaching process with the composite-coated electrodes was related to possible mass transport limitation through the electrodeposited porous Ni surrounding the alloy particles.

The HER mechanism on Ni-Al composite-coated electrodes was also investigated through impedance measurements [92, 93]. Volmer-Tafel mechanism was found to be the easiest pathway for HER on these electrodes with the Volmer reaction being the RDS with a small contribution of the Heyrovsky reaction [92]. The mechanism changed to the Volmer-Heyrovsky when the electrodes were electrochemically oxidized after the leaching. The Volmer and Heyrovsky reactions were both RDSs in the case of electrochemically oxidized electrodes [92, 93].

Plasma sprayed electrodes

Chade *et al.* [99] investigated the performance of plasma sprayed electrodes with different thicknesses of Ni-Al alloy layer, i.e. 30, 100 and 300 µm. Compared to the smooth Ni with 1 cm^2 surface area, they reported significantly higher electroactive areas (Table 2.6), which was attributed to a substantial increase in the porosity after leaching which was confirmed by SEM analysis. Although increasing the coating layer from

30 to 100 µm gave *ca.* 5 times higher surface area, 300 µm alloy thickness gave only a slight increase compared to 100 µm. They explained this by inefficient leaching of the alloy with 300 µm thickness. The calculated kinetics data from current-voltage curves and impedance measurements were also in agreement with the CV results, although a slight increase in R_{ct} was reported from 100 to 300 µm thickness. This was attributed to the blockage caused by H_2 bubbles. However, a possible influence of composition on electrochemical performance was not considered. Since the leaching efficiency was suggested to be low with the 300 µm thickness, it is highly likely that remaining Al phases might influence the electrochemical activity.

Table 2.6. Comparison of plasma sprayed electrodes with different alloy thicknesses, reproduced from [99].

Alloy thickness before leaching (µm)	Electroactive area measured by CV (cm^2)	i_0 at 30 ºC (A/cm^2)	R_{ct} calculated at 30 ºC (Ωcm^2)
30	480	0.00031	9.075
100	2436	0.0123	0.208
300	2696	0.0176	0.332

Schiller *et al.* [95] investigated the plasma sprayed electrodes prepared from different precursor alloys. As demonstrated in Figure 2.15, plasma sprayed electrodes gave significantly higher activities towards HER compared to a perforated Ni sheet. Addition of Mo to the precursor alloy either by allowing it to obtain a Ni-Al-Mo ternary alloy or by mixing powders proved to be beneficial for the electrode performance. This was attributed to the synergetic effects between Ni and Mo discussed earlier.

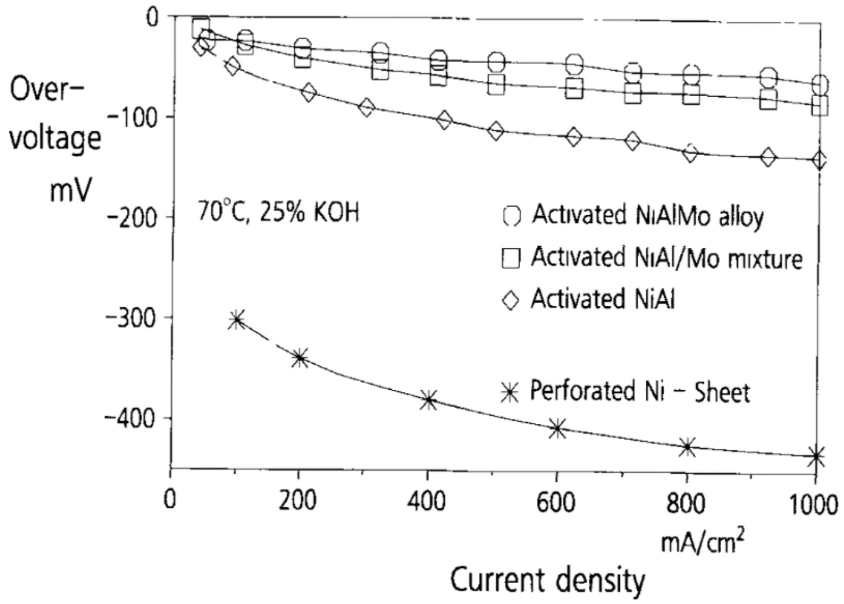

Figure 2.15. The effect of precursor alloys in the HER activity of plasma sprayed electrodes in 25 wt% KOH at 70 ºC [95].

Heat-treated electrodes

Martinez *et al.* [102] investigated HER on electrodes prepared by melting a mixture of Ni and Al powders (50 wt.% each) at 1600 ºC followed by annealing at 700 ºC for 24 h. They leached the samples either for 30 min or 3 h and compared the results with unleached electrodes. Figure 2.16 shows the change in the morphology of electrodes with leaching. Two distinguishable phases with dark and light grey before leaching were attributed to Al_3Ni and Al_3Ni_2 phases respectively. After leaching, the pores and cracks were formed. The XRD patterns proved the presence of only Al_3Ni and Al_3Ni_2 phases even after 3 h leaching with decreased intensities. Electrodes with 30 min of leaching gave an overpotential *ca.* 24 % lower than that with the unleached sample, whereas increasing the leaching time from 30 min to 3 h decreased the overpotential by *ca.* 7.5 % at a current density of 0.15 A/cm^2. However, the increase in the exchange current densities with the leaching time was not significant; 0.00121 A/cm^2 (unleached), 0.00134 A/cm^2 (leaching for 30 min) and 0.00170 A/cm^2 (leaching for 3 h).

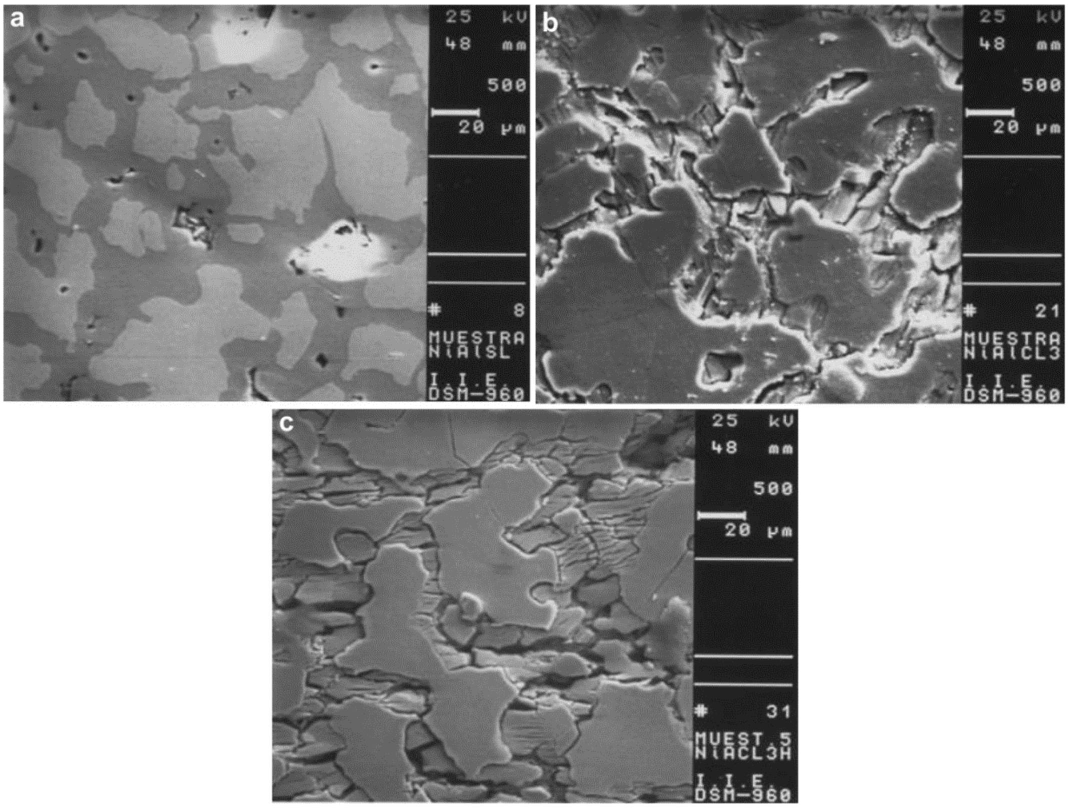

Figure 2.16. SEM images of heat treated electrodes before and after leaching; (a) before leaching (b) leached for 30 min (c) for 3 h in 6 M NaOH solution [102].

Rami and Lasia [101] sintered a commercial Ni-Al alloy containing 50 wt.% Ni at 1400 ºC under high pressure (*ca.* 101.3 MPa) and leached it in 30 wt.% NaOH aqueous solution for 1 h at 70 ºC. The roughness was of the order of 20000, which was 2.5-10 times higher than those of composite coated electrodes. The exchange current density of this electrode was *ca.* 17000 times higher than that of a polycrystalline Ni electrode. However, the electrode was very fragile and not feasible for industrial applications. They also suggested that the concentration polarization in narrow pores or blocking of the electrode surface by the generated hydrogen bubbles might be occurring during the reaction based on the non-linearity of Tafel curves that was observed with as-leached electrodes. Non-linear Tafel plots were also reported by Tanaka *et al.* [118] after leaching of Al from Al_3Ni and Al_3Ni_2 phases.

Los *et al.* [103] investigated the HER activity of electrodes prepared by melting Ni-Al alloy (with 50 wt.% Ni) and Ni powder together in different ratios. After leaching, the electrode with 80 wt.% alloy composition (a total Ni content of 60 wt.%) gave an overpotential of 0.182 V at 250 mA/cm^2 in 1 M NaOH electrolyte solution at 25 ºC, which was almost 3 times less than that of the 60 wt.% alloy composition. The lower activity with the 60 wt.% alloy composition was attributed to the possible formation of AlNi during the heat treatment which might be resistant to the leaching process. However, they did not study the microstructural properties of the electrodes. Although electrode performance was improved by adding more alloy, they reported a decreasing robustness with increasing initial Ni-Al alloy content. The electrode with 80 wt.% alloy composition disintegrated during HER.

Hu *et al.* [104] studied the leaching process on rapidly quenched samples (prepared from mixtures of Ni and Al powders melted at 1300 ºC in a vacuum induction furnace) with respect to various parameters including alloy composition, particle size, leaching temperature and solution concentration. As expected, increasing Al content in the alloy gave a higher H_2 generation rate during leaching. The effect of particle size was studied on alloys (80 wt.% initial Al) with a particle size range of 31.8-173.6 µm. Larger particle sizes gave lower leaching rates, which was explained by the decrease in the reaction area per same amount of alloy with larger particle size. The leaching rate for a 31.8 µm particle size was 2.5 times higher than that of the 173.6 µm particle size. They also reported improved leaching rate in higher alkaline concentrations. However, it must be noted that they only investigated the concentrations of NaOH between 0.231 and 0.693 M, which was an unusual concentration range for a leaching process, since highly concentrated alkaline solutions have been advised for the removal of Al [84, 102]. The temperature was also found to be significant on the leaching rate, which was almost 13 and 6 times higher at 60 ºC than those at 20 and 30 ºC respectively. They concluded that leaching process on their samples could be explained by a reaction-controlled shrinking core model. They attributed this to the homogeneous microstructure and highly populated structural defects within the alloy resulting from the rapid quenching method. However they did not investigate the performance of the electrodes for HER nor the porosity characteristics.

The electrocatalytic activities towards HER were also investigated on pressed and heated electrodes. Chen and Lasia [105] studied two different heating temperatures; 400 and 700 ºC for Ni and Al powder mixtures with a 50 wt.% Ni content. Figure 2.16 shows the SEM images of electrodes before and after leaching. Heating at 400 ºC did not change the microstructure of the electrodes significantly in comparison to only pressed samples (Figure 2.17). XRD analysis showed only Ni and Al peaks for these samples before leaching. After leaching, the porosity of electrode heated at 400 ºC was slightly higher than that of as-pressed electrode. As shown in Figure 2.16, heating at 700 ºC resulted in a different microstructure with an increased porosity after leaching. The XRD patterns proved the presence of Al_3Ni and Al_3Ni_2 before leaching, whilst Al and Ni were no longer detected. This was attributed to the diffusion of molten Al into Ni forming the intermetallic phases of Al_3Ni and Al_3Al_2. The best electrochemical performance was reported for the electrode heated at 700 ºC (Table 2.7) due to the increased surface area resulting from leaching of Al from Al_3Ni and Al_3Ni_2. Although XRD results for 400 ºC heating did not show the presence of any intermetallic phases before leaching, they suggested that improved activity compared to as-pressed electrodes might be due to some interdiffusion of Al into Ni at the surface layer resulting in a slightly higher surface area after leaching. However, the surface area and porosity characteristics of electrodes were not quantified to correlate their trends with that of the electrocatalytic activity.

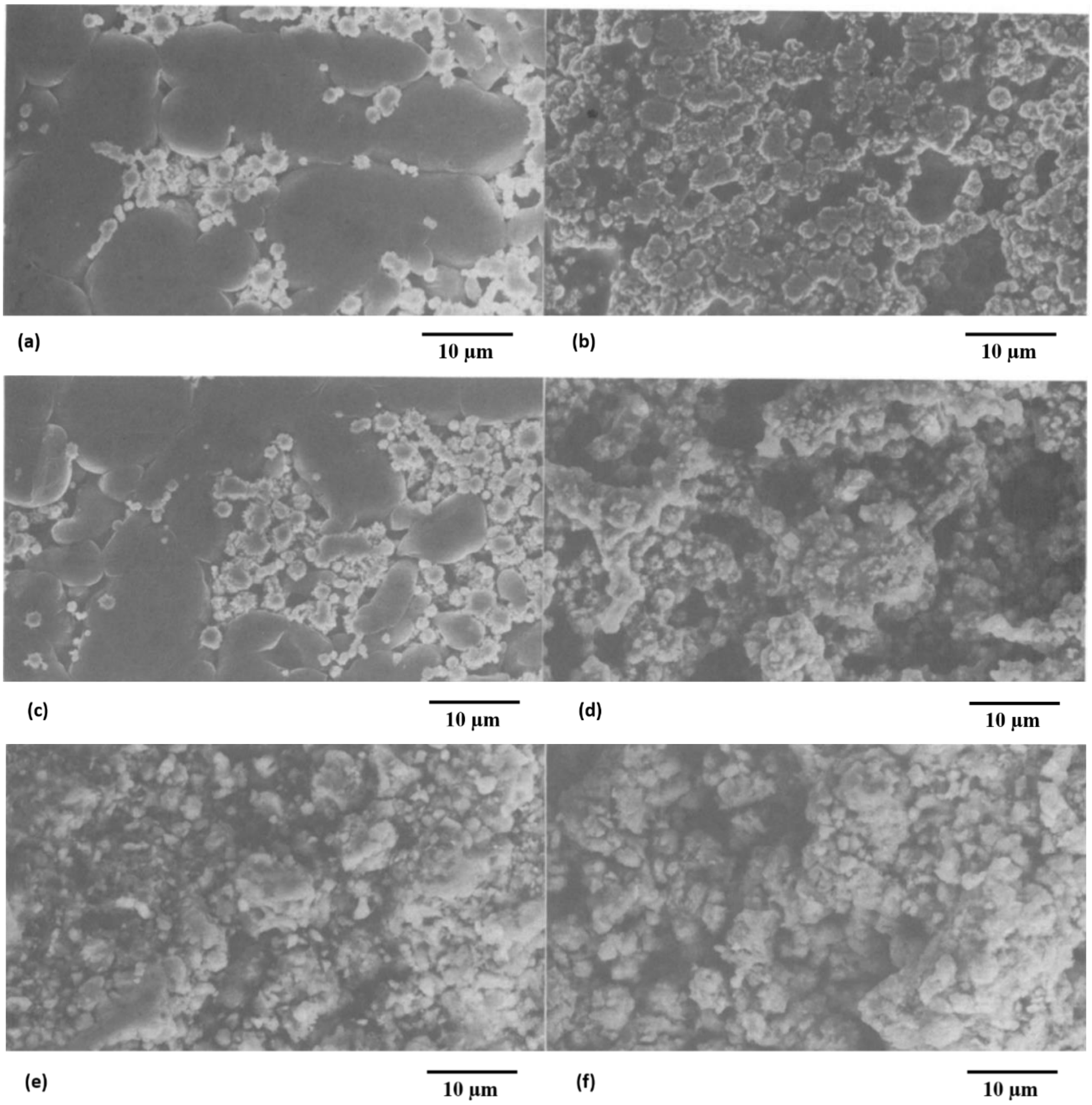

Figure 2.17. SEM images of electrodes prepared by mixing Ni and Al powders (with a Ni content of 50 wt.%), where (a) as-pressed electrode before leaching; (b) as-pressed electrode after leaching; (c) electrode heated at 400 ºC before leaching; (d) electrode heated at 400 ºC after leaching; (e) electrode heated at 700 ºC before leaching; (f) electrode heated at 700 ºC after leaching [105].

Table 2.7. Comparison of electrocatalytic activities of pressed and heated Ni-based electrodes in 1 M NaOH solution at 25 ºC, reproduced from [105].

Electrode	Only pressed	Pressed and heated at 400 ºC	Pressed and heated at 700 ºC
Overpotential at 250 mA/cm^2 (V)	0.363	0.293	0.128
Log i_0 (A/cm^2)	-3.20	-2.84	-2.02

Pressed electrodes

Hitz and Lasia [107] studied the performance of pressed electrodes prepared from Ni and Al or Zn powders. Increasing the Zn content of the mixture from 50 to 70 wt.% only gave a slight improvement in the electrode activity after leaching (Table 2.8). Electrode prepared with 50 wt.% Al was more active towards HER than those with 50 and 70 wt.% Zn contents. This was explained by the increased surface area based on the roughness results calculated from the impedance measurement. However, they did not investigate the microstructural properties of the electrodes.

Table 2.8. Kinetic parameters for pressed powder electrodes in 1 M NaOH at 25 ºC, reproduced from [107].

Electrode	Overpotential at 100 mA/cm^2 (V)	Log (i_0) (A/cm^2)	R_{ct} at -0.15 V (Ωcm^2)	Roughness
Ni: Zn (50:50 wt.%)	0.301	-3.40 ± 0.03	8.64	5700
Ni:Zn (30:70 wt.%)	0.285	-3.19 ± 0.04	8.01	6300
Ni:Al (50:50 wt.%)	0.268	-2.66 ± 0.04	1.72	6800

Chen and Lasia [108] also studied HER on pressed mixtures of Ni and Zn powders. They reported an increasing activity with higher Zn contents in the mixture (Figure 2.18) which was explained by the increase in the porosity based on the SEM images. In comparison to electrodeposited Ni-Zn electrodes, they were less active towards HER and the leaching time was 6 times longer.

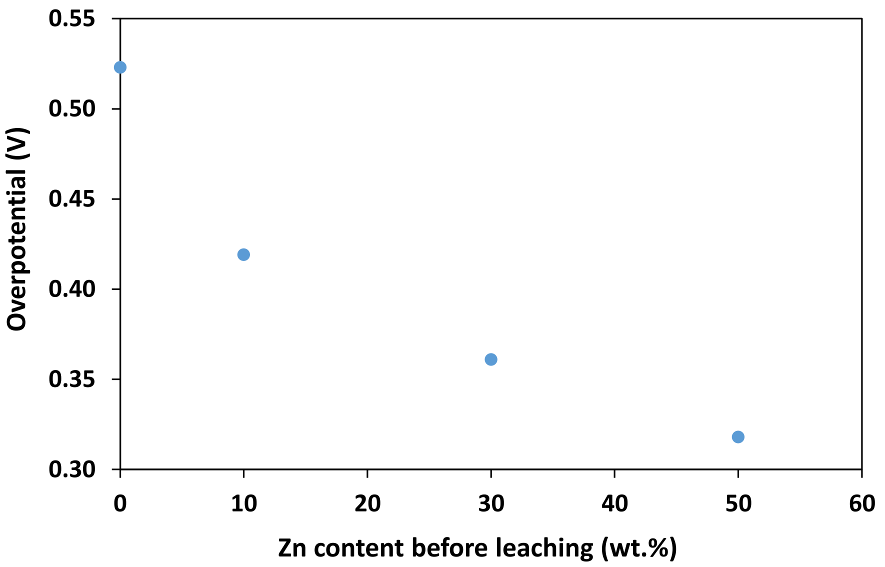

Figure 2.18. The effect of initial Zn content on the HER overpotential at 250 mA/cm^2 in 1 M NaOH at 25 ºC, reproduced from [108].

Brennecke and Ewe [106] investigated the performance of porous Ni electrodes prepared by mixing a porous Ni, i.e. Ni T255 and Ni-Al alloy (with 50 wt.% Ni) powders with a weight ratio of 3:2. The mixture was hot-pressed after heating at 400 ºC. After leaching, the electrode has a BET surface area of *ca.* 100 m^2/g and porosity of *ca.* 77 %. They reported that the total porosity increased only by *ca.* 10 % after the removal of Al compared to electrodes prepared by only Ni T255. Although they mentioned about adding a salt filler (Na_2CO_3) to the metallic powder mixture, they did not report any information about the effect of using this filler on the microstructural and electrochemical properties. It was not clear whether improved electrocatalytic activity of leached electrodes compared to smooth Ni electrodes was mainly due to the macroporous Ni T255 structure or microporosity created during the removal of Al.

2.7.5. Overview

Porous Ni electrodes with increased surface areas gave improved electrocatalytic activities towards HER compared to smooth Ni electrodes. Several techniques have been used to prepare the precursors, which were then treated in an alkaline solution to create a porous structure. Since different electrochemical test conditions were chosen by different authors, it was not possible to make a direct comparison of the performance. Table 2.9 only compares the ones tested in 1 M NaOH or KOH electrolyte solution at 25 ºC. For the same composition, using Ni-Al precursors instead of a Ni-Zn combination resulted in more active electrodes. This can be explained by Al having a relatively higher activity towards alkaline solutions than Zn, resulting in a more efficient leaching with Al and hence a greater surface area.

In general, the lowest overpotentials were recorded with the electrodes prepared from a precursor containing a commercial Ni-Al alloy. This is due to the presence of Al_3Ni and Al_3Ni_2 in the starting Ni-Al alloy mixture. It has been shown that the leaching of Al from the intermetallic phases of Al_3Ni and Al_3Ni_2 resulted in a greater surface area than that created during the leaching of Al from a mixture of Al and Ni metals. However, a detailed analysis on the porosity characteristics has not been reported for the comparison of porous electrodes prepared from different compositions of precursor phases. It must be also noted the electrodes compared in Table 2.9 were treated under different leaching conditions which might also affect the activity of the final product through the change in the composition and/or porosity characteristics.

Table 2.9. Comparison of porous Ni electrode overpotentials measured in 1 M NaOH or KOH electrolyte solution at 25 °C.

Powder Mixture	Electrode preparation method	Overpotential at 250 mA/cm^2 (V)	Composition after leaching	Porosity	Reference
Ni-Al alloy (15-18 mg/cm^2) on deposited Ni	Composite-coating	0.217	Ni and Cu as a substrate (not quantified)	Not quantified	[94]
Ni-Zn alloy with 72 wt.% Zn	Electro-deposition	0.206	Not reported	Increased porosity from 30 to 72 wt.% Zn based on SEM images (not quantified)	[88]
Ni-Zn alloy with 30 wt.% Zn		0.402	Not reported		
Ni-Al alloy (50 wt.% Ni) + Ni with 50 wt.% alloy	Heat treatment	0.174	Not reported	Not reported	[103]
Ni-Al alloy (50 wt.% Ni)	Heat treatment	0.186	Ni	Not quantified	[101]
Ni + Al with 50 wt.% Al	Heat treatment	0.128	Ni	Not quantified	[105]
Ni + Al with ~54 wt.% Al	Heat treatment	0.253	Ni (containing an Al content)	Not quantified	[97]
Ni-Al alloy (50 wt.% Ni)	Pressing	0.156	Not reported	Not reported	[103]
Ni + Al with 50 wt.% Al	Pressing	0.363	Ni	Not quantified	[105]
Ni + Zn with 50 wt.% Zn	Pressing	0.301	Not reported	Not quantified	[107]
Ni + Al with 50 wt.% Al		0.268	Not reported	Not quantified	

Better electrocatalytic activities were usually reported with increasing Al or Zn content in the precursor due to the higher surface area created during the leaching. However, there was a trade-off between the activity and robustness of the electrodes. It must be noted that a few researchers observed a decrease in the electrode activity with decreasing initial Ni content, while some did not report a significant change. The final compositions of the electrodes after leaching were not analysed by most of the studies.

In general, an increase in the Al leaching reaction rate was observed with higher leaching temperatures. However, the effect that this could have on the electrochemical activity of porous electrodes leached at different temperatures have not been investigated for HER in alkaline electrolysers. It is likely that a possible change in the pore structure resulting from different leaching rates might influence the use of these pores during the reaction. Some authors discussed about the possible inefficient use of pores during HER due to generated H_2 being trapped inside the pores and reducing the accessibility of pores to the electrolyte solution. However, a detailed analysis of the effect of pore morphology on the electrochemical activity of porous electrodes in alkaline electrolysers has not been reported.

2.8. Summary

The main focus of this literature review is on Ni-based electrocatalysts for HER in alkaline electrolysers. A great deal of studies have been made to improve the electrocatalytic activity of Ni-based electrodes for HER by alloying it with different metals in an attempt to benefit from the synergetic effects resulting from different electronic configurations and/or hydrogen adsorption properties. Although enhanced activities were achieved on some alloys such as Ni-Mo and Ni-Ti, there was not a consistency in the trends studied by different researchers on similar alloys and a definite rationalization was not agreed upon for the explanation of electrocatalytic activity of alloys. Some studies concluded increased surface areas resulting from the alloy preparation process could be partially or mainly responsible for the improvement in the activity.

Since the textural properties of an electrocatalyst is also of importance for its performance as its chemical nature, some researchers have investigated the performance of porous Ni electrodes prepared by leaching the Al or Zn content from a Ni-based precursor alloy or powder mixture. Several techniques have been used to prepare the precursors which were then treated in different leaching conditions to create a porous structure. In general, improved activities were reported due to increased surface area. The porosity formation was confirmed through SEM images and in a few studies BET surface areas were reported. Some authors estimated the surface roughness by fitting the impedance data with a proposed circuit model for HER. Nevertheless, the validity of this method was doubted due to challenges with modelling a highly porous electrode structure. Furthermore, possible inefficient use of pores during the reaction was pointed out by some authors. However, a detailed study of the porosity characteristics with respect to preparation conditions and its relation to electrode activity towards HER has not been reported.

Some researchers reported increasing activities with higher Al or Zn contents in the starting alloy or metals mixture, while others observed a slight change or an opposite trend. Usually, it was assumed that leaching was complete and the composition of the final product was not reported. Some researchers identified the phases present before and after the leaching process, however, a quantitative or semi-quantitative analysis of intermetallic phases present with respect to different preparation conditions have not been reported. The composition and quantity of intermetallic phases available in the precursor materials can influence the leaching reaction leading to a change in the physical and chemical properties of the porous Ni electrodes.

Amongst several techniques used to prepare the precursors for porous Ni electrodes, heat treatment has the greatest potential for the large scale industrial applications. The electrodeposition method requires careful control of the operating parameters and bath conditions to achieve an even and uniform deposition for the preparation of large electrodes [89]. Plasma spraying, on the other hand, needs complex systems increasing the cost of the technique [99]. Heat treatment can offer a more economical and amenable option for the mass production. Therefore, a detailed study on the influence of different preparation conditions on the microstructural properties of the porous Ni-based electrodes would not only help establish relationship between the microstructure and electrochemical performance but also reveal useful guidelines on how to control the textural properties of porous catalysts prepared through a powder metallurgy technique.

Use of a binder was not mentioned in any of the studies that employed pressing and sintering techniques to prepare the precursors for porous Ni electrodes. In powder metallurgy, a binder agent is often added to the metallic mixture before pressing in order to bind or glue the finer metal and/or alloy particles and hence increase the compactness of the mixture and achieve a better “green strength” [124]. It is then burned off during sintering process. Therefore, industrial applications would require using a binder agent to improve the robustness of the electrodes. It is highly likely that the properties of the binder could affect the textural characteristics of the final product.

Finally, the electrochemical performances of the electrodes were mostly tested in a half-cell configuration where the conditions were not representative of an industrial alkaline electrolyser operation. The circulation of electrolyte solution, higher operating temperatures and electrolyte concentrations as well as the presence of an electrode-membrane interface for zero-gap electrolysers could result in different performance characteristics compared to those of electrodes tested through an ex-situ half-cell configuration. The electrode overpotentials were mostly reported at current densities $\leq$ 250 mA/cm^2, which is far below the target operational current density for advanced alkaline electrolysers. It is likely that at desirable current densities (> 500 mA/cm^2) for industrial applications, mass transport limitations might become more significant when the porous Ni electrodes are used.

3.Experimental Methods

3.1. Materials and Processing

3.1.1. Materials

The purchased materials, solutions and gases are listed in Table 3.1. In addition, ultrapure water (supplied by a Sartorius Arium Pro Water Purifier) with a resistivity of 18.2 MΩ x cm which meets the American Society for Testing and Materials (ASTM) Type I water quality standards was used to prepare the leaching and electrolyte solutions as well as rinsing the samples and glassware.

Table 3.1. Raw materials suppliers and purity.

Materials	Form	Supplier	Purity
Nickel Type 255	Powder (Fisher sub-sieve size 2.2-2.6 µm)	Vale, UK	> 99.7 %
Nickel-Aluminium alloy	Powder	Sigma-Aldrich, UK	> 95.0 %
N,N’Ethylene Bisstearamide	-Prills (Mean particle size 130 µm)	Lonza, Switzerland	Data not available
Sigmacell cellulose	Powder (Mean particle size 20 µm)	Sigma-Aldrich, UK	≥ 95.0 %
Potassium hydroxide	Pellets	Sigma-Aldrich, UK	≥ 85.0 %
Potassium sodium tartrate tetrahydrate	Powder or crystals	Sigma-Aldrich, UK	99.0 %
Sulfuric acid	Solution (2.5 M in H_2O)	Sigma-Aldrich, UK	-
Argon	Gas	BOC,UK	99.999 %

3.1.2. Porous Electrode Preparation

3.1.2.1. Green Pellet

The starting materials were commercial nickel-aluminium (Ni-Al) alloy mixture consisting of 50 wt.% Ni and 50 wt.% Al and nickel (Ni) 255. In this study, the commercial Ni-Al alloy mixture is referred to as the starting alloy. N,N’Ethylene Bisstearamide ($C_{38}H_{76}N_2O_2$) referred to as wax was chosen as a binder agent. Wax-polymer binders are commonly used in power metallurgy due to their low cost, easy processing and lack of hazards [125].

Ni, starting alloy and binder were accurately weighed in an anti-static, polystyrene weighing boat using a XP5003S balance (Mettler-Toledo) and mixed together thoroughly with a spatula until the colour of the powder mixture was homogenous. Table 3.2 shows the formulations used to study the different parameters of interest. Ni to starting alloy weight ratio was 60:40 excluding the samples prepared to study the effect of the starting alloy concentration. The total weight of Ni and starting alloy was 3.00 g and 0.20 g of wax binder was added to the metal mixture to obtain a binder concentration of 6.25 wt.% of the total weight. For the study on the effect of binder concentration, the total weights of metal mixtures were 2.50 and 2.25 g and the binder amounts were 0.44 and 0.75 g corresponding to the binder concentrations of 15 and 25 wt.% respectively. The total weight was reduced for higher binder concentrations in order to prepare electrode disks that could fit in the electrolyser cell.

Table 3.2. Formulations of the samples used in the present work.

Parameter of interest	Sample nomenclature	Ni to starting alloy weight ratio	Binder concentration (wt. %)
Sintering temperature	Ni60:Alloy40-B6.25	60:40	6.25
Starting alloy concentration	Ni100-B6.25	100:0	6.25
	Ni90:Alloy10-B6.25	90:10	6.25
	Ni80:Alloy20-B6.25	80:20	6.25
	Ni60:Alloy40-B6.25	60:40	6.25
	Ni40:Alloy60-B6.25	40:60	6.25
Binder concentration	Ni60:Alloy40-B6.25	60:40	6.25
	Ni60:Alloy40-B15	60:40	15
	Ni60:Alloy40-B25	60:40	25
Binder particle size	Ni60:Alloy40-B6.25	60:40	6.25
Leaching temperature	Ni60:Alloy40-B6.25	60:40	6.25

To determine the effect of the binder particle size, as-received wax (with a mean particle size of *ca.* 130 µm) was ground and separated into different particle size ranges, i.e. 20-45 µm, 45-75 µm, 75-200 µm and > 200 µm using stainless steel (SS) sieves (Fisher Scientific) with woven wire mesh sizes of 20, 45, 75 and 200 µm. Sigmacell cellulose with a mean particle size of 20 µm was also investigated for this purpose.

After each mixture was prepared, it was placed in a stainless steel pellet die with a diameter of 32 mm (manufactured by ITM Power) and pressed under a pressure of 1.2 ton/cm^2 for 5 min using a hydraulic press (Moore). A pair of pellets were prepared for each particular preparation condition. In the present study, samples after powder compaction are referred to as as-pressed samples.

3.1.2.2. Sintering

The pressed samples were placed in alumina crucibles (Almath Crucibles) which contained a folded Ni mesh. This acted as a cushion for the pellets and enabled easier movement of gases generated during the decomposition of the binder. Sintering was carried out in a tube furnace (Lenton) equipped with recrystallized alumina work-tube under an inert Argon (Ar) gas atmosphere. A sintering temperature of 650 ºC was chosen to investigate the different parameters of interest excluding the effect of sintering temperature which was studied with the sintering temperatures of 625, 650, 700, 750 and 900 ºC.

The samples were heated from room temperature to a target temperature, e.g. 650 ºC with a heating ramp of 5 ºC/min and sintered at this temperature for 2 h. The samples were then furnace cooled to ambient temperature before they were taken out. The dimensions and weights of the samples were recorded before and after the sintering process. In the present study, samples that were characterized after sintering are referred to as as-sintered samples.

3.1.2.3. Leaching

An aqueous solution of 5 M KOH containing 10 wt.% K-Na tartrate tetrahydrate was used as a leaching solution to remove the Al content in as-sintered samples. A leaching temperature of 70 ºC, which has been one of the most common options in the literature, was used during the investigations of different preparation parameters. The effect of leaching temperature was studied at 30, 50, 60, 70 and 80 ºC. The solution volume was 250 ml for each sample. Polypropylene sheets were used to cover the tops of the beakers preventing the evaporation of the solution during the leaching process. A water bath (Cole-Parmer Digital Utility Water Bath) was used to control the leaching temperature. Once the target temperature, e.g. 70 ºC was achieved, the pellets were inserted into the solution and left for leaching for 18 h. Afterwards the leached samples were rinsed thoroughly with deionised water for several times. Finally, they were stored in 4 M KOH aqueous solution at ambient temperature until required for electrochemical testing.

3.1.2.4. Drying and Passivation

Once the leached samples were electrochemically tested within the electrolyser cell, selected samples were dried for material characterisation. Samples were taken from 4 M KOH storage solution and rinsed 3 times with deionised water. They were then submerged in deionised water for 15 min and the pH of the rinsing water was verified to be neutral using Litmus paper. After rinsing, they were dried in a tube furnace for 2 h at 200 ºC under an inert Ar atmosphere. The heating ramp was 5 ºC/min. Passivation of the samples was performed at room temperature, by switching of the Ar flow followed by a furnace cool to ambient. Then, one of the tube furnace sealings was opened to allow air to gradually penetrate inside the tube furnace and slowly oxidize the samples. After 2 h, the samples were removed from the tube furnace and left in air for 1 h to ensure sufficient oxidation of the surface. Finally, the dimensions and weights of the dried pellets were recorded. In the present study, samples that were characterized after leaching and electrolyser cell test are referred to as as-leached samples.

3.2. Electrolyser Cell Test

The electrochemical performance of the leached samples for hydrogen evolution was tested in an alkaline electrolyser cell (Figure 3.1). While the samples were tested at the cathode (negative) side, a woven wire stainless steel (SS) mesh was used at the anode (positive) side. They were separated by an anion conducting membrane developed by ITM Power with a thickness of 0.17 mm. A 4 M KOH aqueous solution was used as an electrolyte solution and was supplied to both anode and cathode sides. Once sufficient direct current (DC) was passed through the electrodes, water was reduced to generate hydrogen (H_2) and hydroxyl (OH^-) ions at the cathode. The OH^- ions lose their electrons (e^-) at the anode side producing oxygen (O_2) and water.

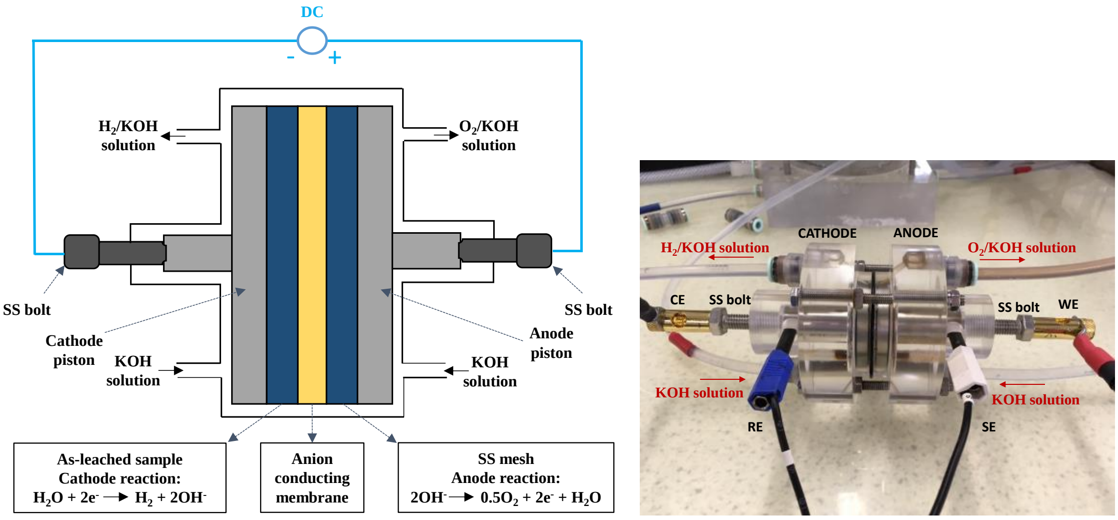

Figure 3.1. Simplified diagram of the alkaline electrolyser cell (not to scale) (left) and the photo of the alkaline electrolyser cell (right), where CE is counter electrode; RE is reference electrode; SE is sense electrode; WE is working electrode and SS is stainless steel.

As shown in Figure 3.1 (right), acrylic cell halves were used as a body to construct the electrolyser cell. Both cathode and anode sides had SS pistons which functioned as a flow field as well as electrical connections to the electrodes. The bolts were fastened by using a torque wrench to precisely apply the same pressure, i.e. 20 bar onto the pistons-electrodes-membrane assembly each time.

Before each cell construction, pistons and SS mesh were sonicated 3 times, firstly in ultrapure water for 2 min, secondly in 2.5 M H_2SO_4 solution for 2 min and lastly in ultrapure water for a further 2 min. Finally, they were rinsed with 4 M KOH solution before insertion into the cell halves. It must be noted that the pistons were marked as cathode and anode pistons and only used for one side.

DC current required for the electrochemical reaction was supplied by IviumStat potentiostat connected to IviumBoost Current Booster. The measurements were taken in the 2-electrode mode, where working electrode (WE) and counter electrode (CE) of the potentiostat were plugged into the drilled holes on M8 SS bolts at the anode and cathode sides of the cell respectively (Figure 3.1). The reference electrode (RE) sensor was plugged into a hole on the side of the cathode piston, whereas the sense electrode (SE) was connected to the anode side through the hole on the side of the anode piston. Since the current is applied between WE and CE and the voltage is measured between RE and SE, this configuration excluded the contribution of connection resistances between the parts of WE-anode bolt, CE-cathode bolt, anode bolt-piston and cathode bolt-piston to the cell voltage.

Figure 3.2 demonstrates the overall electrolyser cell test facility including the balance-of-plant (BOP) components. Inlets and outlets of the electrodes were connected to the acrylic separation tank, where the electrolyte solution was stored, using polyflon tubing with an OD of 6 mm. Polyflon tubing was chosen due to its chemical resistance to the alkaline solution.

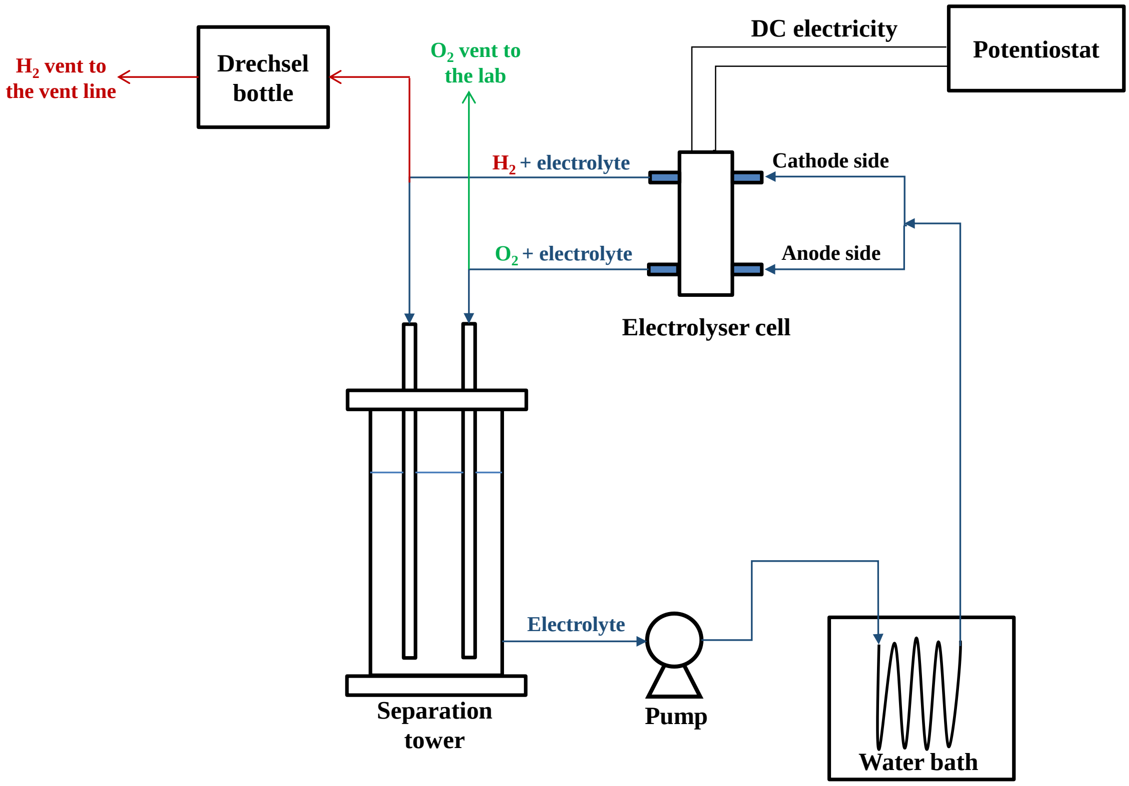

Figure 3.2. Simplified schematic diagram of the electrolyser cell test facility including the BOP.

The electrolyte solution was circulated at 60 °C to both anode and cathode sides using a peristaltic pump (Masterflex L/S Variable-Speed Drive; 100 rpm connected to Masterflex L/S two-channel Easy-Load II pump head) at a speed of 30 ml/min. H_2 and O_2 gases were separated from the electrolyte solution as they passed through the separation tower. O_2 was vented to the lab, whereas H_2 gas was passed through a dreschel bottle before being vented through the H_2 vent line.

ChronoPotentiometry (CP) technique was employed to study the electrolyser cell performance at different current densities (Table 3.3). During the CP measurement, a constant current defined by the user was applied to the electrochemical cell and the corresponding voltage was recorded within a duration with an interval time set by the user. Since the properties of membrane and anode side remained constant, the change in the cell voltage indicated the variations in the electrocatalytical properties of the samples used at the cathode side.

Before recording the voltage data, a current value of 8 A was applied for 10 min to reduce the surface oxides and clean the cathode surface through H_2 gas generation. During the CP measurement a duration of 5 min was used at each current step which was sufficiently long enough to achieve equilibrium. The voltage was recorded every 0.1 s and the average of the last 20 s of measured voltage data points was used to draw the relationship between current density and corresponding voltage for tested samples.

Table 3.3. Currents and corresponding current densities applied by the CP method.

Applied current (A)	Corresponding current density* (A/cm^2)
8.0	1
7.2	0.9
6.4	0.8
5.6	0.7
4.8	0.6
4.0	0.5
3.2	0.4
2.4	0.3
1.6	0.2
0.8	0.1
0.4	0.05
0.2	0.025
0.1	0.0125
0.05	0.00625

*calculated by using the geometric surface area, i.e. 8 cm^2

3.2.1. Reproducibility Test

The reproducibility of the electrolyser cell test was investigated by measuring the cell voltages of the same electrode in 3 different days. Although the parameters of electrochemical test were not changed, different pieces of membrane and SS mesh were used to check whether they could lead to a significant variation in the total cell voltage. Each time a different batch of electrolyte solution was used. The reproducibility of electrochemical evaluation of electrodes was checked with 5 different batches prepared in the same conditions but pressed, sintered, leached and tested in different days.

3.3. Sample Characterization Techniques

3.3.1. Gas Sorption Technique

Gas sorption technique was used to investigate the surface area and porosity characteristics of the tested samples. The method is based on the physical (or "van der Waals") adsorption of an adsorbable gas (adsorptive) at the external and accessible internal surfaces of a solid (the adsorbent) [126]. The amount of gas adsorbed on an adsorbent surface is a function of temperature, pressure of the adsorbed gas (the adsorbate) and interaction between the adsorbate and adsorbent [127]. Since the quantity of adsorbed gas is measured at a constant temperature on a particular gas-solid interface, the relationship between the volume of the adsorbate and the equilibrium pressure of the gas is referred to as a sorption isotherm.

The evolution of sorption isotherms and the hysteresis between them can reveal useful information about the porosity characteristics of a solid, i.e. pore shape, size, volume and surface area [127]. Based on International Union of Pure and Applied Chemistry (IUPAC) classifications, there are six main types of sorption isotherms (Figure 3.3). Type I isotherms are often obtained on microporous (< 2 nm) solids, where the accessible micropore volume rather than the internal surface area governs the limiting uptake. Type II isotherms are attributed to a non-porous or macroporous (> 50 nm) solid, where unrestricted monolayer-multilayer adsorption occurs. Type III isotherms are observed when the interactions between adsorbate-adsorbate play a significant role. Type IV isotherms are characteristics for mesoporous (2-50 nm) solids with the hysteresis loop related to the capillary condensation occurring within the mesopores. Similarly Type V isotherms also show pore condensation; however they indicate relatively poor attractive interactions between the adsorbent and the adsorbate. Finally, Type V isotherms characterize stepwise multilayer adsorption on a uniform non-porous surface [128].

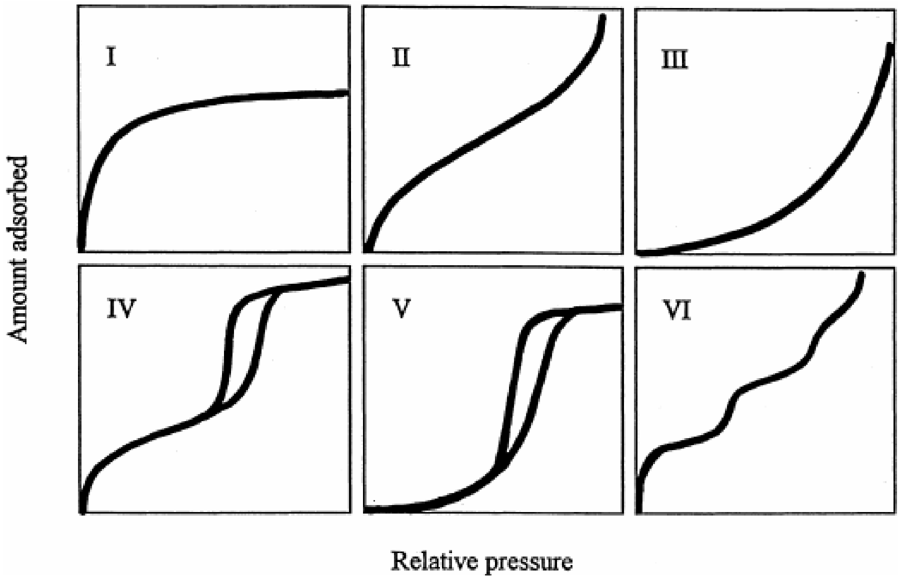

Figure 3.3. IUPAC classifications of gas sorption isotherms [128].

The shapes of the hysteresis loops are often attributed to the presence of specific pore structures and corresponding adsorption mechanism. Figure 3.4 shows different shapes of hysteresis loops. Type H1 is suggested for solids with narrow distributions of uniform mesopores where network effects are typically insignificant. However, this type of hysteresis has also been observed in networks of ink-bottle pores where the width of the neck size distribution is similar to the width of the pore/cavity size distribution [129]. Type H2(a) is found in solids with more complicated pore structures where network effects are more significant and pore-blocking/percolation in a narrow range of pore necks can occur. Similarly, Type H2(b) also indicates pore blocking, however the size distribution of neck widths is now much larger. Type H3 is observed with non-rigid aggregates of plate-like particles giving rise to slit-shaped pores. Similarly, Type H4 loop is typically related to narrow slit-like pores, but microporosity is now indicated by Type I isotherm character. Finally, Type H5 is attributed to certain pore structures with both open and partially blocked mesopores [129].

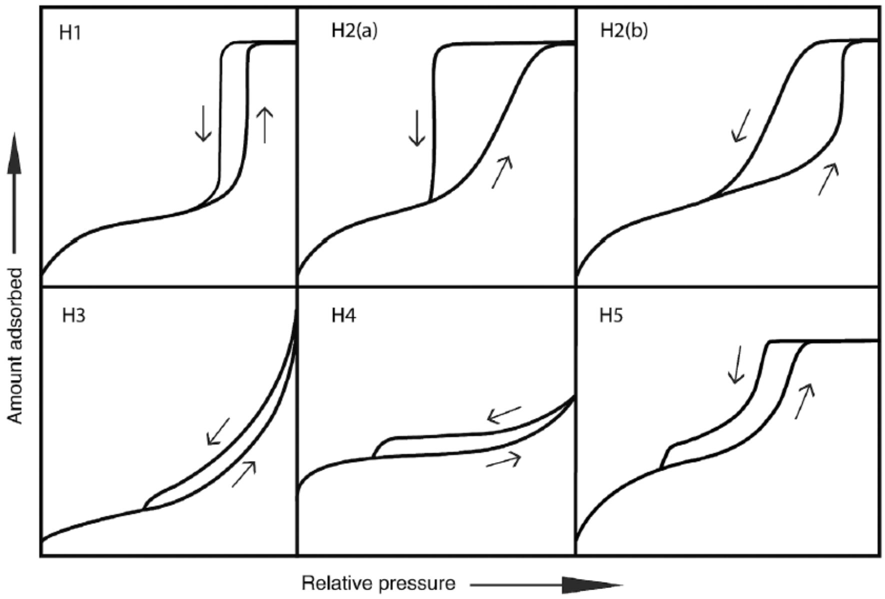

Figure 3.4. IUPAC classifications of hysteresis loops [129].

The Accelerated Surface Area and Porosimetry System (ASAP 2420, Micrometrics) was used to perform the gas sorption analysis on samples. As the original sample size (disk with a 32 mm diameter) was too large to fit into the sample tubes, they were broken into 16 pieces. The range of the sample weight was 2.5-3 g. The samples were degassed under vacuum at 200 ºC for 15 h before the analysis to remove moisture and other adsorbed gases. The sample weights were recorded before and after degassing. Nitrogen (at its boiling temperature, -196.15 ºC) was used as an adsorptive due to its readily availability and commonly usage for gas sorption analysis. Finally, textural properties of the samples were calculated from the nitrogen sorption isotherms via

MicroActive Version 4.03.01 Software (Micromeritics) using appropriate models described in the following subsections.

3.3.1.1. Brunauer, Emmett and Teller Method

The Brunauer, Emmett and Teller (BET) theory, which is commonly used for type II and type IV isotherms, was used to calculate the specific surface area using the Equation 3.1 [81] where P is the pressure; P_0 is the saturation pressure of the adsorbate; V is the volume of the adsorbate adsorbed at the equilibrium pressure, P; V_m is the volume of adsorbate representing a completely filled monolayer; and C is the BET constant related to energy of the monolayer adsorption.

$$\frac{P/P_0}{V(1-P/P_0)} = \frac{1}{V_m C} + \frac{C-1}{V_m C} \times \frac{P}{P_0} \tag{3.1}$$

The C value can be expressed as Equation 3.2 [81], where E_1 is the average heat of adsorption in the first layer; E_L is the heat of liquefaction; R is the universal gas constant and T is the temperature.

$$C = e^{(E_1-E_L)/RT} \tag{3.2}$$

From the Equation 3.1, $(P/P_0)/(V(1-P/P_0))$ is plotted against P/P_0 from which the intercept, $1/V_mC$ and slope, $(C-1)/V_mC$ may be obtained by linear regression. The linearity range of the BET plot is limited to the relative pressure (P/P_0) range of 0.05-0.3 for type II and IV isotherms [129]. Two criteria should be considered to find the appropriate linear range of the BET plot;

- the intercept in other terms C constant must be positive and
- ($V(1-P/P_0)$) must continuously increases with P/P_0 [83].

Once the intercept, i, and slope, s, are defined V_m can be obtained from Equation 3.3;

$$V_m = \frac{1}{s+i} \tag{3.3}$$

Finally, BET specific surface area (S_{BET}) is calculated by Equation 3.4 where N is the Avogadro's number (6.02×10^{23} molecules/mole), A_{CS} is the cross sectional area of the adsorbate molecule, M is the molecular weight of the adsorbate gas and w is the sample weight [127].

$$S_{BET} = \frac{V_m N A_{cs}}{Mw} \tag{3.4}$$

In this work, multipoint BET surface area was calculated from 5 data points in the P/P_0 range of 0.08-0.25. C values were *ca.* 80 and the correlation coefficient was more than 0.99999.

3.3.1.2. Barrett-Joyner-Halenda Model

The Barrett-Joyner-Halenda (BJH) model was applied for the mesopore size (2-50 nm) analysis including the pore size distribution and volume. It is based on the Kelvin equation with a correction term for the thickness of the multilayer adsorption considering the capillary condensation in the pores to calculate the pore size distribution of meso- and small macropore size range up to *ca.* 140 nm. The modified Kelvin equation [130] with the assumption of a cylindrical pore shape is;

$$\ln(P/P_0) = \frac{-2\gamma V_m}{RT(r_p - t_c)} \tag{3.5}$$

where P/P_0 is the relative pressure; γ is the surface tension of the bulk fluid; V_m is the molar liquid volume; R is the universal gas constant; T is the temperature; r_p is the pore radius and t_c is the thickness of the adsorbed multilayer film, which is formed prior to pore condensation [130]. The thickness of the adsorbed layer was calculated using Harkins and Jura model which is one of the most commonly used and most generally applicable thickness expressions;

$$t = \left(\frac{A}{B - log(P/P_0)}\right)^{1/2} \tag{3.6}$$

where t is the thickness and A (13.990) and B (0.034) are the empirical constants [131, 132].

3.3.1.3. Dubinin-Astakhov Model

The area and volume of the micropores were obtained using the Dubinin-Astakhov (D-A) model;

$$Q = Q_0 e^{-(\frac{A}{\beta E_0})^n} \tag{3.7}$$

where Q is the quantity adsorbed at the relative pressure P/P_0; Q_0 is the limiting pore volume; A is the adsorption potential; β is the affinity coefficient which is 0.33 for N_2; E_0 is the characteristic energy of adsorption and n is the Astakhov exponent which is usually selected to be between 1 and 3 to obtain the best linear regression fit [132]. The adsorption potential, A can be expressed as;

$$A = RTln(P/P_0) = -\Delta G \tag{3.8}$$

where R is the universal gas constant; T is temperature and ΔG is the change in the Gibbs free energy [132]. Equation 3.7 can be rearranged as below;

$$InQ = lnQ_0 - \left(\frac{RT}{\beta E_0}\right)^n \left(In\frac{P_0}{P}\right)^n \tag{3.9}$$

lnQ is plotted against $In^n(P/P_0)$ which produces a straight line over a certain range of gas pressures. From the intercept of the straight line Q, the quantity adsorbed is identified. In this work, the Astakhov exponent value of 2 was used and 5 data points within the relative pressure range of 0.02-0.06 were selected in the linear region of the D-A transformed isotherm plot to determine the micropore area and volume.

3.3.2. Helium Pycnometer

Helium (He) pycnometer was employed to measure the skeletal volume/density of the samples which revealed information about the amount of open and closed pores. Pycnometer measures the volume of a solid using the gas displacement method and the ideal gas law where the gas penetrates through all pores that are accessible to its molecules; with He often being used as a displaced gas due to its small size [132]. The pressure change resulting from the displacement of He by a solid substance in a chamber with a precisely known volume was measured and corresponding volume is calculated by the Boyle’s law (Equation 3.10) for a given amount of a gas at a constant temperature within a closed system;

$$PV = k \tag{3.10}$$

where P and V are the pressure and volume of the gas respectively and k is a constant [127].

AccuPyc 1330 gas pycnometer (Micromeritics) was used to perform the He pycnometer measurements. Purge fill pressure and run fill pressure were set at 134.45 kPa. The equilibrium rate was 0.0345 kPa/min. The reported volumes were an average of 10 measurements per sample.

The skeletal volume measured by the He pycnometer is the sum of the volume of the fully dense material and closed pores within the sample. Table 3.4 describes three different volume terms used in this work. For a solid with a known theoretical density and mass, the volume of closed pores can be calculated using the values of skeletal and theoretical volumes. Similarly, the amount of open pores can be estimated by using the skeletal and geometric volumes.

Table 3.4. Definitions of volumes [133].

Volume Definition	**Volumes included in definition**		
	Solid material	Open pores	Closed pores
Theoretical volume: The volume of the solid matter excluding all pores and voids (BSI*)	✓		
Geometric volume: The volume estimated from the measurements of its physical dimensions	✓	✓	✓
Skeletal volume: The sum of the volumes of the solid material and closed pores within the pieces (implied by ASTM* D3766)	✓	✓	

* BSI: British Standards Institute and ASTM: American Society for Testing and Materials

In this work, the dimensions of the final samples, which were in the form of disks, were measured by a calliper to identify the geometric volume. The theoretical density of the samples was estimated using the results from the Rietveld refinement analysis for the Al-Ni intermetallic compounds. The bulk densities of AlNi, $Al_{0.84}Ni_{1.16}$, $AlNi_3$ and Ni used in the calculations are 5.92, 6.37, 7.44 and 8.91 g/cm^3 respectively [134].

3.3.3. Mercury Intrusion Porosimetry

Mercury intrusion porosimetry (MIP) was used to study the macroporosity characteristics. MIP is a standard technique for characterizing the pore features with sizes typically up to *ca.* 350 µm [135]. It is based on the fact that mercury (Hg) as a non-wetting liquid does not penetrate into the pores and cracks of a substance unless a pressure is applied to make it do so. The pressure required to intrude Hg into the pores increases with decreasing pore sizes. This law is expressed by the Washburn equation

(Equation 3.11) which is a modified Young-Laplace equation with the assumption of cylindrical pore shape;

$$P = \frac{2\gamma\, cos\theta}{r_{pore}} \tag{3.11}$$

where P is the pressure applied to Hg for intrusion; γ is the surface tension of Hg; Θ is the contact angle between the solid and Hg; r_{pore} is corresponding pore size [127].

AutoPore IV mercury porosimeter (Micromeritics) was employed to perform the MIP measurements on the samples of interest. A Micromeritics penetrometer for solid media with 5 cm^3 sample volume and 0.366 cm^3 stem volume was used. To begin, a blank run was carried out with the penetrometer excluding any sample and this was used as a correction method for the analysis with the samples. The sample weight used was *ca.* 0.3 g to give a resulting stem volume used of 50 %. The corresponding density of Hg was entered manually each time based on the laboratory temperature. The equilibrium time interval was set to 30 s. The data from MIP measurements were analysed using MicroActive Version 4.03.01 Software (Micromeritics).

3.3.4. Powder X-Ray Diffraction

Powder X-ray diffraction (PXD) was employed to identify and quantify the phases present in the samples before and after the leaching process. The technique relies on the fact that the atomic positions and distances between the atoms of a crystalline material cause the X-rays to diffract into specific directions which yields information about the crystal structure. Bragg's law [136] describes the principle of the X-ray diffraction;

$$n\lambda = 2d\sin\theta \tag{3.12}$$

where n is the order of the diffraction; λ is the X-ray wavelength; d is the inter-planar spacing between diffracting planes and Θ is the angle between the incident X-ray and the scattered X-ray signal.

PXD experiments were performed on a D8 ADVANCE Diffractometer (Bruker) using a Cu Kα X-ray source (λ=1.5406 Å) which operates at 40 kV and 35 mA with a 0.6 mm exit slit. The diffraction patterns were collected using a Sol-XE energy dispersive detector with a data range of 10-90 º in 2Θ, a step size of 0.02 º and a dwelling time of 4 s at each step for the phase identification. Pieces from the bulk samples were ground into a powder using a mortar and pestle. The sample powders were dispersed on a single crystal silicon wafer sample holder and the surface of the powders were smoothened using a rectangular glass wafer. X-ray diffraction patterns were produced in the form of a plot of reflected intensities versus 2Θ, the diffraction angle. Different phases were analysed by indexing them against reference diffraction data from International Crystal Structure Database (ICSD) through the EVA software (Bruker).

3.3.4.1. Rietveld Refinement

After the phase identification analysis, Rietveld or profile refinement technique was used to quantify the concentrations of multiple phases in the samples of interest, as well as identifying the composition of a single phase. This technique uses a non-linear least squares method to refine various pattern variables and crystal structural properties of a theoretical model until it matches the measured powder diffraction profile. It requires a rational initial approximation of several parameters including unit cell dimensions, peak shape properties and coordinates of all atoms in the crystal structure model [137]. Equation 3.13 [137] shows the principle of the Rietveld refinement technique;

$$M = \sum_{i=1}^{n} w_i \, (Y_i^{obs} - Y_i^{cal})^2 \qquad (3.13)$$

where M is the minimized function; w_i is the weight assigned to the i^{th} data point; Y_i^{obs} and Y_i^{cal} are the observed and calculated intensities of a point i of the PXD pattern respectively and n is the total number of the measured data points.

The intensity, Y_i of the ith point can be described as [137];

$$Y_i = b_i + \sum_{j=1}^{m} I_j \left[y_j(x_j) + 0.5 y_j(x_j + \Delta x_j) \right] \tag{3.14}$$

where b_i is the background; I_j is the integrated intensity of the j^{th} Bragg reflection; y_j is the intensity of the overlapped individual Bragg peak at a point j; x_j is $2\Theta_i$-$2\Theta_j$; Δx_j is the difference between the Bragg angles of the $K\alpha_2$- $K\alpha_1$ components in the doublet (if present) and m is the number of Bragg reflections contributing to the intensity of the j^{th} data point.

Considering Equation 3.14 and a single phase crystalline material, Equation 3.13 can be modified to the following expression [137];

$$M = \sum_{i=1}^{n} w_i \left(Y_i^{obs} - \left[b_i + K \sum_{J=1}^{m} I_j y_j(x_j) \right] \right)^2 \tag{3.15}$$

where K is the phase scale factor; $y_j(x_j)$ is the peak shape function and x_j is $2\Theta_j^{cal}$-$2\Theta_i$.

For a material with multiple phases, the total contribution of each crystalline phase is considered as follows [137];

$$M = \sum_{i=1}^{n} w_i \left(Y_i^{obs} - \left[b_i + \sum_{l=1}^{p} K_l \sum_{J=1}^{m} I_{l,j} y_{l,j}(x_{l,j}) \right] \right)^2 \tag{3.16}$$

where l is the number presenting a crystalline phase and p is the total number of the phases present.

The two most commonly used empirical peak shape functions are [137];

Gauss: $$y(x) = G(x) = \frac{C_G^{1/2}}{H\sqrt{\pi}} e^{(-C_G x^2)} \tag{3.17}$$

Lorentz: $$y(x) = L(x) = \frac{C_L^{1/2}}{H'\pi} (1 + C_L x^2)^{-1} \tag{3.18}$$

where H and H' are the full widths at half maximum (FWHM); x is $(2\Theta_i\text{-}2\Theta_j)/H_j$, C_G and C_L are 4ln2 and 4 for Gauss and Lorentz functions respectively.

The FWHM are expressed as follows [137];

For Gauss: $$H = (U \tan^2 \theta + V \tan \theta + Z)^{1/2} \tag{3.19}$$

For Lorentz: $$H' = (U/\cos \theta) + V \tan \theta \tag{3.20}$$

where U, V and Z are free variables.

In Rietveld refinement analysis the goodness of the fit is often expressed using the X^2 term [138];

$$X^2 = \frac{1}{n} \sum_{i=1}^{n} w_i (Y_i^{obs} - Y_i^{cal})^2 \tag{3.21}$$

The X^2 term should be ≥ 1 with the lower the X^2 the better the fit [138].

For the Rietveld refinement, the PXD patterns were collected with a data range of 15-150 ° in 2Θ, a step size of 0.01 ° and a dwelling time of 4 s at each step. All computations were performed using General Structure Analysis System (GSAS) program coupled with a graphical interface EXPGUI. The entry data for theoretical models were obtained from the ICSD.

3.3.5. Scanning Electron Microscopy

Scanning electron microscopes (SEM, Philips XL30 and XL30 ESEM-FEG) equipped with an energy dispersive spectroscopy (EDX, Oxford Instruments X-MAX) were used to investigate the morphology and elemental composition of the samples. For surface analysis, a small piece was broken from the sample with *ca.* 0.2 cm^2 surface area, whereas cross section analysis was performed on sample pieces with 0.4-1 cm length cut using a razor blade and stuck onto a carbon tape. SEM with secondary electron (SE) and back-scattered electron (BSE) modes were used at 20 kV with a spot size of 4 corresponding to a beam diameter of ca. 2 µm. Livetime and process time were set at 40-50 s and 5 s respectively for the EDX analysis using the INCA Energy Software. The overall surface and cross-section compositions of each sample were calculated by averaging the results of scans with approximately 70 µm x 70 µm dimensions at 2000x magnitude from 5 different locations from the sample of interest.

3.3.6. Inductively Coupled Plasma Mass Spectrometry and Optical Emission Spectrometry

Inductively coupled plasma sources coupled with a mass spectrometry or an optical emission spectrometry (ICP-MS and ICP-OES) were used for analysing the leaching solution and as-leached samples to identify the concentrations of Al and Ni contents. ICP employs a high temperature plasma to produce highly energized positive ions. The sample aerosol travels through the different zones of the plasma where it is dried, vaporized, atomized and ionized. The positively charged sample ions are then separated by the mass to charge ratio and detected by the mass spectrometer [139]. ICP-OES utilizes the distinct wavelengths of light emitted by specific elements, the intensity of which is proportional to the concentration of the metal in the solution [140].

Elemental analysis of a leaching solution was performed using an Agilent 7500 Series ICP-MS system. After the leaching process was completed, the leached sample was removed and the leaching solution was filtered through a filter paper (Fischerbrand QL100 with a pore size range of 5-13 µm) to remove any undissolved solid residuals. Three solution samples were taken from the same leaching solution and diluted volumetrically to 50 ml using a solution mixture of 3.25 vol.% nitric acid (HNO_3) + 2.10 vol.% hydrochloric acid (HCl). The concentrations of Al and Ni were reported for the average of three measurements.

The compositions of as-leached samples were analysed through a Perkin Elmer 2000 ICP-OES instrument. Samples were ground into a powder and *ca.* 5 mg of each sample was analysed. 2 ml of a 3:1 mixture of Aristar grade concentrated HCl and HNO_3 (commonly referred to as aquaregia) was added to the sample and stirred overnight at room temperature. Once all visible solids had dissolved, the samples were diluted volumetrically to 50 ml using ultra-pure water. A 10 ml aliquot of this solution was then used for analysis. Certified 1000 ± 2 ppm Ni and Al calibration standards in 2 vol.% HNO_3 were obtained separately from Sigma Aldrich and ten solutions were independently volumetrically prepared in order to give a suitable range of nine standards for calibration, with each standard containing an identical concentration of each element of interest (100 ppm, 80 ppm, 40 ppm, 20 ppm, 10 ppm, 5 ppm, 0.5 ppm, 0.1 ppm, 0 ppm), together with two further known concentration standards to be used for quality control purposes (60 ppm, 1 ppm). Calibration was carried out over this range at 3 different wavelengths per element of interest, i.e. 231.6, 221.6 and 232.0 nm for Ni, 396.2, 308.2 and 394.4 nm for Al with three replicates of data collected at each wavelength. The normalized concentrations of Al and Ni were reported for the average of 9 readings.

3.3.7. Micro Computed Tomography Imaging

Micro computed tomography (micro-CT) imaging was used to analyse the macroporosity characteristics of samples. This non-destructive imaging technique records the individual projections from different viewing directions to rebuild the internal structure of the object [141]. The density gradients within the samples results in the variation of X-ray absorption which enables the analysis of porosity features as well as different phases present in the scanned samples.

A ZEISS Xradia 500 Versa three-dimensional (3D) X-ray microscope which offers multi-length scale imaging across variable magnifications down to 0.5 µm was used to scan porous electrode samples. Figure 3.5 shows the internal view of an Xradia 500 Versa X-ray microscopy. The electrode disk was securely and vertically glued on a sample holder as presented in Figure 3.5 (a). In order to maximize the geometric magnification hence the image resolution, the source was kept as close to the sample as possible, whilst the detector was pulled away (Figure 3.5 (b)). This was due to the fact that the geometric magnification is defined by;

$$\text{Geometric magnification} = (a+b) / a \tag{3.22}$$

where *a* is the distance between the source and object and *b* is the distance between the detector and object [141].

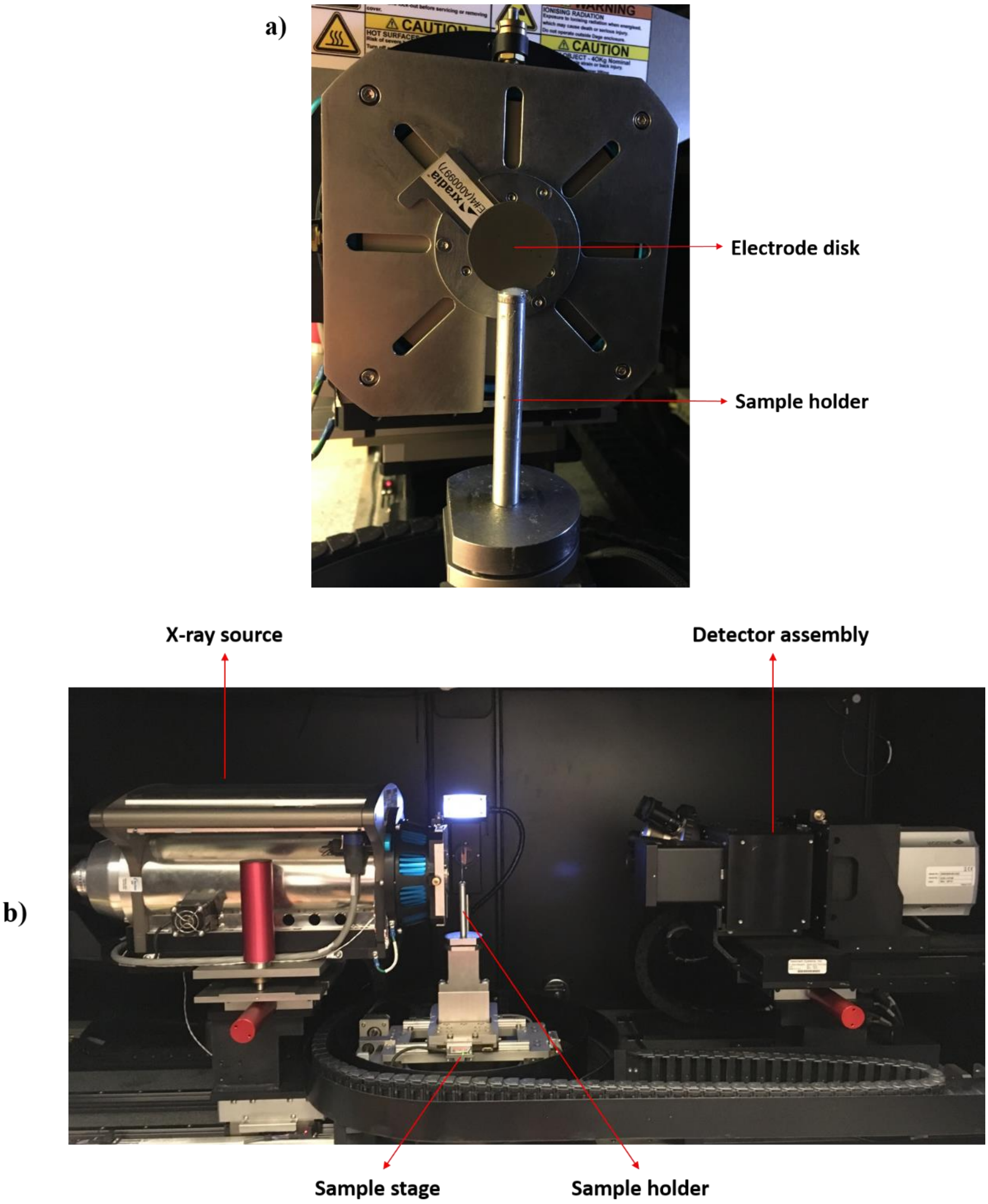

Figure 3.5. Internal view of an Xradia 500 Versa X-ray microscopy; where (a) close view of the sample holder; (b) major components.

Table 3.5 summarizes the micro-CT scan parameters. As-leached Ni60:Alloy40-B6.25 samples were scanned with X-ray set to a source voltage of 80 kV and a target current of 87 µA apart from high resolution scan where the source voltage and target current were 100 kV and 90 µA respectively. The source-object distance is dependent on the sample size and field of view which defines the radius of the sample rotation. As the radius of the sample rotation rises, the distance between the sample and source is increased to prevent the sample from hitting the source during the rotation. That is why the lowest source-object distance was with the high resolution scan where the size of the sample was the smallest.

The highest pixel resolution (numbers of pixel) for the detector offered by an Xradia 500 Versa X-ray microscopy is 2048 x 2048 pixels. However, there is a trade-off between the detector resolution and scan duration, with the greater the numbers of pixels the longer the scans. The voxel size (scan resolution) is dependent on chosen pixel resolution and scan size, since these three parameters relate to each other via;

$$\text{Pixel size} = (\text{Scan size})/(\text{Number of the pixels}) \qquad (3.23)$$

Therefore, there is a compromise between the size of the scanned region and scan resolution. During the low resolution scan the whole electrode disk was scanned with a resolution of 32 µm, whilst the scan size and resolution was 6 x 6 mm and 3 µm respectively for the medium resolution scan which was carried out either on a central or outer location as demonstrated in Figure 3.6. The smallest voxel size, i.e. 0.5 µm was achieved with the high resolution scan which gave a scan size of 0.5 x 0.5 mm. Unlike low and medium size scans, for the high resolution scan the electrode disk was broken into small pieces and a piece with a size of *ca.* 0.6 mm was chosen to carry out the scan.

For the low and medium resolution scans 1600 projections were acquired during the rotation of 360 °, corresponding to a rotation step of 0.225 °, while the number of projections and rotation step were 3200 and 0.113 ° respectively for the high resolution scan.

Table 3.5. Micro-CT scan parameters. Scans were taken on as-leached Ni60:Alloy40-B6.25 samples.

Scan parameter	Specifications		
	Low resolution scan	Medium resolution scan	High solution scan
Source filter	LE4	LE4	LE4
Voltage (kV)	80	80	100
Current (µA)	87	87	90
Sample diameter (mm)	32.5	32.5	0.6
Source-object distance (mm)	65	26	10
Detector-object distance (mm)	70	265	16
Optical magnification	0.4X	0.4X	20X
Image size (pixels)	1024 x 1024	2048 x 2048	994 x 994
Scan size (mm x mm)	32.5 x 32.5	6 x 6	0.5 x 0.5
Voxel size (µm)	32.5	3.0	0.5
Number of projections	1600	1600	3200
Rotation step size (°)	0.225	0.225	0.113
Scan duration (h)	0.7	10.9	13.5

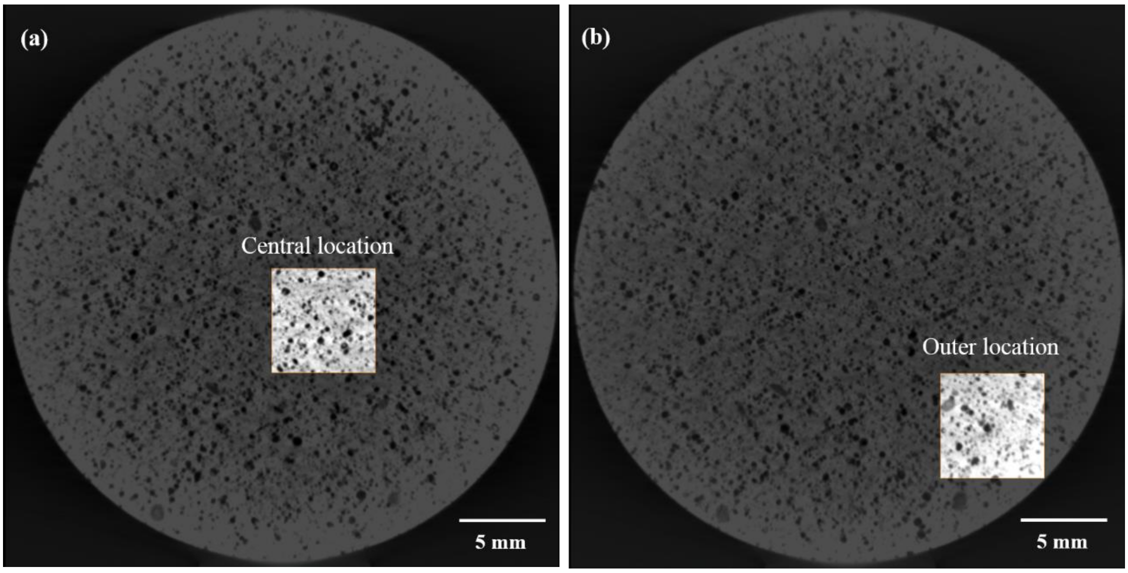

Figure 3.6. Micro-CT scan locations for the medium resolution scans, where (a) central location and (b) outer location.

Figure 3.7 summarizes the workflow for the steps followed to analyse the micro-CT scans. A set of 2D projections that were collected during the data acquisition were reconstructed using the ZEISS Scout-and-Scan Control System. The resultant 3D grayscale structures of scanned samples were processed, visualized and analysed using Avizo 9.3 3D software. Non-local means filtering was used to reduce the noise and improve the image quality. The improved grayscale images were then segmented using the interactive thresholding module, which prompts users to select an appropriate grayscale value with a 2D or 3D visual feedback. Thresholding resulted in binary images, where pixels were assigned a value of “1” or “0” depending on whether or not they were within the selected threshold range. In order to analyse pore size distribution more accurately, pores that appeared to be touching were separated using the watershed algorithm. Finally, segmented 3D images were labelled and analysed.

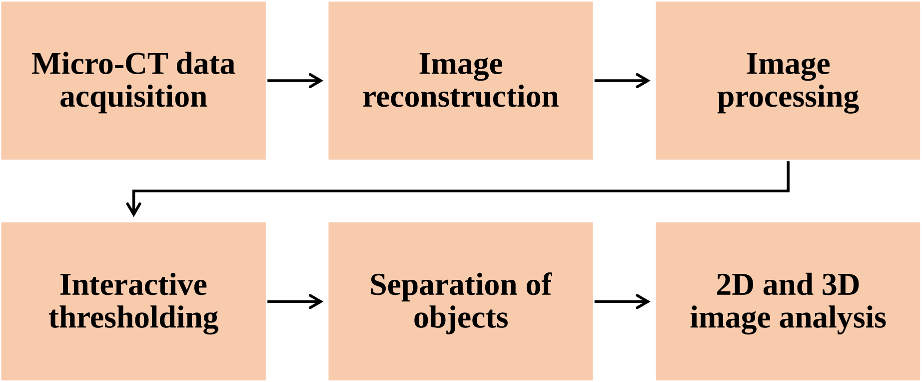

Figure 3.7. Summary of the workflow for the steps followed to analyse data from the micro-CT scans using the Avizo 9.3 software.

3.3.8. Thermogravimetric Analysis

Thermogravimetric analysis (TGA) was performed to identify the decomposition temperatures of the binder agents, i.e. wax and cellulose during sintering conditions. This technique monitors the change in the weight of a sample as a function of temperature or time while the sample is subjected to a controlled temperature programme. It can provide information about various physical and chemical phenomena such as decomposition, thermal stability, vaporization, as well as kinetics parameters of materials. A TGA consists of a sample holder located in a furnace where it is heated or cooled. The sample holder is supported by a precision balance to monitor the weight of a sample during the analysis. An inert or reactive gas flows over the sample.

A Netzsch 209 F1 Iris was used to perform TGA on as-pressed samples. A sample piece with a weight of *ca.* 10 mg was placed into an alumina crucible sealed in an aluminium pan. Samples first were held at a temperature of 30 ºC under an Argon flow at atmospheric pressure with a flow rate of 100 ml/min in order to allow the system to stabilise before measuring the mass loss during heating at 5 ºC/min up to 650 ºC. A buoyancy calibration was run before each measurement under identical conditions employed during the sample analysis. To determine the true mass loss of a sample the blank test was subtracted from the sample test.

3.3.9. Laser Diffraction Analysis

Laser diffraction technique was used to identify the particle size distribution of as-received wax. This method indirectly measures the particle size distribution of a sample using light scattering patterns of the particles. It is based on the fact that scattering angle of the incident light beam is inversely proportional to the particle size [142]. Figure 3.8 demonstrates a typical set-up of laser diffraction analysis in which the sample is dispersed in a carrier gas or a suitable liquid media and circulated through the path of a laser beam. As a light beam passes through the dispersion media, it is scattered by particles creating angular scattering patterns. The detector measures the intensity of light scattered by particles as a function of scattering angle. Finally, a data processor derives the size of the particles from the light scattering information using the Lorenz-Mie theory. Based on this theory, the scattering of light by particles are dependent on;

- equivalent spherical diameter of the particle,
- the angles of scattering,
- the wavelength of the incident light,
- differences in refractive indices between sample and the media in which particles are dispersed [142].

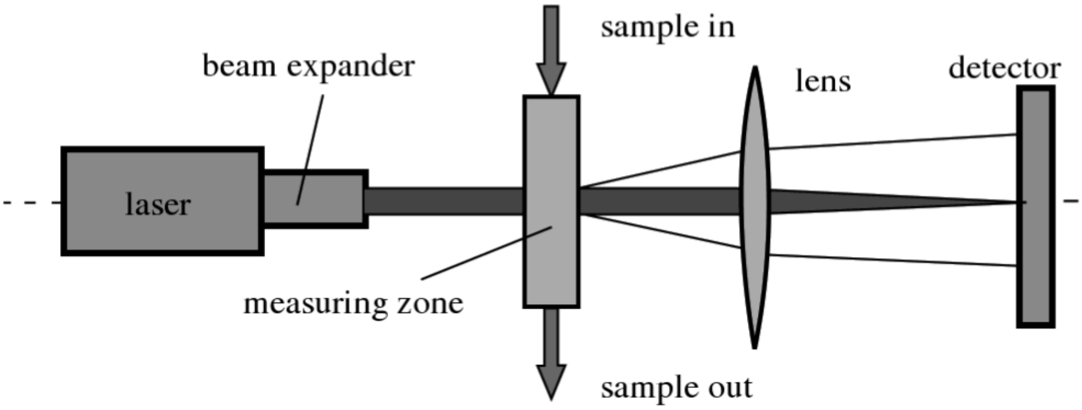

Figure 3.8. A typical set-up for laser diffraction technique used to measure the particle size distribution [142].

A Mastersizer 3000 and its software from Malvern Instruments was used to analyse the particle size distribution of as-received wax (binder agent) using the laser diffraction technique based on the Lorenz-Mie theory. The powder samples were analysed in the dry dispersion mode in which the particles were dispersed in air. The particle size was reported as a volume equivalent sphere diameter for the average of 3 measurements.

4. Results

4.1. Introduction

The preparation conditions can influence the chemical, physical and electrochemical characteristics of electrode materials. In this study, various parameters have been investigated to control the microstructural properties of porous Ni-based electrodes;

- sintering temperature,
- starting alloy to Ni ratio,
- leaching temperature,
- binder properties (concentration and particle size),

The resultant porous electrodes were analysed using different characterization techniques summarized in Figure 4.1.

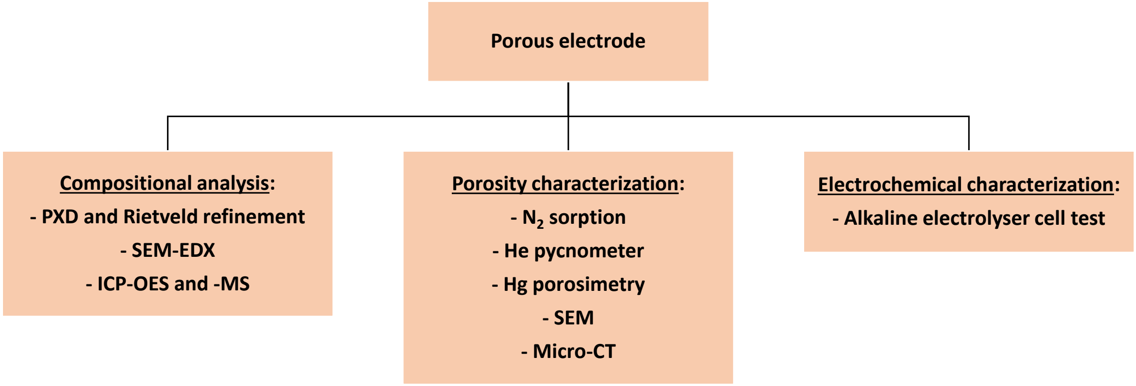

Figure 4.1. Characterization techniques used to study the composition, porosity characteristics and electrochemical performance of porous electrodes.

Section 4.2 details the results for chemical, physical and electrochemical characteristics of porous electrodes sintered at different temperatures, i.e. 625, 650, 700, 750 and 900 ºC. The results for porous electrodes that were prepared from different starting alloy concentrations of 0, 10, 20, 40 and 60 wt.% are reported in Section 4.3. The change in the composition, porosity characteristics and electrochemical performance with respect to different starting alloy to Ni ratios are presented and compared with a Ni electrode.

Section 4.4 reports the results for the electrodes leached at different temperatures, while the results for the effect of binder properties, i.e. binder concentration and particle size in the characteristics of porous electrodes are covered in Section 4.5. The reproducibility test results of various techniques used for the physical, chemical and electrochemical characterizations of electrodes are reported in Appendix 1.

4.2. Effect of Sintering Temperature

Different sintering temperatures, i.e. 625, 650, 700, 750 and 900 ºC were investigated for Ni60:Alloy40-B6.25 samples prepared from a metal composition of 60 wt.% Ni-40 wt.% starting alloy and a binder concentration of 6.25 wt.%. The initial trials with 600 ºC, as the sintering temperature, resulted in fragile electrodes. Therefore, a minimum temperature of 625 ºC was required to achieve a desirable electrode robustness. All samples were leached for 18 h at 70 ºC in 5 M KOH solution containing 10 wt.% K-Na tartrate tetrahydrate.

After the electrochemistry cell test, electrodes were rinsed, dried and passivated as described in Section 3.1.2.4 and analysed through various material characterization techniques. Section 4.2.1 presents the microstructural analysis of samples sintered at different temperatures. The intermetallic phases present in the samples before and after leaching were identified and quantified through PXD and Rietveld refinement analysis for different sintering temperatures and are reported in Section 4.2.2.1. The overall compositions of as-leached samples were determined through 3 different techniques, i.e. ICP-OES, Rietveld refinement and EDX analysis and are presented in Section 4.2.2.2. Section 4.2.3 covers the porosity characteristics of as-leached samples. Finally, Section 4.2.4 reports the electrolyser cell test results.

4.2.1. Microstructural Analysis

Starting materials

First, SEM-SE images were taken on starting materials; Ni 255 (Figure 4.2 (a) and (b)) and starting alloy (Figure 4.2 (c) and (d)) powders. Ni 255 showed a porous and three-dimensional chain-like structure with a relatively uniform size distribution. The particle size range was *ca.* 2-3 µm. The starting alloy, on the other hand, contained particles with varying sizes from *ca.* 1 to 40 µm with relatively flatter surfaces compared to the Ni particles. The EDX analysis of the starting alloy confirmed that the atomic ratio of Al:Ni varied between *ca.* 75:25 and 59:41 corresponding to the intermetallic phases of Al_3Ni and Al_3Ni_2.

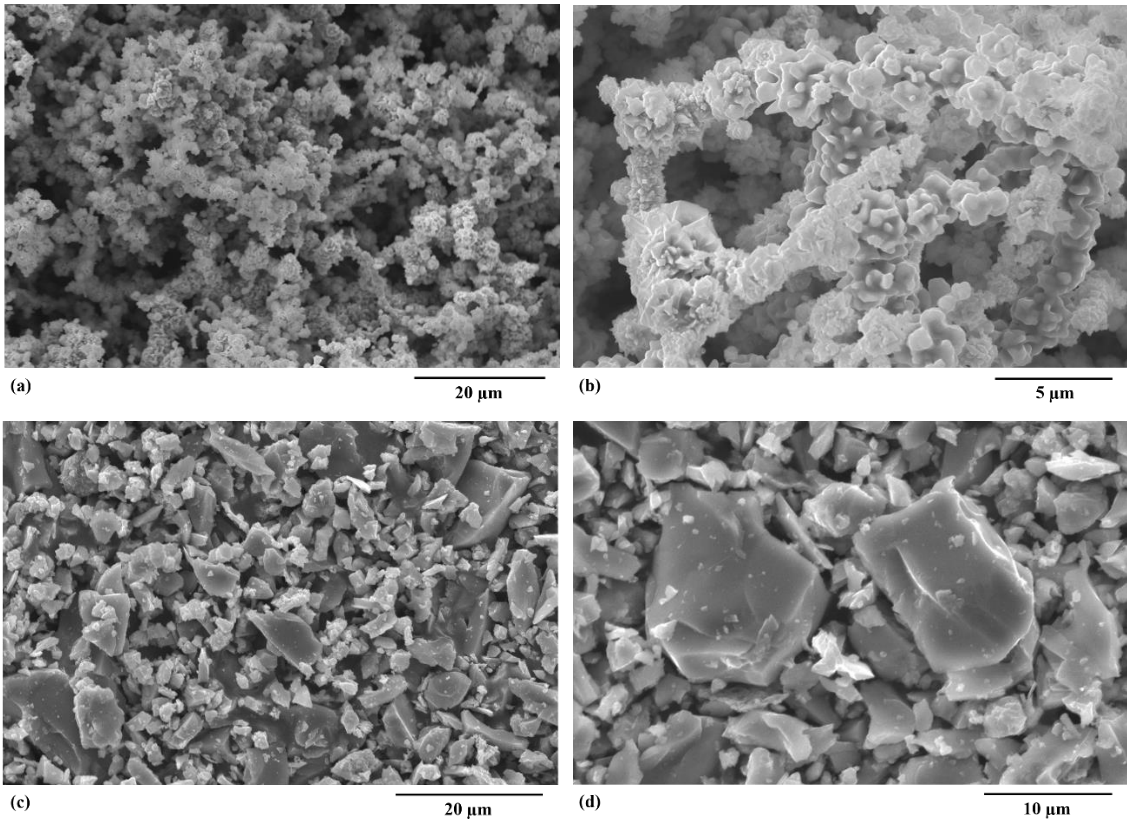

Figure 4.2. SEM-SE images of starting materials with different magnifications; (a) and (b) Ni 255; (c) and (d) starting alloy.

Surface analysis

This section gives the results of the surface of the sample disks, while the cross-sectional analysis is covered in the next section.

Figure 4.3 demonstrates an example of low magnification SEM-SE image taken from a Ni60:Alloy40-B6.25 sample sintered at 650 ºC. Large cavities with varying sizes from *ca.* 15 up to 450 µm were present on the surface. All samples prepared using as-received wax as a binder agent had these large cavities with similar sizes on their surfaces regardless of the sintering temperature.

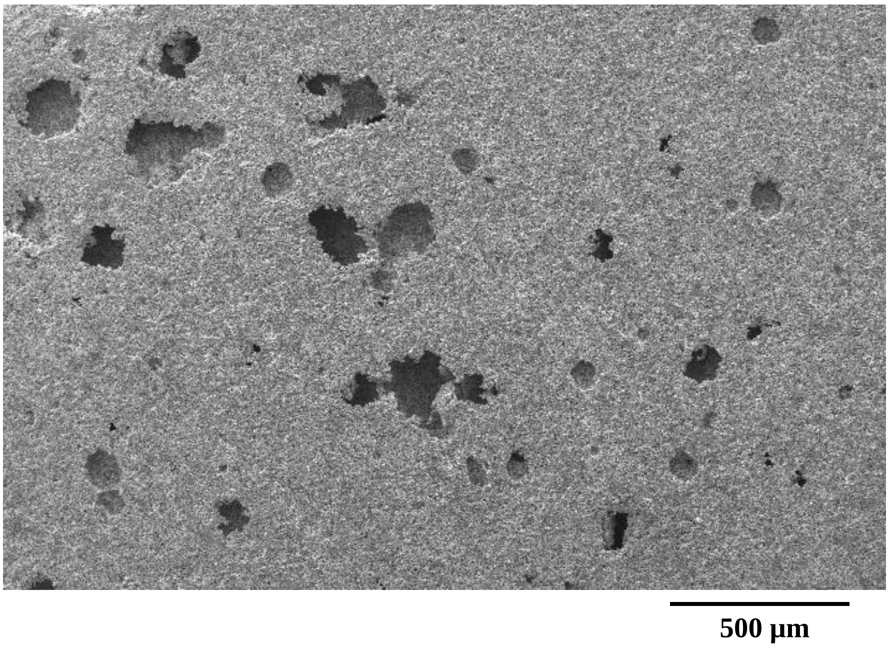

Figure 4.3. A low magnification SEM-SE image from the surface of a Ni60:Alloy40-B6.25 sample sintered at 650 ºC. As-received wax with a concentration of 6.25 wt.% was used as a binding agent.

SEM-SE and -BSE images were taken on the surface of the samples (after sintering at different temperatures) from an area excluding the large cavities (> 15 µm) demonstrated in Figure 4.3 and are presented in Figure 4.4. SEM-SE images of samples sintered at 625-750 ºC exhibited similar morphological features, whereas some neck formations were observed for the sample sintered at 900 ºC. Higher magnification representative SEM-SE images of samples sintered at 650 and 900 ºC are reported in Appendix 3.

Macropores with varying sizes from *ca.* 0.4 to 8 µm were detected on the surfaces of all samples regardless of the sintering temperatures. SEM-BSE images proved the presence of particles with different atomic numbers. The brightest particles in Figure 4.4 (b), (d), (f) and (h) were Ni, which mostly maintained its chain-like structure. As the sintering temperature increased from 650 to 750 ºC, Ni particles slightly lost their brightness in the BSE images. The surface EDX analysis indicated that Ni particles contained *ca.* 8 at.% Al in samples sintered at 750 ºC. Alloy particles with various particle sizes were distributed randomly within the Ni structure. Based on the surface EDX analysis, the majority of the alloy particles had an Al content in the range of 59-73 at.% for samples sintered at 625 and 650 ºC. As the sintering temperature increased from 650 to 750 ºC, the EDX results indicated less Al-rich alloy particles and more particles with an Al content within the range of 41-58 at.%. The SEM-BSE image from the sample sintered at 900 ºC (Figure 4.4 (j)), did not have the bright Ni phase and gave the most homogenous phase distribution of particles amongst all samples. The surface EDX analysis revealed that particles which formed interparticle necks (Figure 4.4 (i) and (j)) had an Al content within the range of 25-39 at.%, whereas an Al:Ni atomic ratio of *ca.* 50:50 was detected for other particles present in the sample after sintering at 900 ºC.

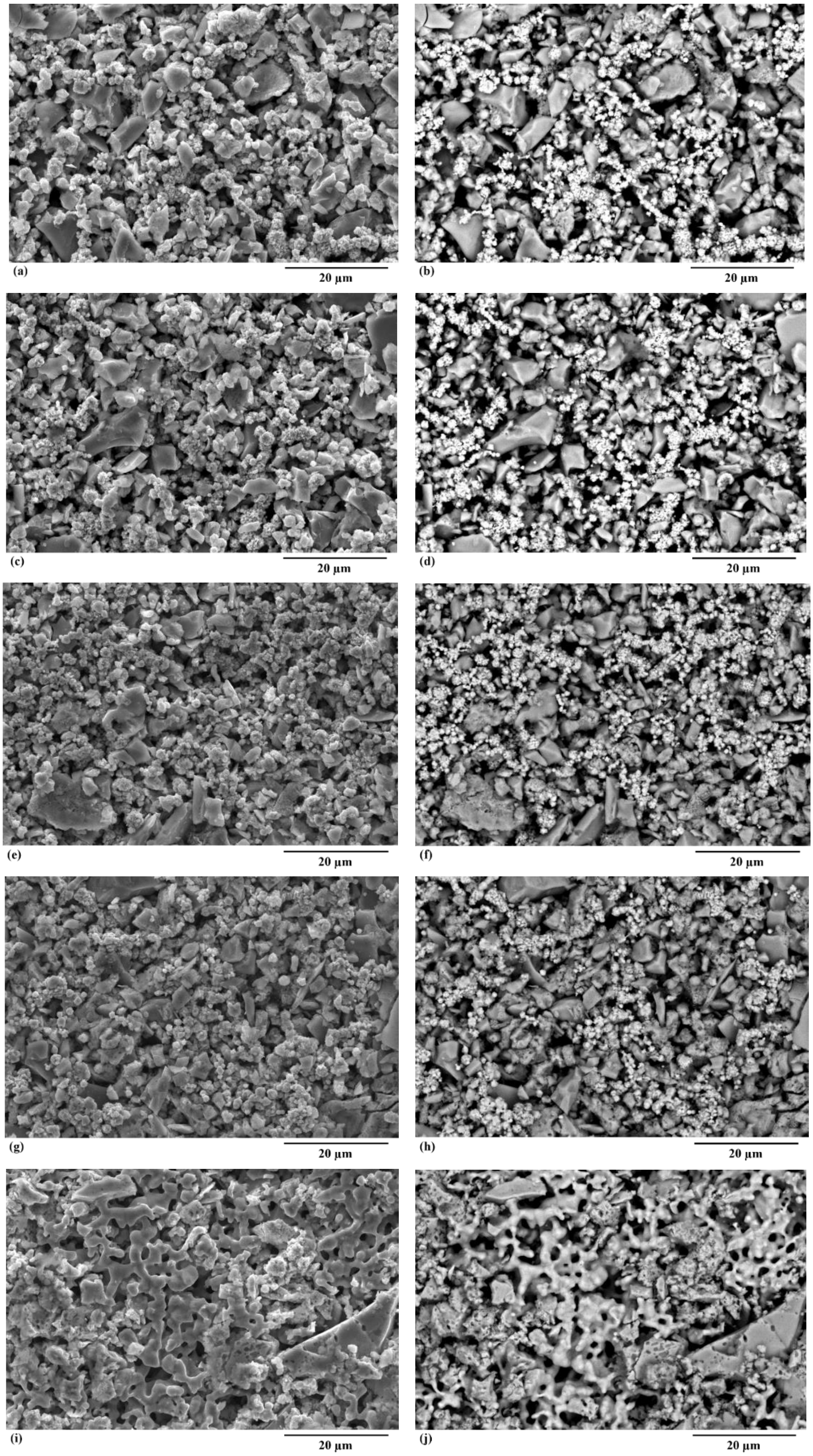

Figure 4.4. SEM-SE (left) and -BSE (right) images of the surfaces of as-sintered Ni60:Alloy40-B6.25 samples sintered at different temperatures; (a) and (b) 625 ºC; (c) and (d) 650 ºC; (e) and (f) 700 ºC; (g) and (h) 750 ºC; (i) and (j) 900 ºC.

Figure 4.5 shows some high-magnification SEM-SE images of alloy particles from the surfaces of as-pressed and as-sintered Ni60:Alloy40-B6.25 samples. Before sintering, the alloy particles mostly had relatively smooth surfaces without any pores that could be detected by the SEM (Figure 4.5 (a) and (b)). Some particles were cracked during pressing (Figure 4.5 (b)). In the samples sintered at 625 and 650 ºC, the majority of alloy particles had relatively smooth surfaces. However, pores with irregular shapes and sizes were also observed on some of the alloy particles as demonstrated in Figure 4.5 (c), (d), (e) and (f). Samples sintered at 700 ºC also contained smooth and rough particles similar to those observed with 625 and 650 ºC. However, some alloy particles had pores with regular shapes and sizes (with an average size of *ca.* 0.2 µm) on their surfaces as shown in Figure 4.5 (h). After sintering at 750 ºC, alloy particles with smooth surfaces became less frequent, whereas particles having regular pores were more common compared to lower temperatures (Figure 4.5 (i) and (j)). The sizes of these pores varied between *ca.* 0.1 and 1 µm. As demonstrated in Figure 4.5 (k) and (l), the porosity on the surfaces of the alloy particles became most significant and greatest in size (up to *ca.* 5 µm) when the sintering temperature increased from 750 to 900 ºC.

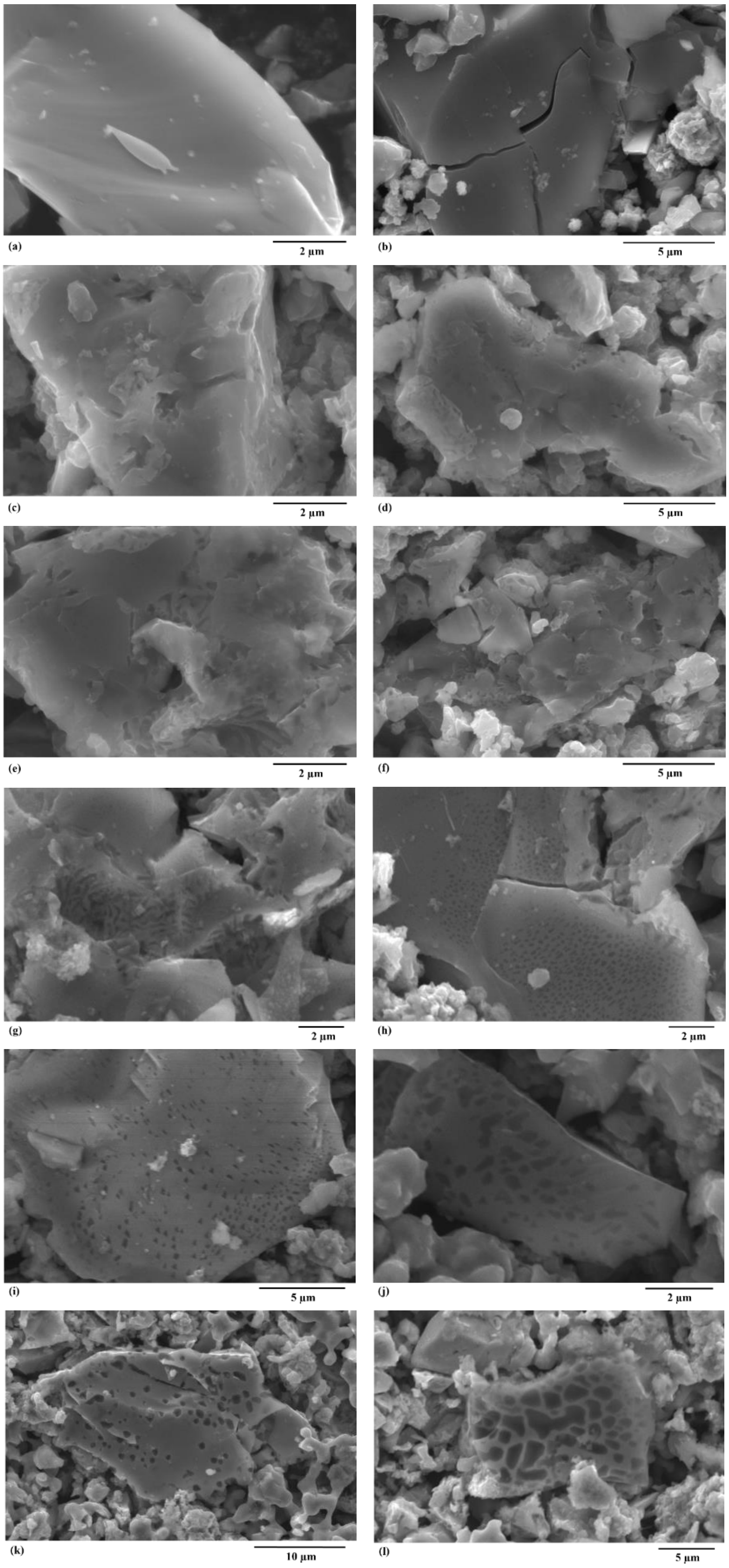

Figure 4.5. High magnification SEM-SE images of the surfaces of alloy particles present in Ni60:Alloy40-B6.25 samples before and after sintering, where (a) and (b) as-pressed; (c) and (d) sintered at 625 ºC; (e) and (f) sintered at 650 ºC; (g) and (h) sintered at 700 ºC; (i) and (j) sintered at 750 ºC; (k) and (l) sintered at 900 ºC.

Representative SEM images of as-leached Ni60:Alloy40-B6.25 samples are reported in Appendix 4. SEM-SE images did not indicate any significant change in the microstructure of these samples during leaching (Figure A4.1). The effect of leaching Al on the appearance of particles from the precursor alloys was not detected by conventional SEM technique. High magnification SEM-SE images of alloy particles in as-leached samples (Figure A4.2) were similar to those observed in as-sintered samples (Figure 4.5). The EDX analysis of alloy particles in as-leached samples sintered at 625 and 650 ºC showed that the Al content mostly varied between 9-22 at.%. However, as the sintering temperature increased from 650 to 750 ºC, greater Al contents were also detected from 30 to 43 at.%. In the case of 900 ºC, as-leached alloy particles had similar compositions to those revealed for as-sintered samples.

Cross-sectional analysis

This section reports the results of the cross-sections of the sample disks. As demonstrated in Figure 4.6, all samples had similar cross-sections regardless of the sintering temperature. The thickness of the samples was 1.50 ± 0.02 mm, which was slightly higher than that measured before sintering; 1.45 ± 0.02 mm. The increase in the sintering temperature from 625 to 900 °C did not affect the thickness of samples. The cavities with varying sizes from *ca.* 15 up to 450 µm were observed in the cross-sections of both as-sintered and as-leached samples. The distribution of these cavities across the cross-section was not homogeneous.

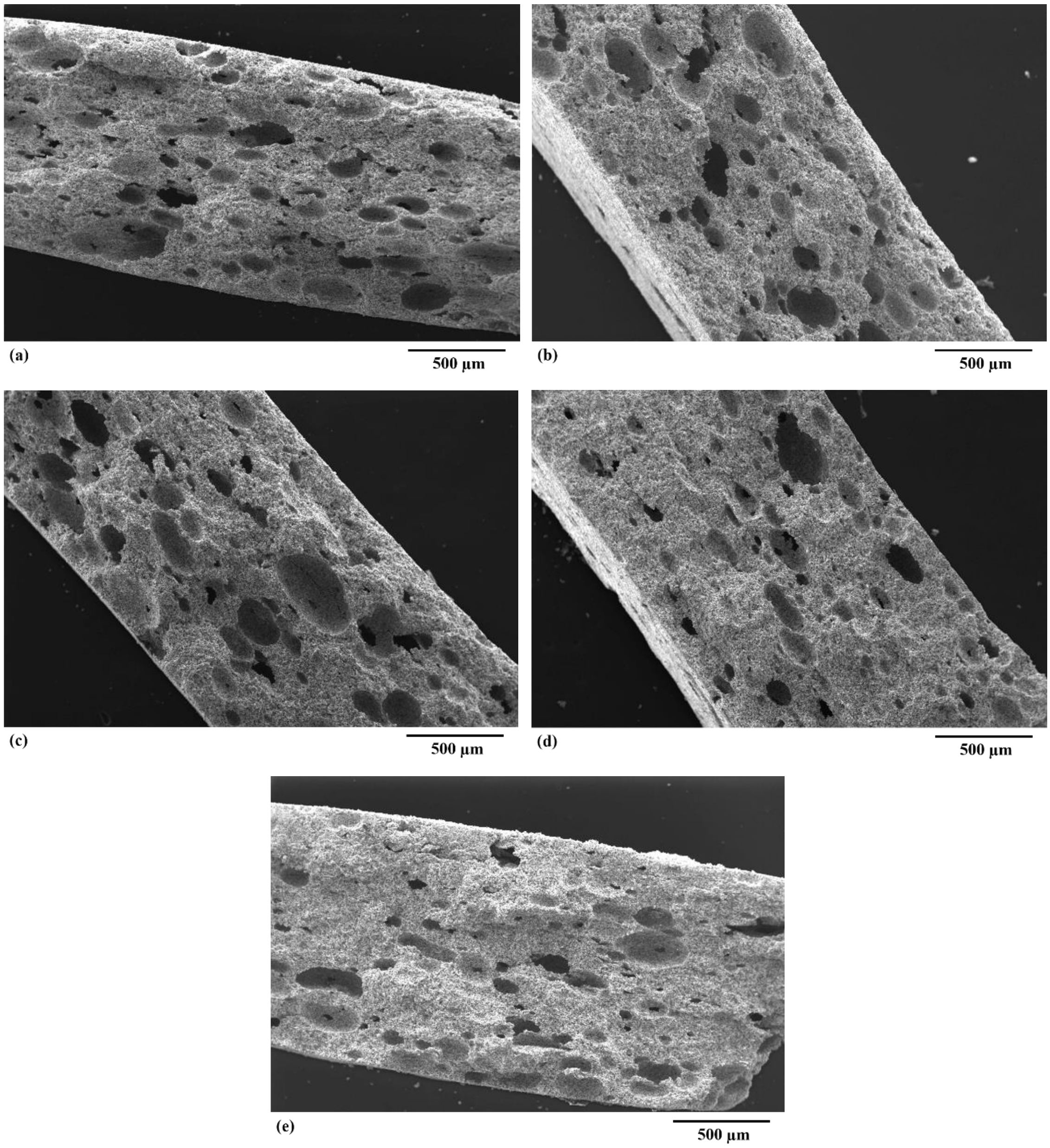

Figure 4.6. SEM-SE cross-section images of Ni60:Alloy40-B6.25 samples sintered at different temperatures; (a) 625 ºC; (b) 650 ºC; (c) 700 ºC; (d) 750 ºC; (e) 900 ºC.

Table 4.1 gives the EDX analysis results of alloy particles for as-sintered Ni60:Alloy40-B6.25 samples with respect to the sintering temperature. Compared to the surface EDX results, the cross-sectional EDX analysis of as-sintered samples indicated a decrease in the frequency of alloy particles with an Al content in the range of 59-73 at.%. Whereas cross-sections contained more alloy particles with lower Al concentrations (40-58 at.%). For instance, the percentage of the Al-rich particles (with an Al content of ≥ 59 at.%) detected on the cross-section of an as-sintered sample was *ca.* 20 % less than that detected on the surface, when samples were sintered at 650 ºC. This compositional difference between the cross-section and surface became less significant as the sintering temperature increased from 625 to 900 ºC. In the case of 900 ºC, the alloy particles in the cross-section had similar Al compositions to those revealed on the surface which were in the range of 40-55 at.%.

Table 4.1. EDX results of alloy particles for the surface (S) and cross-section (CS) of Ni60:Alloy40-B6.25 samples after sintering at different temparatures from 625 to 900 ºC.

Measurement	Atomic Al concentration (at.%)									
	625 ºC		650 ºC		700 ºC		750 ºC		900 ºC	
	S	CS	S	CS	S	CS	S	CS	S	CS
1	61	60	66	41	59	44	63	50	47	45
2	67	44	63	65	50	49	59	44	54	51
3	65	59	42	52	64	62	55	53	49	40
4	59	54	67	59	54	67	43	67	53	49
5	45	67	59	62	62	54	49	63	45	46
6	55	61	66	45	44	66	60	52	45	50
7	65	64	43	63	66	56	51	46	48	40
8	53	52	64	51	43	47	56	45	46	52
9	63	50	73	54	49	51	68	59	41	53
10	61	45	54	60	61	59	44	61	49	51

Similarly, the EDX analysis of as-leached samples also indicated varying Al:Ni ratios of the particles between the surface and cross-section. The frequency of Al contents in the range of 30-45 at.% was greater in the cross-section compared to those detected on the surface of the samples sintered up to 750 ºC. The cross-sectional EDX results of as-leached samples was similar to that of as-sintered samples for 900 ºC.

4.2.2. Phase Analysis

4.2.2.1. Intermetallic Phases

PXD analysis

The intermetallic phases present in samples before and after leaching were identified through the PXD analysis. Figure 4.7 (a) and (b) show the phases present in the starting metal mixture before sintering (60 wt.% Ni-40 wt.% starting alloy) and in Ni60:Alloy40-B6.25 samples after sintering at different temperatures; i.e. 625, 650, 700, 750 and 900 ºC. The starting mixture consisted of Ni, Al_3Ni and Al_3Ni_2, with Al-rich phases being sourced from the starting alloy. The structures of Ni, Al_3Ni and Al_3Ni_2 are face-centred cubic (with Fm3m space group), primitive orthorhombic (with Pnma space group) and primitive hexagonal (with P-3m1 space group) respectively. Ni60:Alloy40-B6.25 samples sintered from 625 ºC up to 750 ºC also had the Al_3Ni_2 phase. However, there was no evidence of the presence of Al_3Ni in any samples regardless of their sintering temperatures. Al-rich phases were not detected with samples sintered at 900 ºC. Up to 750 ºC, as-sintered samples consisted of Al_3Ni_2, AlNi, $AlNi_3$ and Ni, whilst only $AlNi_3$ and an AlNi phase with a higher Ni composition, i.e. $Al_{0.84}Ni_{1.16}$ were identified for samples sintered at 900 ºC. AlNi, $AlNi_3$ and $Al_{0.84}Ni_{1.16}$ have the primitive cubic structure with the Pm3m space group. It must be noted that during the handling of as-sintered samples, an increased robustness was observed as the sintering temperature increased.

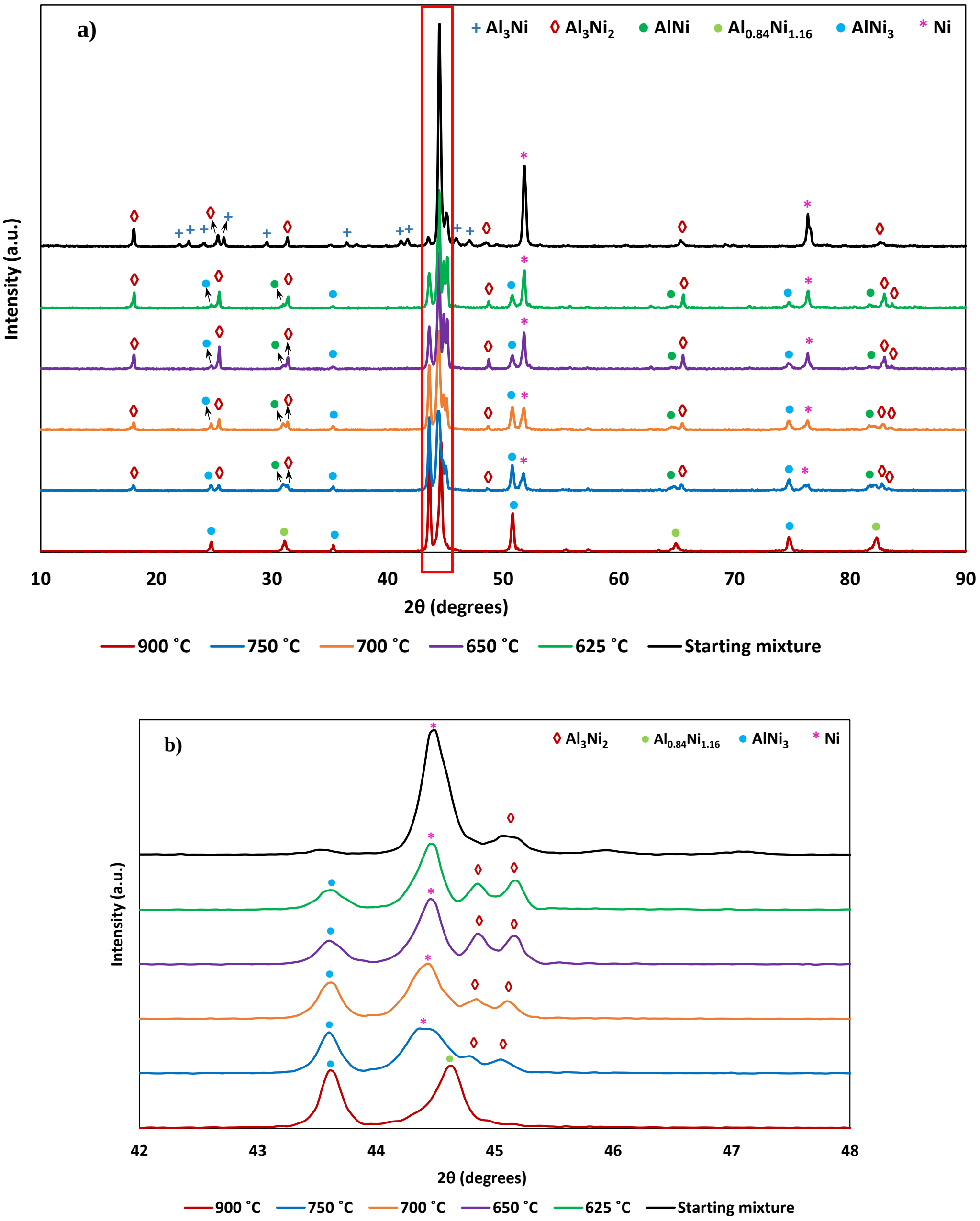

Figure 4.7. PXD patterns of the starting metal mixture and Ni60:Alloy40-B6.25 samples sintered at different temperatures, where (a) for the 2Ø range of 10-90 °; (b) enlarged from the marked area in (a).

As shown in Figure 4.8, after leaching, Al_3Ni_2 disappeared, whereas $AlNi_3$ and AlNi were still present in as-leached Ni60:Alloy40-B6.25 samples sintered up to 750 ºC. For the sample sintered at 900 ºC, the leaching process did not change the intermetallic phases present in the sample.

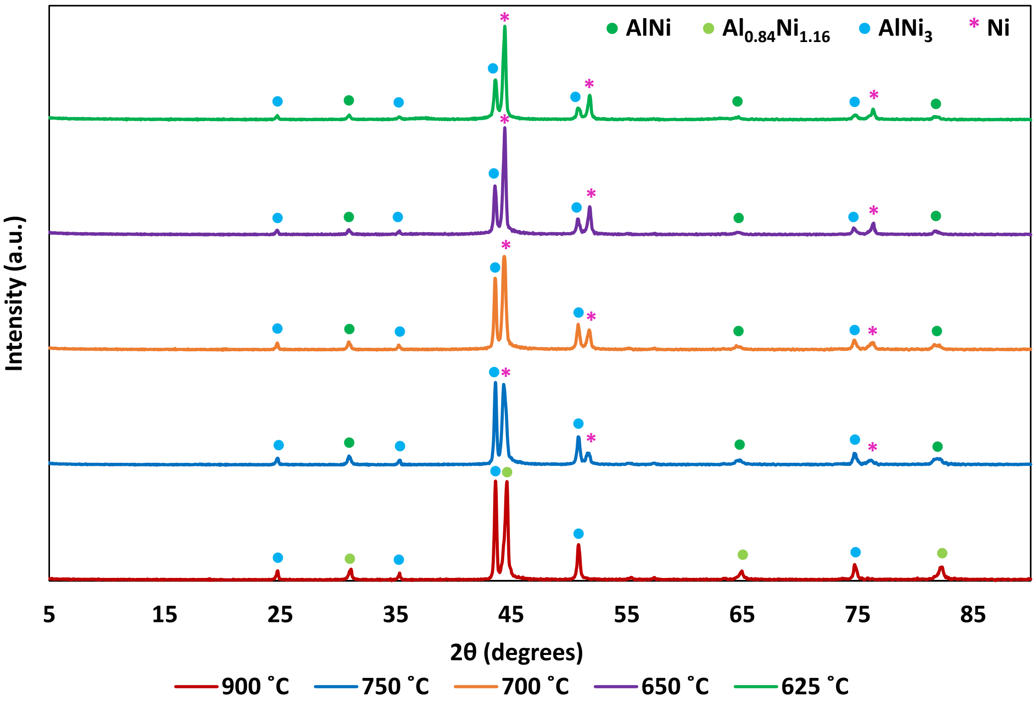

Figure 4.8. PXD patterns of as-leached Ni60:Alloy40-B6.25 samples sintered at different temperatures from 625 to 900 °C.

The starting alloy powder consisting of two Al-rich phases (Al_3Ni and Al_3Ni_2) was also sintered at 650 ºC and leached at the same conditions described at the beginning of Section 4.2. The PXD patterns of as-received, as-sintered and as-leached starting alloy powders (Figure A5.1) are reported in Appendix 5 and compared to that of an as-leached Ni60:Alloy40-B6.25 sample sintered at 650 ºC (Figure A5.2). The PXD analysis showed that the starting alloy contained only Al_3Ni and Al_3Ni_2 after sintering (Figure A5.1 (b)), which were completely depleted during leaching leaving broadened Ni and NiO peaks behind (Figure A5.1 (c)). Despite the broadened Ni peaks observed with as-leached alloy powder, the widths of the Ni peaks for as-leached samples were similar to those for Ni 255 (Figure A5.2).

Rietveld refinement

A quantitative analysis of intermetallic phases was performed through the Rietveld refinement technique as described in Section 3.3.4.1. Figure 4.9 demonstrates the change in the actual weights of different phases present in Ni60:Alloy40-B6.25 samples before and after leaching with respect to the sintering temperature. Before sintering, the starting metal mixture contained 60 wt.% Ni and 40 wt.% Al-rich phases (a mixture of Al_3Ni and Al_3Ni_2 with an overall Ni composition of *ca.* 50 wt.%). As-sintered samples contained less Al_2Ni_3 and Ni and more AlNi and $AlNi_3$ as the sintering temperature increased from 625 to 750 ºC. Sintering at 750 ºC resulted in *ca.* 2.7 and 3.3 times less Al_2Ni_3 and Ni and *ca.* 3.4 and 2.6 times more AlNi and $AlNi_3$ in weight respectively in comparison to sintering at 625 ºC. At 700 and 750 ºC, AlNi became the dominant phase with an approximate concentration of 40 wt.%. After leaching, samples contained more Ni regardless of the sintering temperature. The increase in the Ni weight was *ca.* 56, 50, 33 and 27 % for the samples sintered at 625, 650, 700 and 750 ºC respectively. Whereas there was no strong evidence of a change in the amounts of AlNi and $AlNi_3$ during leaching. In the case of sintering at 900 ºC, as-leached samples contained similar amounts of $Al_{0.84}Ni_{1.16}$ and $AlNi_3$ to those estimated before leaching.

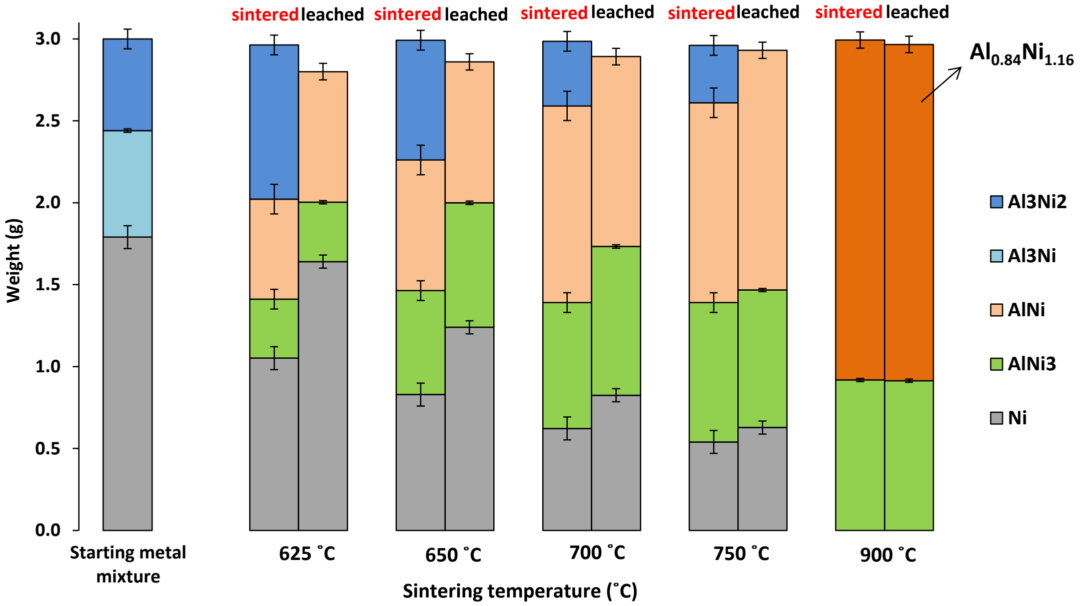

Figure 4.9. Rietveld refinement analysis results for the amounts of intermetallic phases present in the starting metal mixture and as-sintered and as-leached Ni60:Alloy40-B6.25 samples sintered at different temperatures from 625 to 900 ºC.

Rietveld refinement analysis also enabled the determination of lattice parameters of Ni and AlNi phases present in the samples before and after leaching. As demonstrated in Figure 4.10 (a), the samples sintered at 625 and 650 ºC had Ni phase with similar lattice parameters. However, from 650 to 750 ºC, the lattice parameter increased. In the case of AlNi phase, the lattice parameter showed a decreasing trend with increasing sintering temperatures (Figure 4.10 (b)), with the decrease from 750 to 900 ºC being most significant. This decrease was most significant from 750 to 900 ºC. The leaching process did not have a significant influence on the lattice parameters of Ni and AlNi which were similar to those determined before leaching.

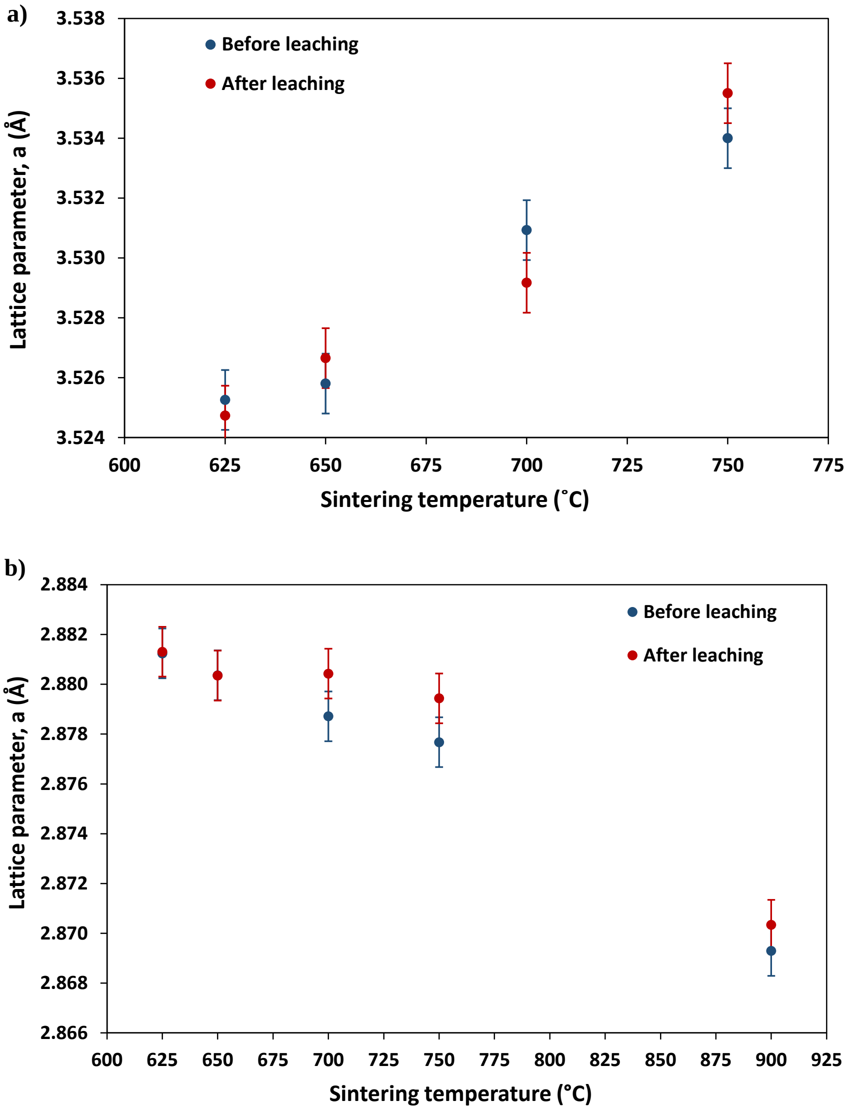

Figure 4.10. Rietveld refinement results of lattice parameters of (a) Ni and (b) AlNi phases for as-sintered and as-leached Ni60:Alloy40-B6.25 samples sintered at different temperatures; 625, 650, 700, 750 and 900 ºC.

4.2.2.2. Overall Composition

Figure 4.11 presents compositional analysis results from three different techniques; ICP-OES, Rietveld refinement and EDX cross-sectional analysis for as-leached Ni60:Alloy40-B6.25 samples sintered at different temperatures. It was assumed that all samples only contained Al and Ni elements. An increase in un-leached Al content was observed as the sintering temperature rose from 625 to 900 ºC. Samples sintered at 625 ºC had an Al weight content almost 2 times less than that sintered at 750 ºC.

Sintering at 900 ºC resulted in a similar Al composition to that before leaching. The leaching solutions after leaching the samples sintered at 650 and 900 ºC were also sampled and tested through the ICP-MS technique to identify the Al content dissolved during the reaction. Results from the ICP-MS analysis are reported in Appendix 6. The remaining Al contents calculated for as-leached samples (Table A6.2) were in agreement for the compositional analysis results from other techniques.

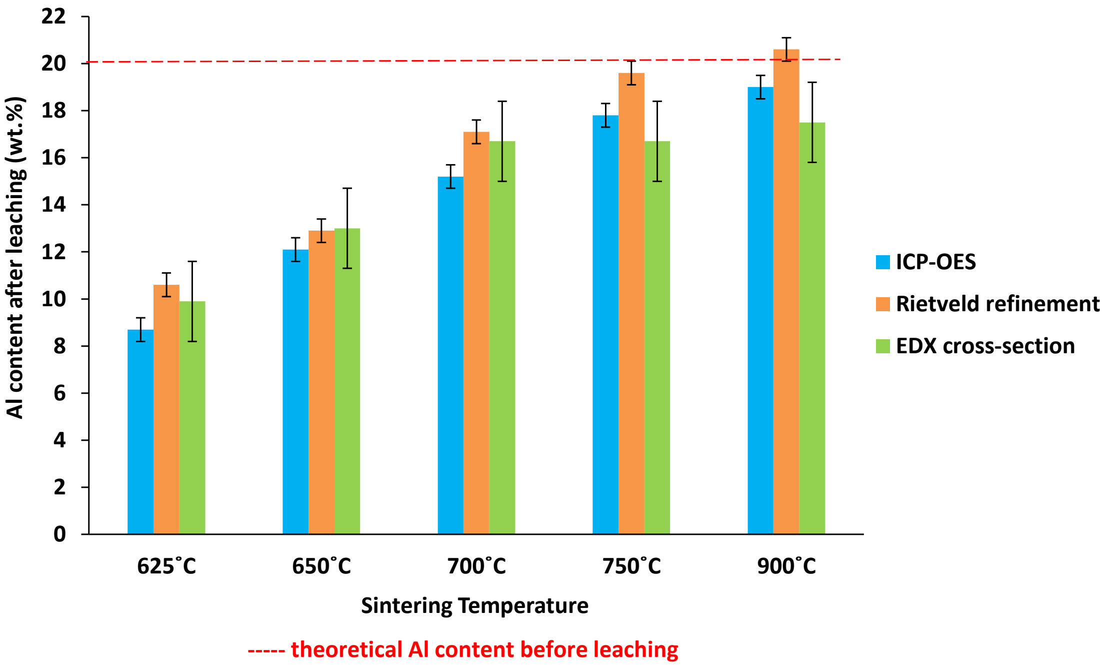

Figure 4.11. Results of ICP-OES, Rietveld refinement and EDX cross-section analyses for the Al contents of as-leached Ni60:Alloy40-B6.25 samples sintered at different temperatures from 625 to 900 ºC.

The EDX compositional analysis was also performed on the surface of as-leached sample pellets and compared to the results from the EDX cross-sectional analysis (Figure 4.12). The Al weight concentration on the surface increased almost linearly with the sintering temperature. The sample sintered at 625 ºC gave an Al surface concentration of 4.6 ± 1.2 wt.%, which was *ca.* 3 and 4 times lower than those identified for samples sintered at 750 and 900 ºC respectively. Assuming all samples contained 20 wt.% Al on the surface before leaching, *ca.* 80, 60, 50 and 40 % of the initial Al content were removed from the surface during leaching for the samples sintered at 625, 650, 700 and 750 ºC respectively. Compared to the cross-section, lower Al compositions were identified on the surface of as-leached samples except from that sintered at 900 ºC, which gave similar Al contents on its surface and cross-section. The surface Al concentrations of samples sintered at 625 and 750 ºC were *ca.* 50 and 25 % lower than those measured on the cross-sections of these samples respectively.

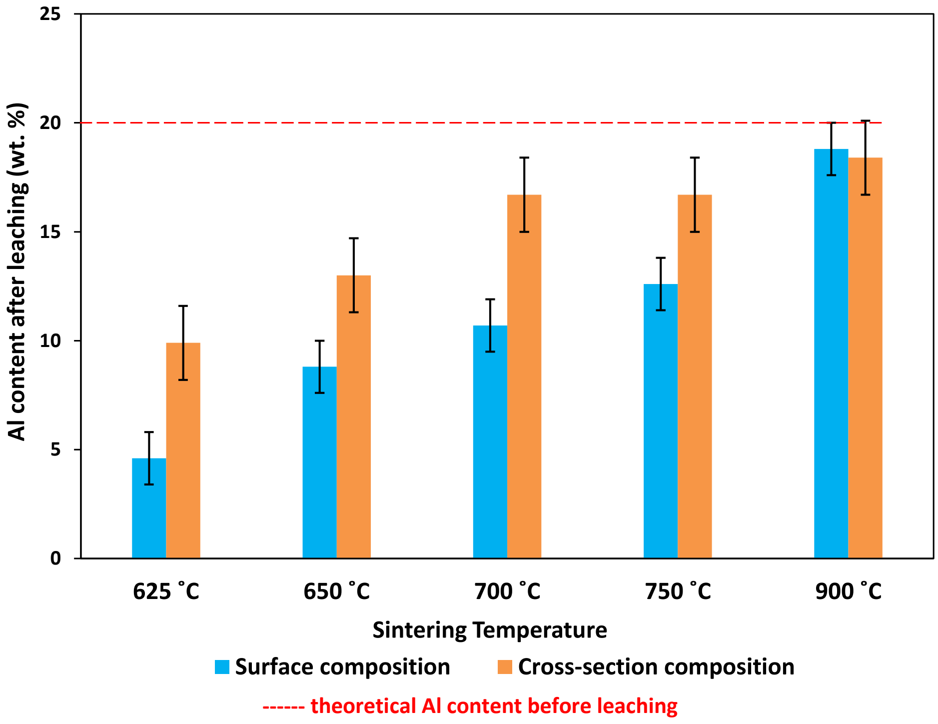

Figure 4.12. EDX results for the Al contents of the surface and cross-section of as-leached Ni60:Alloy40-B6.25 samples sintered at different temperatures from 625 to 900 ºC.

4.2.3. Porosity Characteristics

N_2 sorption and He Pycnometer

Figure 4.13 demonstrates N_2 sorption and He pycnometer results for the porosity characteristics of as-leached Ni60:Alloy40-B6.25 samples sintered at different temperatures from 625 to 900 ºC. There was an upward trend in the micro- and mesoporosity with higher sintering temperatures. Increasing the sintering temperature from 650 to 900 ºC reduced the specific surface area by almost 90 % through a significant loss of micro- and mesoporosity. The macropore volume, on the other hand, was not influenced by the sintering temperature.

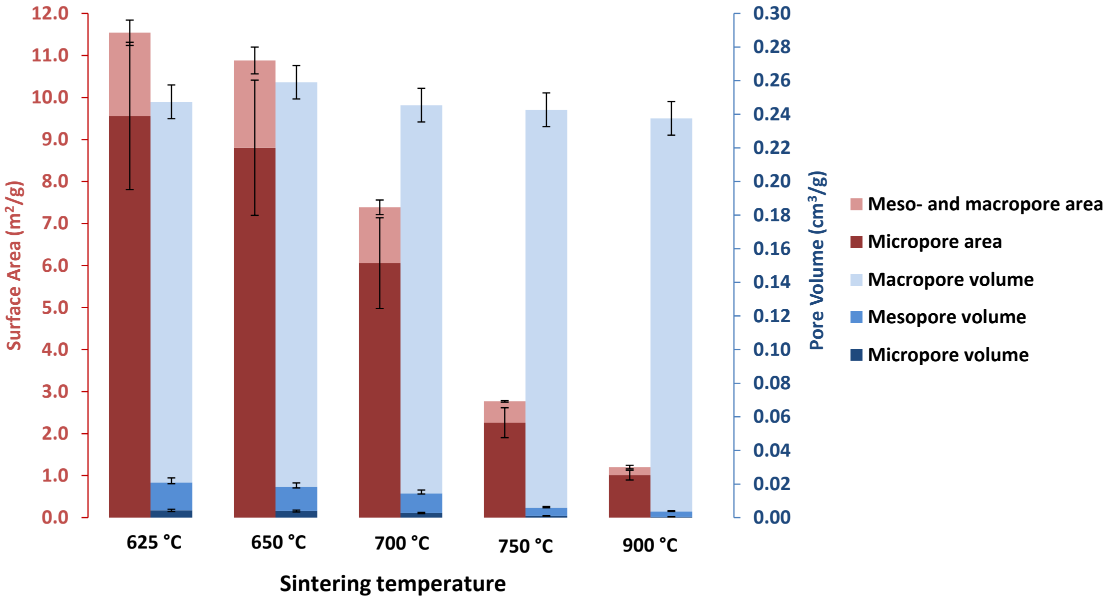

Figure 4.13. N_2 sorption and He pycnometer results for the porosity characteristics of as-leached Ni60:Alloy40-B6.25 samples sintered at different temperatures from 625 to 900 ºC.

The porosity characteristics of samples before and after sintering at 650 and 900 ºC were also determined and compared to those of as-leached samples. As shown in Figure 4.14, before leaching, the difference in the porosity features was not substantial for samples sintered at 650 and 900 ºC. Compared to the sample pellet prepared by pressing the starting metal mixture without a binder, sintering did not change micro- and mesoporosity features significantly. The specific macropore volume, however, was *ca.* 50 % more when the binder was used. After leaching, sintering at 900 ºC gave similar results to those estimated before leaching, whereas a significant increase in the micro- and mesoporosity was observed for the as-leached sample sintered at 650 ºC. The skeleton densities measured by means of He pycnometer were *ca.* 5.4 g/cm^3 for as-pressed (without a binder) and as-sintered samples regardless of the sintering temperature.

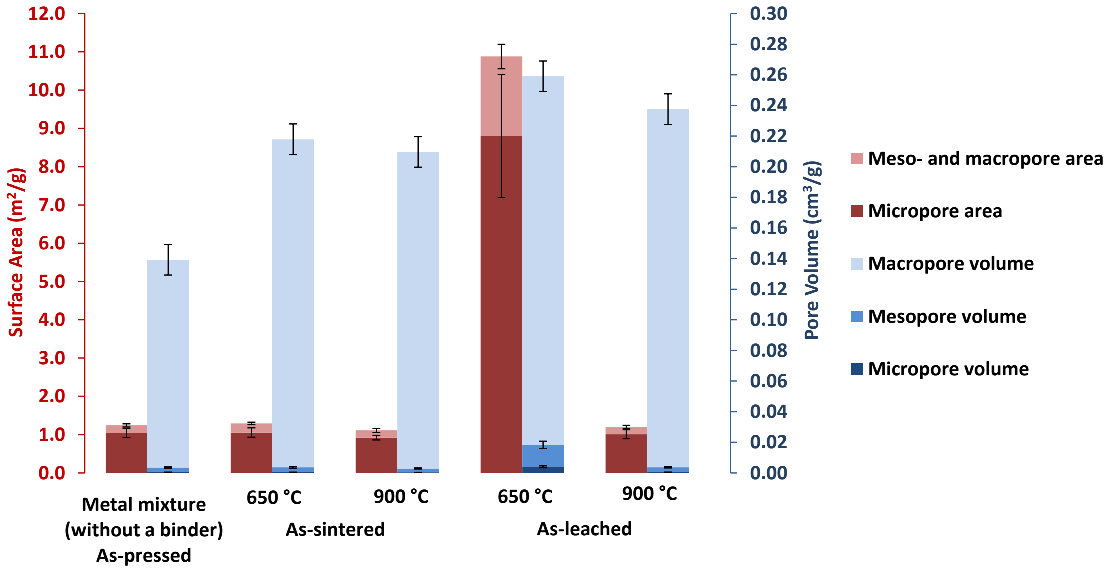

Figure 4.14. N_2 sorption and He pycnometer results for the porosity characteristics of as-pressed, as-sintered and as-leached Ni60:Alloy40-B6.25 samples, where samples were sintered at 650 or 900 °C.

Figure 4.15 presents the mesopore size distribution for as-leached Ni60:Alloy40-B6.25 samples sintered at different temperatures. The mesoporosity concentrated within the pore size range of 2-12 nm regardless of the sintering temperature. The mesopore volume was negligible for samples sintered at 900 °C in comparison to samples sintered at lower temperatures.

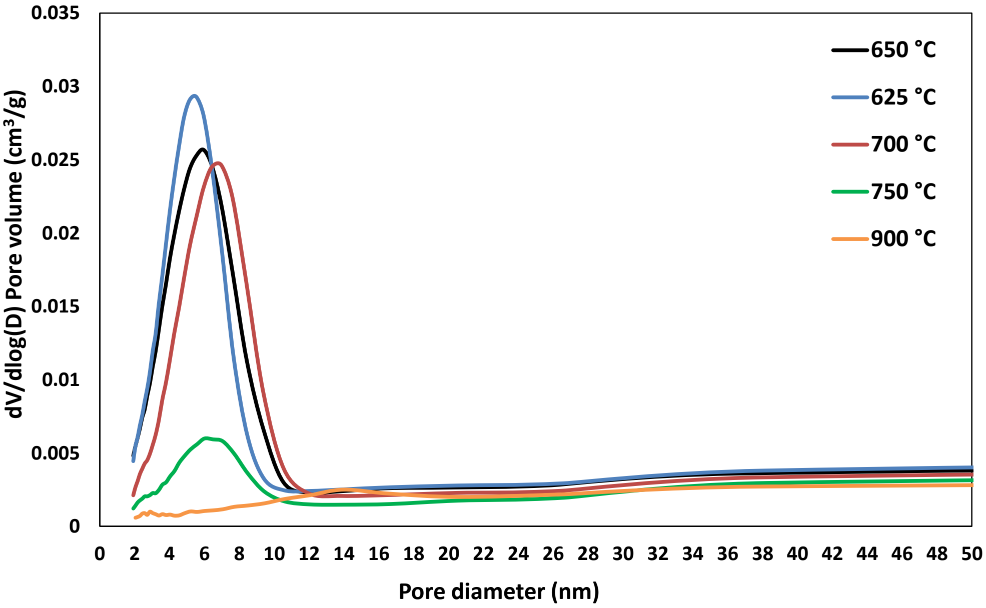

Figure 4.15. N_2 sorption results for the mesopore size distribution of as-leached Ni60:Alloy40-B6.25 samples sintered at different temperatures from 625 to 900 °C.

As reported in Section 4.2.1, regardless of the sintering temperature, sample pellets had similar thicknesses hence similar disk volumes. The contributions of material, closed and open pores to the disk volume were also calculated for as-leached Ni60:Alloy40-B6.25 samples using the He pycnometer results. As demonstrated in Figure 4.16, increasing the sintering temperature from 625 to 900 °C did not significantly change the volumes of material, closed and open pores, which accounted for *ca.* 34, 7 and 59 % of the disk volume respectively.

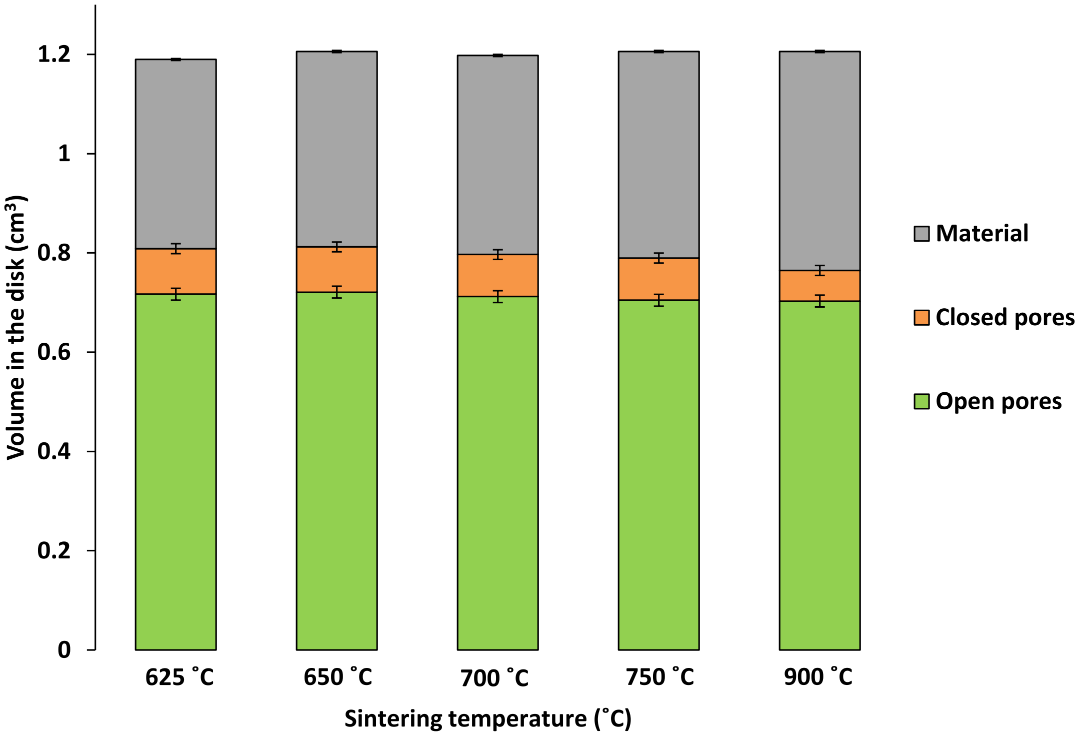

Figure 4.16. He pycnometer results for the contributions of material, closed and open pores to the disk volume of as-leached Ni60:Alloy40-B6.25 samples sintered at different temperatures from 625 to 900 °C.

MIP

Figure 4.17 gives the MIP results for the pore size distributions of as-leached Ni60:Alloy40-B6.25 samples sintered at 650 and 900 ºC. The majority of pores accumulated in the size range of *ca.* 0.2-5 µm. Sintering at 650 and 900 ºC gave similar distribution profiles apart from the peak observed at pore sizes around 3 nm, which was greater with the 650 ºC sintering temperature. The large macropores observed in SEM images with sizes from *ca.* 15 up to 450 µm were not detected by the MIP technique since the MIP measures the throat or pore channel size from the sample surface towards that pore body rather than the actual internal pore size. As shown in Table 4.2, the porosity measured by means of MIP was *ca.* 60 % regardless of the sintering temperature.

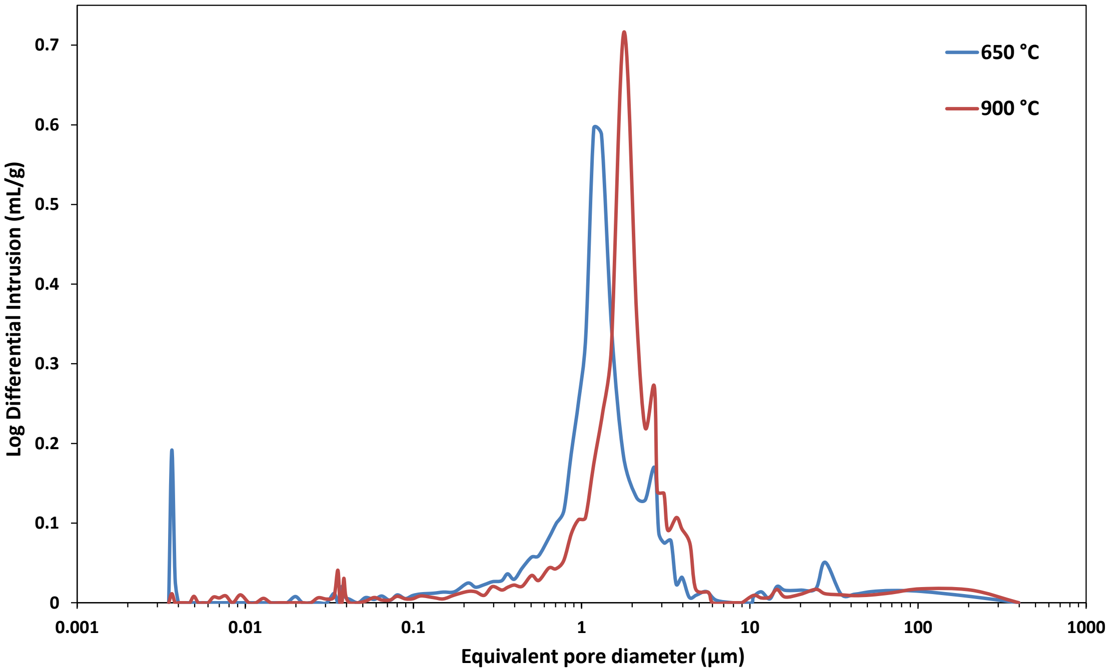

Figure 4.17. MIP results for the pore size distributions of as-leached Ni60:Alloy40-B6.25 samples sintered at 650 and 900 ºC.

Table 4.2. MIP results for the porosity of as-leached Ni60:Alloy40-B6.25 samples sintered at 650 and 900 ºC.

Sintering temperature (ºC)	Hg intrusion volume (± 0.01 ml/g)	Porosity (± 2 %)
650	0.23	61
900	0.22	60

4.2.4. Electrochemical Performance

Figure 4.18 shows the trend in the electrolyser cell voltage-current density curves and Table 4.3 compares the cell voltages measured at 1 A/cm^2 with respect to the sintering temperature used during the preparation of cathode samples. There was an increasing trend in the cell voltage with higher sintering temperatures. Sintering at 900 ºC resulted in the lowest electrochemical performance, while samples sintered below 750 ºC had the best performance. The electrode sintered at 900 ºC led to a *ca.* 10 % higher cell voltage at 1 A/cm^2 compared to that sintered at 625 ºC. The differences in the cell voltages measured with the cathode sintered at 900 ºC and a Ni cathode prepared by pressing only Ni powder and sintering it at 650 ºC were within the margin of error for the electrolyser cell test. Regardless of the sintering temperature the electrodes gave significantly lower cell voltages in comparison to the typical voltages reported in the literature for a conventional alkaline electrolyser cell operating at 0.1 and 0.4 A/cm^2 current densities.

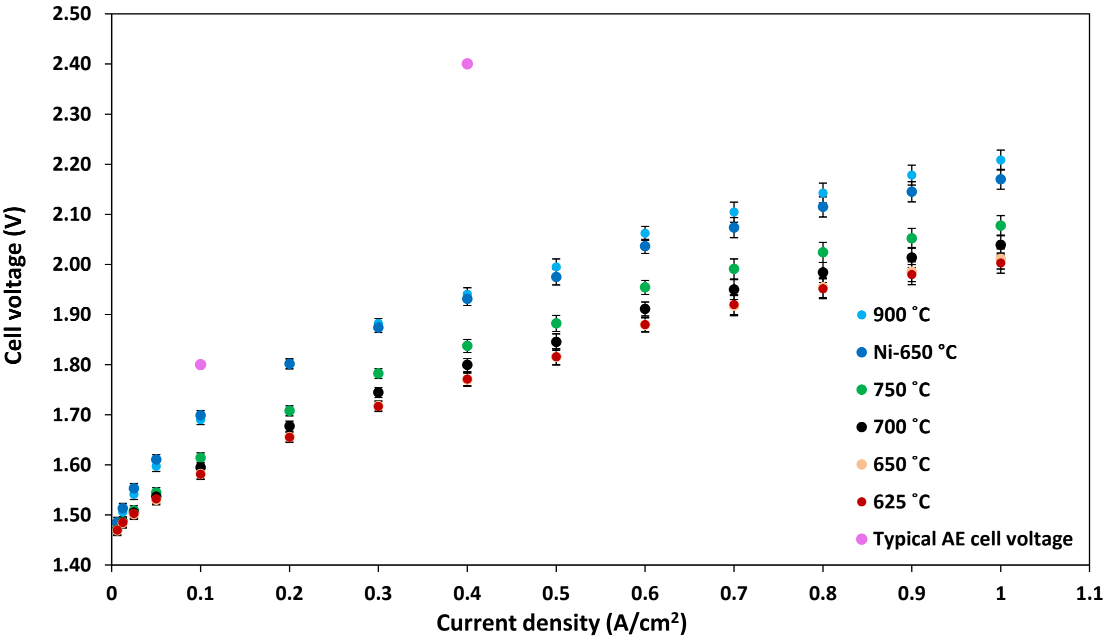

Figure 4.18. Electrolyser cell voltage-current density curves measured using cathodes sintered at different temperatures. Conventional alkaline electrolysers (AEs) often operate at current densities up to 0.4 A/cm^2 (from Table 1.1)

Table 4.3. Electrolyser cell voltages measured at 1 A/cm^2 using cathodes sintered at different temperatures.

Sintering temperature (ºC)	625	650	700	750	900
Cell voltage at 1 A/cm^2 (± 0.02 V)	2.00	2.01	2.04	2.08	2.21

Table 4.4 gives the observations of the mechanical performance of electrodes before and after the electrolyser cell test. Although the electrochemical activity decreased, better robustness of electrodes was observed as the sintering temperature rose. The electrodes sintered at 900 ºC showed excellent mechanical performance regardless of the number of the cell tests.

Table 4.4. Observations on mechanical performance of electrodes sintered at different temperatures.

Sintering temperature (ºC)	Mechanical strength of as-sintered and as-leached samples	Observations after the alkaline electrolyser cell test
625 650	Sufficient	No significant change in the mechanical performance after the test. However, care was required during handling of electrode.
700	Good	Easier handling than the samples sintered at lower temperatures.
750	Very good	Mechanical strength was still very good.
900	Excellent	Excellent robustness regardless of the number of cell tests.

4.3. Effect of Starting Alloy Concentration

The effect of starting alloy to Ni ratio in the characteristics of as-leached samples was investigated using the starting alloy concentrations of 0, 10, 20, 40 and 60 wt.% of the total metal mixture and compared to the properties of a Ni sample. Initially, samples were only prepared from the starting alloy powder without addition of Ni powder.

However, the resultant sample disks were extremely fragile and it was not feasible to test them in an alkaline electrolyser cell. Therefore, a maximum starting alloy concentration of 60 wt.% was chosen to investigate its effect on the characteristics of Ni-based electrodes.

All samples contained 6.25 wt.% as-received wax before sintering them at 650 ºC. Leaching of Al took place at 70 °C for 18 h in 5 M KOH aqueous solution containing 10 wt.% K-Na tartrate tetrahydrate.

The results for chemical and physical characterization tests are reported in Sections 4.3.1 and 4.3.2, while the electrolyser cell test results are presented in Section 4.3.3.

4.3.1. Microstructural Analysis

Figure 4.19 presents SEM-SE and -BSE images of as-sintered Ni and as-leached samples prepared from different starting alloy to Ni ratios. Due to the porous morphology of Ni 255, a macroporous structure was observed for all samples. The sizes of pores varied between *ca.* 0.2 and 10 µm. There was an increasing trend in the macroporosity with higher starting alloy concentrations.

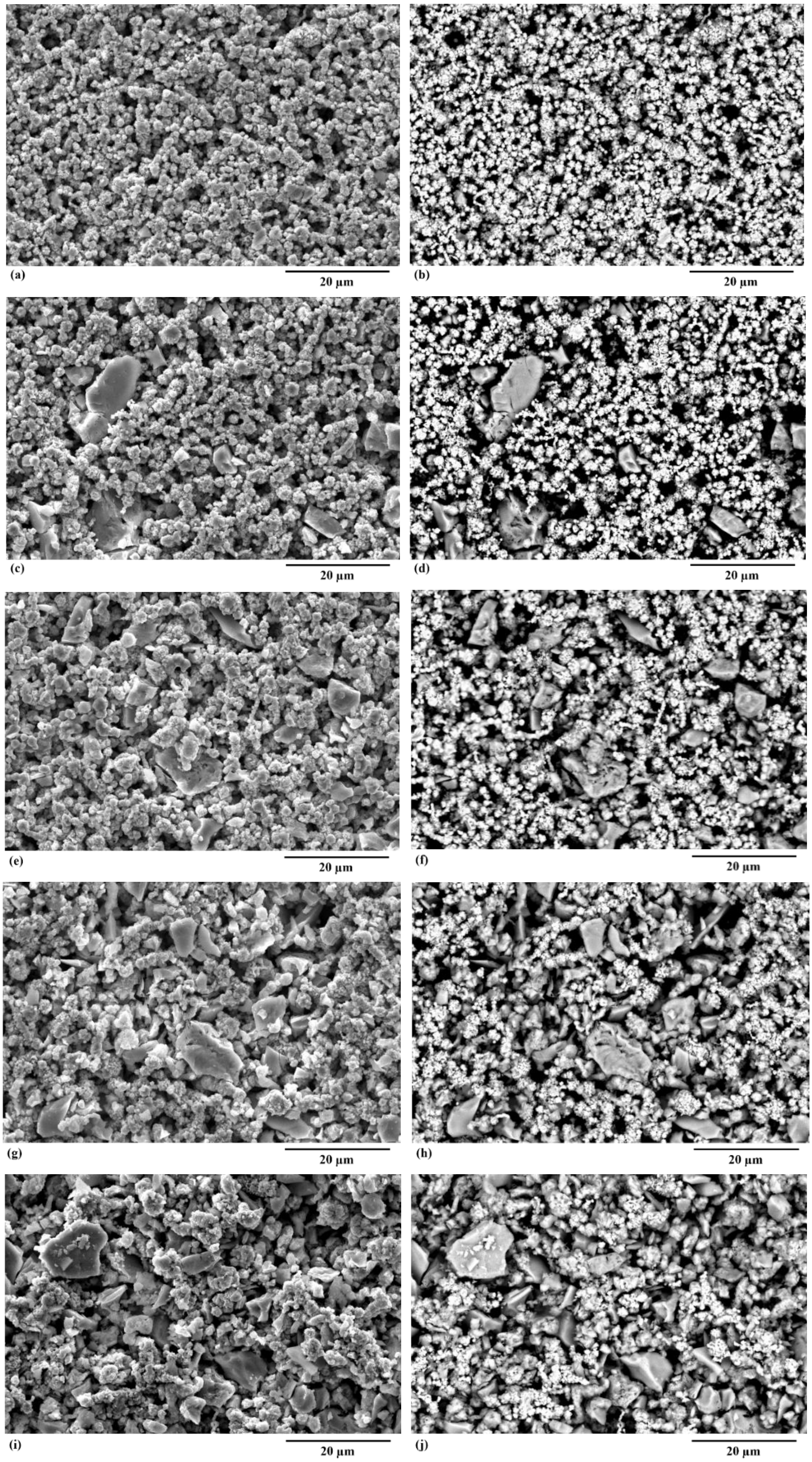

Figure 4.19. SEM-SE (left) and -BSE (right) images of the surfaces of as-leached samples with respect to the starting alloy concentration in the metal mixture before leaching; (a) and (b) 0 wt.%; (c) and (d) 10 wt.%; (e) and (f) 20 wt.%; (g) and (h) 40 wt.%; (i) and (j) 60 wt.%.

4.3.2. Phase Analysis

4.3.2.1. Intermetallic Phases

PXD analysis

The intermetallic phases present in as-leached samples were identified for different starting alloy concentrations through the PXD analysis. As demonstrated in Figure 4.20, all samples consisted of AlNi, $AlNi_3$ and Ni regardless of the initial starting alloy compositions.

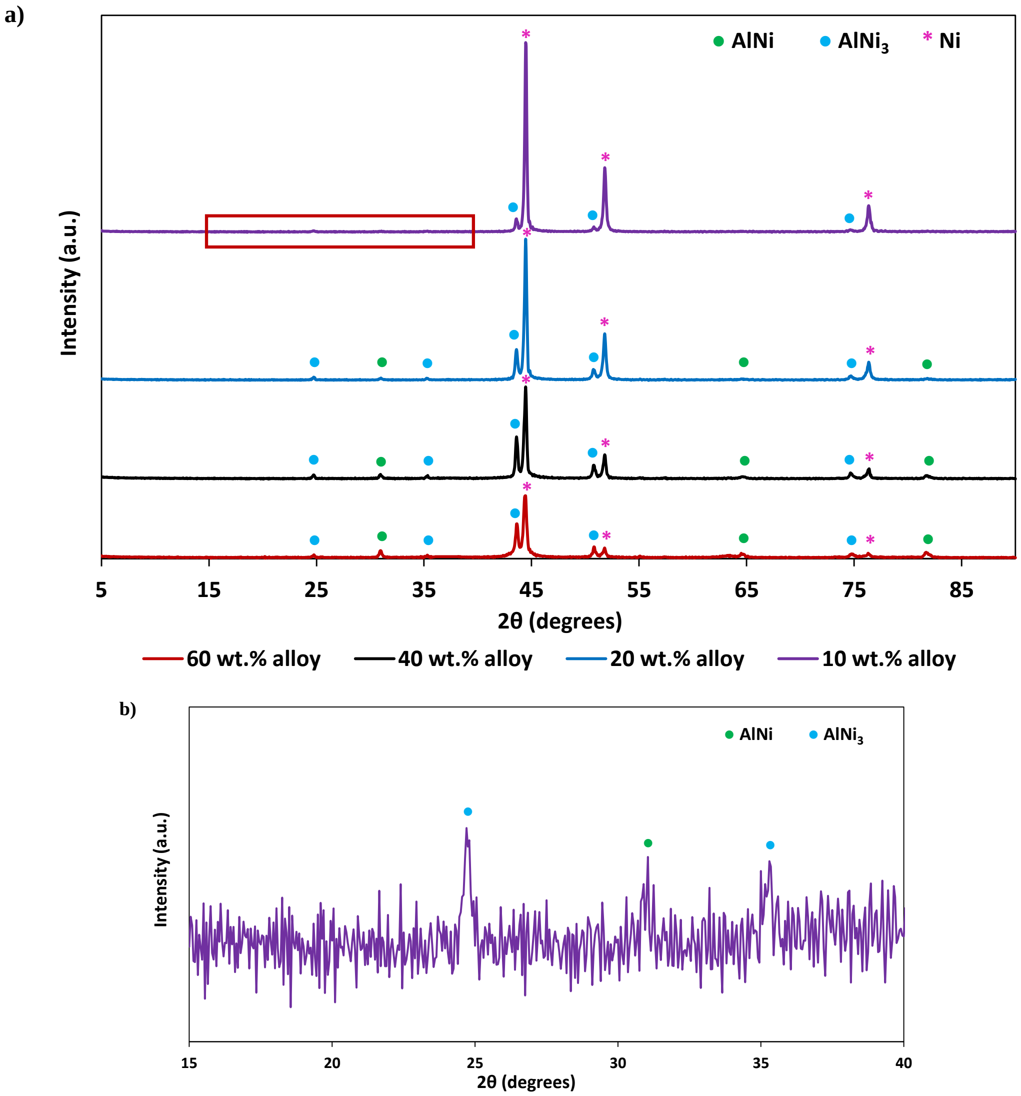

Figure 4.20. PXD patterns of as-leached samples with respect to the starting alloy concentration before leaching, where a) for the 2Ø range of 10-90 °; b) enlarged from the marked area in (a) for the 10 wt.% starting alloy concentration.

Rietveld refinement

Figure 4.21 shows Rietveld refinement results for the actual weights of intermetallic phases present in as-leached samples prepared from different starting alloy concentrations. Ni was the dominant phase for the alloy concentrations of 10 and 20 wt.%. As the starting alloy ratio rose, the amount of Ni decreased, whereas AlNi showed an increasing trend. The sample prepared from the 60 wt.% starting alloy was mainly made of AlNi, whose amount was *ca.* 5 times more than that estimated for the sample prepared from the 10 wt.% alloy concentration. As the starting alloy concentration was increased from 10 to 40 wt.%, the weight of $AlNi_3$ also rose. However, for the 60 wt.% alloy, it was lower than that determined for the 20 wt.% alloy.

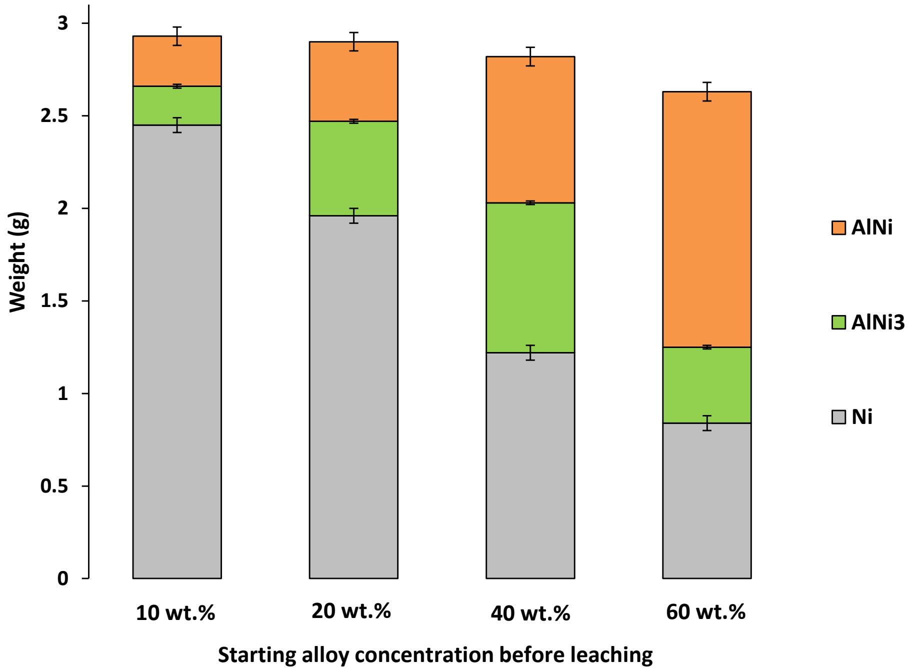

Figure 4.21. Rietveld refinement results for the quantities of intermetallic phases present in as-leached samples prepared from different starting alloy concentrations.

4.3.2.2. Overall Composition

As demonstrated in Figure 4.22, increasing the starting alloy concentration in the metal mixture from 10 to 60 wt.% resulted in higher remaining Al contents of as-leached samples. Based on the ICP-OES analysis, final Al compositions of as-leached samples were *ca.* 2.7, 6.2, 12.1 and 17.2 wt.% when prepared from the metal mixtures theoretically containing 5, 10, 20 and 30 wt.% Al respectively before leaching.

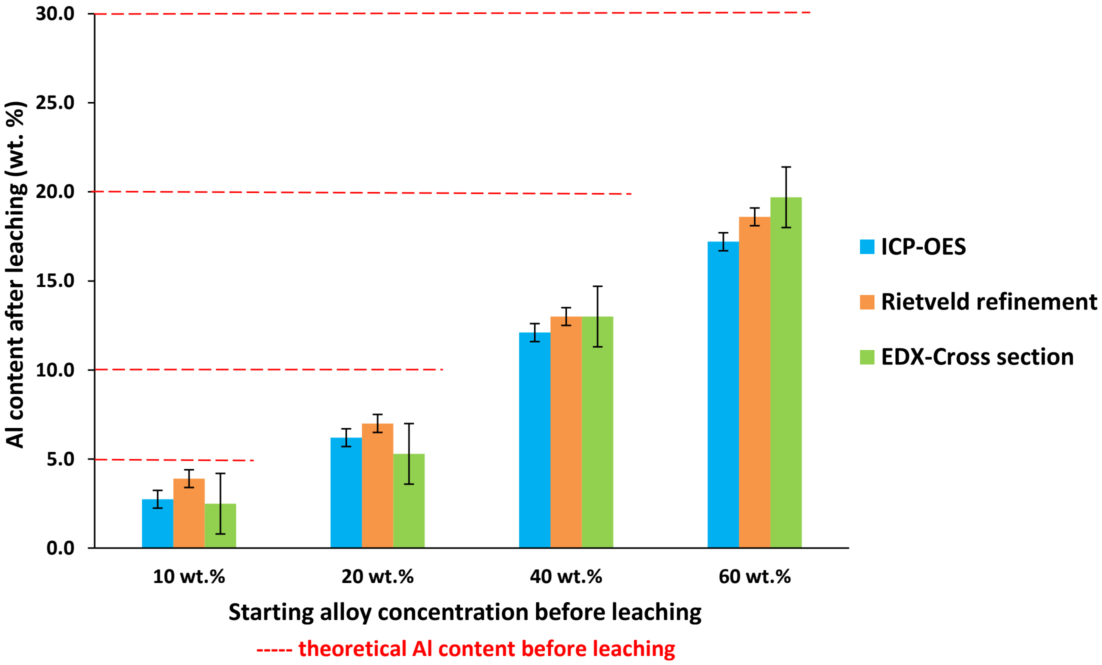

Figure 4.22. Results of ICP-OES, Rietveld refinement and EDX cross-section analyses for the Al contents of as-leached samples prepared from different starting alloy concentrations.

As shown in Figure 4.23, there was an increasing trend in the Al content for both surface and cross-section with higher starting alloy concentrations. Increasing the starting alloy concentration from 10 to 60 wt.% increased the surface and cross-section Al content by almost 6 and 8 times respectively. The EDX analysis on the surface and cross-section gave similar Al compositions for as-leached samples prepared from 10 and 20 wt.% starting alloy concentrations. The difference in Al contents of the surface and cross-section was more significant as the starting alloy ratio was increased, with the 60 wt.% alloy concentration giving almost 7 % higher Al in the cross-section compared to the surface composition.

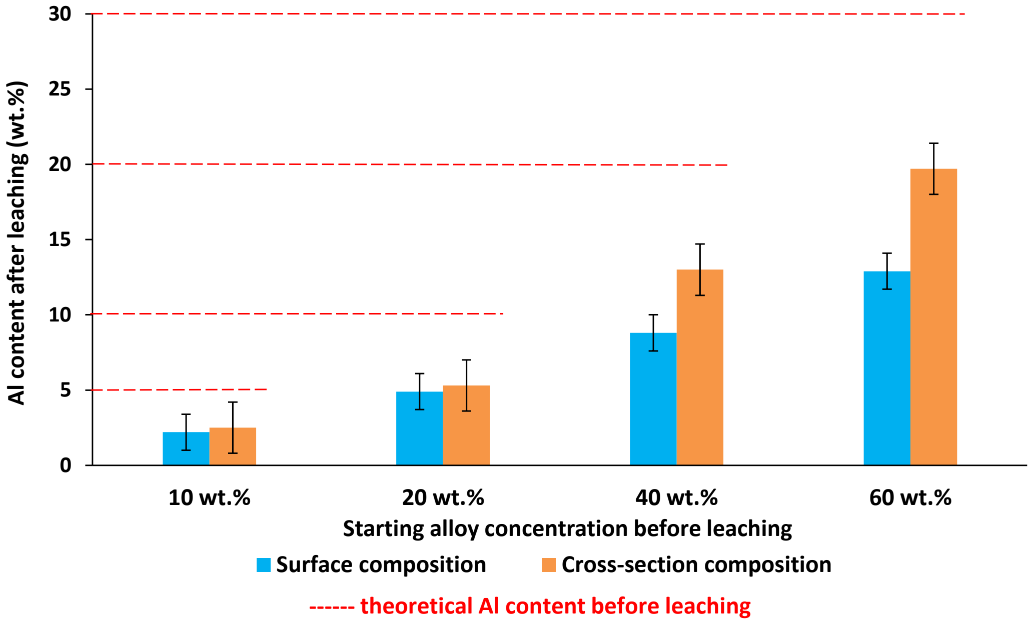

Figure 4.23. EDX composition results for the surface and cross-section of as-leached samples prepared from different starting alloy concentrations.

4.3.3. Porosity Characteristics

N_2 sorption and He pycnometer

Figure 4.24 demonstrates the porosity characteristics measured by N_2 sorption and He pycnometer techniques for as-leached samples prepared from different starting alloy to Ni weight ratios. There was an increasing trend in the micro-, meso- and macroporosity with higher starting alloy concentrations. The specific micropore area and area of other pores measured for an as-leached sample prepared from the 60 wt.% starting alloy concentration was *ca.* 16 and 11 times greater than those measured for a Ni sample prepared by only pressing and sintering Ni powder. Macroporosity also showed an upward trend as the starting alloy concentration increased, with the 60 wt.% alloy concentration giving an almost 2 times higher specific macropore volume than the Ni sample.

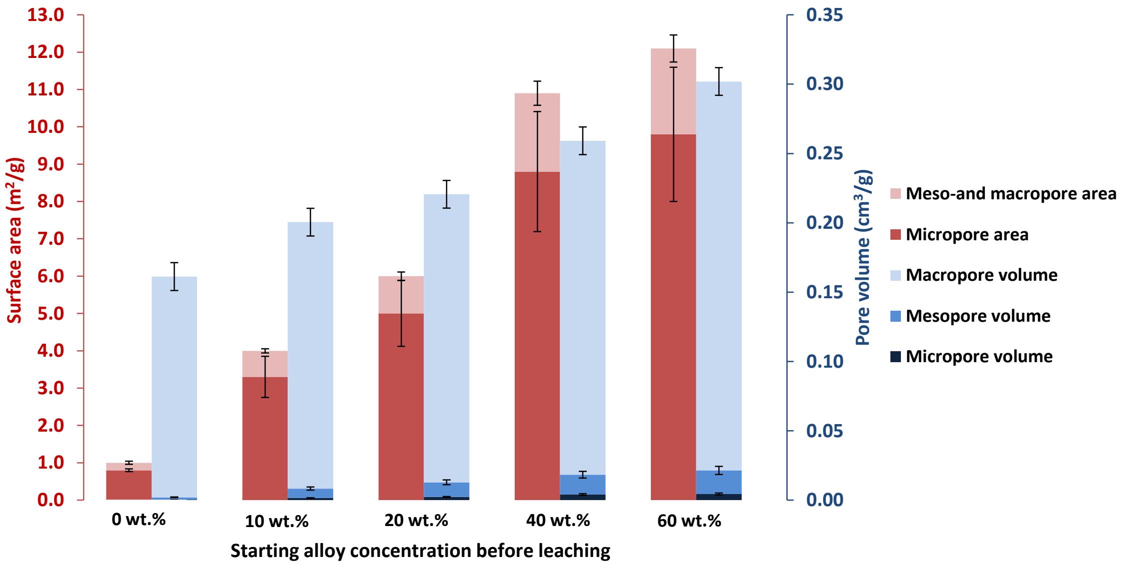

Figure 4.24. **N_2 sorption and He pycnometer results for the porosity characteristics of as-sintered Ni and as-leached samples prepared from different starting alloy concentrations.**

Figure 4.25 shows the mesopore size distribution of as-leached samples prepared from different starting alloy concentrations. The size of mesopores was in the range of *ca.* 2-13 nm. In general, there was an increasing trend in the mesopore volume with higher alloy concentrations, where the change from 40 to 60 wt.% starting alloy concentration was less significant. The mesoporosity was negligible for the Ni sample.

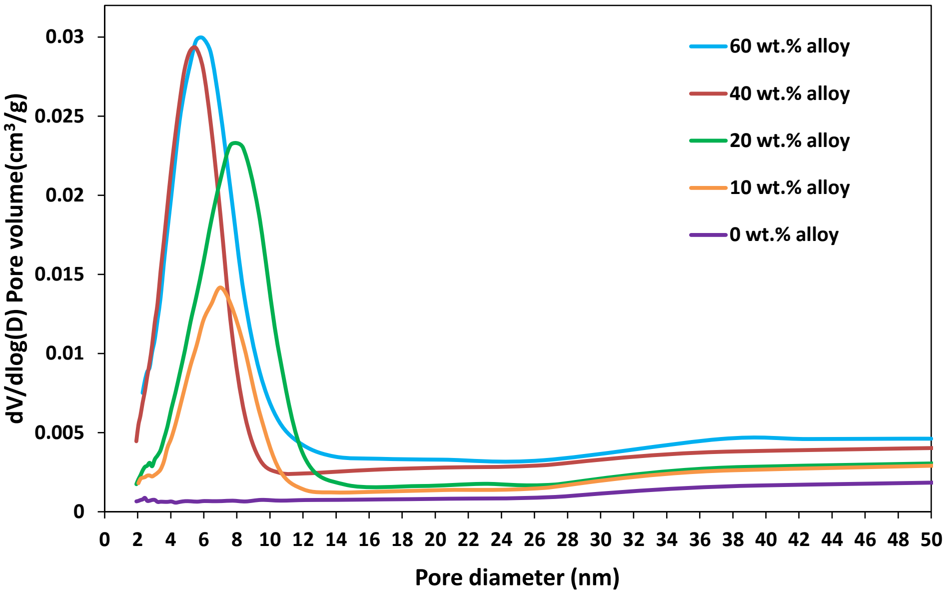

Figure 4.25. **N_2 sorption results for the mesopore size distribution of as-sintered Ni and as-leached samples prepared from different starting alloy concentrations.**

Figure 4.26 presents volumetric ratios of material, closed and open pores in the disk volume of as-sintered Ni and as-leached samples with respect to the starting alloy concentration. As the starting alloy content increased from 0 to 60 wt.%, the thickness of the disks, hence the disk volume rose by *ca.* 46 % through an increase in the volume of material, closed and open pores, with the increase in open pores being the most significant for the disk volume. The sample prepared from the 60 wt.% alloy concentration gave *ca.* 1.4 and 17 times greater volumes of open and closed pores respectively compared to the Ni sample. The ratio of open pores in the disk volume was *ca.* 60 vol.% for all samples regardless of the starting alloy content. However, closed pores showed an increasing volumetric concentration in the disk volume as the starting alloy content rose, with the 60 wt.% alloy concentration giving a *ca.* 9 vol.% closed pores.

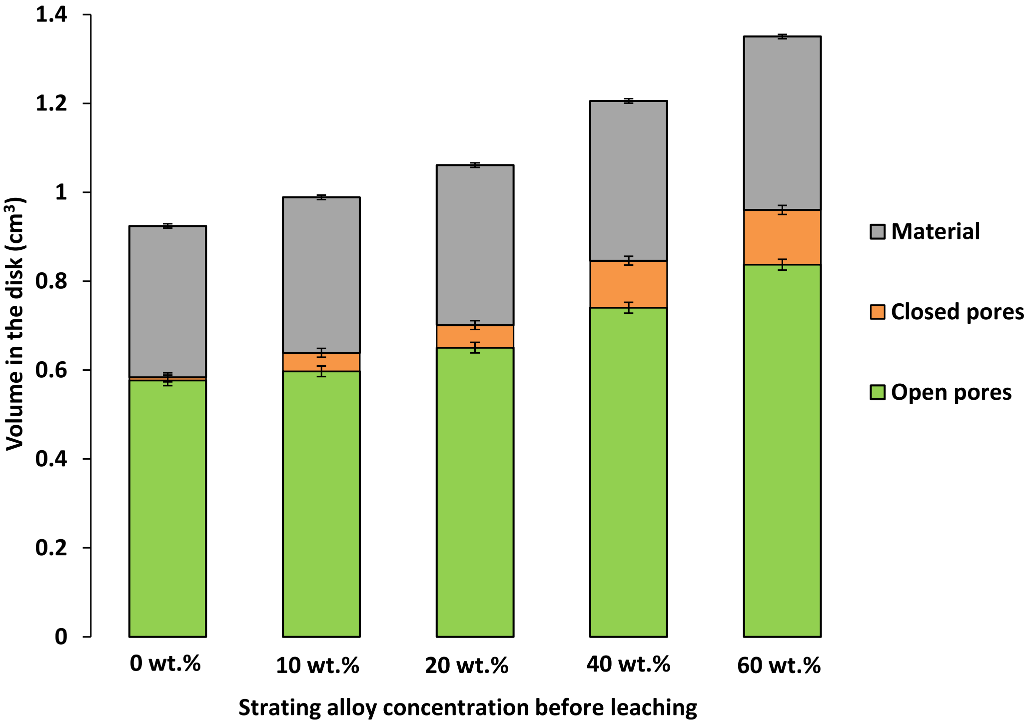

Figure 4.26. He pycnometer results for the contributions of material, closed and open pores in the disk volume of as-sintered Ni and as-leached samples prepared from different starting alloy concentrations.

MIP

Pore size distributions were also measured through the MIP technique for as-leached samples prepared from 10 and 40 wt.% alloy concentrations and compared to that of an as-sintered Ni sample. As demonstrated in Figure 4.27, the majority of pores accumulated in the size range of *ca.* 0.3-5 μm regardless of the alloy ratio. Alloy concentrations of 10 and 40 wt.% gave similar pore size distribution profiles apart from the peak observed for pore sizes of *ca.* 3 nm, which was greater with the 40 wt.% starting alloy. Ni sample, on the other hand, did not have pores in this mesopore region and the total Hg intrusion volume per sample mass was lower than those identified for the samples prepared from the starting alloy concentrations of 10 and 40 wt.% (Table 4.5). The porosity measured by means of MIP were *ca.* 61 % regardless of the starting alloy to Ni ratio.

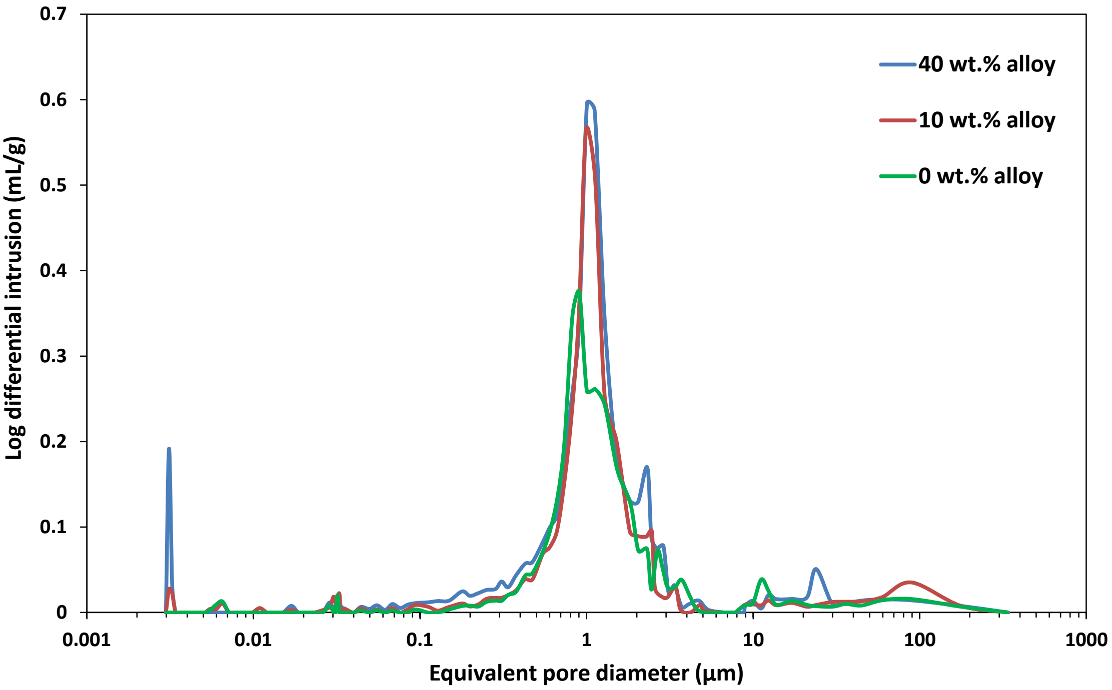

Figure 4.27. MIP results for the pore size distribution of as-sintered Ni and as-leached samples prepared from different starting alloy concentrations.

Table 4.5. MIP results for the total Hg intrusion volume and porosity of as-leached Ni60:Alloy40-B6.25 samples prepared from different starting alloy concentrations.

Alloy concentration (wt.%)	Hg intrusion volume (± 0.01 ml/g)	Porosity (± 2 %)
0	0.17	61
10	0.20	63
40	0.23	61

4.3.4. Electrochemical Performance

As shown in Figures 4.28 and 4.29, the cell voltage decreased as the starting alloy concentration in the metal mixture increased from 0 to 60 wt.%. Using starting alloy to Ni weight ratios of 10:90, 20:80, 40:60 and 60:40 reduced the cell voltage at 1 A/cm^2 by *ca.* 2.5, 5, 7.2 and 7.9 % respectively in comparison to using a Ni cathode.

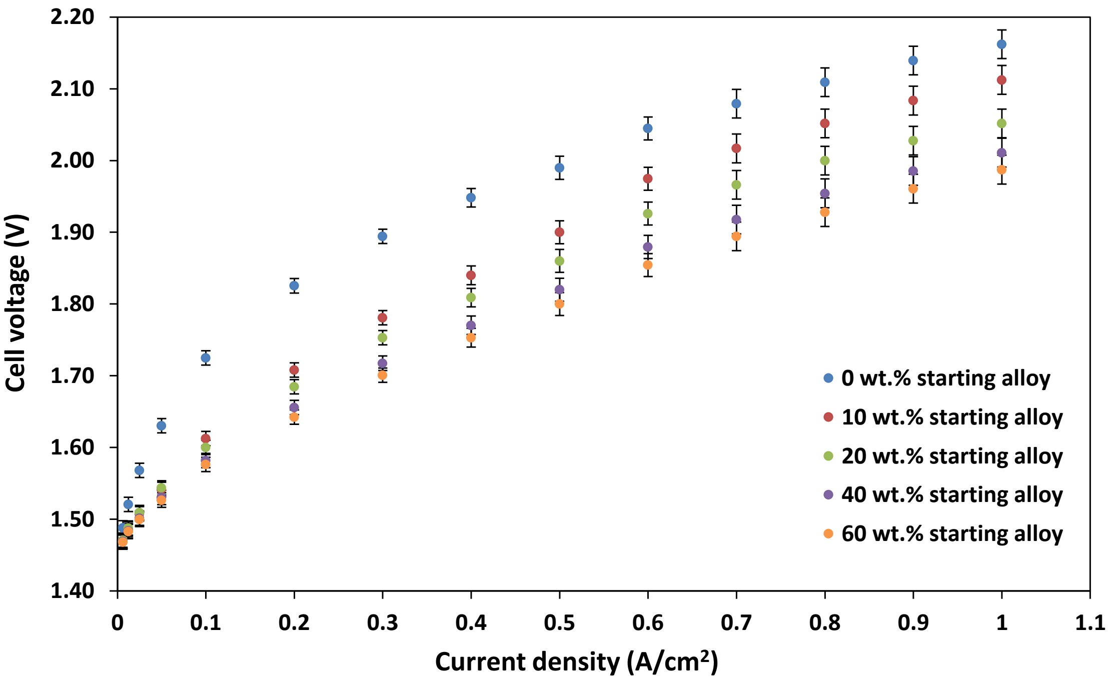

Figure 4.28. Electrolyser cell voltage-current density curves measured using cathodes prepared from different starting alloy concentrations.

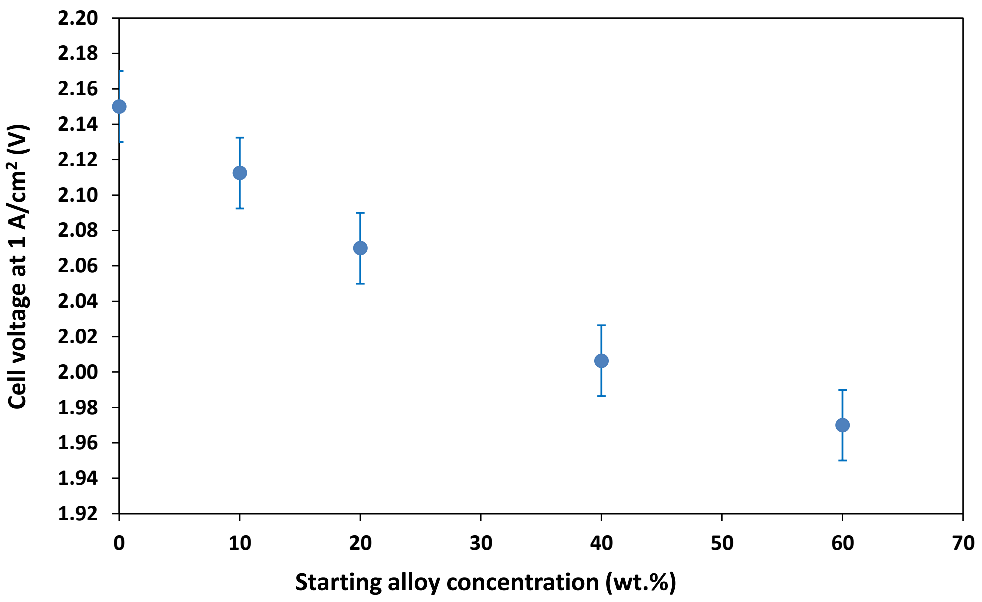

Figure 4.29. Electrolyser cell voltages measured at 1 A/cm^2 using cathodes prepared from different starting alloy concentrations.

Table 4.6 gives the observations of the mechanical performance of electrodes before and after the electrolyser cell test. The robustness of the electrodes reduced as the starting alloy concentration was increased, with the electrodes prepared from the 60 wt.% starting alloy not being feasible for industrial applications.

Table 4.6. Observations on mechanical performance of electrodes prepared from different starting alloy concentrations.

Starting alloy concentration (wt.%)	Mechanical strength of as-sintered and as-leached samples	Observations after the alkaline electrolyser cell test
0	Excellent	Excellent robustness regardless of the number of cell tests.
10	Very good	Mechanical strength was still very good.
20	Good	Mechanical strength was still good.
40	Sufficient	No significant change in the mechanical strength after the test. However, care was required during the handling of electrode.
60	Poor	Slight piston marks were observed on the electrode surface after the test. Extra care was required to handle the electrodes as they were fragile.

As mentioned earlier in Section 4.3.3, samples prepared from different starting alloy concentrations gave varying thicknesses. In order to see whether the thickness of the cathodes had an influence on the electrolyser cell voltage, the electrochemical activities of cathodes prepared from the 10 wt.% alloy concentration with three different thicknesses, i.e. 1.23, 1.47 and 1.82 mm were compared to those observed for cathodes prepared from 40 and 60 wt.% alloy concentrations. As shown in Figure 4.30, regardless of their thicknesses, cathodes prepared from the 10 wt.% alloy concentration gave similar results, which were higher than those measured when the starting alloy concentrations of 40 and 60 wt.% were used.

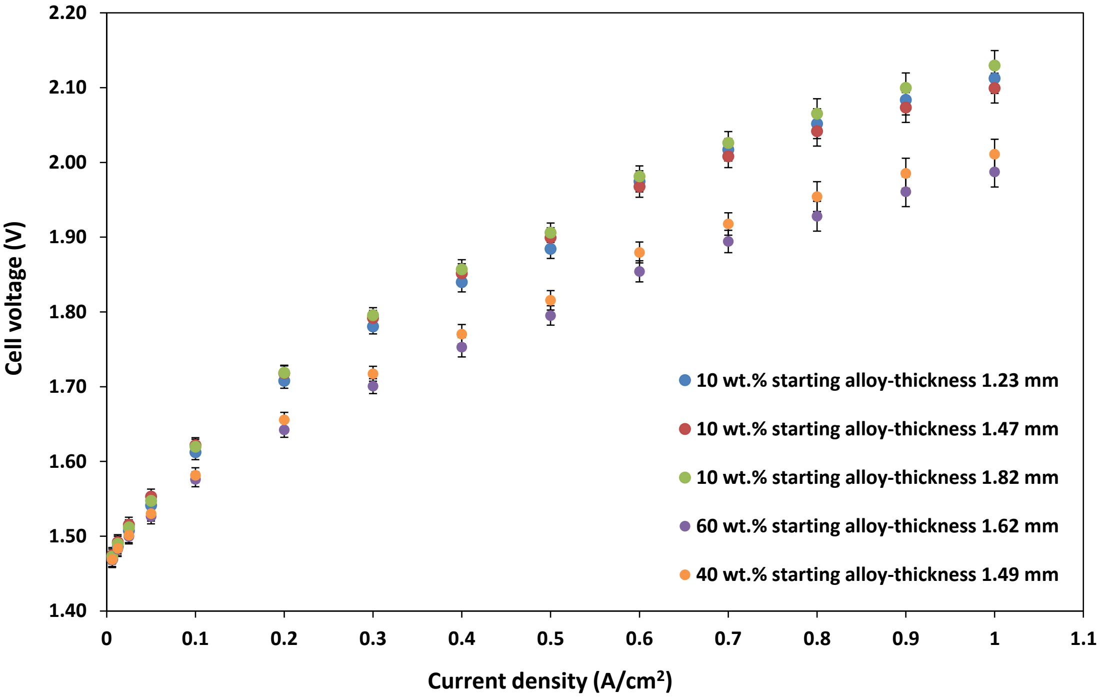

Figure 4.30. Electrolyser cell voltage-current density curves measured using cathodes with different thicknesses and starting alloy concentrations.

4.4. Effect of Leaching Temperature

The effect of leaching temperature was studied for Ni60:Alloy40-B6.25 samples prepared from a metal composition of 60 wt.% Ni-40 wt.% starting alloy before leaching. As-received wax, with a mean diameter of 130 µm, was used as a binder agent with a concentration of 6.25 wt.% before sintering. Samples were sintered at 650 ºC.

Five different leaching temperatures were studied, i.e. 30, 50, 60, 70 and 80 ºC. All samples were leached for 18 h in 5 M KOH containing 10 wt.% K-Na tartrate tetrahydrate of the total weight. Visual examinations indicated that the rate of leaching reaction increased as the leaching temperature rose. Consequently, faster and more significant release of H_2 gas bubbles was observed at higher leaching temperatures. After leaching completed, the quantity and size of the bubbles stayed attached to the electrode surface were greater when leaching was carried out at lower temperatures.

Results for the physical and chemical characterization tests are reported in Sections 4.4.1 and 4.4.2, while electrolyser cell test results are presented in Section 4.4.3.

4.4.1. Phase Analysis

4.4.1.1. Intermetallic phases

PXD analysis

Intermetallic phases present in Ni60:Alloy40-B6.25 samples after leaching at different temperatures were identified through PXD analysis. As demonstrated in Figure 4.31, all samples contained AlNi, $AlNi_3$ and Ni, whose peak heights were similar regardless of the leaching temperature.

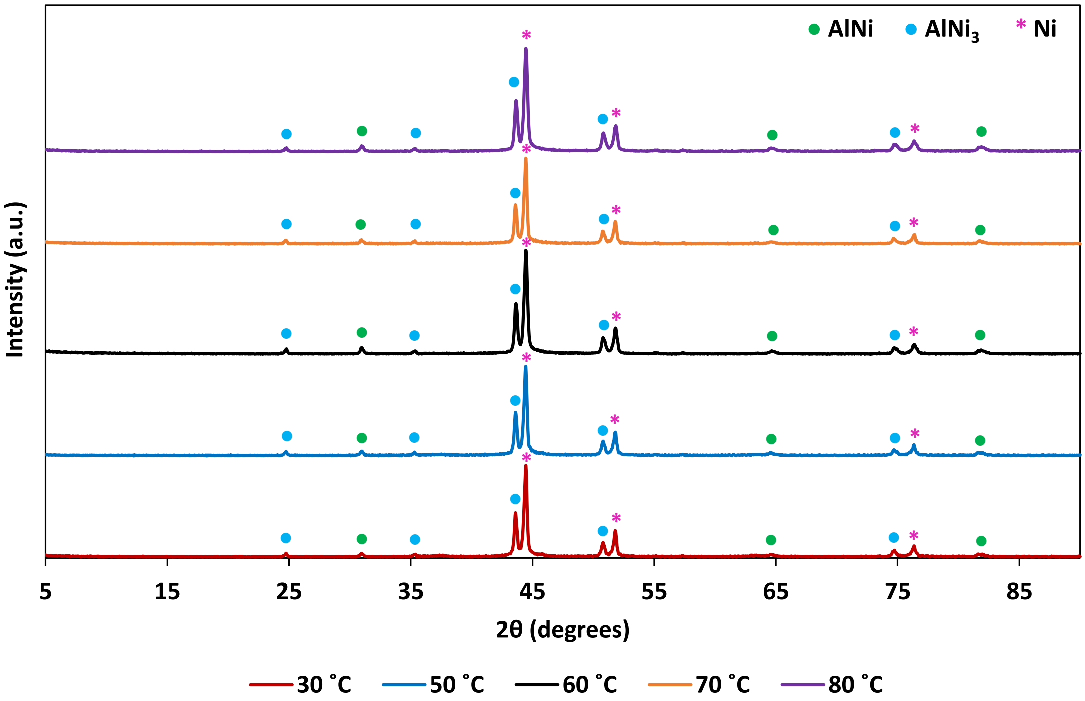

Figure 4.31. PXD patterns of as-leached Ni60:Alloy40-B6.25 samples with respect to the leaching temperature.

Rietveld refinement

Figure 4.32 shows the amount of each phase estimated through the Rietveld refinement analysis for Ni60:Alloy40-B6.25 samples leached at different temperatures. Increasing the leaching temperature from 30 to 80 ºC did not change the weight fractions of AlNi, $AlNi_3$ and Ni significantly. The dominant phase was Ni with a concentration of *ca.* 40 wt.%, while AlNi and $AlNi_3$ had similar ratios of *ca.* 30 wt.% regardless of the leaching temperature.

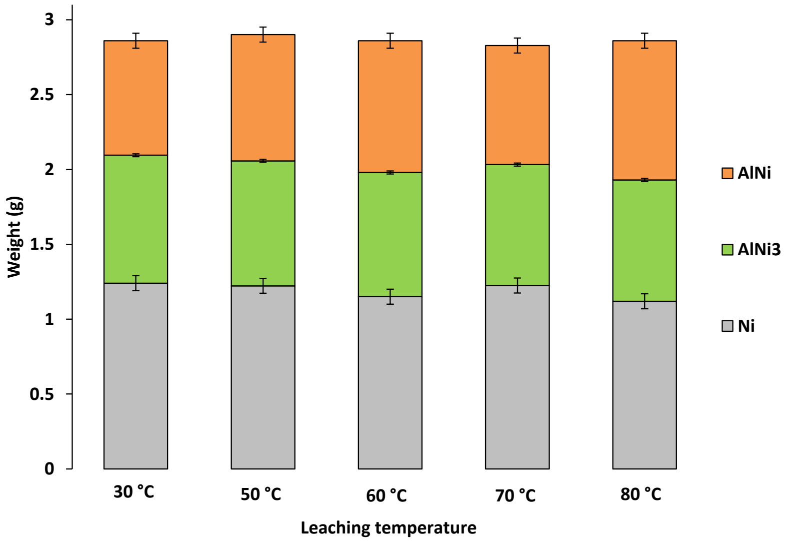

Figure 4.32. Rietveld refinement results for the quantities of intermetallic phases present in as-leached Ni60:Alloy40-B6.25 samples leached at different temperature; 30, 50, 60, 70 and 80 ºC.

4.4.1.2. Overall Composition

Overall compositions of as-leached Ni60:Alloy40-B6.25 samples were measured by Rietveld refinement, EDX analysis and ICP-OES (The latter technique was used to check 3 of the samples). As demonstrated in Figure 4.33 all samples gave similar Al contents after leaching, which were *ca.* 13 wt.% regardless of the leaching temperature.

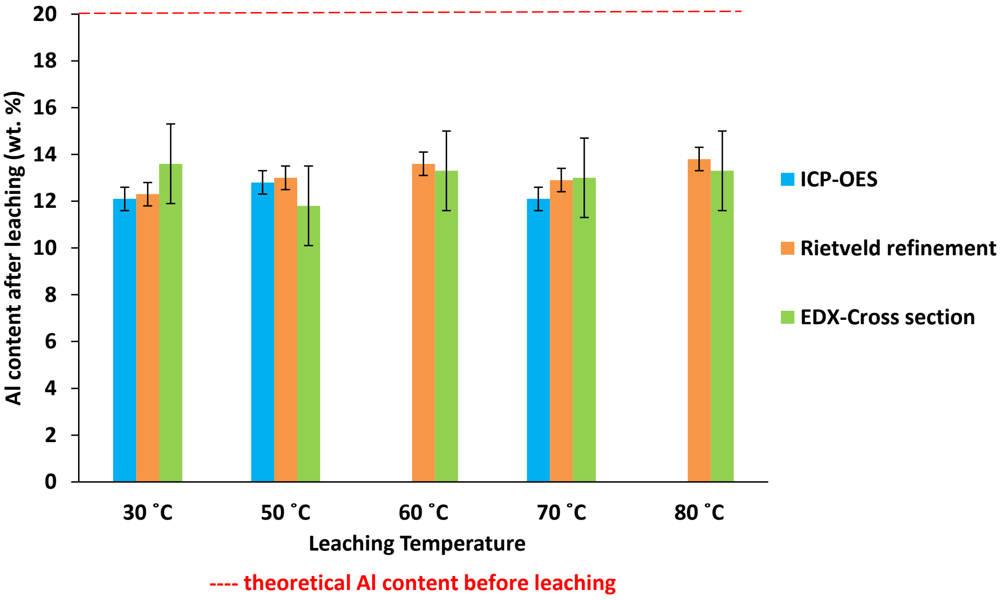

Figure 4.33. Results of ICP-OES, Rietveld refinement and EDX analyses for the Al contents of Ni60:Alloy40-B6.25 samples leached at different temperatures from 30 to 80 ºC, with the ICP-OES only being employed to determine the compositions of samples leached at 30, 50 and 70 ºC.

Figure 4.34 compares EDX analysis results from the surface and cross-section of as-leached samples. Regardless of the leaching temperature, surface Al compositions were similar for all samples which were, in general, lower than those of the cross-section.

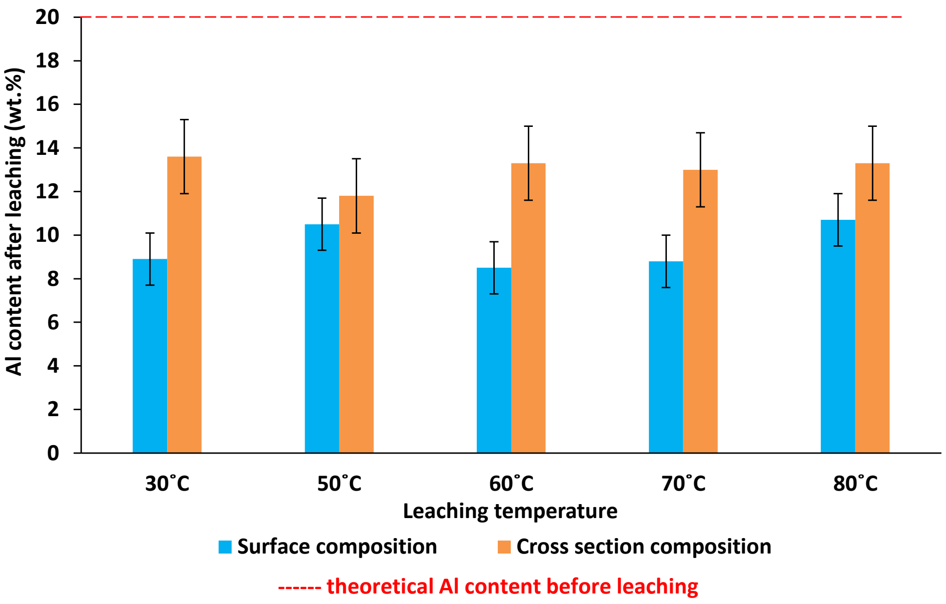

Figure 4.34. EDX composition results for the surface and cross-section of Ni60:Alloy40-B6.25 samples leached at different temperatures; 30, 50, 60, 70 and 80 °C.

4.4.2. Porosity Characteristics

N_2 sorption and He pycnometer

Samples leached at different temperatures were analysed through N_2 sorption and He pycnometer techniques. Figure 4.35 presents N_2 sorption isotherms, where the shape of the hysteresis loop shows a dependence on the leaching temperature. As explained in Section 3.3.1, shapes of the hysteresis loops are often attributed to the presence of specific pore structures. Leaching at 30 and 50 ºC gave hysteresis loops similar to the type H4 in IUPAC classifications (Figure 3.4), which are usually related to the presence of narrow slit-like pores. On the other hand, H2(a) type hysteresis was observed for samples leached at 60, 70 and 80 °C, with 80 ºC giving a slightly different shape than others. H2(a) type often indicates a complicated pore structure, where network effects are more significant and pore-blocking/percolation in a narrow range of pore necks can occur.

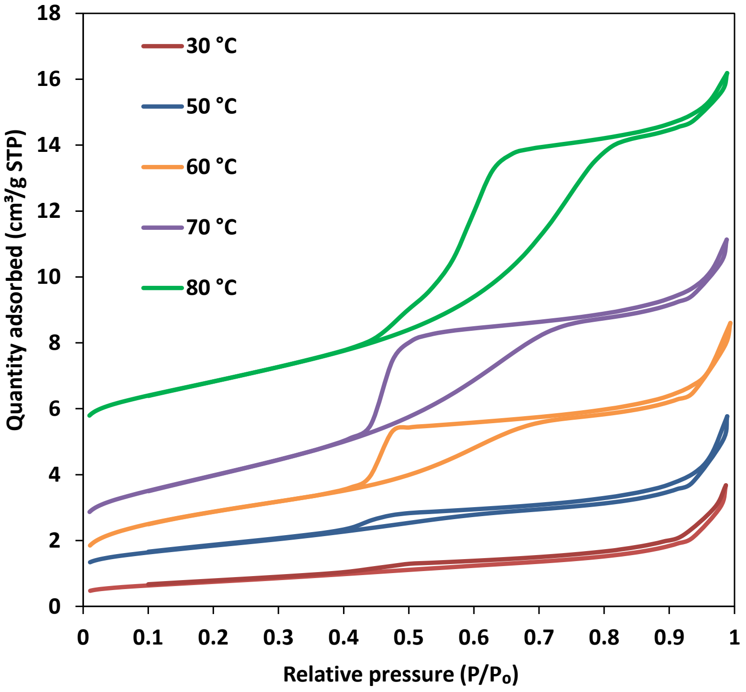

Figure 4.35. N_2 sorption isotherms of Ni60:Alloy40-B6.25 samples leached at different temperatures; 30, 50, 60, 70 and 80 ºC.

Figure 4.36 demonstrates the effect of leaching temperature in the porosity characteristics of as-leached Ni60:Alloy40-B6.25 samples. The macroporosity was not influenced by the leaching temperature. However, increasing the leaching temperature from 30 to 60 ºC improved the specific surface area by almost 4 times through a significant increase in the micro- and mesoporosity. The specific micropore area was similar (8.5 ± 1.5 m^2/g) for samples leached at 60, 70 and 80 ºC. The change in mesoporosity from 60 to 80 ºC was also within the experimental errors. The specific mesopore volume measured for the sample leached at 80 ºC was *ca.* 3.6 times higher than that of the sample leached at 30 ºC. Figure 4.37 shows the change in the mesopore size distribution with respect to the leaching temperature. The greatest amount of mesopores was observed with the leaching temperature of 80 ºC, whose size range was *ca.* 2-14 nm. As the leaching temperature decreased, the specific mesopore volume reduced and pore size was shifted to lower values. The size range of mesopores was *ca.* 2.0-6.0 nm and 2.0-4.5 nm for samples sintered at 30 and 50 ºC respectively.

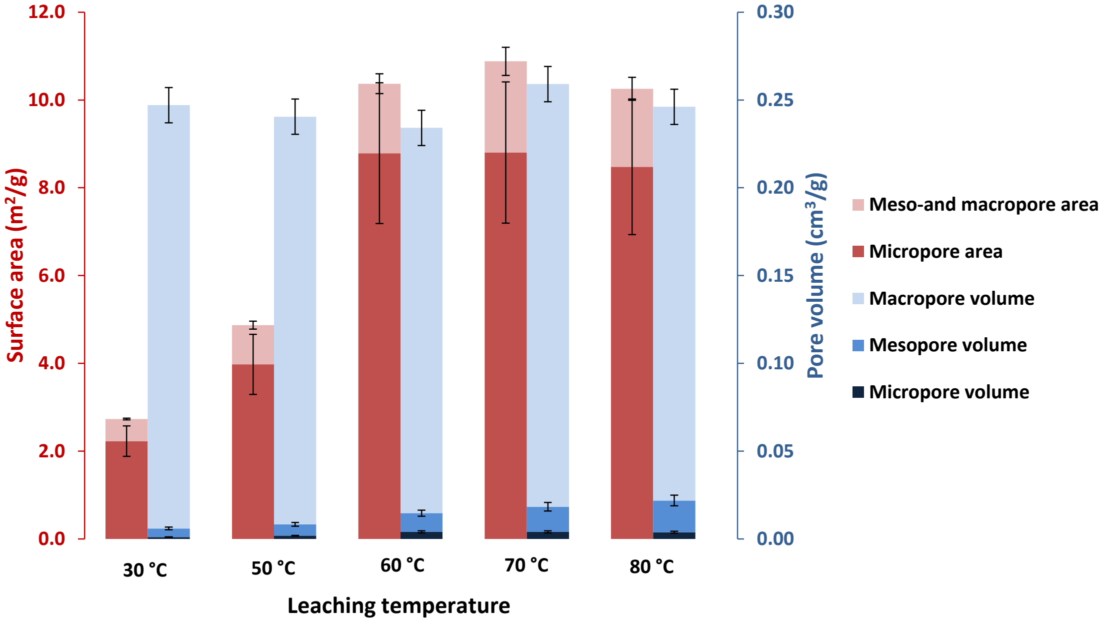

Figure 4.36. N_2 sorption and He pycnometer results for the porosity characteristics of Ni60:Alloy40-B6.25 samples leached at different temperatures; 30, 50, 60, 70 and 80 ºC.

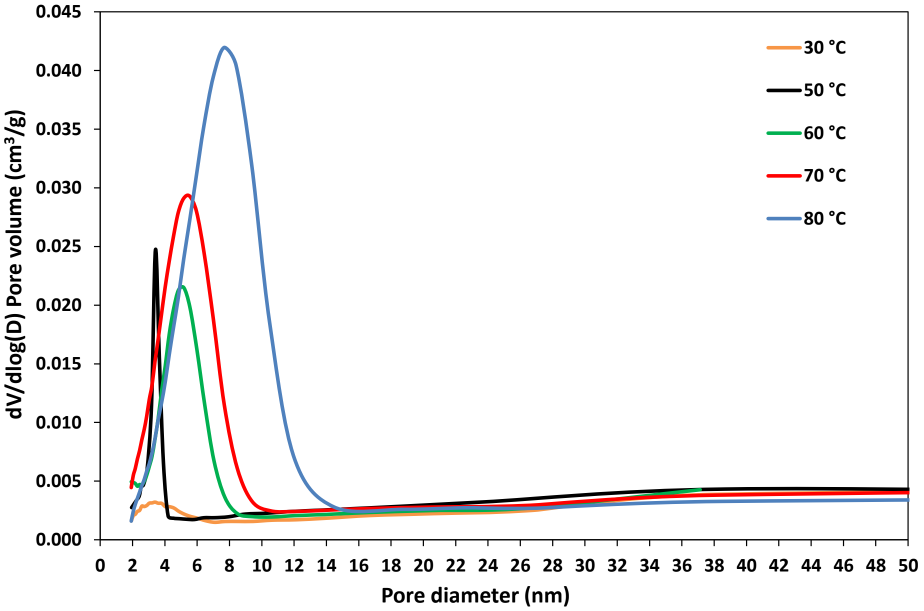

Figure 4.37. N_2 sorption results for the mesopore size distribution of Ni60:Alloy40-B6.25 samples leached at different temperatures; 30, 50, 60, 70 and 80 ºC.

The volumetric contributions of material, closed and open pores in the disk volume were also estimated for Ni60:Alloy40-B6.25 samples leached at different temperatures. As demonstrated in Figure 4.38, increasing the leaching temperature did not change the volumetric ratios of material, open and closed pores, which were ca. 32, 58 and 10 % respectively for Ni60:Alloy40-B6.25 samples.

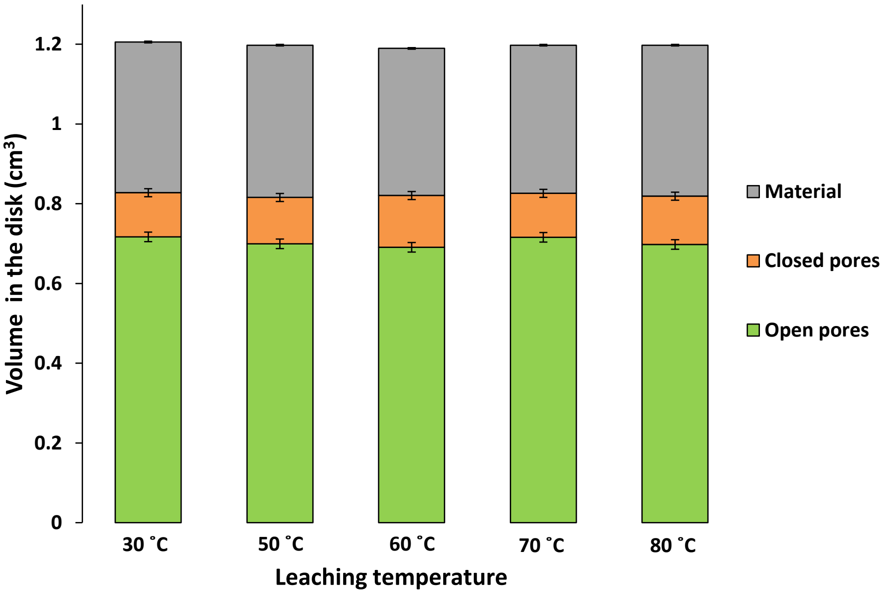

Figure 4.38. He pycnometer results for the contributions of material, closed and open pores to the disk volume of as-leached Ni60:Alloy40-B6.25 samples.

4.4.3. Electrochemical Performance

Electrolyser cell voltages were measured using cathodes leached at different temperatures and are presented in Figure 4.39. The electrochemical performance of the cathodes did not change significantly with the leaching temperature.

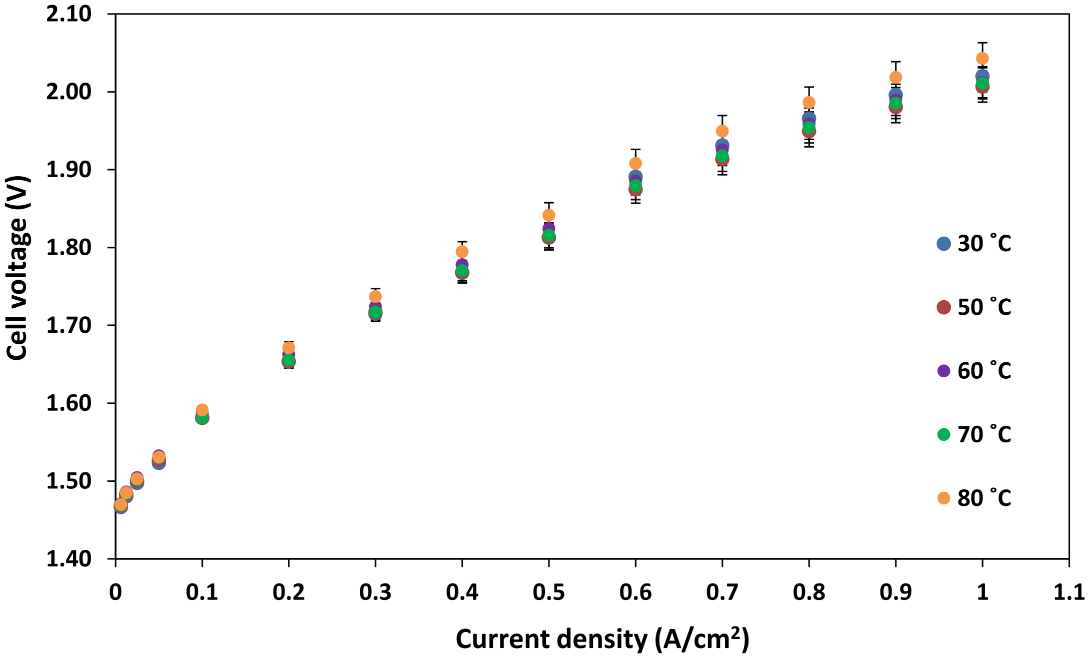

Figure 4.39. Cell voltage-current density curves measured using cathodes leached at different temperatures; 30, 50, 60, 70 and 80 °C.

4.5. Effect of Binder

The effect of binder was studied for Ni60:Alloy40 samples prepared from a metal composition of 60 wt.% Ni-40 wt.% starting alloy. They were leached at 70 °C for 18 h in 5 M KOH solution containing 10 wt.% K-Na tartrate tetrahydrate of the total weight.

Section 4.5.1 gives results for the influence of binder concentration, while Section 4.5.2 covers the effect of binder particle size. Additional analysis on the decomposition temperature of wax and cellulose binders during sintering is reported in Appendix 7, while SEM-SE images of as-received wax are given in Appendix 8.

4.5.1. Effect of Binder Concentration

The effect of binder amount was studied using as-received wax with a mean particle size of *ca.* 130 µm. Laser diffraction results for the particle size distribution of as-received wax are reported in Appendix 9. Binder concentrations of 6.25, 15 and

25 wt.% were investigated. Initially, sintering was carried out at 650 ºC, however, the samples with 15 and 25 wt.% binder concentrations were very fragile and fell apart during the electrolyser cell test. Sintering at 900 ºC led to less fragile samples enabling the investigation of samples with higher binder amounts. Therefore, the sintering temperature of 900 ºC was chosen to study the effect of binder concentration.

As reported in Section 3.1.2 the total weight of starting materials was reduced for higher binder concentrations (15 and 25 wt.%) in order to obtain electrode disks that could fit in the electrolyser cell. The initial weights of metal mixtures were 3.00, 2.50 and 2.25 g in the samples with the binder concentrations of 6.25, 15.0 and 25.0 wt. % respectively.

The results from physical and chemical characterization tests are reported in Sections 4.5.1.1., 4.5.1.2 and 4.5.1.3, while the electrolyser cell test results are presented in Section 4.5.1.4.

4.5.1.1. Microstructural Analysis

Figure 4.40 presents low magnification SEM-SE images of as-leached Ni60:Alloy40 samples prepared from three different binder concentrations; 6.25, 15 and 25 wt.%. Large macropores with varying sizes from *ca.* 15 µm up to *ca.* 450 µm were observed on the surfaces and cross-sections of the samples. Increasing the binder concentration from 6.25 to 25 wt.% gave greater amounts of these macropores resulting in highly porous structures and rougher surfaces. There was a decreasing trend in the average thickness of pore walls, with the 25 wt.% binder concentration giving the lowest wall thicknesses in comparison to lower binder amounts. Cross-section images also showed an increasing pore connectivity with higher binder concentrations.

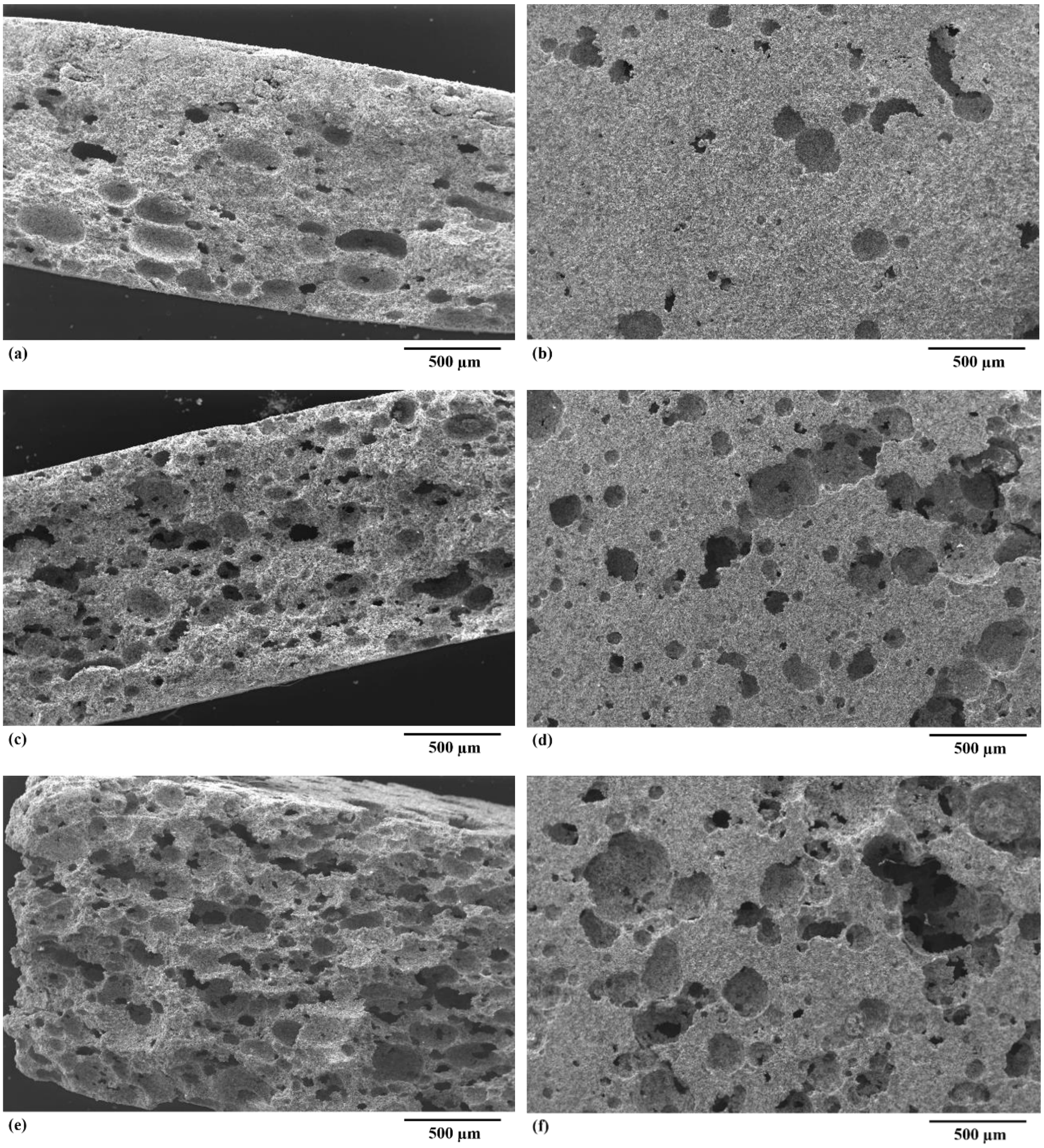

Figure 4.40. SEM-SE images of cross-sections (left) and surfaces (right) of as-leached samples prepared from different binder (as-received wax with a mean particle size of 130 µm) concentrations; where (a) and (b) Ni60:Alloy40-B6.25; (c) and (d) Ni60:Alloy40-B15; (e) and (f) Ni60:Alloy40-B25.

Figure 4.41 gives examples of SEM-SE images of the macropores in the cross-section of samples. Some of large macropores had windows with varying sizes; 20-70 µm being the common size range. An increase in the number of these windows was observed as the binder concentration rose from 6.25 wt. % (Figure 4.41 (a)) to 25 wt.% (Figure 4.41 (b)).

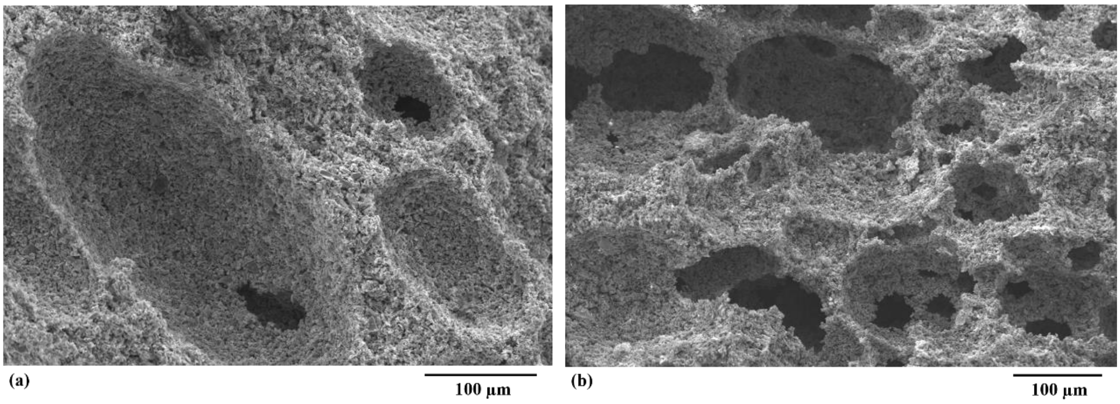

Figure 4.41. Representative SEM-SE images of large macropores on the cross-section of as-leached samples; where (a) Ni60:Alloy40-B6.25; (b) Ni60:Alloy40-B25.

Figure 4.42 shows thicknesses of sample disks measured before and after sintering. As the binder concentration rose, there was an increasing trend in the thickness, with the 25 wt.% binder amount giving an approximately 30 % thicker samples than the 6.25 wt.% binder concentration after sintering. The comparison of thicknesses measured before and after sintering showed that the thickness of the disks increased by *ca.* 3.8 and 5.3 % during sintering for the binder concentrations of 6.25 and 25 wt. % respectively.

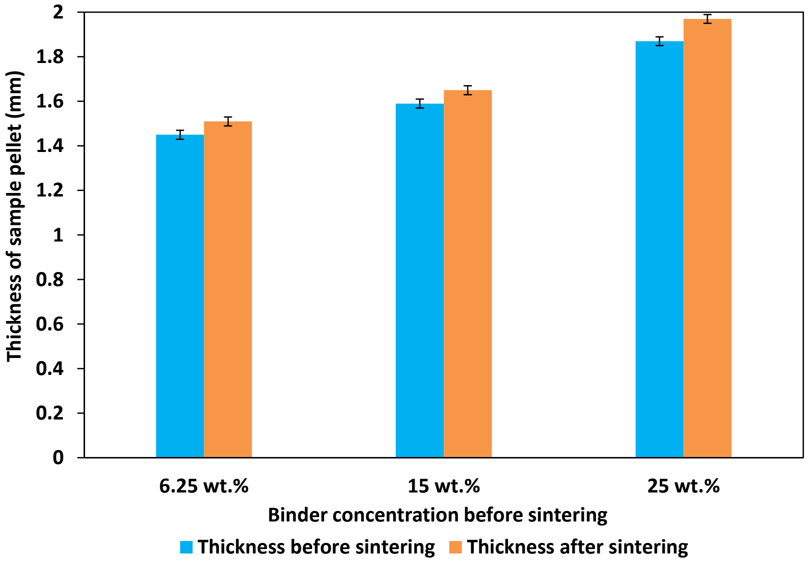

Figure 4.42. The change in the thickness of Ni60:Alloy40 samples measured before and after sintering with respect to the binder concentration.

4.5.1.2. Phase Analysis

4.5.1.2.1. Intermetallic Phases

PXD and Rietveld refinement

Figure 4.43 presents the PXD patterns of as-leached Ni60:Alloy40 samples prepared from different binder concentrations. All samples contained two intermetallic phases of $Al_{0.84}Ni_{1.16}$ and $AlNi_3$. The Rietveld refinement analysis gave similar weights fractions of phases regardless of the binder concentration (Figure 4.44). The dominant phase was $Al_{0.84}Ni_{1.16}$ with a concentration of 67.4 ± 1.5 wt.%.

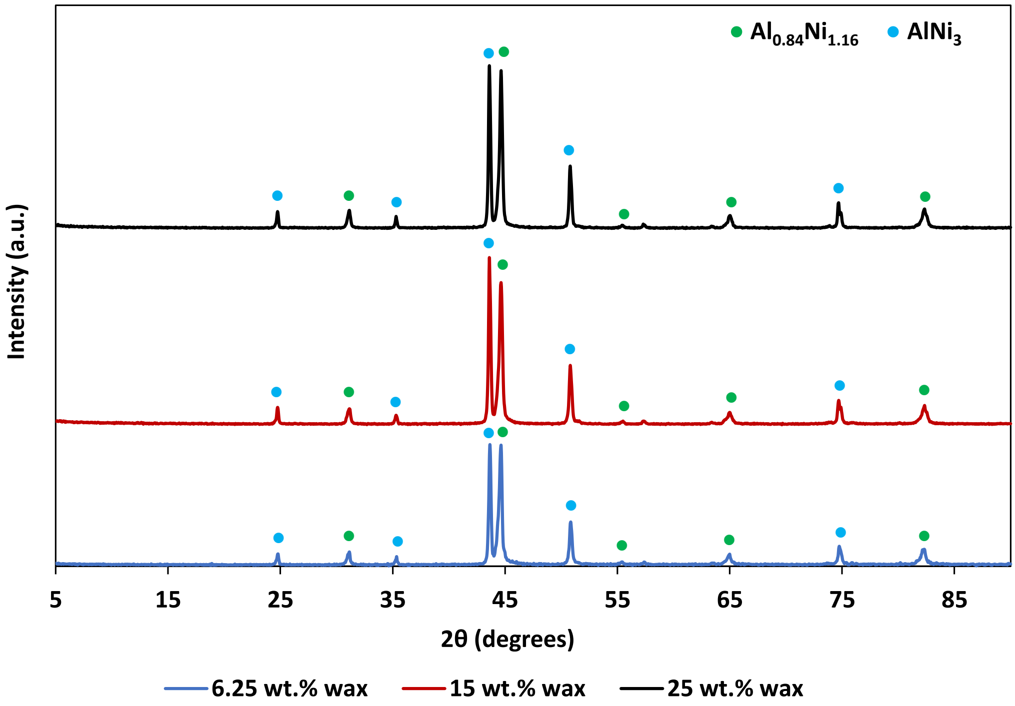

Figure 4.43. PXD patterns of as-leached samples with respect to different binder concentrations; where (a) Ni60:Alloy40-B6.25; (b) Ni60:Alloy40-B15; (c) Ni60:Alloy40-B25.

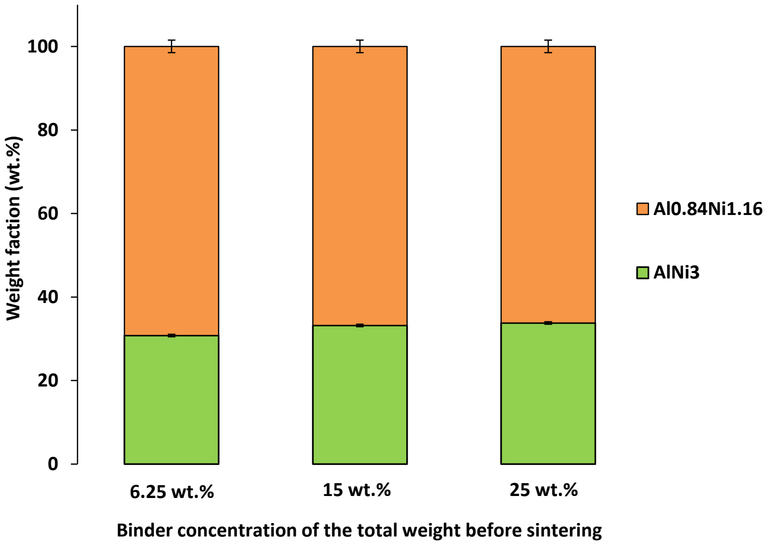

Figure 4.44. Rietveld refinement analysis results for weight ratios of intermetallic phases present in as-leached samples prepared from three different binder concentrations; where (a) Ni60:Alloy40-B6.25; (b) Ni60:Alloy40-B15; (c) Ni60:Alloy40-B25.

4.5.1.2.2. Overall Composition

Figure 4.45 gives normalized Al compositions determined through Rietveld refinement and EDX cross-sectional analyses for as-leached samples. Based on the Rietveld refinement technique, all samples had similar Al contents, which were close to the theoretical Al content before leaching. i.e. *ca.* 20 wt.%. The EDX cross-sectional results showed lower Al contents in comparison to Rietveld refinement results, especially for samples prepared from higher binder concentrations of 15 and 25 wt.%. However, the difference in the compositional results between Rietveld refinement and EDX cross-sectional analyses was within the margin of error.

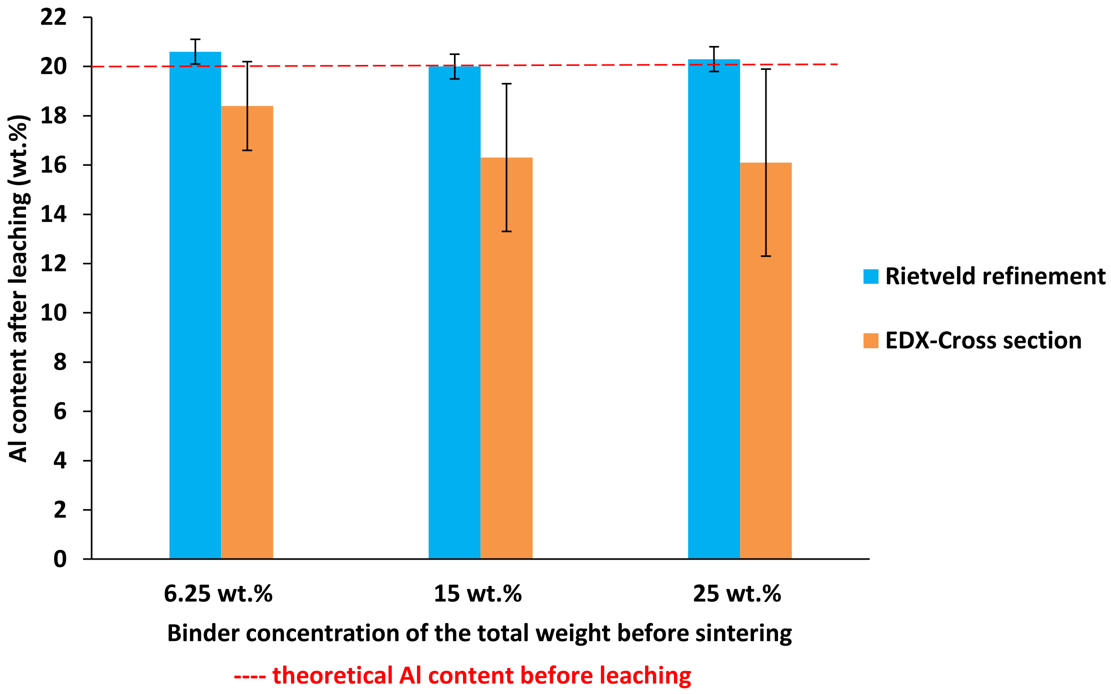

Figure 4.45. Rietveld refinement and EDX cross-section results for Al contents of as-leached samples prepared from three different binder concentrations; where (a) Ni60:Alloy40-B6.25; (b) Ni60:Alloy40-B15; (c) Ni60:Alloy40-B25.

Figure 4.46 compares the Al content results from the EDX analysis on the surface and cross-section of as-leached samples. The difference in the Al composition between the surface and cross-section was within the experimental errors regardless of the binder concentration. Although EDX results implied a decrease in Al content by *ca.* 12 % as the binder concentration increased from 6.25 to 25 wt.%, this change was within the margin of error for EDX analysis.

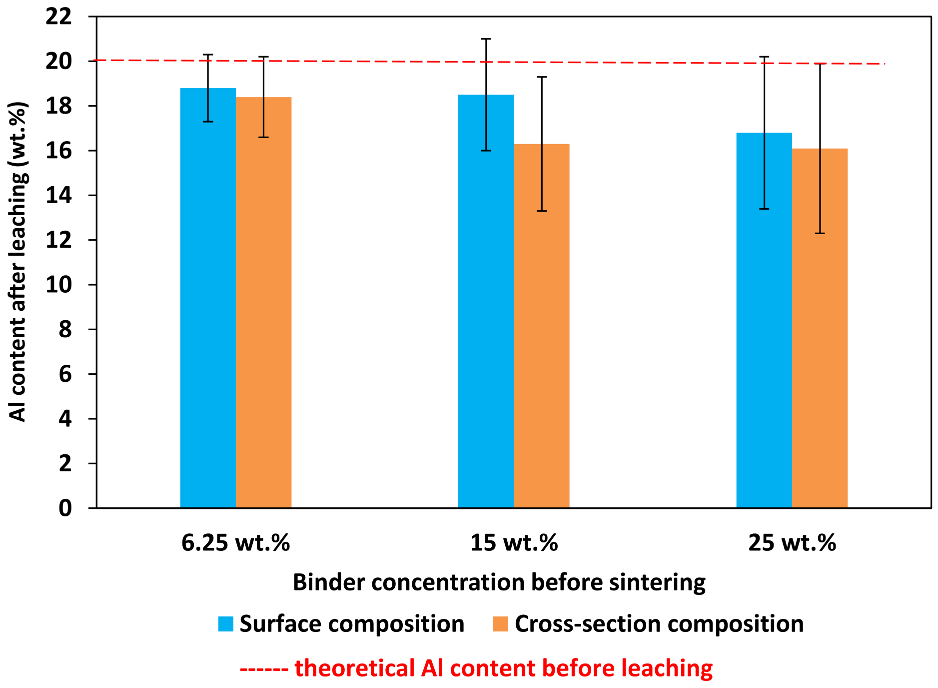

Figure 4.46. EDX composition results for the surface and cross-section of as-leached samples prepared from three different binder concentrations; where (a) Ni60:Alloy40-B6.25; (b) Ni60:Alloy40-B15; (c) Ni60:Alloy40-B25.

4.5.1.3. Porosity Characteristics

N_2 sorption and He pcynometer

Figure 4.47 presents the porosity characteristics of as-leached samples prepared from the binder concentrations of 6.25, 15 and 25 wt.%. The changes in micro- and mesoporosity with respect to the binder concentration were within the margin of error (± 13 %). The macroporosity, on the other hand, increased significantly with greater binder concentrations. Using 25 wt.% binder more than doubled the specific macropore volume in comparison to the binder concentration of 6.25 wt.%.

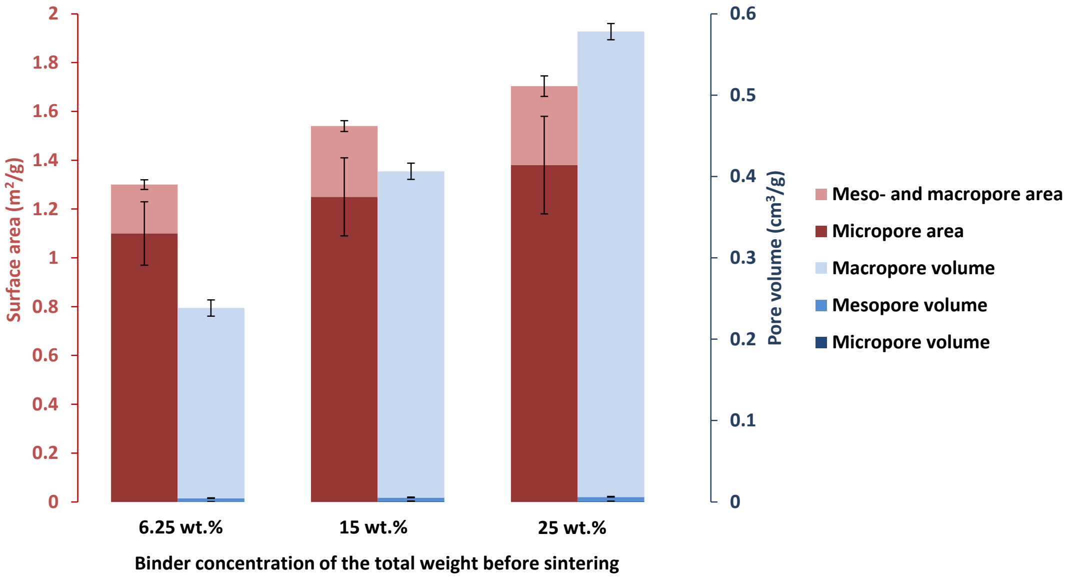

Figure 4.47. N_2 sorption and He pycnometer results for porosity characteristics of as-leached Ni60:Alloy40 samples prepared from three different binder concentrations.

Figure 4.48 shows the ratios of material, closed and open pores in the disk volume for as-leached samples prepared from different binder concentrations. As the binder concentration increased from 6.25 to 25 wt.%, the volumetric concentration of open pores increased by *ca.* 31 %. Closed pores, on the other hand, had similar volumetric ratios (*ca.* 3 vol.%) in the disk volume regardless of the binder amount. There was a decreasing trend in the volumetric ratio of materials with higher binder concentrations.

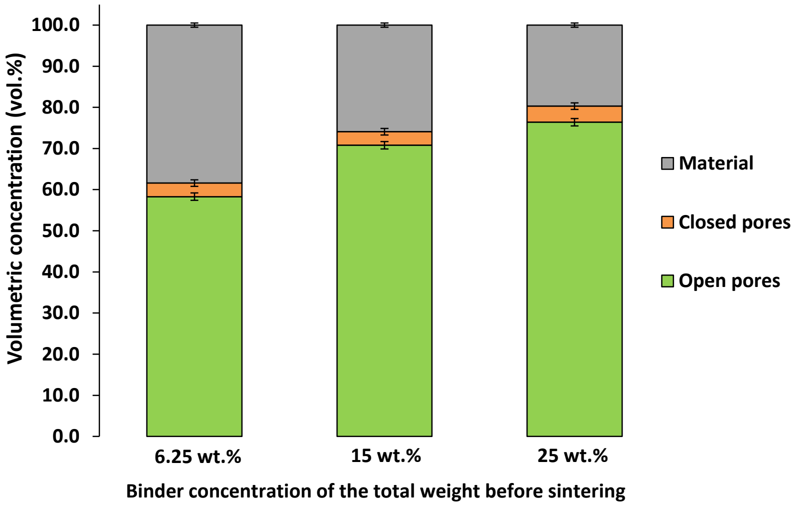

Figure 4.48. He pycnometer results for the concentrations of material, closed and open pores in the disk volume of as-leached Ni60:Alloy40 samples prepared from three different binder concentrations of 6.25, 15 and 25 wt.%.

MIP

As demonstrated in Figure 4.49, increasing the binder concentration from 6.25 to 25 wt.% also changed the pore size distribution measured by means of MIP for as-leached Ni60:Alloy40 samples. Using the 6.25 wt.% binder amount gave macropores with a size range of *ca.* 0.2-6 µm. However, increasing the binder concentration from 6.25 to 25 wt.% split the distribution into a bimodal, where the majority of macropores were now within the size range of *ca.* 9-400 µm. As shown in Table 4.7 the total Hg intrusion volume per sample weight more than doubled, while the porosity rose by *ca.* 30 % as the binder concentration increased from 6.25 to 25 wt.%.

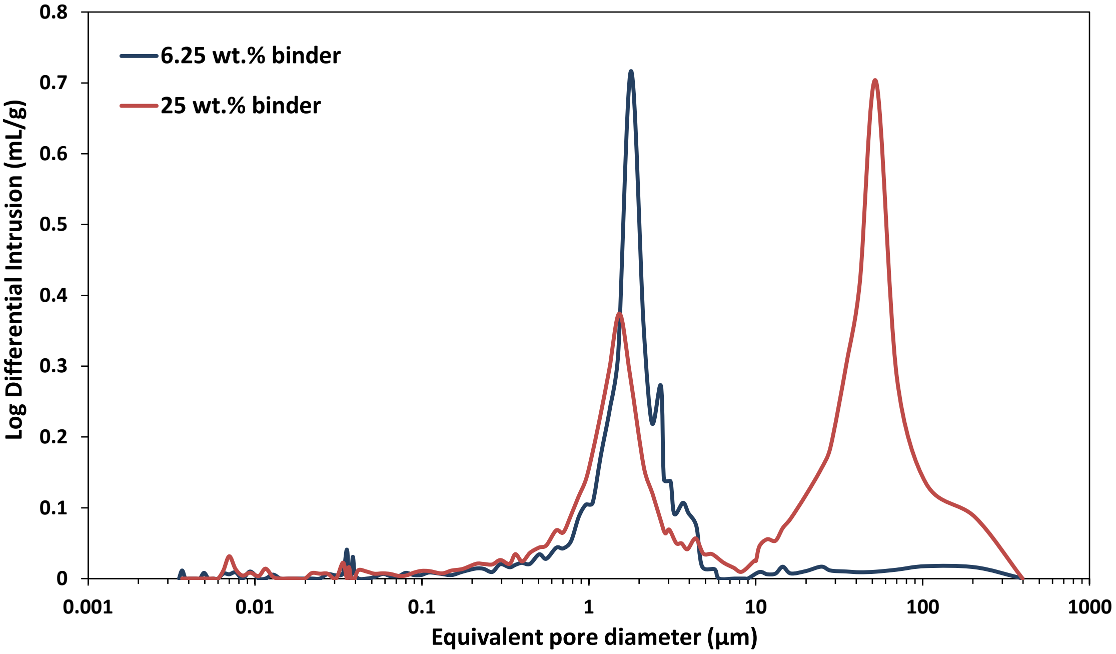

Figure 4.49. MIP results for the pore size distributions of as-leached Ni60:Alloy40 samples prepared from the binder concentrations of 6.25 and 25 wt.%.

Table 4.7. MIP results for the total Hg intrusion volume and porosity of as-leached Ni60:Alloy40 samples prepared from the binder concentrations of 6.25 and 25 wt.%.

Binder concentration (wt.%)	Hg intrusion volume (± 0.01 ml/g)	Porosity (± 2 %)
6.25	0.22	60
25	0.49	77

4.5.1.4. Electrochemical Performance

Figure 4.50 gives the electrolyser cell voltages measured using the cathodes prepared from binder concentrations of 6.25, 15 and 25 wt.%. Increasing the binder concentration from 6.25 to 25 wt.% resulted in a downward trend in the electrolyser cell voltage, with the 25 wt.% binder concentration giving a cell voltage *ca.* 4 % less than that measured with the 6.25 wt.% binder concentration at 1 A/cm^2.

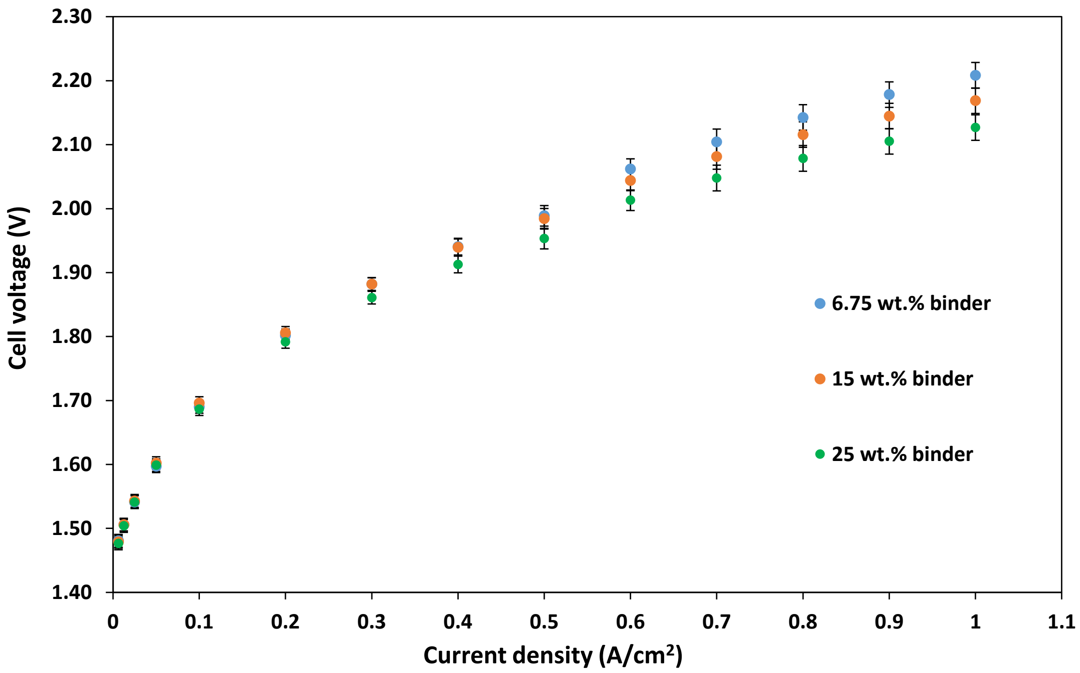

Figure 4.50. Electrolyser cell voltage-current density curves measured using cathodes prepared from different binder concentrations; 6.25, 15 and 25 wt.%.

Table 4.8 gives the observations of the mechanical performance of electrodes before and after the electrolyser cell test. The robustness of the electrodes decreased significantly as the binder concentration rose, with the electrodes prepared from ≥ 15 wt.% binder concentrations resulting in very fragile electrodes that are not feasible for industrial applications.

Table 4.8. Observations on mechanical performance of electrodes prepared from different binder concentrations; 6.25, 15 and 25 wt.%.

Binder concentration (wt.%)	Mechanical strength of as-sintered and as-leached samples	Observations after the alkaline electrolyser cell test
6.25	Sufficient	No significant change in the mechanical performance after the test. However, care was required during the handling of electrode.
15	Poor	Difficult to handle and required extra care. Slight piston marks were observed on the electrode surface.
25	Extremely poor	Significant piston marks were observed on the electrode surface after the test. The thickness of electrode reduced where the piston pressed against the electrode surface. The electrode started falling apart even after the first cell test.

4.5.2. Effect of Binder Particle Size

The effect of binder particle size was investigated using wax with different particle size ranges, i.e. 20-45 µm, 45-75 µm, 75-200 µm and > 200 µm, as well as cellulose with a mean particle size of 20 µm. Ni60:Alloy40-B6.25 samples were prepared from a metal composition of 60 wt.% Ni-40 wt.% starting alloy and a binder concentration of 6.25 wt.% before sintering. Sintering was carried out at 650 ºC.

Results for physical characterization techniques are presented in Section 4.5.2.1 and 4.5.2.2, while the electrolyser cell test results are reported in Section 4.4.5.3. The laser diffraction results for the particle size distribution of as-received wax is reported in Appendix 9.

4.5.2.1. Microstructural Analysis

Figures 4.51 and 4.52 show representative SEM-SE images of the cross-sections and surfaces of as-leached Ni60:Alloy40-B6.25 samples prepared using binders with different particle sizes respectively. As the particle size of the binding agent increased, the surface and cross sections of the electrodes became rougher due to the presence of large macropores. More homogenous distribution of these macropores was observed when small particle size range was used. The sizes of these macropores were in the range of *ca.* 3-30 µm for the cellulose and varied between 20 and 45 µm for the ground wax. Using as-received wax with a mean particle size of *ca.* 130 µm resulted in larger macropores of differing sizes and a less homogenous distribution across the cross-section and surface. Some of the pores were as large as *ca.* 450 µm. This morphology was observed with all samples prepared using 6.25 wt.% as-received wax as a binder, regardless of the change in preparation conditions such as sintering temperature, alloy ratio and leaching conditions. Lastly, using wax with sizes of more than 200 µm gave the largest macropores with the least homogenous distribution. It must be noted that electrodes showed decreasing robustness as the binder particle size increased.

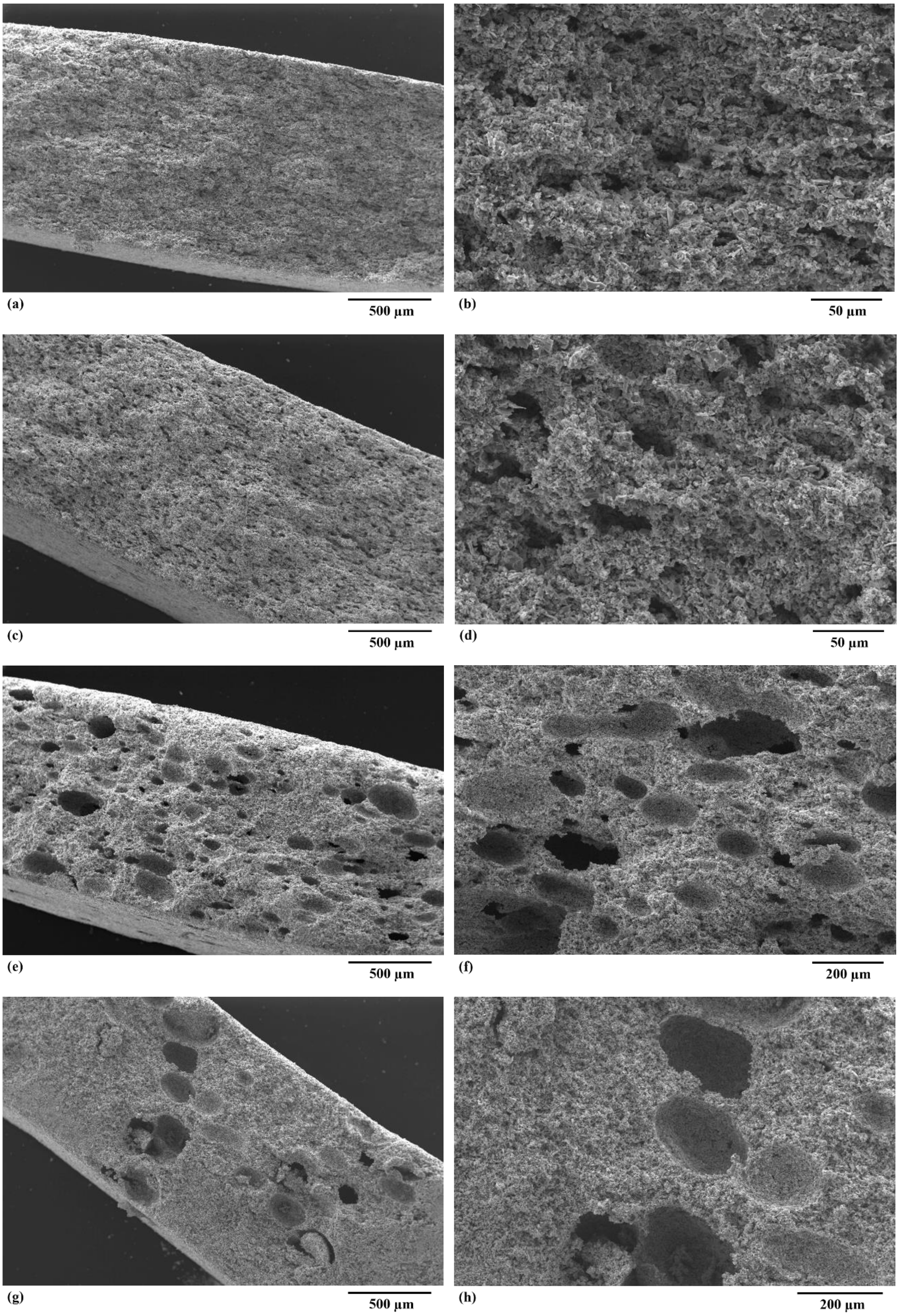

Figure 4.51. Representative SEM-SE images of the cross-sections of as-leached Ni60:Alloy40-B6.25 samples prepared using binders with different particle sizes; (a) and (b) cellulose (average size, 20 µm); (c) and (d) ground wax (20-45 µm); (e) and (f) as-received wax (average size, 130 µm); (g) and (h) wax (> 200 µm).

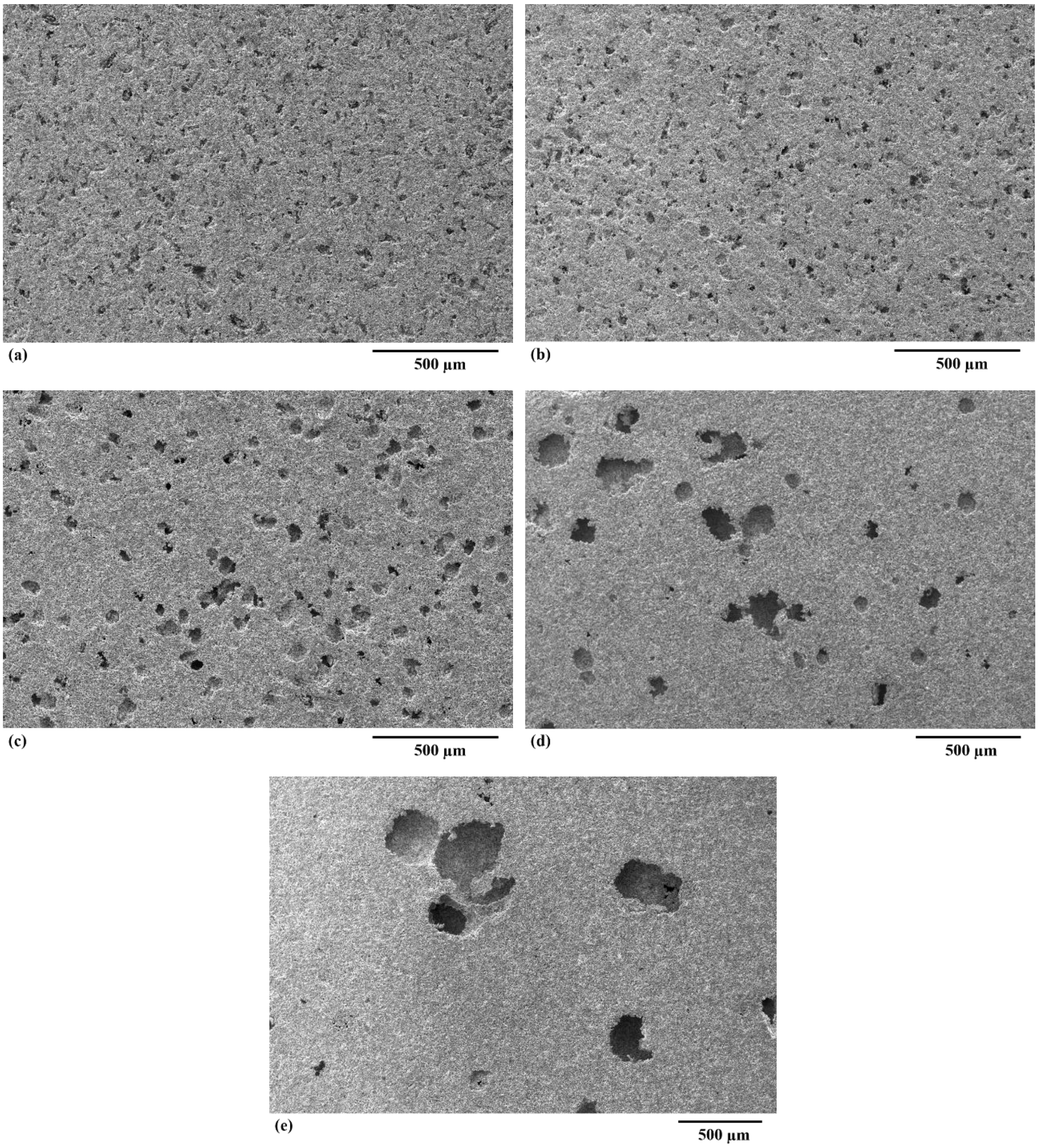

Figure 4.52. Representative SEM-SE images of the surfaces of as-leached Ni60:Alloy40-B6.25 samples prepared using binders with different particle sizes; (a) cellulose (average size, 20 µm); (b) ground wax (20-45 µm); (c) ground wax (45-75 µm); (d) as-received wax (average size, 130 µm); (e) wax (> 200 µm).

A higher magnification SEM-SE image of a cross-sectional area of the sample prepared from wax binder with particle sizes more than 200 µm, where the largest macropores (> 200 µm) were excluded, showed the presence of pores with a size range of *ca.* 0.5-10 µm on the cross-section (Figure 4.53). These pores were observed with all samples regardless of their preparation conditions.

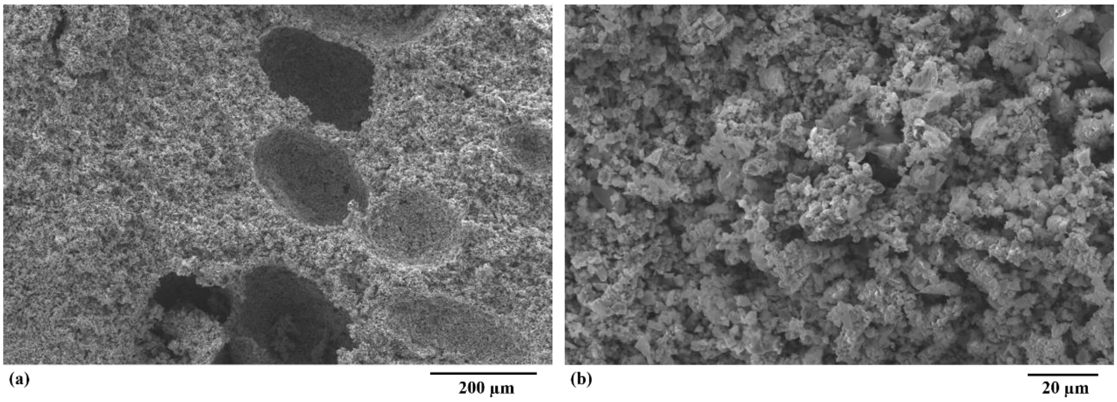

Figure 4.53. Low (left) and high (right) magnification SEM-SE images from a cross-sectional area of a Ni60:Alloy40-B6.25 sample prepared using wax binder with sizes > 200 µm, where (a) includes; (b) excludes large macropores (> 200 µm).

Figure 4.54 gives thicknesses of sample disks before and after sintering with respect to the binder particle size. Sintering process did not change the thickness significantly. The variations in the thickness of samples disks with varying binder particle sizes were within the experimental errors.

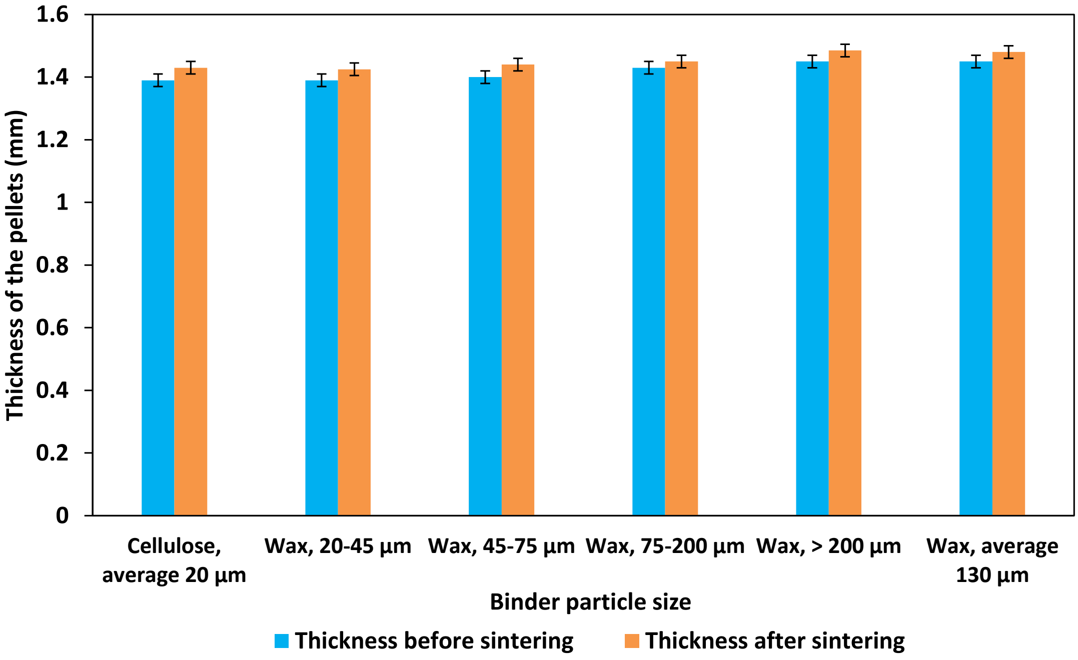

Figure 4.54. The change in the thickness of Ni60:Alloy40-B6.25 samples measured before and after sintering with respect to the binder particle size.

4.5.2.2. Porosity Characteristics

N_2 sorption and He pycnometer

Figure 4.55 shows porosity characteristics of as-leached Ni60:Alloy40-B6.25 samples prepared using a cellulose or wax binder with different particle sizes. Regardless of the binder type and particle size, all samples gave similar micro-, meso- and macroporosity, with the variations in the porosity features being within the experimental errors.

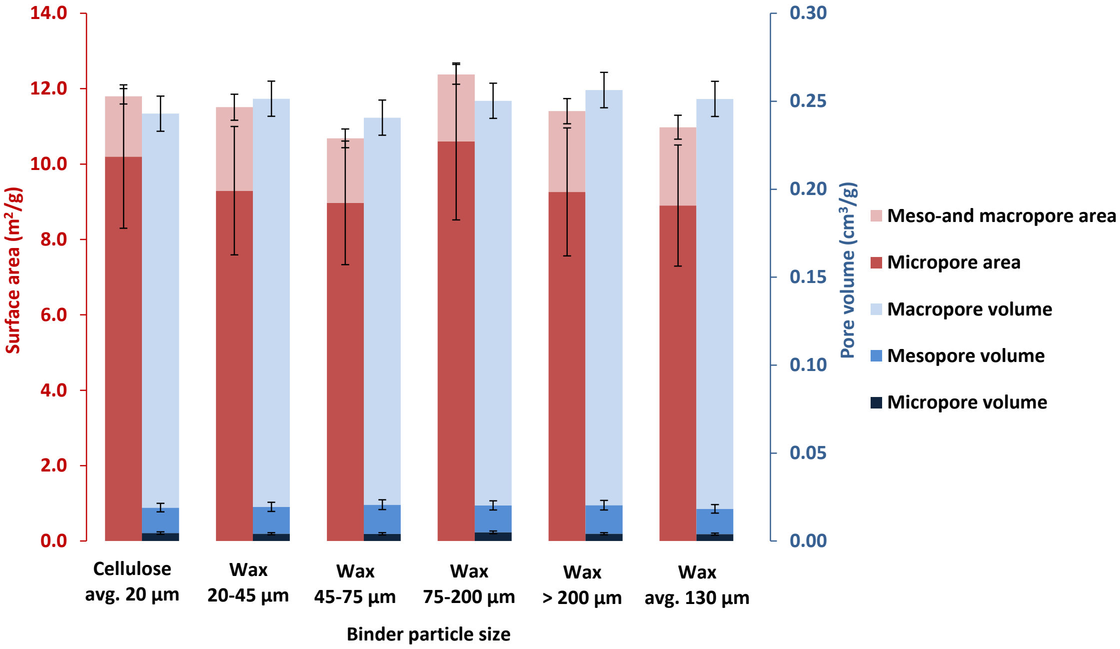

Figure 4.55. N_2 sorption and He pycnometer results for porosity characteristics of as-leached Ni60:Alloy40-B6.25 samples prepared using a cellulose or wax binder with different particle sizes.

The ratios of material, closed and open pores in the disk volume were also estimated for as-leached Ni60:Alloy40-B6.25 samples from the He pycnometer results. As demonstrated in Figure 4.56, using the binders with different particle sizes did not change the volumes of material, closed and open pores significantly.

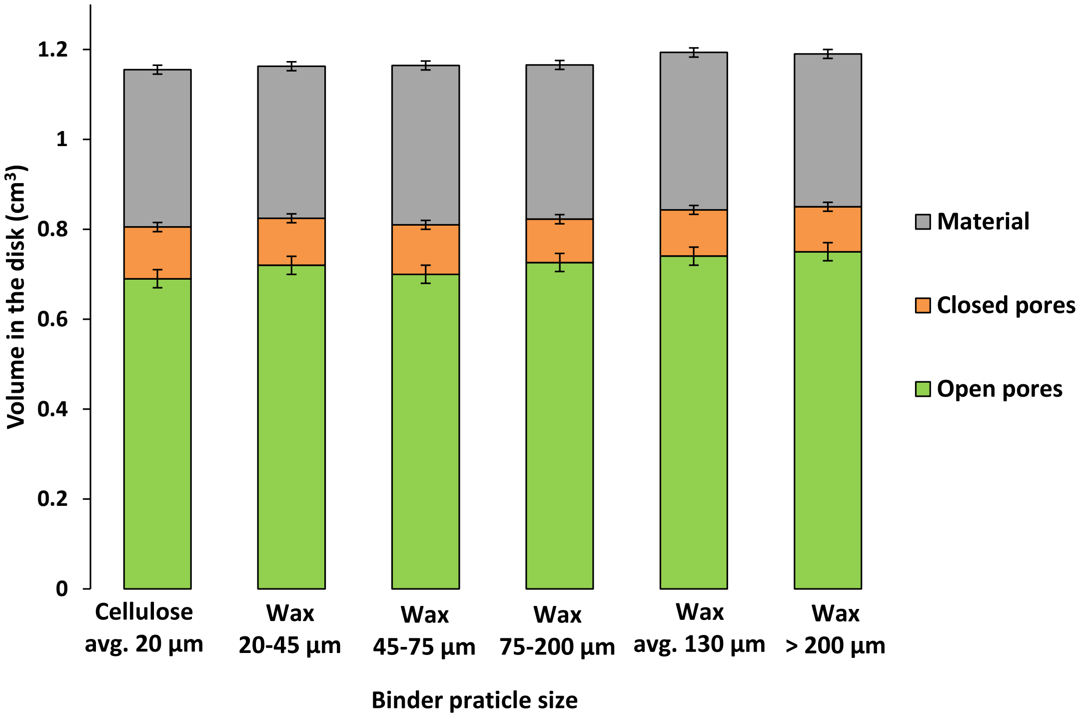

Figure 4.56. He pycnometer results for the contributions of material, closed and open pores to the disk volume of as-leached Ni60:Alloy40-B6.25 samples prepared using a cellulose or wax binder with different particle sizes.

MIP

Figure 4.57 presents the MIP results for the pore size distributions of as-leached Ni60:Alloy40-B6.25 samples prepared from different binder particle sizes. Surprisingly, using wax with particle sizes more than 200 µm gave macropores mostly accumulating in the size range of *ca.* 0.2-1.7 µm in addition to a smaller peak in the size range of *ca.* 1.7-9 µm. However, large macropores (with sizes ≥ 200 µm) observed in SEM images were not detected by the MIP technique. Similarly, the pore size distribution of the sample prepared from as-received wax with a *ca.* 130 µm mean diameter did not include large macropores observed in SEM images with varying sizes from *ca.* 15 up to *ca.* 450 µm. MIP results indicated pores accumulated in the size range of *ca.* 0.2-5 µm. Samples prepared from cellulose and ground wax with a particle size range of 20-45 µm gave a macroporosity distribution in a similar size range to as-received wax, however peaks were slightly wider. The macroporosity identified by SEM images for these binders with sizes of *ca.* 20 µm and 20-45 µm for the cellulose and ground wax respectively were also not detected by the MIP technique. As shown in Table 4.9, all samples gave similar Hg intrusion volumes per sample weight and the porosity was 60 ± 2 % regardless of the binder type and particle size range.

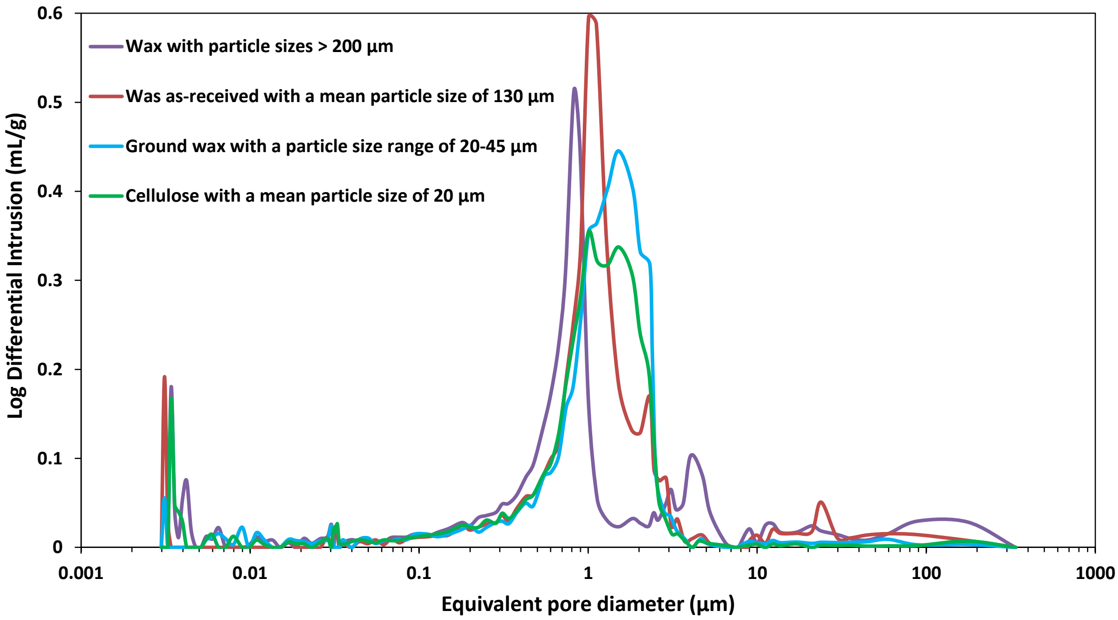

Figure 4.57. MIP results for the pore size distributions of as-leached Ni60:Alloy40-B6.25 samples prepared using wax or cellulose binders with different particle sizes.

Table 4.9. MIP results for the porosities of as-leached Ni60:Alloy40 samples prepared using wax or cellulose binders with different particle sizes.

Binder	Particle size range (µm)	Hg intrusion volume (± 0.01 ml/g)	Porosity (± 2 %)
Cellulose	A mean of 20	0.21	60
As-received wax	A mean of 130	0.23	62
Ground wax	20-45	0.23	62
Wax	> 200	0.20	58

4.5.2.3. Electrochemical Performance

As shown in Figure 4.58, similar electrolyser cell voltages were recorded regardless of the change in the particle size of the binder agent used during the preparation of the cathode samples.

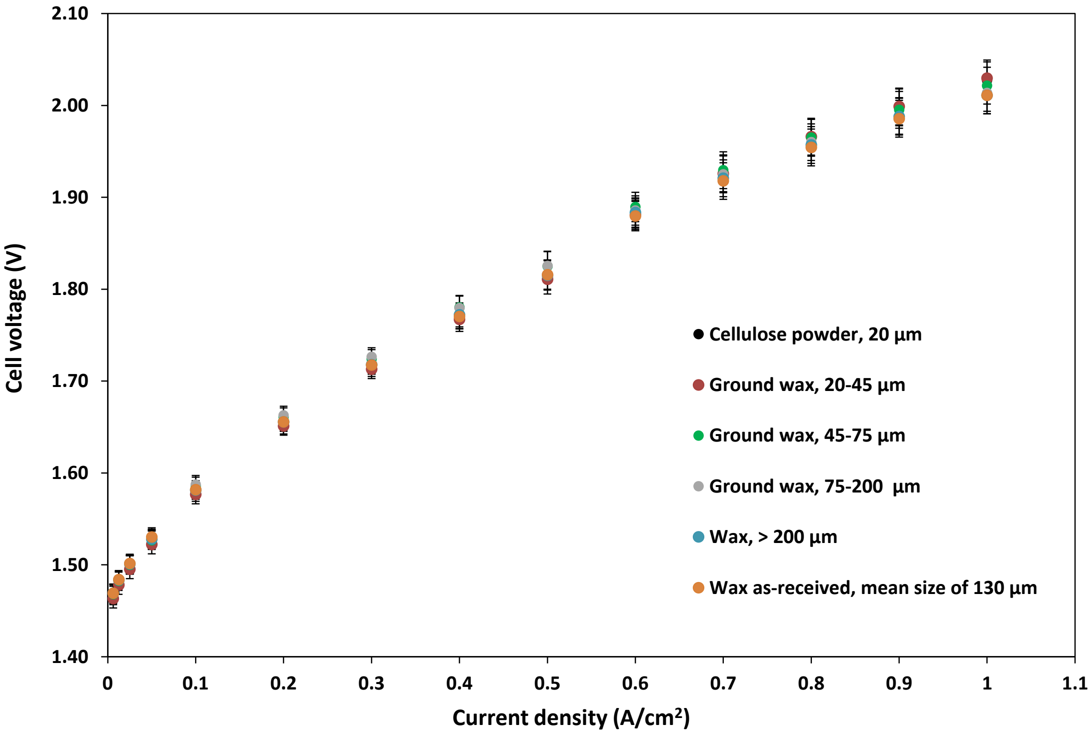

Figure 4.58. Cell voltage-current density curves measured using cathodes prepared using binders with different particle sizes.

4.6. Micro-CT Analysis

Micro-CT scans were carried out on two Ni60:Alloy40-B6.25 samples prepared from a metal composition of 60 wt.% Ni-40 wt.% starting alloy and a binder concentration of 6.25 wt.%. As-received wax with an average particle size of *ca.* 130 µm was used as a binder agent for the first sample, while other was prepared using ground wax with a particle size range of 20-45 µm.

After the electrolyser cell test, electrodes were rinsed, dried and passivated as described in Section 3.1.2.4 and examined through the micro-CT technique. Section 4.6.1 presents the nature of the reconstructed images from the raw dataset. The porosity characteristics are reported in Section 4.6.2, while the phase analysis is covered in Section 4.6.3.

4.6.1. Reconstructed Images

Figure 4.59 shows the 3D grayscale view of a Ni60:Alloy40-B6.25 sample from a medium resolution scan with a scan resolution of 3 µm (detailed in Table 3.5) including representative grayscale images from the xy, xz and yz planes. The presence of different gray classes in the images from white to black colour indicated the density gradients within the scanned sample. Black regions signify very low density, i.e. pores where there is no material, the dark grey areas signify regions with a medium density, e.g. Al-rich phases (3.98-4.90 g/cm^3), the light grey areas are for a high density, e.g. AlNi and/or $AlNi_3$ (5.92-7.44 g/cm^3) and finally white regions are for the most dense material, i.e. Ni with a density of 8.91 g/cm^3. Some of the grayscale images showed the presence of localised Al-rich regions within the sample. These dark grey islands had some cracks inside them (Figure 4.59, xy plane image).

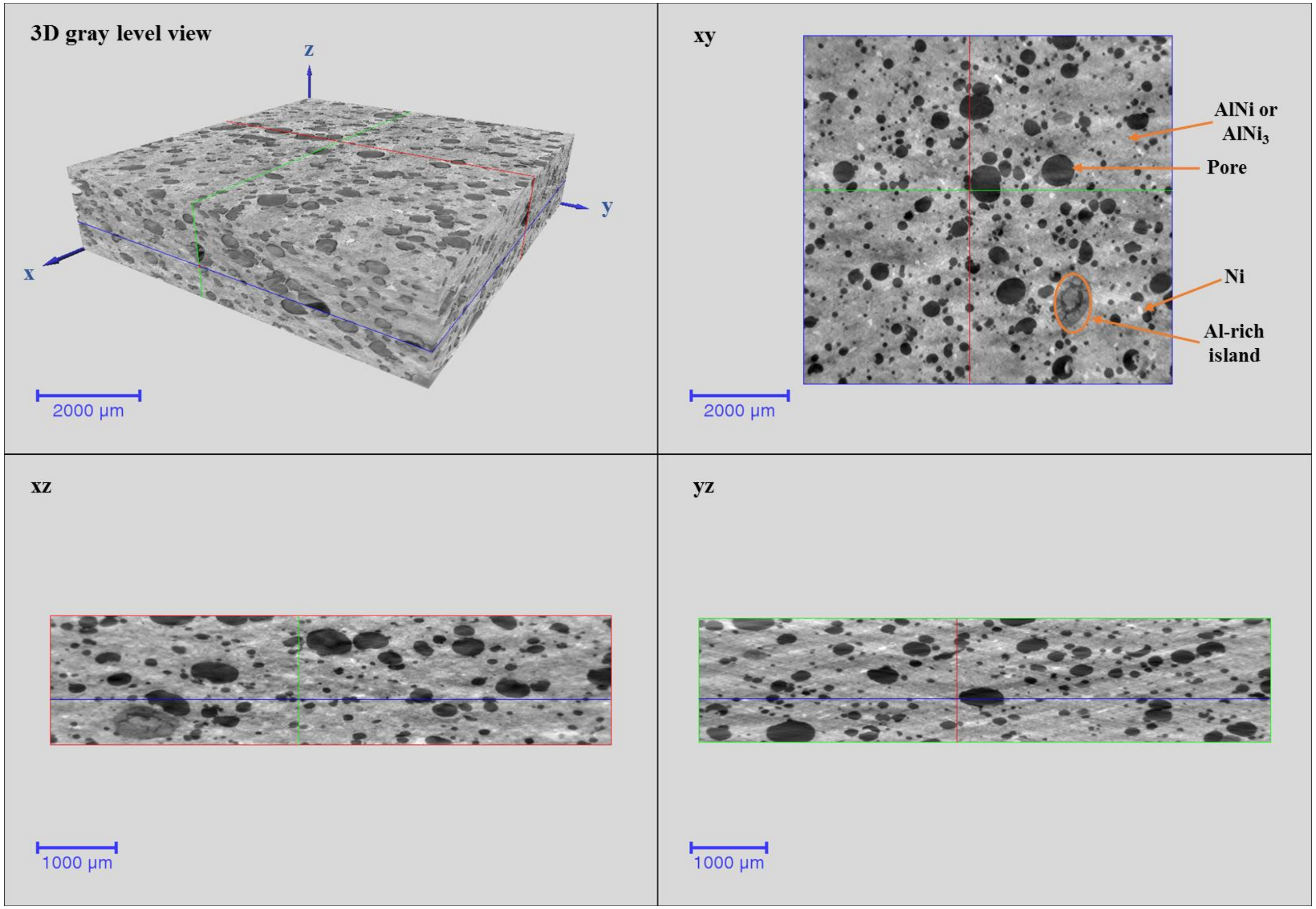

Figure 4.59. 3D grayscale view and representative grayscale images from xy, xz and yz planes of a medium resolution micro-CT scan for a Ni60:Alloy40-B6.25 sample prepared using wax as-received as a binder. Blue, red and green lines show the locations of the slices for xy, xz and yz planes respectively. The scan resolution was 3 µm.

Figure 4.60 gives an example of a grayscale histogram of a scanned sample. Although the grayscale micro-CT images of the same sample in Figure 4.59 indicated the presence of at least three different constituents, i.e. from black to white, the grayscale histogram showed only two peaks. The small peak with the lower grayscale values corresponded to the pore phase, while the large peak with higher grayscale values represented the material. There was not a sufficient grayscale difference to precisely distinguish the different intermetallic phases. Based on the grayscale images, a threshold value was assigned to the white colour region (corresponding to the Ni phase) after a number of iterations. Anything other than pores or Ni was referred to as the alloys. Table 4.10 gives examples of grayscale values selected for different constituents in a scanned sample.

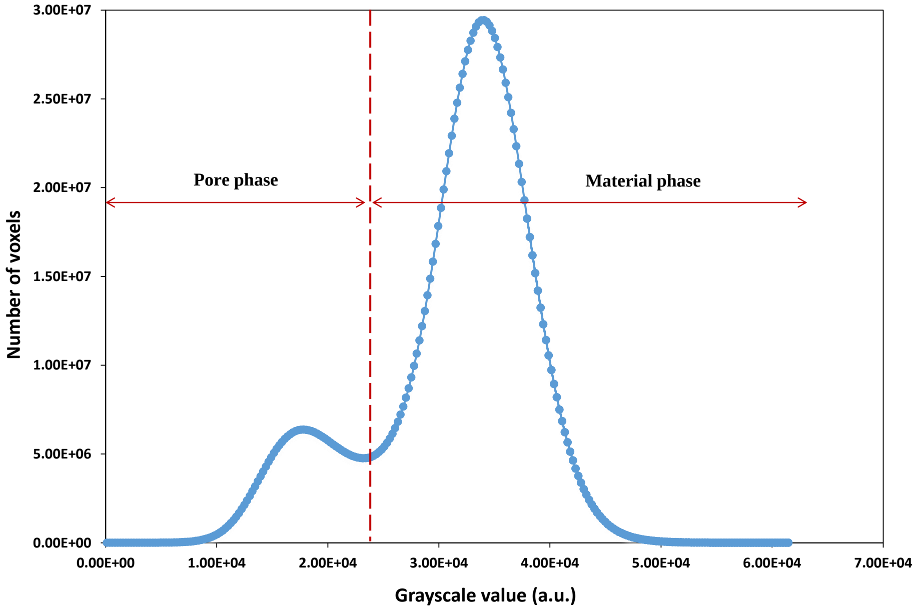

Figure 4.60. Grayscale histogram of a micro-CT scan of a Ni60:Alloy40-B6.25 sample.

Table 4.10. Grayscale values used to analyse the different constituents present in a scanned sample.

Constituent	Grayscale value (a.u.)
Pores	< 24,000
Alloys	24,000-38,000
Ni	> 38,000

4.6.2. Porosity Analysis

Table 4.11 gives the porosity results for the same sample from the micro-CT scans with different resolutions. As the scan resolution increased from 0.5 to 32.5 µm, the total porosity decreased from 43.8 to 9.8 %. As explained in Section 3.3.7, there is a compromise between the scan field size and the resolution. Although smaller pore sizes were able to be detected when the scan resolution was lower, the scan field area was reduced.

Table 4.11. Micro-CT porosity results for a Ni60:Alloy40-B6.25 sample where the scans were carried out with different scan resolution.

Scan	Scan resolution (voxel size) (µm)	Scan field size (mm)	Porosity (%)
High resolution scan	0.5	0.5 x 0.5	43.8
Medium resolution scan	3.0	6.0 x 6.0	16.9
Low resolution scan	32.5	32.5 x 32.5	9.8

As shown in Table 4.12 the porosity results for the medium resolution scans from two different locations, i.e. central and outer locations (demonstrated in Figure 3.6) were similar. This proved that the scan field size of 6 x 6 mm was large enough to be representative where the porosity did not show a dependence on the scan location. Therefore, the spatial porosity fluctuations and pore size distribution were studied using the results from the medium resolution scans of the central location.

Table 4.12. Micro-CT porosity results for the medium resolution scans of a Ni60:Alloy40-B6.25 sample where the scans were carried out on two different locations. The scan resolution and field of view were 3 µm and 6.0 x 6.0 mm respectively.

Scan location*	Porosity (%)
Central location	16.9
Outer location	16.8

*Scan locations are demonstrated in Figure 3.6.

4.6.2.1. Spatial Porosity Fluctuations

The porosities of 2D-slices were estimated through each plane for a Ni60:Alloy40-B6.25 sample that was prepared using as-received wax as a binder. The locations of planes through the scanned sample are presented in Figure 4.59. As reported in Table 4.8, the total porosity measured for this sample was 16.9 % when the scan resolution was 3 µm. Figure 4.61 shows the changes in the porosity with respect to the 2D slice number through different planes. The fluctuations in the porosity were the least significant with xy plane which represents the cross-section of the sample. The porosity varied between 10.5 and 19.9 % for the xz plane and between 12.5 and 21.0 % for the yz planes. There was no upward or downward trends through different planes, where the fluctuations in the porosity were rather random.

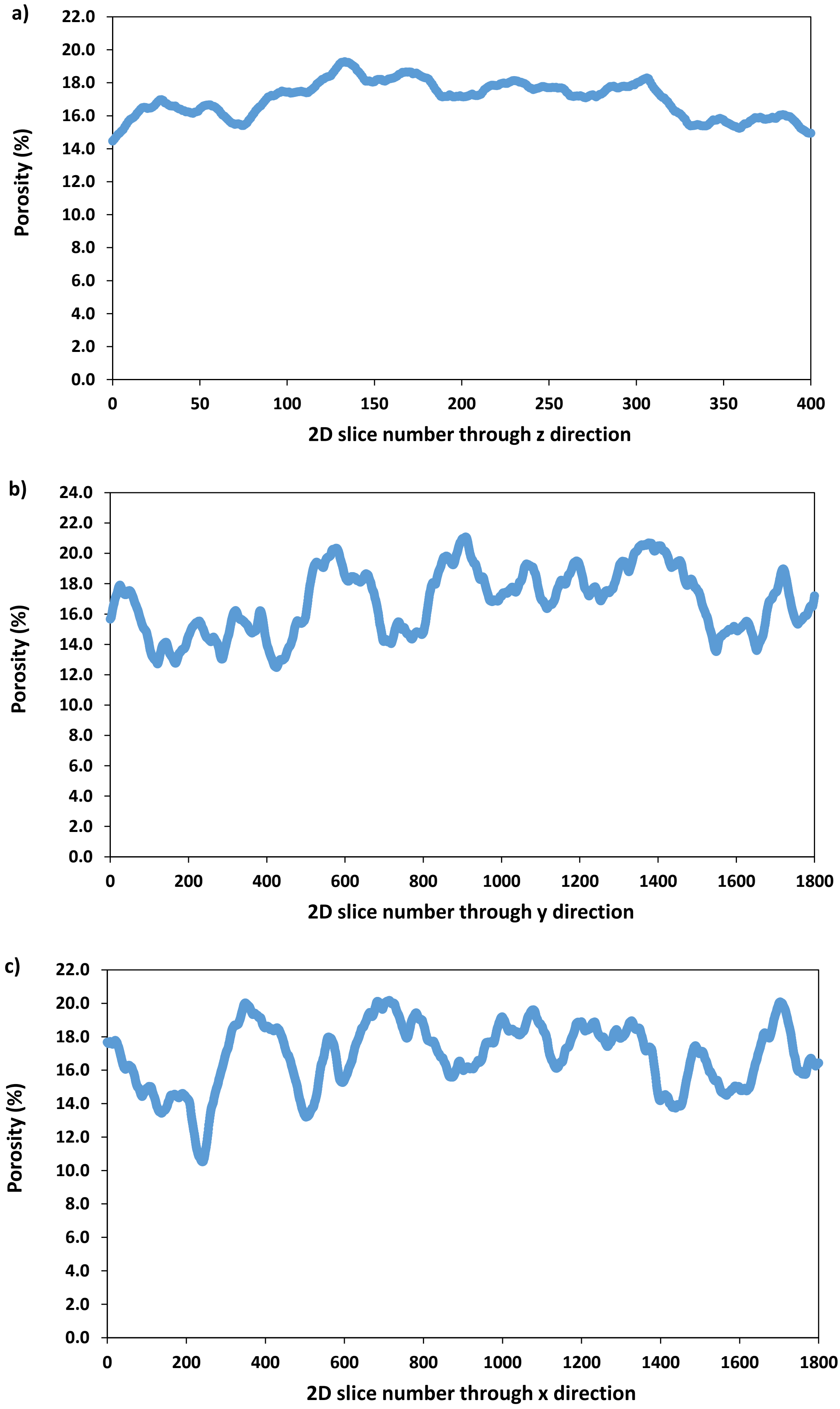

Figure 4.61. Micro-CT results for the spatial macroporosity fluctuations in 2D slices of different planes for a Ni60:Alloy40-B6.25 sample prepared using as-received wax as a binder, where (a) xy plane; (b) xz plane; (c) yz plane. The scan resolution was 3 µm.

4.6.2.2. Macropore Size Distribution

The macropore size distribution was studied for two different Ni60:Alloy40-B6.25 samples which preparation conditions were same apart from the binder particle size range. As-received wax with an average particle size of *ca.* 130 µm was used as a binder agent for the first sample, while the second sample was prepared using ground wax with a particle size range of 20-45 µm. Figure 4.62 demonstrates the pore size distribution profiles of two samples based on the equivalent spherical diameters. When as-received wax was used, the greatest relative number of macropores was observed in the size range of 5-10 µm. Despite having the lowest relative number, 46 % of the pore volume was occupied by the pores with sizes of > 200 µm followed by the size range of 75-200 µm giving a relative volume of 45 %. When ground wax was used, the majority of macropores accumulated in the size of 20-45 µm which accounted for 34 % of the total pore volume. The relative pore volume was the greatest with the pore size of 45-75 µm. There were no pores detected with the sizes of > 200 µm.

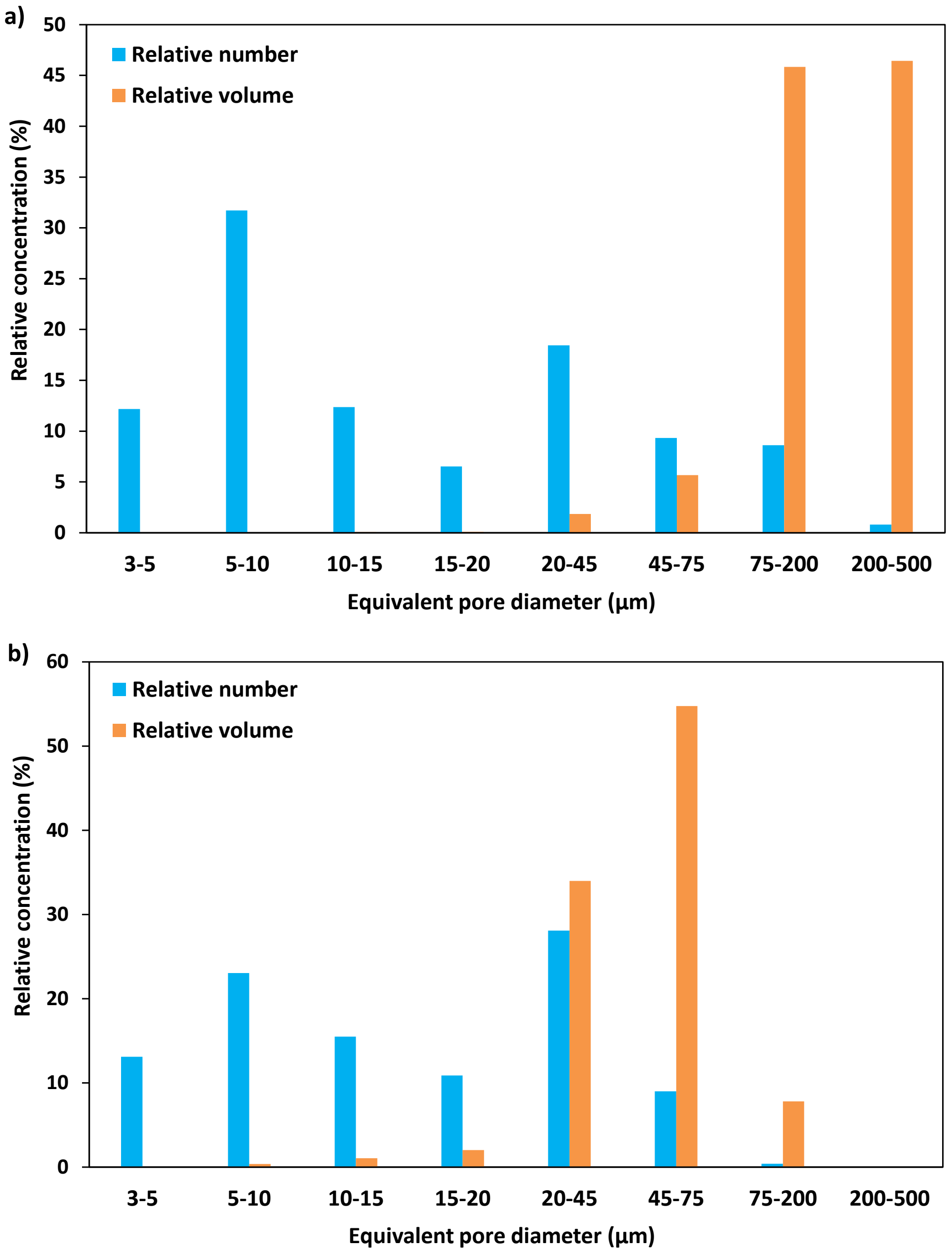

Figure 4.62. Micro-CT results for the pore size distributions of Ni60:Alloy40-B6.25 samples prepared using (a) as-received wax with an average particle size of 130 µm; (b) ground wax with a particle size range of 20-45 µm. The scan resolution was 3 µm.

Figure 4.63 shows the 3D representation of macropores detected in the sample prepared using as-received wax with respect to their size range and location within the scanned sample. Despite the greatest relative numbers of pores with less than 20 µm, the total pore volume was dominated by the pores larger than 75 µm. The distributions of pores were fairly even without any distinguishable accumulation of pores within the scanned sample. The least even distribution of pores was observed with the size range of more than 200 µm which relative number was the lowest (Figure 4.63 (d)). Lastly, the shape of pores were mainly ellipsoidal or spherical regardless of the size range.

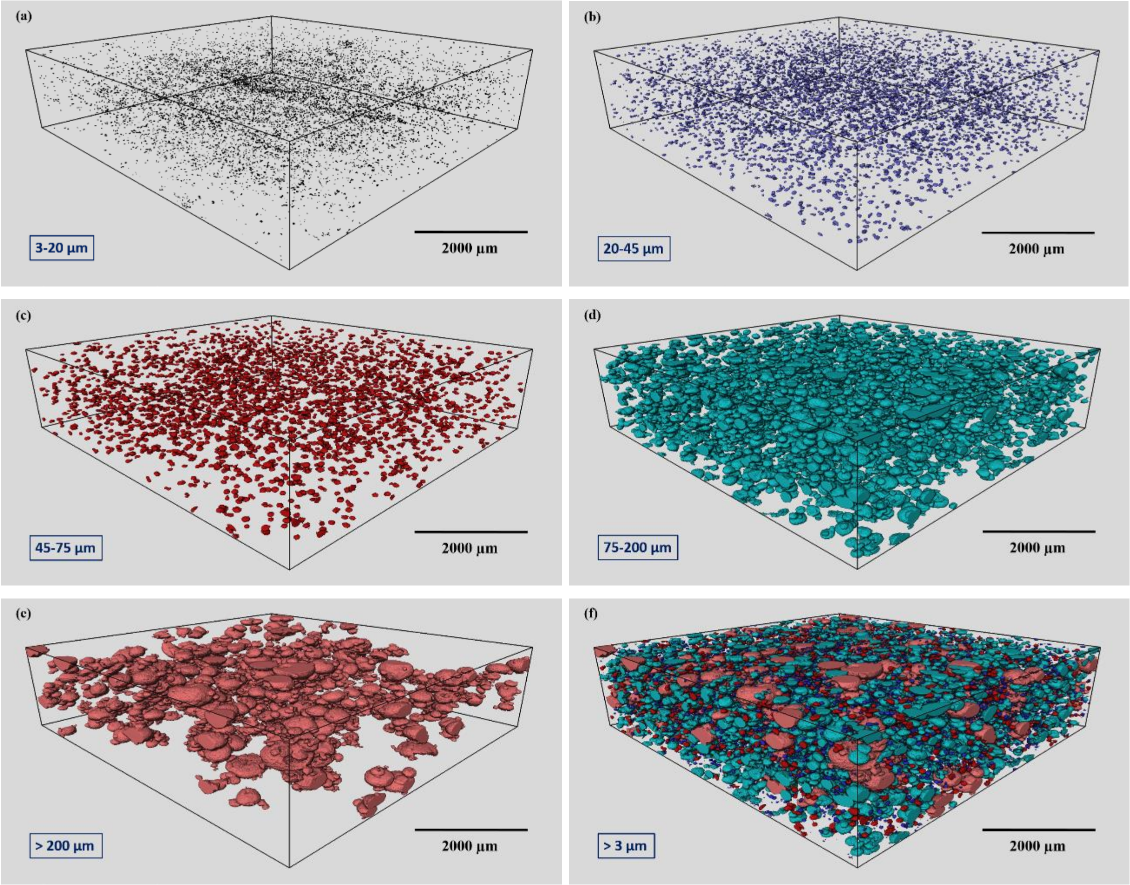

Figure 4.63. 3D visualizations of macropores locations detected for a Ni60:Alloy40-B6.25 sample with respect to the pore size range, where (a) 3-20 µm; (b) 20-45 µm; (c) 45-75 µm; (d) 75-200 µm; (e) > 200 µm; (f) > 3 µm. As-received wax was used as a binder during the preparation of the sample. The scan resolution was 3 µm.

4.6.2.3. Pore Geometry

The pore geometry was studied for two Ni60:Alloy40-B6.25 samples prepared using binders with different particle size ranges as described in Section 4.6.2.2. As reported earlier, the majority of macropores detected by the micro-CT scan had ellipsoidal shapes. Although the pore size distributions were reported for the equivalent spherical diameter, the highest and lowest diameters measured for each pore, referred to as the length and width of the pore respectively, were also analysed to determine the aspect ratio (length/width ratio). Figure 4.64 presents the results of the aspect ratios from medium resolution scans with a scan resolution of 3 µm. When as-received wax was used as a binder during the preparation of the sample, the average aspect ratio was 2.5, with the majority of pores having an aspect ratio in the range of 2-4. Using ground wax with a particle size range of 20-45 µm reduced the relative number of pores with larger aspect ratios (> 2) by 30 %, while the pores with the aspect ratio of 1-2 increased by almost 2 times.

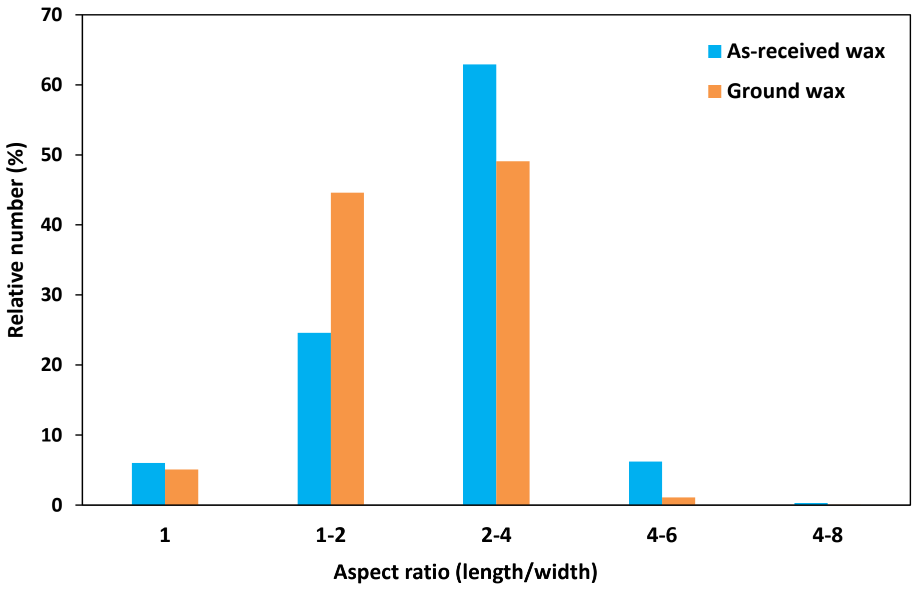

Figure 4.64. Micro-CT results for the relative number of macropores with different aspect ratios (length/width), where as-received wax (with an average particle size of 130 µm) and ground wax (with a particle size range of 20-45 µm) were used as a binder to prepare the samples. The scan resolution was 3 µm.

4.6.2.4. Combined Porosity Results with Other Techniques

Table 4.13 gives the combined results for relative volumes of different pore size ranges measured by N_2 sorption, He pycnometer and micro-CT techniques for a Ni60:Alloy40-B6.25 sample prepared using as-received wax as a binder. The micro- and mesopores accounted for ca. 7 % of the total pore volume, while the majority of pore volume, i.e. *ca.* 70 % were rather occupied by the small macropores (0.05-3 µm). Large macropores (> 3 µm) accounted for *ca.* 24 % of total pore volume.

Table 4.13. Combined results for the relative volumes of different pore size classes measured by N_2 sorption, He pycnometer and micro-CT techniques for a Ni60:Alloy40-B6.25 sample prepared using as-received wax as a binder.

Pore size range (µm)	Relative volume (%)
< 0.05	7
0.05-0.5	31
0.5-3	38
3-32.5	10
> 32.5	14

4.6.3. Phase Analysis

Figure 4.65 shows the 3D representation of different phases from a medium resolution scan (with scan resolution of 3 µm) with respect to their locations within the scanned sample, while Table 4.14 gives the volumetric concentrations of each constituent in the scanned volume. The volumetric concentration of the Ni phase by the micro-CT analysis was *ca.* 10.9 vol.%. The 3D images implied an increase in the concentration of Ni on the sample surface. Based on the medium resolution scan the majority of the volume (*ca.* 72.2 vol.%) was occupied by the alloys.

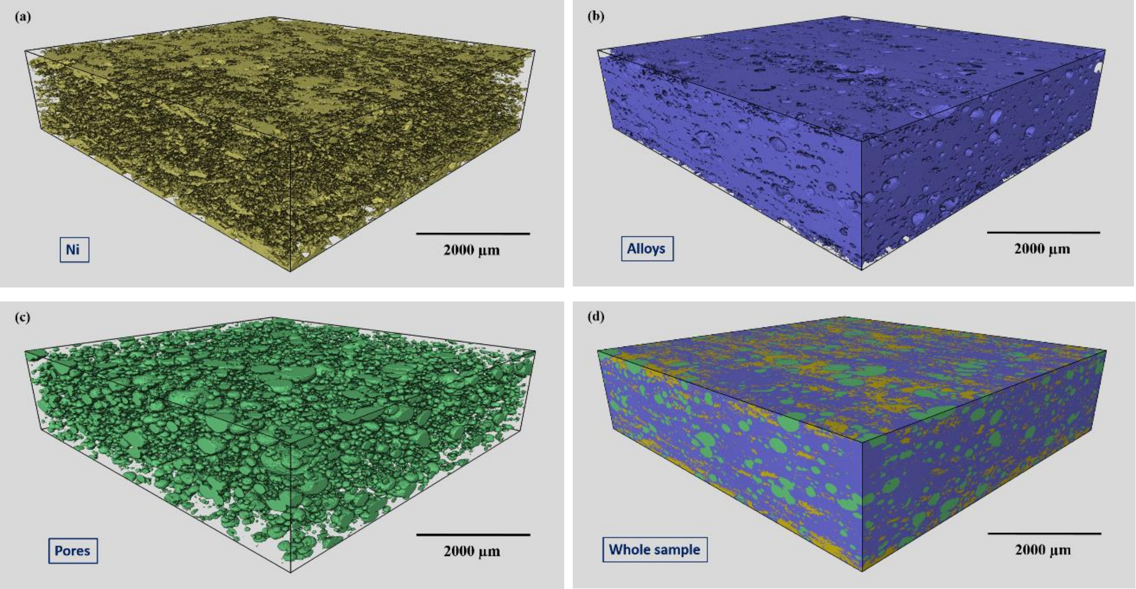

Figure 4.65. 3D visualisation of phase analysis from a medium resolution micro-CT scan of an as-leached Ni60:Alloy40-B6.25 sample prepared using wax as-received as a binder, where (a) the Ni phase; (b) alloys; (c) pores; (d) whole sample with 3 main constituents. The scan resolution was 3 µm.

Table 4.14. Micro-CT medium resolution scan results for the volumetric concentrations of different constituents present in an as-leashed Ni60:Alloy40-B6.25 sample. The scan resolution was 3 µm, therefore the porosity corresponded to the pores with sizes of > 3 µm.

Constituent	Volumetric concentration (%)
Ni	10.9
Alloys	72.2
Pores	16.9

A spatial analysis was performed for the Ni phase based on the micro-CT scan results. As shown in Figure 4.66, the binary images of slices taken for the xy-plane (corresponding to the cross-section) confirmed a variation in the Ni concentration between the surface and cross-section of the sample disk. The highest Ni concentration was observed on the surface (Figure 4.66 (a)), which gradually decreased towards the middle of the cross-section. This was quantified by plotting the volumetric concentration of Ni against the position of the slice in the cross-section (Figure 4.67). The Ni concentration was as high as *ca.* 24 vol.% on the surfaces, whereas it gradually reduced down to *ca.* 4 vol.% in the middle. It must be noted that the change in the illumination of slices through the cross-section may also have an effect on the spatial phase analysis. The surface slices may be slightly more illuminated than those in the cross-section leading to an increased thresholding of the brightest phase, in this case Ni, from middle to the surface.

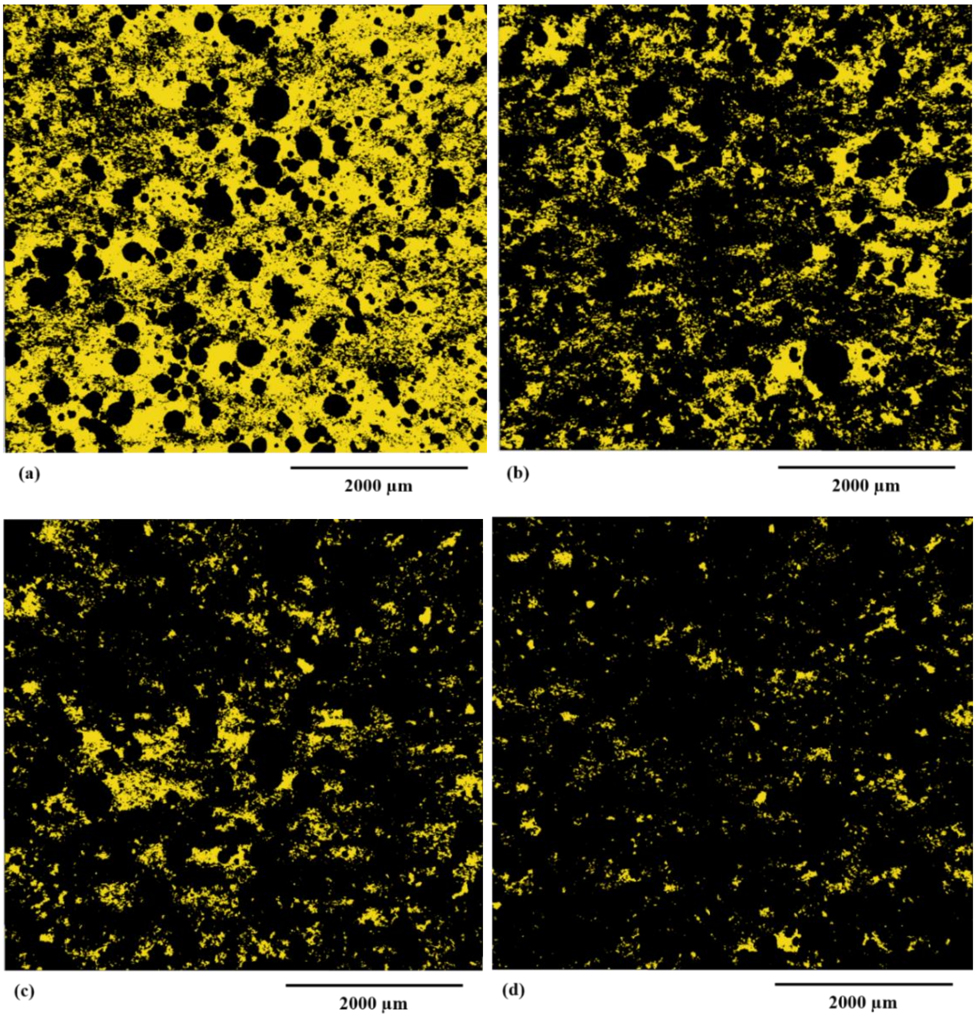

Figure 4.66. Binary micro-CT scan images of slices taken through the xy-plane (corresponding to the cross-section); where the distance from the surface is (a) 0 (on the surface); (b) 0.14 mm; (c) 0.35 mm; (d) 0.69 mm (in the middle). Yellow regions represent the Ni phase, while all other phases including porosity is in black colour. The scan resolution was 3 µm.

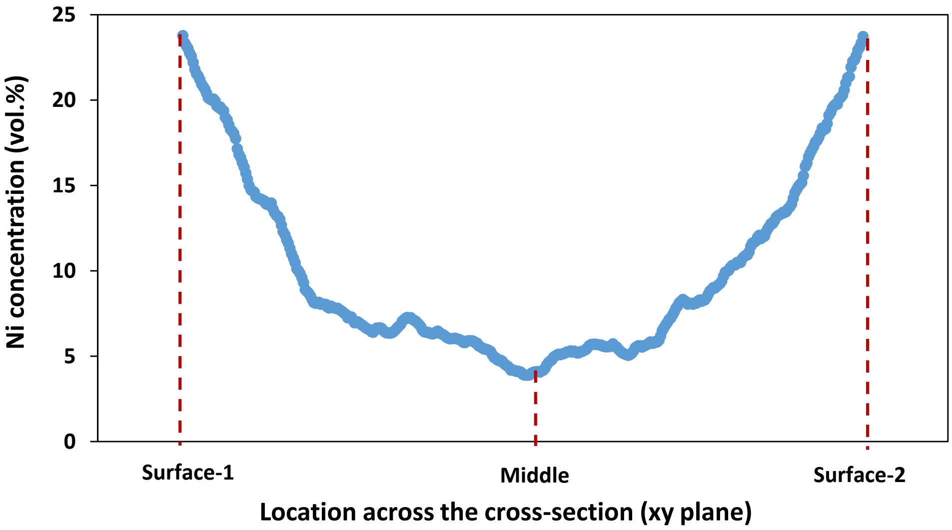

Figure 4.67. Micro-CT medium resolution scan results of the Ni concentrations calculated for the 2D slices through the cross-section of an as-leached Ni60:Alloy40-B6.25 sample. The scan resolution was 3 µm.

5. Discussion

5.1. The Effect of Sintering Temperature

5.1.1. Structural Change during Sintering

5.1.1.1. Intermetallic phases

The properties of precursor alloys are of importance as different intermetallic phases affect the leaching reaction to varying degrees leading to variations in electrode composition, porosity, mechanical properties and catalytic activity [84]. PXD and EDX results reported in Sections 4.2.1 and 4.2.2 clearly indicate that a change in the phases occurred in samples during sintering which can be directly attributed to the system moving towards thermodynamic equilibrium. This can be best explained by using the Al-Ni phase diagram, Figure 5.1. Before sintering, Ni60:Alloy40-B6.25 samples consisted of 40 wt.% Al-rich phases from starting alloy, a mixture of Al_3Ni and Al_3Ni_2 with a Ni composition of 50 wt.% and 60 wt.% Ni (red circles) giving an overall Ni composition of *ca.* 80 wt.% (green circle). If thermodynamic equilibrium was achieved, the samples would have a phase combination on the equilibrium line for this composition (green dotted line in Figure 5.1) depending on the sintering temperature. After 2 h of sintering at 625, 650, 700 and 750 ºC samples consisted of Al_3Ni_2, AlNi, $AlNi_3$ and a Ni-based structure (containing an Al content and referred to as (Ni) phase in the present work) showing that equilibrium was not achieved at these temperatures (blue dots and arrows in Figure 5.1). As the sintering temperature increased from 625 to 750 ºC, samples contained less Al_3Ni_2 and (Ni) phases and more AlNi and $AlNi_3$ (Figure 4.9). For the case of 900 ºC, only $Al_{0.84}Ni_{1.16}$ and $AlNi_3$ were present in as-sintered samples demonstrating that the phase composition of the samples moved closer to the equilibrium line as the sintering temperature rose. The concentrations of $Al_{0.84}Ni_{1.16}$ and $AlNi_3$ calculated for samples sintered at 900 ºC were *ca.* 69 and 31 wt.% respectively (Figure 4.9). This composition was similar to that of the equilibrium point in the phase diagram for the overall Ni concentration of 80 wt.% and the sintering temperature of 900 ºC. This was due to the increase in the rate of Al diffusion with higher sintering temperatures.

Figure 5.2 shows the temperature dependence of Al diffusion into Ni reported by Allison and Samelson [143]. The diffusion coefficient of Al in Ni at 900 ºC is *ca.* 8.5×10^{-12} cm^2/s, whilst at 625 and 750 ºC the Al diffusion has a coefficient of *ca.* 6.1×10^{-15} cm^2/s and *ca.* 2.5×10^{-13} cm^2/s respectively. The diffusion distance (or depth) at a given temperature can be estimated using Equation 5.1;

$$x \approx \sqrt{D.t} \tag{5.1}$$

Where x is the diffusion distance, D is the diffusion coefficient at a given temperature and t is the sintering duration [144].

Using the Equation 5.1 the approximate distances of Al diffusion in Ni were calculated for 2 h of sintering duration; 0.07 µm at 625 ºC, 0.42 µm at 750 ºC and 2.50 µm at

900 ºC. Consequently, duration of 2 h was sufficiently long enough for the Al diffusion to complete at 900 ºC, whereas longer sintering periods are required to achieve greater diffusion distances and hence to reach equilibrium at lower temperatures.

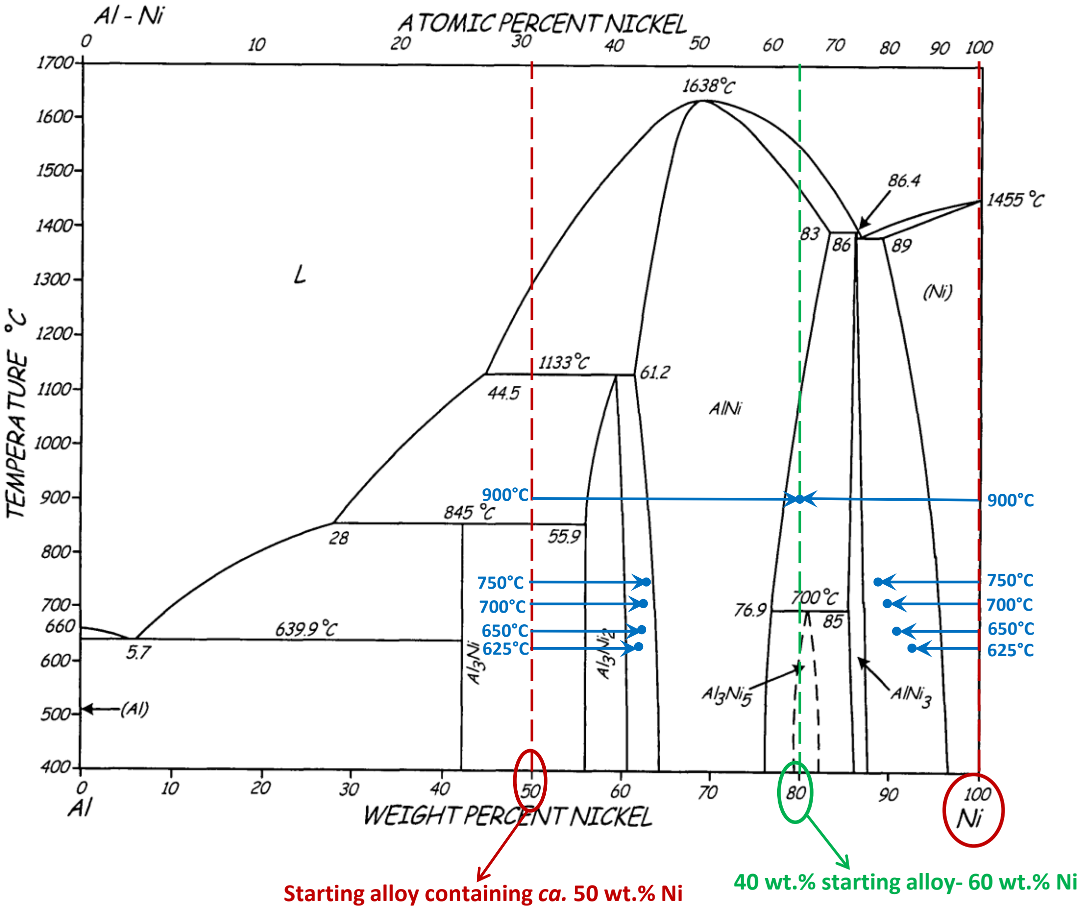

Figure 5.1. Al-Ni phase diagram modified from [145], where red circles highlight the Ni compositions of starting materials, green circle and dotted line indicate the overall Ni composition and the equilibrium line for that concentration respectively and blue dots and arrows show how far the phase compositions moved towards to equilibrium line after sintering at each temperature.

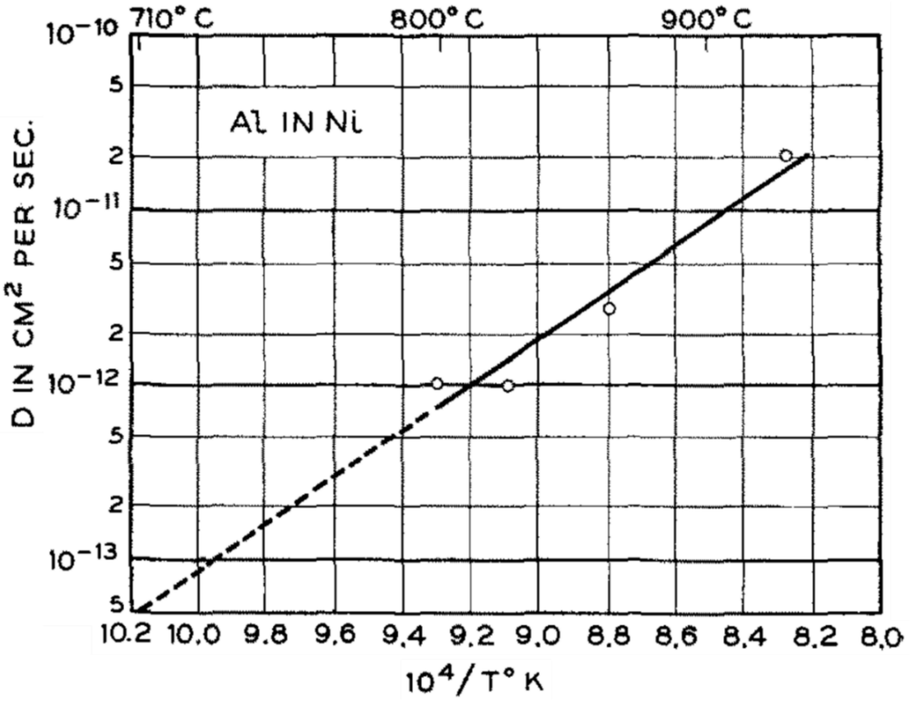

Figure 5.2. Temperature dependence (Arrhenius plot) of the diffusion coefficient of Al in Ni reported by [143]. D is the diffusion coefficient and T is the temperature.

The effect that the sintering temperature has on intermetallic phases was also reported by Chen and Lasia [105], who pressed Ni and Al powders with a weight ratio of 50:50 and sintered them at 400 and 700 ºC for 18 h in a N_2 atmosphere. Heating the electrode at 400 ºC gave similar SEM and XRD characteristics to those observed with only pressed samples consisting of two metallic components (Ni and Al). Whereas, Ni and Al disappeared and Al_3Ni, Al_3Ni_2 and AlNi intermetallic phases formed, when samples were sintered at 700 ºC. This was explained by the increased diffusion rate of Al into Ni as 700 ºC is above the melting point of Al (660 ºC). However, the presence of AlNi and unequal amounts of Al_3Ni and Al_3Ni_2 proved that the equilibrium was not achieved for the Ni composition of 50 wt.% despite the 18 h of sintering. This anomaly could be related to there being insufficient time for sintering at 700 ºC (The diffusion coefficient of Al into Ni structure is *ca.* 4.2 x 10^{-14} cm^2/s at 700 ºC [143] corresponding to a diffusion distance of 0.52 µm for the 18 h of sintering.) and the heterogeneity of their samples.

In the present work, the actual compositions of (Ni) and AlNi phases were also determined using the lattice parameters obtained from Rietveld refinement analysis (Figure 4.10). The larger lattice parameters of (Ni) phase observed at higher sintering temperatures (Figure 4.10 (a)) were due to the increased Al content, whereas the decrease in lattice parameter of AlNi phase (Figure 4.10 (b)) was a result of rise in the Ni composition. This was due to Ni atoms having a smaller atomic radius than Al atoms (The atomic radii of Ni and Al atoms are 125 and 143 pm respectively [146]). As Ni atoms are replaced by larger Al atoms cell dimensions increase, while the replacement of Al atoms with smaller Ni atoms decreases the lattice parameter. As demonstrated in Figure 5.3 (a), sintering at 625 and 650 ºC gave similar Al compositions in (Ni) phase, which was 1.0 ± 0.6 at.%. From 650 to 750 ºC, there was an increase in the Al content of (Ni) phase, with sintering at 750 ºC resulting in 5.0 ± 0.6 at.% Al in (Ni) phase. These concentrations are below the maximum Al composition in (Ni) phase which is 9.0 at.% for 625 ºC and 10.5 at.% for 750 ºC (read from Al-Ni phase diagram, Figure 5.1). As shown in Figure 5.3 (b), AlNi contained 52 ± 0.5 at.% Ni for samples sintered at 625 and 650 ºC and 54 ± 0.5 at.% Ni for samples sintered at 700 and 750 ºC. For the case of 900 ºC, the Ni composition of AlNi phase was 58 ± 0.5 at.% corresponding to $Al_{0.84}Ni_{1.16}$ phase. Based on Al-Ni phase diagram, these compositions lie within the limits of Ni composition in AlNi for each sintering temperature. The changes in the actual compositions of (Ni) and AlNi phases, also proved that the composition of samples moved closer to the equilibrium line with higher sintering temperatures.

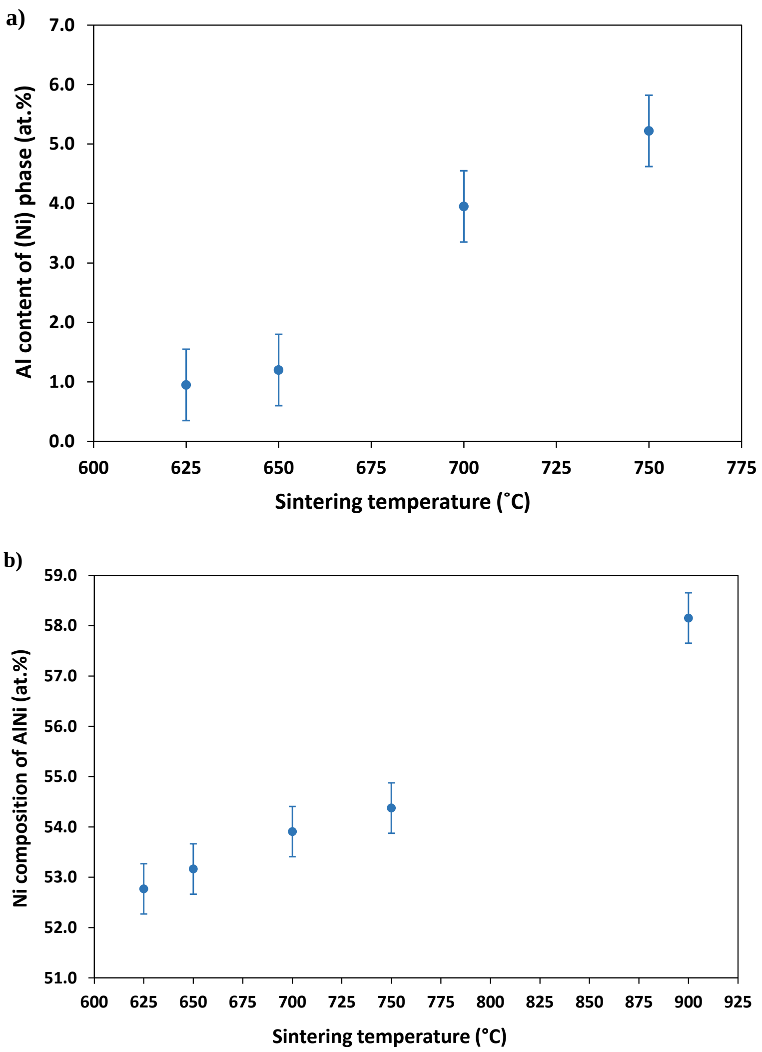

Figure 5.3. Rietveld refinement results of (a) Al content of the (Ni) phase and (b) Ni content of the AlNi phase for Ni60:Alloy40-B6.25 samples sintered at different temperatures; 625, 650, 700, 750 and 900 °C. Using the lattice parameters determined via the Rietveld refinement, Al content for the (Ni) phase was read from [147], while the Ni composition of AlNi was read from [148].

Based on the PXD analysis of intermetallic phases present before and after sintering, following idealistic schemes were proposed for the formation of the phases through the diffusion of Al;

$$Al_3Ni + Ni \rightarrow Al_3Ni_2 \qquad (5.2)$$

$$Al_3Ni_2 + Ni \rightarrow 3AlNi \qquad (5.3)$$

$$AlNi + 2Ni \rightarrow AlNi_3 \qquad (5.4)$$

The entire quantity of Al_3Ni converted into Al_3Ni_2 via Equation 5.2 regardless of the sintering temperature. As mentioned earlier, AlNi formed during the sintering process was not stoichiometric and contained a Ni composition of *ca.* 52-58 at. % based on the sintering temperature (Figure 5.3). In addition, some Al atoms substituted into Ni, creating a (Ni) phase with an Al content in the range of *ca.* 1-5 at.%. Therefore, the overall reaction for the sintering temperatures of 625 ºC (Equation 5.5) and 750 ºC (Equation 5.6) can be written as;

$$2.9Al_3Ni + 1.8Al_3Ni_2 + 19.4Ni \rightarrow 3.0Al_3Ni_2 + 4.5Al_{0.96}Ni_{1.04} + 1.0AlNi_3 + 11.4Al_{0.01}Ni_{0.99} \quad (5.5)$$

$$2.9Al_3Ni + 1.8Al_3Ni_2 + 19.4Ni \rightarrow 1.1Al_3Ni_2 + 8.7Al_{0.91}Ni_{1.09} + 2.7AlNi_3 + 6.0Al_{0.05}Ni_{0.95} \quad (5.6)$$

The stoichiometric coefficients in Equations 5.5 and 5.6 were calculated using the Rietveld refinement results for the quantities of phases present before and after sintering at 625 and 750 ºC respectively. The analysis of molar balances for Al and Ni elements showed that in Equation 5.5, the products side had 2.1 % more Al and 3.6 % less Ni than the reactant sides, whilst in Equation 5.6 the products side had 0.7 % more Al and 1.5 % less Ni than the reactant sides proving that Rietveld refinement results were sufficiently accurate to obtain the stoichiometric coefficients.

5.1.1.2. Diffusion mechanism

For the multicomponent systems containing more than one phase, the concentration gradient is recognized as the main driving force for the inter-diffusion of atoms [125]. In the present study, samples consisted of Ni and Al-rich phases (Al_3Ni and Al_3Ni_2) before sintering which favoured the inter-diffusion of Al atoms resulting in phase transformations. Whereas sintering the starting alloy powder (a mixture of Al_3Ni and Al_3Ni_2) on its own did not change the phase composition (Figure A5.1 in the present study and [101]) since it was already at thermodynamic equilibrium.

As reported in Section 4.3.1, there was no decrease in the dimensions of sample disks after sintering at 625-900 ºC for 2 h. Furthermore, the skeletal densities, specific surface areas and porosity characteristics measured with as-sintered samples at 650 and 900 ºC were similar to those observed before sintering (Figure 4.14). This demonstrated that the diffusion of atoms occurred through a non-densifying mechanism such as surface diffusion, vapour transport or lattice diffusion from the surface where the atoms are taken from the surface and rearranged onto another surface or part of the same surface without shrinking the pores [149].

SEM analysis showed the formation of interparticle necks with the samples sintered at 900 ºC, whereas the SEM-SE images of samples sintered at 625-750 ºC were similar and did not indicate any neck formation (Figure 4.4). Figure 5.4 demonstrates a two-sphere model for the particle interaction during sintering assuming the spherical particles are identical. The absence of interparticle necks with samples sintered at 625-750 ºC shows that the diffusion of atoms occurs at the adhesion stage where the particles are in contact with cohesive bonds (Figure 5.4 (a)). The compaction of the powder mixture through pressing could increase the particle contact and enable the atomic diffusion. In the case of 900 ºC, the neck-like joints were formed between some of the adjacent particles without causing densification (Figures 4.4 and A3.1). This indicated that during the non-densifying mechanism, the distance between the centres of particles remained constant as shown in Figure 5.4 (b) and penetration of particles between each other did not take place (Figure 5.4 (c)).

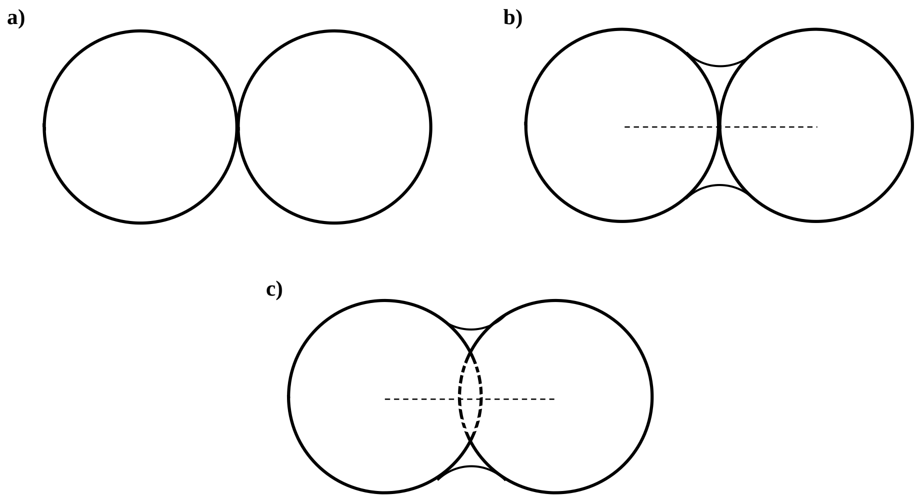

Figure 5.4. Schematic of a two-sphere model for the particle interaction during sintering, where (a) adhesion stage; (b) non-densifying neck growth; (c) densifying neck growth, reproduced from [149].

The formation of interparticle necks at 900 ºC, which was the indicator of improved sintering process, can be explained by the melting points of the phases. Sintering is usually performed at temperatures *ca.* 70 % of the absolute melting point of a material [125]. At shown in Table 5.1, all the sintering temperatures that were investigated in the present study were above the sintering temperature of Al_3Ni (*ca.* 510 ºC). However, during the heat treatment, two competing processes occurred, i.e. sintering and diffusion of Al away from Al-rich phases into Ni. As discussed before, the diffusion of Al from Al_3Ni to Ni formed Al_3Ni_2 (Equation 5.2) which sintering temperature is *ca.* 711 ºC. 625, 650 and 700 ºC are below this point, therefore sintering at these temperatures were less efficient. Although 750 ºC is greater than the sintering temperature of Al_3Ni_2, it is far below the sintering temperatures of AlNi and Ni-rich phases (Table 5.1). Since 900 ºC is greater than 70 % of the melting points of Al_3Ni, Al_3Ni_2 and $AlNi_3$ and relatively closer to that of Ni, sintering process improved at 900 ºC leading to neck formation and increased adhesion between particles.

Table 5.1. The melting points of Al-Ni phases [150].

Phase	Al_3Ni	Al_3Ni_2	AlNi	$AlNi_3$	Ni
Melting point (ºC)	845	1133	1638	1395	1455
70 % of the absolute melting point (ºC)	510	711	1065	895	937

The EDX analysis of as-sintered samples revealed a decrease in the frequency of Al-rich phases and an increase in the number of AlNi phase in the cross-section in comparison to the surface (Section 4.2.1). This indicated that the inter-diffusion of Al was less significant on the disk surface. Even trace Al_3Ni was present at the surface of samples sintered at 625-750 ºC, which was not detected by PXD most likely due to its low concentration in the bulk sample. Since particles on the disk surface had less contact points than those in the cross-section, the diffusion of Al from Al-rich phases into Ni might be less significant. In the case of sintering at 900 ºC, the frequencies of $Al_{0.84}Ni_{1.16}$ and $AlNi_3$ detected by the EDX analysis were similar for the surface and cross-section of the electrodes since equilibrium was achieved and the formation of necks may have improved the atomic diffusion between the particles.

5.1.1.3. Mechanical strength

The mechanical strength of electrodes improved when they were sintered at higher temperatures, with sintering at 900 ºC giving the most robust electrodes. This can be explained by the increase in the strength of adhesion for the inter-particle connections. In this study, metal particles, which were not spherical, already had interfaces formed from being pressed together during the powder compaction stage. Sintering process allowed these physical interfaces to diffuse together. As discussed before, increasing the sintering temperature from 625 to 900 ºC led to improved atomic diffusion and sintering resulting in stronger bonds between the inter-particles and hence an improvement in the mechanical strength.

5.1.2. Selective Leaching of Phases

Ni60:Alloy40-B6.25 samples sintered at 625-750 ºC consisted of Al_2Ni_3, AlNi, $AlNi_3$ and Ni before leaching (Figure 4.7). The PXD analysis showed that the entire quantity of Al_2Ni_3 was depleted during leaching of Al, whereas, in general, there was an increase in (Ni) phase and no remarkable change in AlNi and $AlNi_3$ (Figures 4.8 and 4.9). The EDX analysis on the surface of as-leached samples indicated the presence of (Ni) phase. Whereas the compositions for Al_2Ni_3 was no longer detected after leaching proving that Al was only leached from Al_2Ni_3. These findings are in agreement with the literature [81, 118, 151] where only the Al-rich phases of Al_3Ni and Al_2Ni_3 were reactive towards an alkaline solution. Klein and Hercules [151] investigated the surface composition of Al_3Ni, Al_2Ni_3, AlNi and $AlNi_3$ in the attempt to understand the nature of the differences in the catalytic activity. They observed that Al segregated to the surface due to its lower surface free energy in comparison to Ni. The degree of Al segregation was dependant on the bulk composition and rose as the bulk Al concentration increased. For example, the surface of $AlNi_3$ contains *ca.* 20 % less Ni than the bulk, whereas the surface Ni concentration is *ca.* 50 % less than the bulk Ni concentration for Al_3Ni. These findings were also in agreement with a study by Giuranno *et al.* [152] who reported a decrease in the surface energy with increasing Al compositions following an investigation in the surface tension of Al-Ni alloys. The reactivity of Al-rich phases towards alkaline solutions was attributed to reduced chemical stability in the alkaline solution due to the increase in the Al surface segregation.

For the samples sintered at 900 ºC, there was no phase transformation after the leaching process (Figure 4.9) because the phases present in these samples, i.e. $Al_{0.84}Ni_{1.16}$ and $AlNi_3$ were not leachable. These findings are in agreement with an earlier study by Tanaka *et al.* [118] who did not observe Al leaching from AlNi and $AlNi_3$ phases in concentrated alkaline solutions.

SEM analysis of alloy particles showed that they preserved their basic microstructures after leaching regardless of the sintering temperature (Figures 4.5 and A4.2). In addition, the leaching solutions analysed through the ICP-MS technique did not show an increase in the Ni content of the alkaline solution after the completion of leaching process (Table A6.1 in Appendix A6). The quantity of Al dissolved in the solution was in agreement with the compositional analysis results of the remaining sample considering the initial Al content (Table A6.2). For instance, during leaching of a Ni60:Alloy40-B6.25 sample sintered at 650 ºC, *ca.* 262 mg Al was dissolved based on the ICP-MS analysis corresponding to a remaining Al content of *ca.* 11.8 wt.% which lay within the concentration range of 12.1 ± 0.5 wt.% measured by the ICP-OES for the as-leached sample. This proved that only Al was selectively dissolved during leaching of Al_2Ni_3 retaining the basic microstructure of the precursor alloy. Bakker *et al.* [153] also reported a selective dissolution mechanism for leaching of Al_2Ni_3, where the detailed microstructure of the parent alloy was preserved.

From the Rietveld refinement results (Figure 4.9), the quantity of Ni content in Al_2Ni_3 before leaching was compared to the increase in the amount of Ni in samples after leaching. As demonstrated in Figure 5.5, the increase in the weight of Ni after leaching was similar to the Ni content in Al_3Ni_2 before leaching of samples sintered up to 750 ºC. This showed that leaching of Al_3Ni_2 only produced a (Ni) structure. Based on these findings the leaching reaction was;

$$Al_3Ni_{2(s)} + 6OH^-_{(aq)} + 6H_2O_{(l)} \rightarrow 3Al(OH)_4^-{}_{(aq)} + 3H_{2(g)} + 2Ni_{(s)} \qquad (5.7)$$

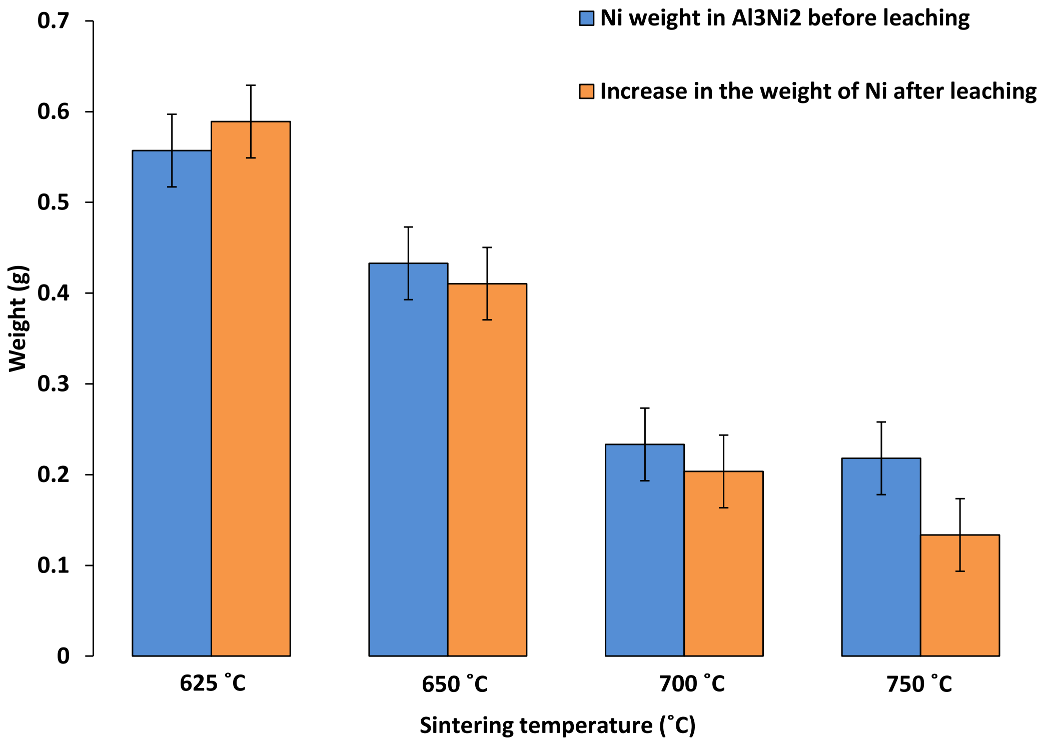

Figure 5.5. Rietveld refinement results for the comparison of Ni weight in Al_3Ni_2 before leaching to the increase in the weight of the Ni after leaching Ni60:Alloy40-B6.25 samples sintered at different sintering temperatures; 625, 650, 700 and 750 °C.

XRD analysis results from earlier studies [97, 100, 118] also revealed that complete leaching of Al_3Ni and Al_2Ni_3 only yielded (Ni) phase. The resultant Ni peaks were broadened which could indicate a nanostructured surface layer with a small crystallite size as well as lattice defects or internal stress [100]. A single broad Ni peak was reported by Rami and Lasia [101] and Chen and Lasia [105] after leaching a mixture of Al_3Ni and Al_2Ni_3 which was attributed to the formation of an amorphous structure. In the present study, PXD patterns of as-leached samples did not indicate broadened Ni peaks, although leaching of starting alloy powder consisting of only Al_3Ni and Al_2Ni_3 resulted in broad Ni peaks (Figures A5.1 (c) and A5.2 in Appendix 5). This was due to the (Ni) phase that was present in as-leached samples being mostly sourced from precursor Ni 255. The weight ratios of Ni 255 to the (Ni) phase created after leaching of

Al_2Ni_3 were ca. 3:1, 4:1, 9:1 and 11:1 for the samples sintered at 625, 650, 700 and 750 ºC respectively.

The influence of detailed micro- and nano-structural properties of precursor alloys on the leaching mechanism is not yet clear. In this study, some Al_2Ni_3 was originated during sintering through the diffusion of Al from the Al_3Ni particles present in the starting alloy (Equation 5.2) and it is not known whether this has any impact on the leaching characteristics of this phase. Bakker *et al.* [153] examined the concentration profile during the leaching of Al_2Ni_3 and observed that some Al_2Ni_3 leached more readily than the rest. They suggested that this phenomenon could be explained through detailed microstructural analysis of the precursor intermetallic phases. However, the analysis techniques were not available to them to investigate the fine structure.

5.1.3. Leaching Efficiency

An increase in un-leached Al content was observed for samples sintered at progressively higher temperatures (Figure 4.11). Figure 5.6 demonstrates the effect of sintering temperature on the concentration of Al_2Ni_3 remaining after sintering and the efficiency of Al removal (calculated from the ICP-OES results based on the reduction in the overall Al content after leaching). The increase in sintering temperature which led to a decrease in the leaching efficiency closely correlated to the amount of available Al_2Ni_3. This was due to Al_2Ni_3 being the only leachable phase present in as-sintered samples. As a result, the amount of Al removed during leaching depended on the concentration of Al_2Ni_3 that remained after sintering.

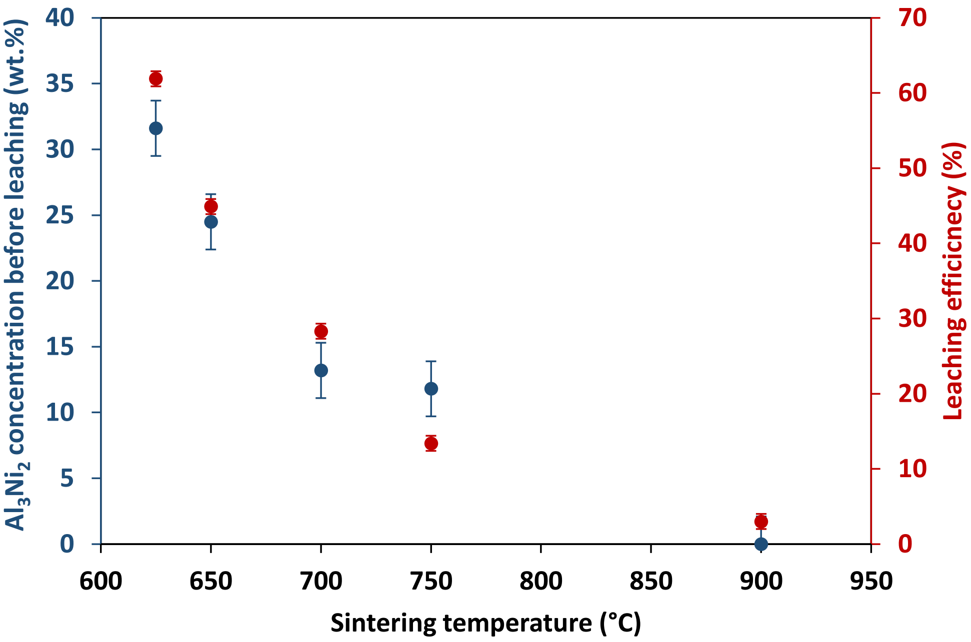

Figure 5.6. The correlation between the Al_3Ni_2 concentrations of as-sintered Ni60:Alloy40-B6.25 samples (from Rietveld refinement results) and the Al leaching efficiency with respect to the sintering temperature. The leaching efficiencies are calculated from the ICP-OES results based on the reduction in the overall Al content after leaching.

The EDX analysis revealed that the Al concentration of as-leached samples was higher in the cross-section than that on the surface (Figure 4.12). Micro-CT analysis for the cross-section of an as-leached sample disk also indicated that Ni concentration was greatest on the surface and decreased towards the middle of the samples (Figures 4.66 and 4.67). Since Al_3Ni_2 was depleted on both surface and cross-section, it demonstrated that the leaching solution was able to penetrate through the samples cross-section. Birry and Lasia [97] reported a leaching length of *ca.* 1.50 mm based on the cross-section view of as-leached samples. In the present study, the total thickness of sample disks was *ca.* 1.50 mm corresponding to a leaching length of 0.75 mm from each surface towards the middle. The concentration difference between the surface and cross-section of as-leached samples could rather be explained by the variations in phase compositions. As reported in Section 4.2.1, after sintering, the surface mostly contained alloys with Al-rich compositions, whereas an increase in the frequency of AlNi, an unleachable phase, was observed in the cross-section. Therefore, the amount of (Ni) phase formed on the surface during leaching of Al was greater than that in the cross-section.

EDX analysis of as-leached alloy particles also indicated that the (Ni) phase formed after leaching of Al_3Ni_2 phase contained an Al content with varying concentrations up to *ca.* 10.0 wt.%. These findings are in agreement with the literature [85, 94, 97, 154] where Al compositions in the range of 3.3-8.0 wt.% were reported for the (Ni) phase created by leaching of Al_3Ni and/or Al_2Ni_3. Some researchers suggested alumina, which may form during leaching, might have precipitated on the (Ni) structure [84, 102]. However, aluminates have a tendency to hydrolyse, if the pH falls. In the present study, an excess of concentrated alkaline solution was used and there was no evidence of alumina in as-leached samples. The Al content in (Ni) phase could rather be explained by the leaching mechanism. Choquette and Brossard [94], who investigated the change in the composition of phases with respect to the leaching duration, showed that leaching of Al from Al_3Ni_2 formed (Ni) phase without the formation of AlNi and $AlNi_3$. The Al content in (Ni) phase, however, cannot be leached away as Al can only be leached from Al-rich phases.

Based on the EDX analysis of as-sintered samples (Section 4.2.1), some particles had an Al:Ni ratio within the range of 49:51-55:45 corresponding to Al_3Ni_2-AlNi binary region in the phase diagram (Figure 5.1). Due to incomplete Al diffusion during sintering some particles might consist of both intermetallic phases. As demonstrated in Figure 5.7, upon contact with the leaching solution Al_3Ni_2 could be leached, while AlNi remains in the structure. The resultant structure would then contain a mixture of (Ni) and AlNi phases.

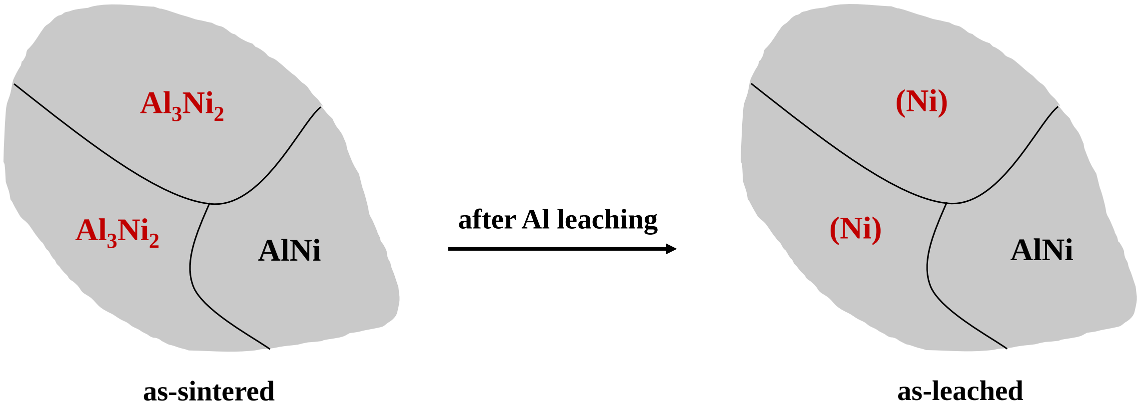

Figure 5.7. Schematic of a compositional change during leaching of a hypothetical particle consisting of Al_3Ni_2 and AlNi before leaching.

5.1.4. Change in the Porosity Characteristics

As reported in Section 4.2.3, N_2 sorption results proved that leaching of Al_3Ni_2, the only leachable phase in as-sintered samples, created microporosity as well as mesopores with sizes in the range of *ca.* 2-12 nm (Figures 4.13 and 4.15). Tanaka *et al.* [118] also reported pores with sizes of *ca.* 1-10 nm from leaching of a Al_3Ni_2 precursor alloy, whereas leaching Al_3Ni resulted in pores with sizes less than 3 nm.

In the present study, the quantity of micro- and mesopores in as-leached samples was found to be dependent on the amount of Al_3Ni_2 remaining after sintering. As the sintering temperature increased from 625 to 750 ºC, samples contained *ca.* 63 % less Al_3Ni_2 resulting in *ca.* 4 times less specific surface area formed during the leaching process (Figures 4.9 and 4.13). The porosity characteristics of as-leached samples sintered at 900 ºC was similar to that before leaching, since these samples consisted of unleachable phases; $Al_{0.84}Ni_{1.16}$ and $AlNi_3$.

The specific surface area of as-leached samples varied between 1.2 m^2/g for 900 ºC and 11.5 m^2/g for 625 ºC (Figure 4.16). Normalizing the specific surface area and porosity data to the mass of Al_3Ni_2, the average surface area and pore volume created by leaching of Al_3Ni_2 was calculated to be 38 ± 7 m^2 and 0.07 ± 0.02 cm^3 per gram of

Al_3Ni_2 respectively. The resultant specific surface area and pore volume per gram of Ni formed during leaching were 70 ± 20 m^2 and 0.13 ± 0.04 cm^3 respectively. Earlier studies reported surface areas typically in the range of 50-100 m^2/g and pore volumes in the range of 0.04-0.14 cm^3/g depending on precursor alloy composition and leaching conditions [84, 85, 153, 155]. In this study, the variations in the surface area and pore volume could be explained by the reproducibility of leaching process as well as errors related to measurement techniques. Foulliux [82] emphasized the difficulty of creating reproducible surface areas even if the same starting alloy is used each time. In order to achieve rigorously similar surface areas, the preparation of a master batch was recommended from which individual samples could be collected as required for hydrogenation, although this method would not be convenient for all applications.

He pycnometer and MIP results showed that the total porosity of as-leached samples was *ca.* 60 % regardless of the sintering temperature. The porosity was predominantly due to macroporosity which specific volume was one order of magnitude greater than that of total micro- and mesopores. As demonstrated in Figure 4.14, the sintering process did not influence the porosity significantly proving that it was non-densifying. Since the composition of starting powder mixture and packing conditions were not altered, samples had a similar specific macropore volume (*ca.* 0.24 cm^3/g) regardless of the sintering temperature which dominated the total porosity.

The volume of closed pores was also unaffected by the sintering temperature (Figure 4.16). This was due to the fact that all samples were prepared from the same metal composition of 60 wt.% Ni-40 wt.% starting alloy and the sintering mechanism was non-densifying.

5.1.5. Electrochemical Performance

As shown in Figure 4.18, sintering at 900 ºC resulted in the lowest electrochemical performance while samples sintered below 750 ºC had the best performance. The electrode sintered at 900 ºC led to a *ca.* 10 % higher cell voltage at 1 A/cm^2 compared to that sintered at 625 ºC. As explained in Section 2.2.1, the cell overpotential is the sum of different overpotentials including anodic and cathodic activation overpotentials, ohmic drop, and concentration overpotential (Equation 2.5). Since the properties of electrolyte solution, membrane and anode were kept constant, the variation in the cell voltage must have been due to the change in the characteristics of the cathode material.

Figure 5.8 demonstrates the cell voltage difference between the cathodes sintered at 650 and 900 ºC with respect to the current density, where 900 ºC gives higher cell voltages. Up to *ca.* 0.3 A/cm^2 the % difference between cell voltages showed a logarithmic growth with rising current densities, where the growth was rapid at the beginning followed by a slower increase. Beyond 0.3 A/cm^2 the difference remained almost constant regardless of the current density. This correlated well with the behaviour of the activation overpotential between the cathode/electrolyte interfaces, which relates to the current density through a logarithmic function (Equation 2.8). As reported in Section 2.2.1.1, the activation overpotential is highly dependent on the electrocatalytic properties and surface characteristics of the electrode material.

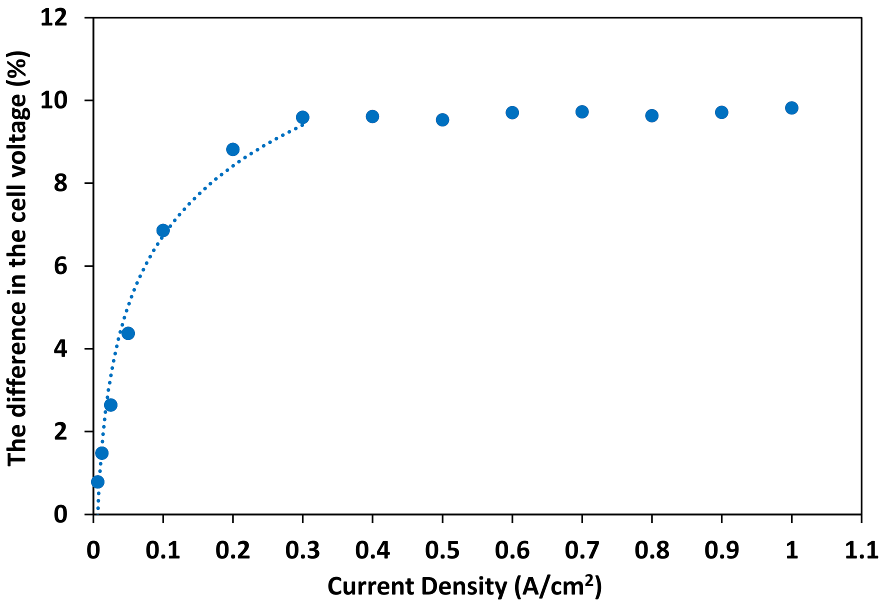

Figure 5.8. Difference in the cell voltages for as-leached Ni60:Alloy40-B6.25 cathodes sintered at 650 and 900 °C, where the cathode sintered at 900 °C gave higher cell voltages.

Figure 5.9 demonstrates the trends in the electrolyser cell voltage and compositional properties of the electrode material with respect to the sintering temperature. Since the operation at the high current densities are desirable for industrial applications to achieve sufficient hydrogen generation rates, the cell voltage measured at 1 A/cm^2 was chosen to compare the performance of different electrodes. As shown in Figure 5.9 (a) the concentration of (Ni) phase decreases from *ca.* 59 wt.% to 0 wt.% as the sintering temperature increased from 625 to 900 °C, whilst the cell voltage increased almost linearly with higher sintering temperatures. This implies an inverse correlation between the cell voltage and (Ni) concentration. Although there was no (Ni) phase in samples sintered at 900 °C, they still showed electrochemical performance. In general, there was an upward trend in the AlNi concentration with higher sintering temperatures where the increase was almost linear. This indicates a direct relationship between the trends in the AlNi content and cell voltage. Whereas there was no direct correlation between the $AlNi_3$ content and the cell voltages as the change in the $AlNi_3$ concentration did not follow a certain trend.

As shown in Figure 5.9 (b) the bulk Al concentration showed an upward trend with higher sintering temperatures up to 750 ºC where the increase in bulk Al content was less significant from 750 to 900 ºC. Surface Al content increased almost linearly apart from the concentration measured at 625 ºC. These findings imply a direct correlation between the trends in the Al content and electrolyser cell voltages, with the surface Al content giving a better correlation than the bulk concentration.

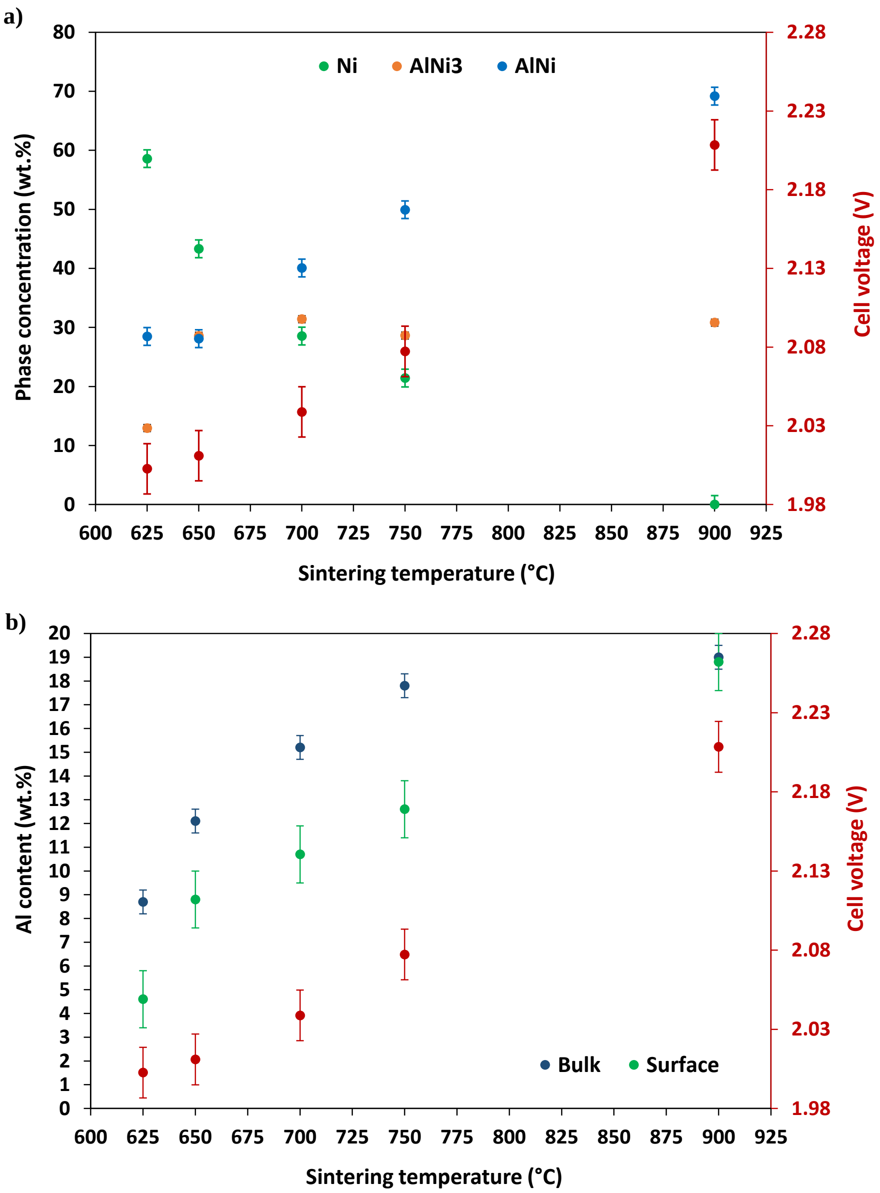

Figure 5.9. The correlation between the cell voltages measured at 1 A/cm^2 and compositional properties of Ni60:Alloy40-B6.25 cathodes sintered at different temperatures, where (a) the concentration of different phases (wt.%); (Ni), AlNi$_3$ and AlNi calculated by Rietveld refinement analysis; (b) bulk and surface Al contents (wt.%). Bulk and surface Al contents were measured by ICP-OES and EDX analysis respectively.

Electrocatalytic performance cannot be explained by only the differences in the composition properties of the electrodes. A rise in the specific surface area available for the reaction should lead to an increase in the exchange current density and reduce the cathodic activation overpotential (Equation 2.8) resulting in a lower cell voltage but generating the same amount of H_2. The correlation between the electrocatalytic activity and change in the pore area of the electrodes is demonstrated in Figure 5.10. The micropore area reduced as the sintering temperature rose, whilst the cell voltage increased almost linearly with increasing sintering temperatures. In general, the total surface area of meso- and macropores had a decreasing trend with higher sintering temperatures mainly due to the reduction in the mesopores created during leaching of Al from Al_3Ni_2 remaining after sintering. The correlation between trends in pore area and cell voltage indicates that cell voltage is inversely proportional to the areas of micropores and other pores, with the former being more significant. Since the micropores accounted for *ca.* 80 % of the total area regardless of the sintering temperature, they have the most significant effect on the specific surface area. Therefore, the change in the total surface area with respect to sintering temperature follows the trend in the micropore area.

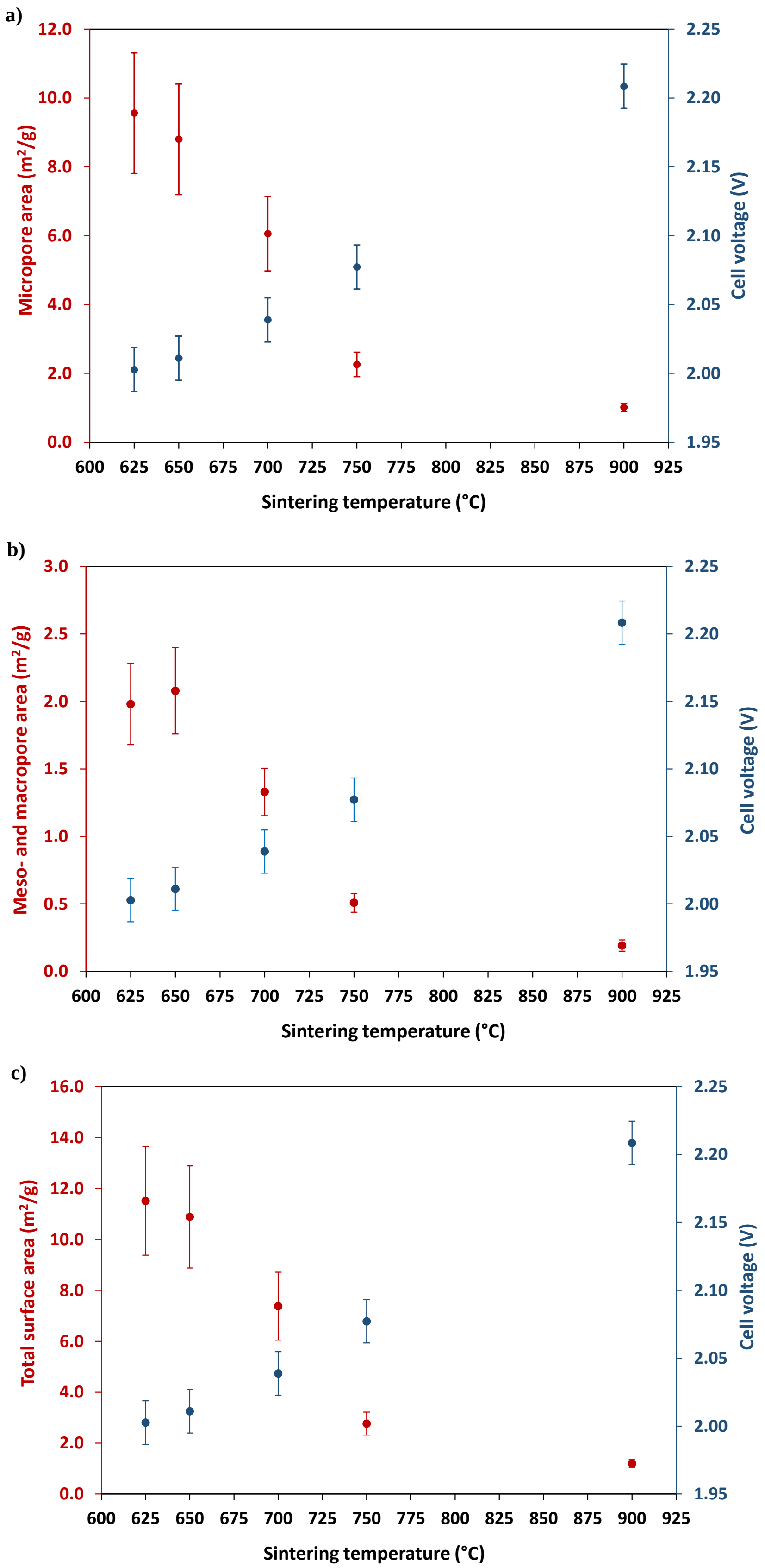

Figure 5.10. The correlation between the cell voltages measured at 1 A/cm^2 and porosity characteristics of cathodes sintered at different temperatures, where (a) micropore area; (b) meso- and macropore area and (c) total surface area. The micropore area was calculated by the DA model and subtracted from the BET surface area to estimate the area of other pores.

5.2. The Effect of Starting Alloy Concentration

Initially, samples were only prepared from the starting alloy powder (consisting of Al_3Ni and Al_3Ni_2 with an overall Ni composition of 50 wt.%) without addition of Ni powder. However, the resultant sample disks were extremely fragile and it was not feasible to test them in an alkaline electrolyser cell. In addition, the starting alloy costs almost 2 times more than Ni [156] hindering the benefit of low cost Ni catalysts. Therefore, the effect of starting alloy concentration has been investigated to correlate the electrochemical performance with the change in textural and compositional properties with a view to establishing a concentration range that would offer a relatively lower cost and more robust catalysts without compromising too much the performance characteristics.

5.2.1. Porosity Characteristics

Micro- and mesoporosity

As the starting alloy concentration increased from 0 to 60 wt. %, there was an upward trend in the micro- and mesoporosity (Figures 4.24). Using 60 wt.% starting alloy increased the specific surface area by *ca.* 3 times in comparison to 10 wt.% starting alloy concentration. This was due to the increase in the amount of Al_3Ni_2, only leachable phase remaining after sintering of samples, with higher starting alloy concentrations. As discussed earlier, leaching of Al from Al_3Ni_2 created micro- and mesoporosity with the latter being in the range of *ca.* 2-12 nm, whilst for samples prepared by only pressing and sintering Ni, the mesoporosity was negligible and the micropore area was *ca.* 5 times less than that of as-leached samples prepared using 10 wt. % starting alloy concentration.

The less significant increase in the micro- and mesoporosity results from 40 to 60 wt.% starting alloy concentrations could be explained by the relatively large margin of error (± 15 %) associated to reproducibility of leaching process as well as errors related to N_2 sorption analysis. The expected change in micro- and mesoporosity from 40 to 60 wt.% starting alloy concentration was within the experimental errors.

Macroporosity

A linear increase in the specific macropore volume was observed as the starting alloy concentration increased from 0 to 60 wt.%, with the 60 wt.% starting alloy giving an almost 2 times higher specific macropore volume than 100 wt. % Ni (Figure 4.24), which was also confirmed by SEM images (Figure 4.19). This can be explained by the difference in the compressibility characteristics of the starting alloy and Ni 255 powders. Compressibility, which is a measure of how much a powder can be densified under an external pressure, depends on;

- inherent hardness of the metal or alloy of interest,
- particles shape and size distribution,
- internal porosity,
- presence of non-metallics,
- addition of alloying elements or binders [149].

The thickness and hence volume of as-pressed samples increased as the starting alloy:Ni weight ratio rose (Figure 4.26), although the compaction (pressing) conditions, the total weight of powder mixture and binder properties were not altered. The volume of electrode disk increased by *ca.* 46 % from 0 to 60 wt.% alloy concentration. The increased volume is partially due to Ni having two times greater skeletal density than the starting alloy, i.e. a mixture of Al_3Ni and Al_3Ni_2 intermetallic phases. The main cause of the increase in disk volumes was due to an increase in the open and closed pores with the former being more significant (Figure 4.26). This showed that the compressibility of Ni 255 powder was greater than that of the starting alloy powder.

As shown in Figure 4.2, Ni 255 has a highly porous and three-dimensional chain-like structure with a greater portion of open pores and interparticles voids in comparison to the starting alloy powder. The comparison of SEM-SE images of Ni 255 powder (Figure 4.2 (a) and (b)) and as-pressed Ni (Figure 4.19 (a)) proved that during the powder compaction Ni lost a great deal of its open pores and interparticles voids resulting in a denser structure than that of the starting alloy. Therefore, a better compressibility was observed with Ni 255 powder in comparison to starting alloy powder and consequently the mechanical strength of samples decreased as the starting alloy concentration increased.

The increase in the volume of closed pores with higher starting alloy concentrations also showed that the inter-particle voids in the alloy powder may be tending to become non-interconnected during compaction more readily than that of the Ni 255 powder and this is probably due to the shape and size of its particles.

5.2.2. Electrochemical Performance

Increasing the starting alloy concentration from 0 to 60 wt. % resulted in a downward trend in the electrolyser cell voltage (Figures 4.28 and 4.29). Using starting alloy to Ni weight ratios of 10:90, 20:80, 40:60 and 60:40 decreased the cell voltage at 1 A/cm^2 by *ca.* 2.5, 5, 7.2 and 7.9 % respectively in comparison to using a Ni cathode prepared by pressing only Ni powder and sintering it at 650 ºC. Figure 5.11 demonstrates the correlation between the electrolyser cell voltages measured at 1 A/cm^2 and compositional properties of the electrode material:

- The $AlNi_3$ concentration had an upward trend up to 40 wt.% starting alloy concentration above which it decreased. There was no direct correlation between the trends in $AlNi_3$ content and cell voltage.
- The AlNi content showed a linear increase with higher starting alloy concentrations. This indicates an inverse correlation between cell voltage and AlNi concentration in the cathode samples.
- The [Ni] concentration had a downward trend with higher starting alloy contents similar to that observed in the cell voltage.
- Bulk and surface Al concentrations increased linearly as the starting alloy concentration increased, whilst the cell voltage had a downward trend implying an inverse relationship between Al content and cell voltage.

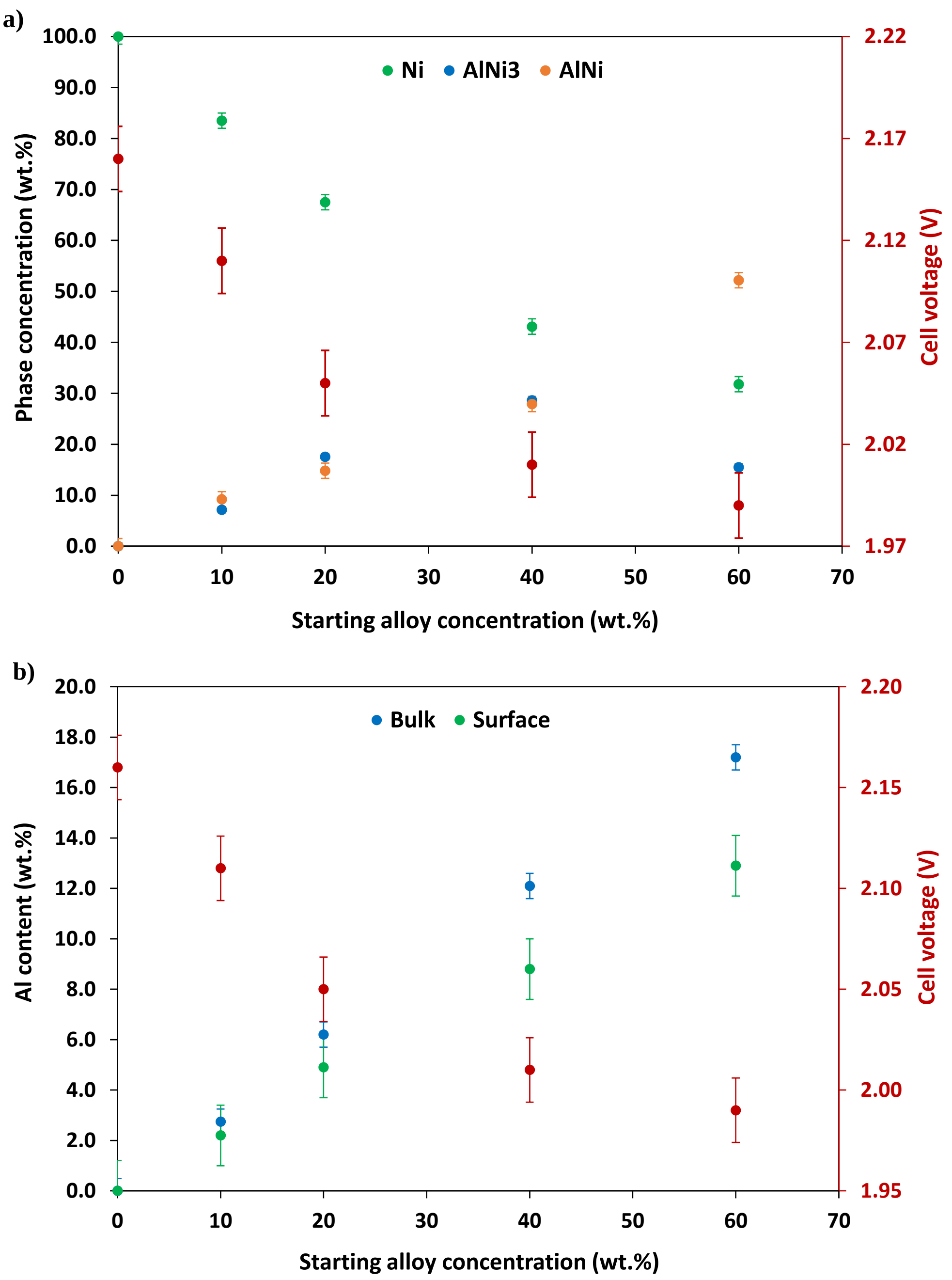

Figure 5.11. The correlation between the cell voltages measured at 1 A/cm^2 and compositional properties of cathodes prepared from different starting alloy concentrations, where (a) the concentration of different phases (wt.%); Ni, AlNi$_3$ and AlNi calculated by Rietveld refinement analysis; (b) bulk and surface Al contents (wt.%). Bulk and surface Al contents were measured by ICP-OES and EDX analysis respectively.

Figure 5.12 demonstrates the relationship between the specific surface area and the cell voltage measured using cathodes prepared from different starting alloy concentrations. The specific area of pores had a upward trend as the starting alloy concentration rose, with the increase from 40 to 60 wt.% starting alloy concentration having a less significant effect on the pore area than others. As discussed before, this was due to the difficulty to create reproducible surface areas during leaching of different batches. However, the greater surface area expected from the 60 wt.% starting alloy concentration lies within the margin of error (± 15 %) indicating that the trend in pore area increased almost linearly with the starting alloy concentration. Similar to findings reported in 5.1.5, there was a good inverse relationship between the cell voltage and specific surface area.

However, the relationship between the trends in the cell voltage and compositional properties reported for the effect of starting alloy ratio contradicts the correlations reported in Section 5.1.5 for the effect of sintering temperature where the cell voltage had a positive correlation with the trends in AlNi, bulk and surface Al contents and an inverse correlation with the change in Ni concentration. The inconsistency in the correlations between the trends in cell voltage and compositional properties could be explained by the influence of surface area. Increasing the sintering temperature resulted in decreasing trends in both overall Ni composition and surface area, whilst the increase in the starting alloy concentration decreased the overall Ni content and increased the surface area. Despite greater Al contents, the electrolyser cell voltage still decreases with increasing surface areas showing that the surface area has a dominant effect on the electrocatalytic activity in comparison to the compositional properties of Ni-based electrodes. This was also confirmed by the comparison of the cell voltages measured using the electrode sintered at 900 ºC, which consisted of $Al_{0.84}Ni_{1.16}$ and $AlNi_3$, and a Ni cathode prepared by pressing only Ni powder and sintering it at 650 ºC. Although the electrode sintered at 900 ºC had an overall Al content of *ca.* 20 wt.%, it gave a similar electrochemical performance to that of the Ni electrode. N_2 sorption analysis showed that both electrodes had a specific surface area of 1.0 ± 0.1 m^2/g. These findings are in agreement with an earlier study by Tanaka *et al.* [118] who observed similar electrochemical activities towards the HER with the electrodes consisting of only AlNi or $AlNi_3$ to that of a Ni electrode. Despite having a compositional difference, the AlNi, $AlNi_3$ and Ni electrodes gave similar overpotentials at the same current densities, which was attributed to the similar surface areas observed with all three electrodes.

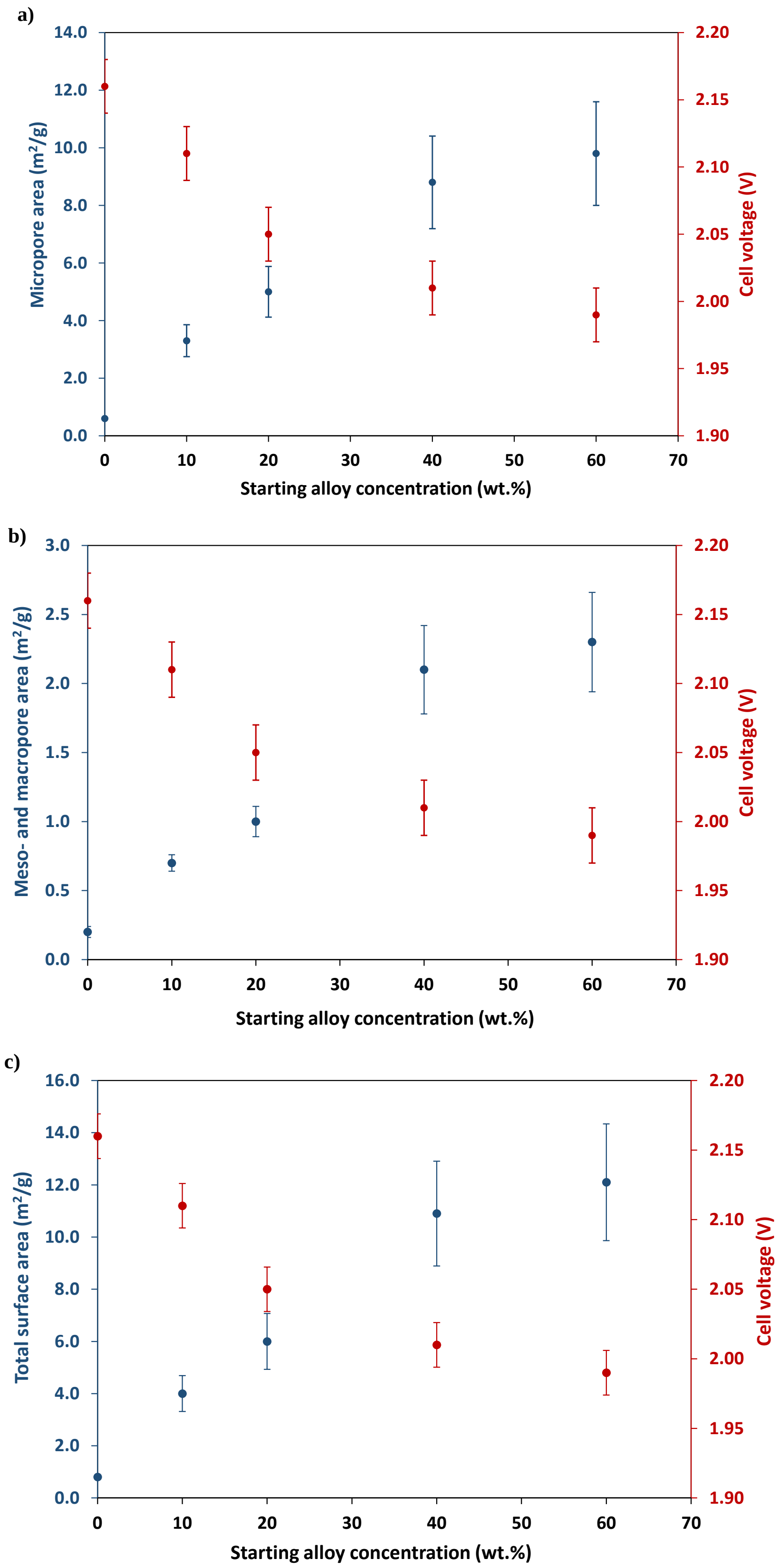

Figure 5.12. The correlation between the cell voltages measured at 1 A/cm^2 and porosity characterictics of cathodes prepared from different starting alloy concentrations, where (a) micropore area; (b) meso- and macropore area and (c) total surface area. The micropore area was calculated by the DA model and subtracted from the BET surface area to estimate the area of other pores.

It must also be noted that the mechanical strength of electrodes decreased significantly with greater starting alloy concentrations despite an improvement in the electrochemical performance. In addition, the starting alloy is more expensive than Ni hindering the benefits of cost-effective Ni catalysts. Therefore, there was a trade-off between the increase in the surface area through greater concentrations of starting alloy in order to achieve better electrocatalytic activity and the robustness and cost of the Ni-based catalysts. It is suggested that the starting alloy concentration should be in the range of 20-40 wt.% in order to achieve relatively robust and inexpensive catalysts without compromising too much electrochemical performance of the porous Ni catalysts.

Lastly, the thickness of the electrode disks increased as the starting alloy concentration increased, with the 60 wt.% starting alloy giving *ca.* 32 % greater thickness than the 10 wt.% starting alloy. In order to investigate the effect of thickness on the electrochemical performance, the electrolyser cell voltages were measured for three cathodes prepared using the same formula, i.e. 10 wt.% starting alloy-90 wt.% Ni with three different thicknesses, i.e. 1.23, 1.47 and 1.82 mm obtained by changing the total amount of starting materials (Figure 4.30). Regardless of the change in thickness, the cell voltages were similar for these three electrodes implying that the cell voltage does not correlate with the increase in the quantity of the material and that the surface nature of the electrode plays a more significant role in electrochemical performance than the bulk properties. This also proved that the change in the cell voltage with respect to starting alloy concentration was not influenced by the variations in the electrode thickness. It is suggested that an optimum quantity of catalyst, which would still give a sufficient mechanical strength while minimizing the material use, should be identified in order to reduce the material cost as well as decreasing the thickness of electrodes, both of which would be beneficial to large scale applications.

5.3. The Effect of Leaching Temperature

5.3.1. Bubble Formation during Leaching

Visual examinations indicated that the rate of leaching reaction (Equation 5.7) increased as the leaching temperature rose from 30 to 80 ºC. Consequently, the H_2 evolution became more vigorous resulting in an increased bubble release rate at higher temperatures. After 18 h of leaching, there was no further release of H_2 bubbles regardless of the leaching temperature. After leaching completed, samples leached at low temperatures (< 50 ºC) had greater numbers of H_2 gas bubbles that stayed attached to their surfaces which were also larger in size compared to those observed at higher leaching temperatures based on casual observations.

The growth and detachment of bubbles generated on a solid surface depend on a balance of forces acting on it which can either favour or oppose the bubble detachment [157, 158]. Bubbles formed during the leaching reaction detach from the solid surface once they reach a critical size. Wallis [159] predicted the detachment diameter of a spherical bubble in an open water pool when the gas is injected through an orifice by the equation below;

$$d_b = 2\left[\frac{\gamma . R_0}{g.(\rho_L - \rho_G)}\right]^{1/3} \tag{5.8}$$

where γ is the liquid surface tension, R_0 is the radius of the gas nozzle, g is the acceleration due to gravity and ρ_L and ρ_G are the densities of liquid and gas respectively. When the leaching temperature increases, both surface tension and density of leaching solution reduce resulting in a decrease in the detachment diameter for the H_2 bubbles. At lower temperatures, bubbles have to grow greater in size in order to detach from the electrode surface which explains why the bubbles that stay attached on the sample surface were greater in size when leaching was carried out at lower temperatures (30 and 50 ºC).

As the leaching temperature increased and the liquid surface tension decreased, the surface tension force, which opposes the detachment [157], was also reduced enabling the bubbles to detach from the surface more easily. This explains why the quantity of bubbles that stays attached to the electrode surface was more significant with lower leaching temperatures.

5.3.2. Compositional Change

The PXD, EDX and Rietveld refinement results showed that the entire quantity of Al_2Ni_3 was depleted during leaching of Al and samples consisted of similar concentrations of AlNi, $AlNi_3$ and Ni after leaching at 30, 50, 60, 70 and 80 ºC (Figures 4.31 and 4.32). Since all samples were prepared from the same metal composition (60 wt.% Ni-40 wt.% starting alloy) and sintering conditions were same, the amount of Al_3Ni_2 remaining after sintering was similar for all samples. The resultant overall Al content was *ca.* 13 wt.% regardless of the leaching temperature (Figure 4.33).

5.3.3. Change in the Porosity Characteristics

Micro- and mesoporosity

Increasing the leaching temperature from 30 to 60 °C improved the specific surface area by almost 4 times through a significant increase in the micro- and mesoporosity (Figure 4.36), whereas 60, 70 and 80 ºC gave similar surface areas, which was 65 ± 2 m^2 per gram of Ni created during leaching. Corresponding pore volumes per gram of Ni formed were *ca.* 0.03 and 0.05 cm^3 for samples leached at 30 and 50 ºC respectively, whilst leaching at higher temperatures gave a pore volume of

0.12 ± 0.02 cm^3/g. The leaching temperature also influenced the mesopore size range, with higher temperatures giving a wider size range. The mesopore size ranges were *ca.* 2.0-6.0 nm and *ca.* 2.0-14.0 nm for samples leached at 30 and 80 ºC respectively. These findings were in agreement with an earlier study by Freel *et al.* [155] who also observed a change in the pore geometry with respect to the leaching temperature. They reported an average pore diameter of 2.5 nm and a pore volume of *ca.* 0.06 cm^3/g for the samples leached at 50 ºC, whilst samples leached at 108 ºC gave a pore diameter of *ca.* 9.6 nm and a pore volume of *ca.* 0.14 cm^3/g.

In addition, N_2 sorption isotherms showed a dependence on the leaching temperature (Figure 4.35) where the shapes of hysteresis loops are often attributed to the presence of specific pore structures (Figure 4.35). Based on the IUPAC classifications for the hysteresis loops (Figure 3.4), leaching at 30 and 50 ºC led to slit-shaped pores, whereas leaching temperatures of 60, 70 and 80 ºC resulted in ink-bottle pores, i.e. narrow pore throats opening to large pore bodies.

Since all samples had similar Al_3Ni_2 concentrations after sintering and the entire quantity of Al_3Ni_2 was consumed during Al leaching, the changes observed in the specific surface area, pore volume and shape with respect to the leaching temperature cannot be related to the leaching efficiency. Rather, it can be attributed to the leaching dynamics that occur at different temperatures. As mentioned earlier, increasing the temperature gave considerably faster leaching reactions compared to those observed at lower temperatures. Consequently, the more intensive alkaline attack might facilitate a drilling effect and create pores similar to the sideway pits observed with pitting corrosion (demonstrated in Figure 2.10 in Section 2.7.2). Whereas at lower leaching temperatures, the less significant alkaline attack might result in narrow through pores which depth might be relatively shallow. This could be explained by the relative speed of atomic rearrangement at the surface in comparison to the rate of Al leaching reaction. As discussed earlier, in Ni-Al intermetallic phases, Al diffuses to the surface due to its lower surface free energy in comparison to Ni. As Al is leached at the surface level, Al will diffuse to the leaching zone in order to reduce the surface energy. If the leaching rate is relatively lower, Al may diffuse to the leaching zones creating pores, whilst faster leaching reactions may drill into the matrix to reach Al, leading to the formation of the cavities of the ink-bottles.

Macroporosity

Leaching temperature did not have any influence on the macroporosity, since leaching of Al did not create macropores and all samples were prepared from the same metal composition (60 wt.% Ni-40 wt.% starting alloy) using the same binder properties and pressing conditions.

5.3.4. Electrochemical Performance

Increasing the leaching temperature from 30 to 80 ºC did not change the electrolyser cell voltage significantly despite the increase in the micro- and mesopore area from 30 to 60 ºC leaching temperature (shown in Figure 4.36). Figure 5.13 demonstrates the relationship between the specific surface area and the cell voltage measured using cathodes leached at different temperatures. There was an increasing trend in the specific surface area up to 60 ºC above which the change was not significant. The electrochemical activity did not directly correlate with the pore area measured by the N_2 sorption technique. Although the electrode leached at 60 ºC had a surface area that was almost 4 times more than that of the electrode leached at 30 ºC, they both gave similar cell voltages showing an inefficient utilization of pore surface area with the electrodes leached at higher temperatures. The inefficient use of pore surface for the electrodes leached at ≥ 60 ºC could be attributed to the ink-bottle pore shape observed with these samples which are more subject to mass transport limitations caused by generated H_2 in comparison to slit-shaped pores created at lower leaching temperatures.

In gas-evolving electrodes such as cathodes in alkaline electrolysers where H_2 is generated, the nucleation of gas bubbles occurs at the electrode surface adjacent to the electrolyte solution that is highly saturated with the dissolved gas [160]. H_2 bubbles formed on the electrode surface grow and once they reach a critical size they get detached from the surface. Bubbles can only form in a pore once a certain degree of supersaturation is achieved [161]. The overpressure pressure (Δp) inside a pore can be calculated using the Young-Laplace equation;

$$\Delta p = \frac{2\sigma \cos\theta}{r_{pore}} \tag{5.9}$$

where σ is the surface tension of electrolyte solution, θ is the contact angle, r_{pore} is the radius of pore [54].

Unless the H_2 concentration of the electrolyte solution inside a pore does not exceed the concentration corresponding to the overpressure in Equation 5.9, the produced H_2 can only leave the pore through diffusion and bubble formation does not take place [54]. Assuming the contact angle for Ni surface is *ca.* 110 º [162] and the surface tension of 4 M KOH electrolyte solution is *ca.* 80 mN/m at 20 ºC [163], the minimum pore size required for H_2 bubbles to form inside a pore would be *ca.* 270 nm at atmospheric operating pressure. In the present study, leaching of Al created micro- and mesopores, with the latter having a size range of 2-6 nm and 2-14 nm for samples leached at 30 and 80 ºC respectively. Since the alkaline electrolyser cell operated at atmospheric pressure, H_2 bubbles did not form inside the micro- and mesopores and the generated H_2 inside the pores could only leave the pores through diffusion. As discussed in Section 5.3.3, leaching Al at 30 and 50 ºC led to slit-shaped pores, whereas leaching temperatures of

60, 70 and 80 ºC resulted in ink-bottle pores. The change in the pore morphology may interfere with the diffusion mechanism. Diffusion of H_2 generated inside the large bodies of ink-bottle pores might be limited by the narrow pore throats. Consequent accumulation of H_2 inside the pores could reduce the accessibility of electrolyte solution to the inside of pore bodies resulting in an inefficient use of pore surface. Whereas diffusion through a slit-shaped pore could be favoured by the uniform pore size and morphology.

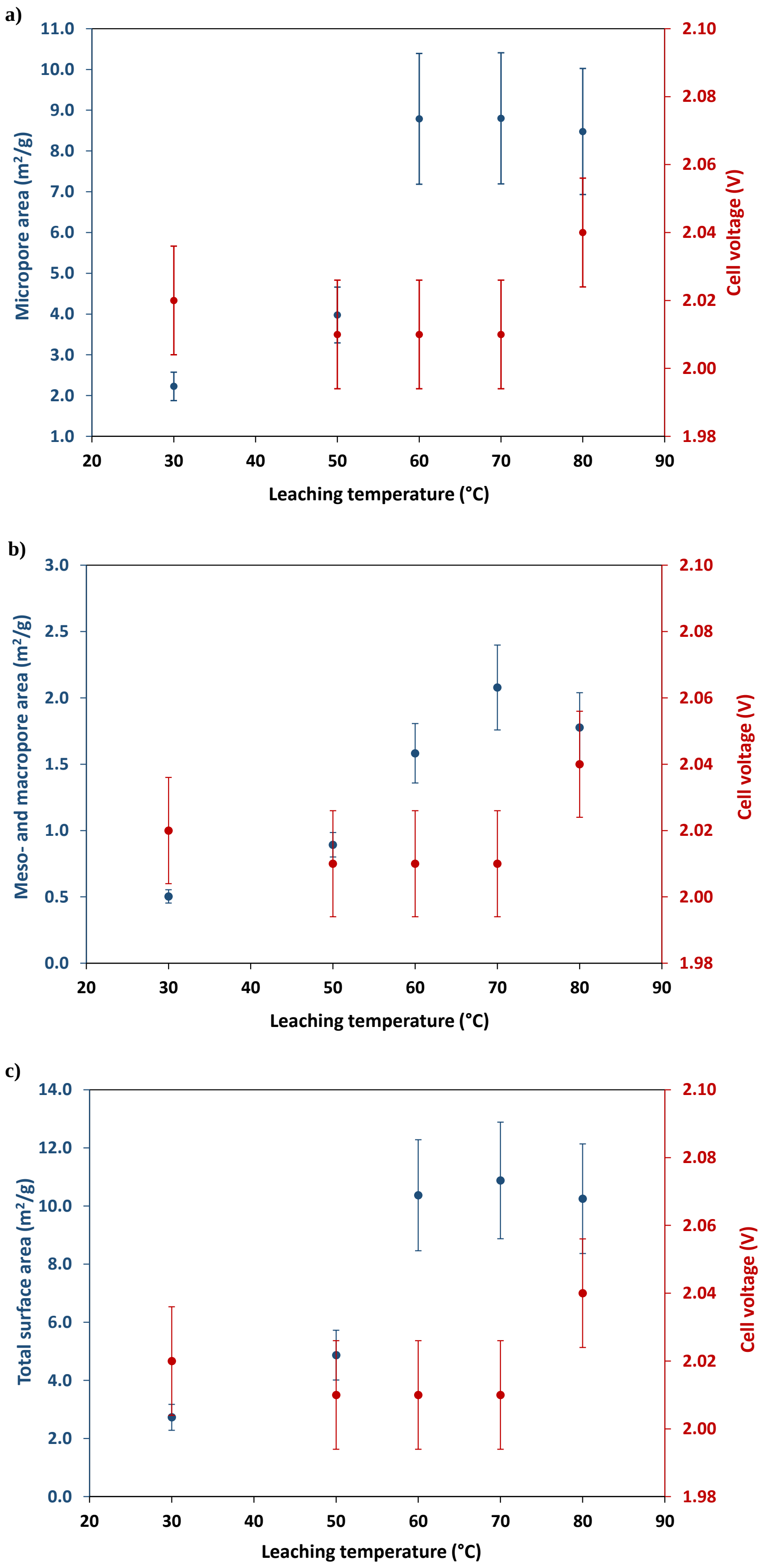

Figure 5.13. The correlation between the cell voltages measured at 1 A/cm^2 and porosity characterictics of cathodes leached at different temperatures, where (a) micropore area; (b) meso- and macropore area and (c) total surface area. The micropore area was calculated by the DA model and subtracted from the BET area to estimate the area of other pores.

5.4. The Effect of Binder Concentration

5.4.1. Composition

The effect of binder amount was studied using as-received wax with the concentrations of 6.25, 15 and 25 wt.%. The sintering was carried out at 900 ºC as lower sintering temperatures resulted in very fragile electrode disks for 15 and 25 wt.% binder concentrations. Since the samples were sintered at 900 ºC, they consisted of *ca.* 67 wt.%. $Al_{0.84}Ni_{1.16}$ and *ca.* 33 wt.% $AlNi_3$ phases from which Al was not leached. Consequently, the Al content in the samples was 20.0 ± 0.5 wt.% based on Rietveld refinement analysis (Figure 4.45). As expected, there was no strong evidence that a change in the binder concentration would lead to a variation in the compositional properties. The differences in the EDX results of Al contents between the samples with different binder concentrations and between surface and cross-section of the same sample were within the experimental errors (Figures 4.45 and 4.46). There was an increasing trend in the margin of error for the EDX analysis, with the higher the binder concentration the greater the experimental error. This was due to the increased surface roughness, which was confirmed by the SEM images (Figure 4.40), reducing the accuracy of measurement.

5.4.2. Change in the Physical Characteristics

As the binder concentration increased from 6.25 to 25 wt.%, the volumetric concentration of open pores in the samples increased by *ca.* 31 % (Figure 4.48). This was due to pores created through the decomposition of binder particles. During sintering of sample disks, wax started decomposing at *ca.* 200 ºC and was completely decomposed once the temperature reached 400 ºC (Figure A7.1). As the wax particles decomposed, they left voids behind them which created additional macropores in the structure. This was confirmed by SEM and micro-CT analyses where the size of large macropores varied between *ca.* 15 and 450 µm and their shape was mainly ellipsoidal or spherical regardless of the size range (Figures 4.40, 4.62 and 4.63). These properties were similar to those of binder particles observed through SEM and laser diffraction techniques (Figures A8.1 and A9.1). The volumetric ratio of closed pores was *ca.* 3 vol.% and was not altered by the change in the binder amount (Figure 4.48). This indicates that the decomposition of wax during sintering mainly created open pores.

The comparison of thicknesses measured before and after sintering showed that the thickness of the disks increased by *ca.* 3.8 and 5.3 % during the sintering when the binder concentration was 6.25 and 25 wt. % respectively (Figure 4.42). This can be explained by the thermal expansion of binder material before the decomposition. The binder wax used in the present work has a melting point of *ca.* 140 ºC and a thermal expansion coefficient of *ca.* 120 x 10^{-6}/ºC [164] corresponding to a *ca.* 0.014 % increase in the volume from room temperature to 140 ºC.

As shown in Figure 5.14 there is a direct correlation between the linear trends in the specific volume occupied by the binder before sintering and the specific macropore volume of as-leached samples with respect to the binder concentration. When the metal mixture was pressed without any binder, the specific macropore volume was 0.13 ± 0.01 cm^3/g (Figure 4.14) corresponding to the macroporosity that already existed in the Ni and starting alloy mixture. This is why the difference between the total specific macropore volume and macropore volume created by the decomposition of binder was *ca.* 0.12 cm^3/g regardless of the binder concentration. These findings are also supported by the micro-CT analysis, where the volume of macropores with sizes of more than 3 µm (scan resolution) is *ca.* 0.07 cm^3/g for a sample prepared from the 6.25 wt.% binder concentration. This was close to the volume occupied by the binder before sintering; *ca.* 0.10 cm^3/g (Figure 5.14) considering the minimum binder particle size was *ca.* 10 µm (Figure A9.1).

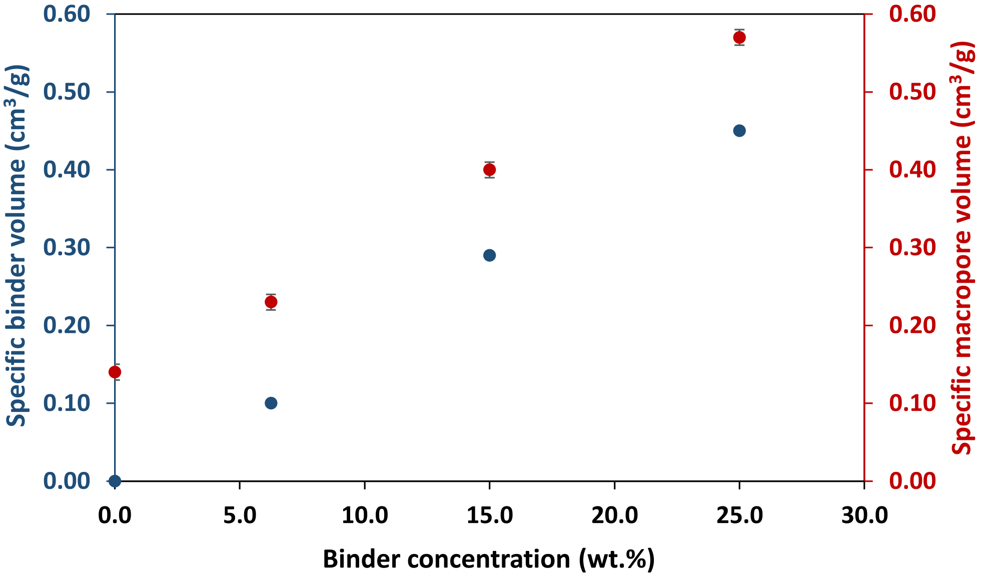

Figure 5.14. Relationship between the specific volume occupied by the binder before sintering and total macropore volume of the final sample. Specific macropore volume was calculated by subtracting the specific volume of micro- and mesopores measured by N_2 sorption from the specific pore volume measured by He pycnometer.

The MIP results for the macropore size distribution changed significantly as the binder concentration increased from 6.25 to 25 wt.% (Figure 4.49), although samples were prepared from the same batch of as-received wax and the binder particle size was not altered. With the 6.25 wt.% binder concentration the MIP only detected the pore sizes of *ca.* 0.2-6 µm, whereas 25 wt.% binder concentration gave a bimodal distribution where the majority of macropores were within the size range of *ca.* 10-400 µm. Surprisingly, the macropore size distribution determined through the MIP did not include the large pores (*ca.* 15-450 µm) identified through the SEM and micro-CT techniques for samples initially containing the 6.25 wt.% binder. This showed its limitation to accurately analyse the pore size distribution since the MIP measures the throat or pore channel size from the sample surface towards that pore body rather than the actual internal pore size [165]. As shown in SEM images (Figures 4.40 and 4.41), not only the amounts of large cavities but also the number of windows between adjacent cavities and pore connectivity from surface towards the cross-section increased significantly as the binder concentration rose from 6.25 to 25 wt.%. Figure 5.15 demonstrates the hypothetical intrusion of Hg from the surface towards the cross-section of samples. With the 6.25 wt.% binder concentration (Figure 5.15 (a)), Hg has to travel through finer channels/throats in order to reach large pore bodies which can only be accomplished by the application of higher pressures. As a result the pores sizes measured by MIP are smaller than those observed by the SEM. In the case of the 25 wt.% binder concentration (Figure 5.15 (b)), Hg may not have had to travel through such fine channels to reach the large pore bodies due to the increased number of windows and connectivity between these cavities allowing MIP to more accurately detect the large pore sizes observed in the SEM images.

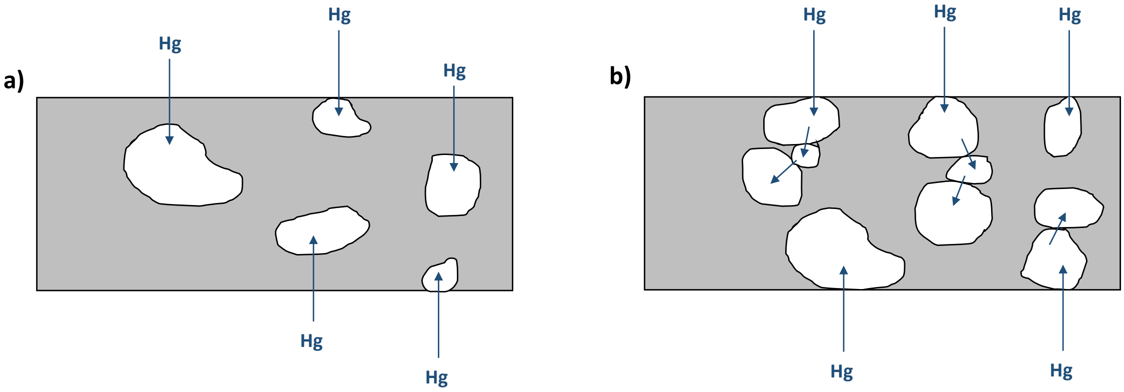

Figure 5.15. A schematic of hypothetical Hg intrusion from the surface through the cross-section of samples disks prepared using (a) 6.25 wt.% and (b) 25 wt.% binder concentration.

As a consequence of increase in the macroporosity which follows greater binder concentrations, the mechanical strength of electrodes reduced significantly. This can be explained by the decrease in the thickness of pore walls and increased numbers of windows between adjacent cavities. The wall thickness has been identified as the key parameter influencing the mechanical strength of porous materials, with the thinner the walls the lower the mechanical strength [166, 167]. SEM analysis (Figures 4.40 and 4.41) showed that greater binder amounts increased the concentration of large macropores in the porous structure resulting in reduced wall thicknesses. In addition, the greater number of windows between the adjacent cavities increased the weak points making electrode disks more fragile.

Furthermore, the surface roughness, which is shown to increase with greater amounts of binder (Figure 4.40), could also pose a problem for the operation of pressured electrolyser systems with a zero-gap configuration where electrodes and thin membrane materials are compressed together at pressures up to 40 bar [26]. The greater concentrations of large cavities on the electrode surface may increase the likelihood of formation of holes in the membrane resulting in reduced membrane lifetime.

As expected, there was no significant difference in micro- and mesoporosity characteristics of the samples with respect to the binder concentration (Figure 4.47). The fluctuations were within the margin of error.

5.4.3. Electrochemical Performance

Increasing the binder concentration from 6.25 to 25 wt.% resulted in a downward trend in the electrolyser cell voltage with the 25 wt.% binder concentration giving a cell voltage *ca.* 4 % less than that measured for the 6.25 wt.% binder concentration at 1 A/cm^2 (Figure 4.50). Figure 5.16 demonstrates the relationship between the specific surface area and the cell voltage measured using cathodes prepared from different binder concentrations. The total surface area shows an increasing trend from 6.25 to 25 wt.% binder concentration, with using 25 wt.% binder giving a *ca.* 30 % greater specific surface area than that measured with the sample prepared from 6.25 wt.% binder. Similar to findings reported earlier, there was an inverse relationship between the cell voltage and specific surface area. However, despite the significant increase in the macroporosity, the improvement in the surface area and resultant decrease in the cell voltage was not substantial due to the low surface area of large macropores (> 15 µm) in comparison to micro- and mesopores. Furthermore, the mechanical strength reduced significantly as the volumetric concentration of large macropores increased. Although a decrease of *ca.* 4 % achieved in the cell voltage by increasing the binder concentration from 6.25 to 25 wt.%, the samples prepared from the 25 wt.% binder concentration were extremely fragile and not practical for industrial applications. Therefore, there was a trade-off between the slight decrease in the cell voltage and robustness of electrodes. It is likely that small macropores may be beneficial as they will not influence the mechanical strength substantially in comparison to large macropores whilst still providing an increase in the surface area for the reaction.

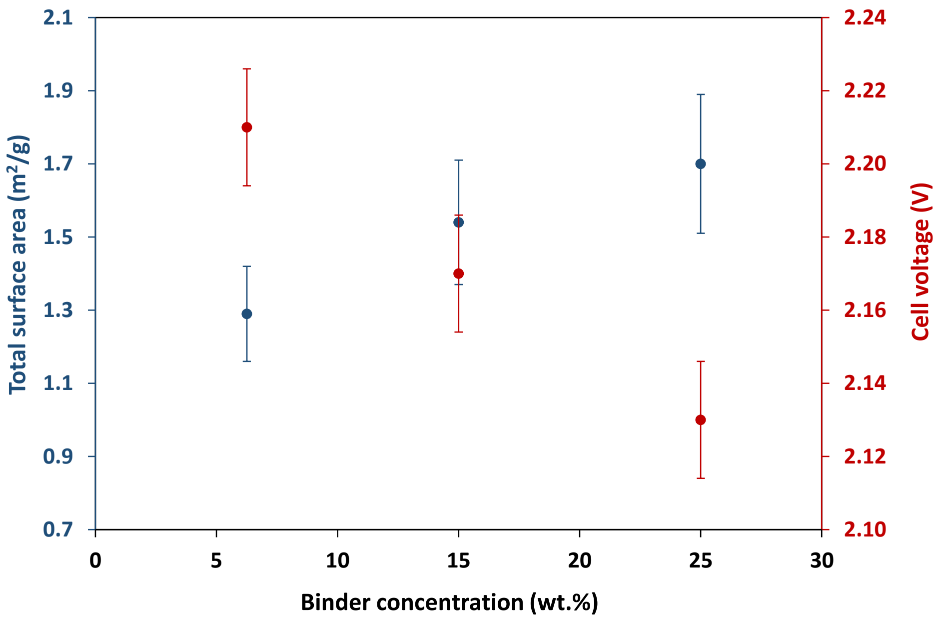

Figure 5.16. The correlation between the cell voltages measured at 1 A/cm^2 and the specific surface area of cathodes prepared from different binder concentrations.

5.5. The Effect of Binder Particle Size

5.5.1. Change in the Physical Characteristics

The effect of binder particle size was studied using wax with different particle size ranges, i.e. 20-45 µm, 45-75 µm, 75-200 µm and > 200 µm, as well as cellulose with a mean particle size of 20 µm with the purpose of investigating the influence of size of large macropores (> 20 µm) on the physical and electrochemical characteristics of electrode samples. SEM analysis on the surface and cross-section of electrode disks confirmed a direct relationship between the binder particle size and the size of macropores present in the samples (Figures 4.51 and 4.52). Since these voids were created during the decomposition of binder particles, the macropores with greater sizes were observed when the binder particle size was increased resulting in samples with a rougher surface and cross-section. This was also supported by the micro-CT analysis where the size and relative volume of macropores showed a strong dependence on the binder particle size (Figure 4.62). The total specific macropore volume, on the other hand, was not altered significantly as the same amount of material (60 wt.% Ni-40 wt.% starting alloy) and binder concentration (6.25 wt.%) were used to prepare the samples regardless of the binder particle size. The effects of starting alloy ratio and binder concentration on the macroporosity were discussed earlier.

The mechanical strength of the sample disks reduced as the binder particle size increased. It has been reported in the literature that in addition to porosity, the pore size distribution also influences the compressive strength of porous materials, with the smaller the pore size the greater the compressive strength [166-168]. As discussed in Section 5.4.2 for the effect of binder concentration, the mechanical strength of the porous materials is determined by the weakest point such as a thin wall. Having larger pores increases the probability of thin walls. Therefore, the greatest robustness was observed with the binder having the smallest particle size range.

As discussed in Section 5.4.2, MIP technique was not be able to accurately measure the pore size distribution and instead reported the size of throats/pore channels from surface to the pore body. Consequently, MIP results did not show the large voids that were observed in the SEM images associated with the binder decomposition. For size range, 0.3-4 µm measured by the MIP there was good agreement with the SEM analysis where the sizes of macropores, excluding the voids created from the binders, were in the range of 0.5-10 µm. This shows that these pores acted as a channel/throat for the larger macropore bodies and were originated from the porous structure of Ni-starting alloy mixture.

Since all samples were prepared from the same metal composition (60 wt.% Ni-40 wt.% starting alloy) and sintering and leaching conditions were same, the resultant micro- and mesoporosity characteristics, which are defined by the amount of Al_3Ni_2 available for Al leaching, were similar for all samples regardless of the change in the binder particle size as expected.

5.5.2. Electrochemical Performance

The electrodes prepared from binders with varying particles size ranges; i.e. 20-45 µm, 45-75 µm, 75-200 µm and > 200 µm showed similar electrochemical activities (Figure 4.58). This was because they all had similar compositions and porosity characteristics. The only difference that there was between the electrodes was the size of the macropores created during the decomposition of binders. Due to significantly lower surface area contribution by these macropores compared to those of the micro- and mesoporosity which dominated the total specific surface area, the size of the macropores do not have any influence on electrochemical performance (Figure 17). The characteristics of large macropores (> 20 µm) were found to have a trivial influence on the electrochemical activity of electrodes, whilst having a significant influence on the mechanical strength.

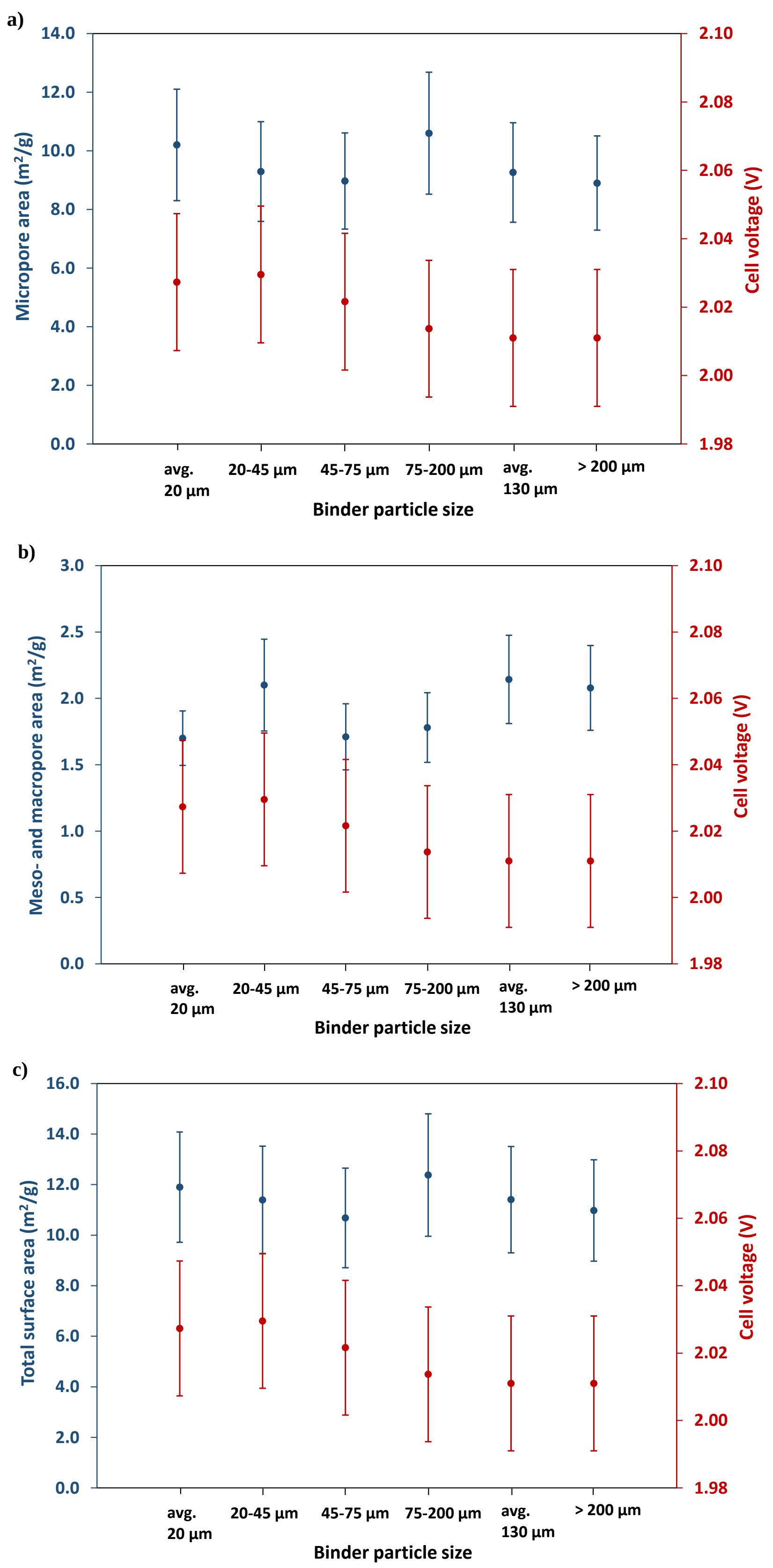

Figure 5.17. The correlation between the cell voltages measured at 1 A/cm^2 and porosity characterictics of cathodes prepared using a cellulose or wax binder with different particle sizes, where (a) micropore area; (b) meso- and macropore area and (c) total surface area. The micropore was calculated by the DA model and subtracted from the BET surface area to estimate the area of other pores.

5.6. Summary

It has been shown that the sintering temperature has a substantial influence on the physical, chemical and mechanical characteristics of porous catalysts prepared from a mixture of Ni and Al-rich phases (Al_3Ni and Al_3Ni_2). The rate of atomic diffusion from Al-rich phases to Ni occurring during the sintering process increased with higher sintering temperatures, reducing the concentrations of Al-rich phases while increasing the quantity of AlNi and $AlNi_3$. Resultant properties of intermetallic phases influenced the efficiency of leaching since Al can only be leached from Al-rich phases. Consequently, the quantity of micro- and mesopores created by Al leaching and chemical composition of as-leached catalysts change with respect to the sintering temperature. Although higher sintering temperatures are desirable to achieve a good mechanical strength through improved bonds between the inter-particles, they lead to Ni-based catalysts with reduced micro- and mesoporosity and increased Al content resulting from greater amounts of unleachable phases. By tuning the composition of intermetallic phases formed during the sintering, the composition and porosity of Ni-based catalysts can be controlled. A possible solution to retain more Al leachable phases after sintering in order to obtain a greater surface area during leaching while still achieving a good mechanical strength would be mixing Ni with Al and/or Al_3Ni rather than a mixture of Al_3Ni and Al_3Ni_2. Since the melting points of Al (640 ºC) and Al_3Ni (845 ºC) are lower than that of Al_3Ni_2 (1133 ºC), a better sintering would occur at relatively lower sintering temperatures while the loss of Al-rich phases would be reduced.

Another way of controlling the micro- and mesoporosity is to change the Ni to starting alloy ratio. Since the starting alloy consists of Al_3Ni and Al_3Ni_2, an increase in the starting alloy concentration leads to increased leaching of Al creating greater amounts of micro- and mesopores. Although resultant catalysts have a higher surface area, the mechanical strength reduces significantly since the compressibility of starting alloy powder is lower than that of Ni, resulting in increased macroporosity. In addition, the starting alloy is more expensive than Ni hindering the benefits of cost-effective Ni catalysts. Therefore, there is a trade-off between the increase in the surface area through greater concentrations of starting alloy and the robustness and cost of the Ni-based catalysts. It is suggested that starting alloy concentration should be in the range of 20-40 wt.% in order to achieve relatively robust and inexpensive catalysts without compromising too much the surface area of the porous Ni-based catalysts.

It has also been shown that the shape and size of the micro- and mesopores created during leaching of Al can be controlled by changing the leaching temperature. Lower leaching temperatures, i.e. 30 and 50 ºC result in pores with a slit shape, whilst the leaching temperatures of 60, 70 and 80 ºC lead to ink-bottle pores due to the change in the leaching reaction rate in comparison to the speed of rearrangement of atoms at the surface. A significant increase in the specific surface area is observed from 30 to 60 ºC, whilst leaching at 60-80 ºC leads to similar surface areas. Since all samples had similar Al_3Ni_2 concentrations after sintering and the entire quantity of Al_3Ni_2 was consumed during the leaching, creating catalysts with similar compositions, the leaching temperature does not influence the leaching efficiency for the leaching duration of 18 h.

The investigation in the properties of binder agent has shown that the size, shape and quantity of binder particles define the properties of cavities created during the sintering process through the decomposition of binder. In this study, the binder particles with sizes more than *ca.* 15 µm have been used to control the macroporosity characteristics. Greater binder concentrations lead to increased macroporosity and surface roughness as well as greater numbers of windows between the adjacent cavities. Consequently, the mechanical strength of porous catalysts reduces due to the decrease in the wall thickness. It has been found that the size of the binder particles also influences the robustness, with the smaller the binder size the greater the robustness.

The comparison of trends in electrochemical performance in alkaline electrolysers with respect to the trends in the textural and compositional properties of as-leached catalysts has shown that the surface area has a dominant effect on the electrocatalytic activity in comparison to the compositional properties of Ni-based electrodes. Since micropores accounts for *ca.* 80 % of total surface area, they have the most significant effect on electrocatalytic activity. However, it has been found that the effective use of micro- and mesopores depends on the pore morphology. The electrodes leached at 60-80 ºC have a greater specific surface area resulting from ink-bottle pores in comparison to electrodes leached at 30 and 50 ºC containing slit-shaped pores, however electrochemical performance has been similar. This shows that slit-shaped pores are more efficiently used during HER in alkaline electrolysers than ink-bottle bottles which can be more subject to mass transport limitations. It has been shown that at atmospheric operating pressure, H_2 bubbles cannot be formed inside the micro- and mesopores and H_2 generated inside the small pores can only leave the pores through the diffusion which appears to be favoured by a slit shape in comparison to ink-bottles. It is suggested that increasing quantities of slit-shaped micro- and mesopores in porous electrodes would improve electrochemical performance for HER in alkaline electrolysers.

It has also been found that the large macropores (with sizes >15 µm) do not influence electrochemical performance in alkaline electrolysers significantly, since their surface areas are substantially lower than those of micro- and mesopores. It is suggested that increasing the amount of large macropores is not advantageous to the production of electrodes for alkaline electrolysers as it results in increased electrode thickness and reduced mechanical strength with no measureable improvement in electrochemical performance. It is likely that small macropores may be beneficial as they will not influence the mechanical strength substantially in comparison to large macropores whilst still providing an increase in the surface area. The shape of these small macropores would be designed with a slit shape to maximize the use of pore area during the reaction. It is also suggested that the minimum pore size that would allow H_2 bubbles to form inside the pores can be estimated using the Young-Laplace equation based on the operating conditions of an alkaline electrolyser, i.e. temperature, pressure and electrolyte solution concentration. Above this pore size, generated H_2 would leave the pores through both bubble formation and diffusion, resulting in improved mass transport of H_2 from the pore surface at high current densities.

Lastly, it has also been shown that the increase in the electrocatalyst quantity does not alter electrochemical performance, proving that the surface properties are more important than the bulk properties. It is suggested that an optimum quantity of catalyst, which would still give a sufficient mechanical strength while minimizing the material use, should be identified in order to reduce the material cost as well as decreasing the thickness of electrodes, both of which would be beneficial to large scale applications.

6. Conclusions

Ni-based electrodes have been extensively studied for HER in alkaline electrolysers in an attempt to improve its electrocatalytic activity through alloying it with other metals or increasing the surface area. However, the role of microstructure on the electrochemical performance has received little attention. The principle objective of this thesis was to investigate the effects of porous catalyst preparation conditions on the microstructural properties with a view to providing guidelines on how to control the textural properties of porous Ni-based catalysts and establishing a relationship between the microstructure and electrochemical performance of porous Ni-based electrodes for HER in alkaline electrolysers. A powder metallurgy technique including powder compaction and sintering has been chosen to prepare Ni-based catalysts as it can offer a more practical, economical and amenable option for mass production in comparison to alternative methods such as electrodeposition and plasma spraying.

A mixture of Ni, starting alloy (consisting of Al_3Ni and Al_3Ni_2) and binder was pressed under a pressure of 1.2 ton/cm^2 for 5 min using a hydraulic press. Pressed samples were sintered under an Ar gas atmosphere for 2 h at a chosen temperature. As-sintered samples were then treated in 5 M KOH containing 10 wt.% K-Na tartrate tetrahydrate for 18 h for leaching of Al. The microstructure of porous electrodes was controlled by changing the following parameters of the preparation process;

- sintering temperature
- starting alloy to Ni ratio
- leaching temperature
- binder properties (concentration and particle size).

6.1. Controlling textural properties

It was shown that the **sintering temperature** has a substantial influence on the physical, chemical and mechanical characteristics of porous catalysts prepared from a mixture of Ni and Al-rich phases (Al_3Ni and Al_3Ni_2). Increasing the sintering temperature from 625 to 900 ºC improved the Al diffusion from Al-rich phases into Ni, resulting in reduced Al_3Ni_2 and (Ni) phase and increased AlNi and $AlNi_3$, with samples sintered at 900 ºC consisting of only $Al_{0.84}Ni_{1.16}$ and $AlNi_3$. Al_3Ni was not detected after sintering regardless of the sintering temperature. The resultant properties of intermetallic phases available after sintering significantly influenced the efficiency of the leaching process since Al can only be leached from Al-rich phases. Although higher sintering temperatures gave a better mechanical strength through the formation of stronger bonds between the interparticles, they led to a decrease in the quantity of micro- and mesopores created by leaching of Al and an increase in unleached Al content. It is suggested that by tuning the composition of intermetallic phases formed during the sintering, the composition and porosity of Ni-based catalysts can be controlled. A possible solution to retain more Al leachable phases after sintering in order to obtain a greater surface area during leaching while still achieving a good mechanical strength would be mixing Ni with Al and/or Al_3Ni rather than a mixture of Al_3Ni and Al_3Ni_2. Since the melting points of Al (640 ºC) and Al_3Ni (845 ºC) are lower than that of Al_3Ni_2 (1133 ºC), a better sintering would occur at relatively lower sintering temperatures while the loss of Al-rich phases would be reduced.

Starting alloy to Ni ratio was also found to be a significant parameter for controlling the textural properties. Since the starting alloy consists of Al_3Ni and Al_3Ni_2, an increase in the starting alloy concentration leads to increased leaching of Al creating greater amounts of micro- and mesopores and hence resulting in a higher specific surface area. Using 60 wt.% starting alloy increased the specific surface area by *ca.* 3 times in comparison to 10 wt.% starting alloy concentration. For samples prepared by only pressing and sintering Ni, the mesoporosity was negligible and the micropore area was *ca.* 5 times less than that of as-leached samples prepared using 10 wt. % starting alloy concentration. Although greater alloy concentrations resulted in a higher surface area, the mechanical strength reduced significantly since the compressibility of starting alloy powder is lower than that of Ni, resulting in increased macroporosity. In addition, the starting alloy is more expensive than Ni hindering the benefits of cost-effective Ni catalysts. Therefore, there is a trade-off between the increase in the surface area through greater concentrations of starting alloy and the robustness and cost of the Ni-based catalysts. It is suggested that starting alloy concentration should be in the range of 20-40 wt.% in order to achieve relatively robust and inexpensive catalysts without compromising too much the surface area of the porous Ni-based catalysts.

It was demonstrated that the shape and size of the micro- and mesopores created during leaching of Al can be controlled by changing the **leaching temperature.** N_2 sorption isotherms showed that leaching at lower temperatures, i.e. 30 and 50 ºC resulted in pores with a slit shape, whilst the leaching temperatures of 60, 70 and 80 ºC led to ink-bottle pores. This is attributed to the increase in the leaching rate with higher leaching temperatures which influences the relative speed of atomic rearrangement at the surface in comparison to the rate of Al leaching reaction. If the leaching rate is relatively lower, Al may diffuse to the leaching zones creating pores, whilst faster leaching reactions may drill into the matrix to reach Al, leading to the formation of the ink-bottle pores. Increasing the leaching temperature from 30 to 60 °C improved the specific surface area by almost 4 times through a significant increase in the micro- and mesoporosity, whilst leaching at 60, 70 and 80 ºC gave similar surface areas.

The investigation of the properties of **binder** agent showed that the size, shape and quantity of binder particles define the properties of cavities created during the sintering process through the decomposition of binder. The binder particles with sizes more than *ca.* 15 µm have been used to control the macroporosity characteristics. Greater binder concentrations led to increased macroporosity and surface roughness as well as greater numbers of windows between the adjacent cavities. Consequently, the mechanical strength of porous catalysts reduced due to the decrease in the wall thickness. It was also found that the size of the binder particles influences the robustness of the porous catalysts, with the smaller the binder size the greater the robustness.

6.2. Electrochemical performance

The electrochemical performance of porous Ni-based electrodes have been tested in an alkaline electrolyser cell. The trends in electrolyser cell voltage, which decreases as the electrocatalytic activity of electrodes increases, were compared to the trends in the compositional and microstructural properties. It was shown that the surface area has a dominant effect on the electrocatalytic activity in comparison to the compositional properties of Ni-based electrodes. Despite greater Al contents, the electrolyser cell voltage still decreases with increasing surface areas.

Since micropores account for *ca.* 80 % of total surface area, they have the most significant effect on electrocatalytic activity. However, it was found that the effective use of micro- and mesopores depends on the pore morphology. The electrodes leached at 60-80 ºC have a greater specific surface area resulting from ink-bottle pores in comparison to electrodes leached at 30 and 50 ºC containing slit-shaped pores, however electrochemical performance has been similar. Although the change in the pore size and volume with respect to leaching temperature has been reported by an earlier study, the effect that this has on the electrochemical performance for HER in alkaline electrolysers has not been investigated. The present study showed that slit-shaped pores are more efficiently used during HER than ink-bottle bottles which can be more subject to mass transport limitations. It was shown that at atmospheric operating pressure, H_2 bubbles cannot be formed inside the micro- and mesopores and H_2 generated inside the small pores can only leave the pores through the diffusion which appear to be favoured by a slit shape in comparison to ink-bottles. It is suggested that increasing the quantities of slit-shaped micro- and mesopores in porous electrodes would improve electrochemical performance for HER in alkaline electrolysers.

It was also found that the large macropores (with sizes >15 µm) do not influence electrochemical performance in alkaline electrolysers significantly, since their surface areas are substantially lower than those of micro- and mesopores. It was concluded that increasing the amount of large macropores is not advantageous to the production of electrodes for alkaline electrolysers as it results in increased electrode thickness and reduced mechanical strength with no measureable improvement in electrochemical performance. It is likely that small macropores may be beneficial as they will not influence the mechanical strength substantially in comparison to large macropores whilst still providing an increase in the surface area. The shape of these small macropores would be designed to be a slit shape in order to maximize the use of pore area during HER. It is also suggested that the minimum pore size that would allow H_2 bubbles to form inside the pores can be estimated using the Young-Laplace equation based on the operating conditions of an alkaline electrolyser, i.e. temperature, pressure and electrolyte solution concentration. Above this pore size, generated H_2 would leave the pores through both bubble formation and diffusion, resulting in improved mass transport of H_2 from the pore surface at high current densities.

Lastly, it was also shown that the increase in the electrocatalyst quantity does not alter electrochemical performance, proving that the surface properties are more important than the bulk properties. It is suggested that an optimum quantity of catalyst, which would still give a sufficient mechanical strength while minimizing the material use, should be identified in order to reduce the material cost as well as decreasing the thickness of electrodes, both of which would be beneficial to large scale applications.

7. Future Work

The investigation of sintering temperature showed that there was a trade-off between the mechanical strength and Al-rich phases available after sintering of a mixture of Ni and Al-rich phases (Al_3Ni and Al_3Ni_2). A possible solution to retain more Al leachable phases after sintering hence to obtain a greater surface area during leaching while still achieving a good mechanical strength would be mixing Ni with Al and/or Al_3Ni rather than a mixture of Al_3Ni and Al_3Ni_2. Future work should investigate the properties of porous Ni-based catalysts prepared from the mixtures of Ni with Al and/or Al_3Ni.

The investigation of Al leaching temperature showed that the slit-shaped micro- and mesopores were created at lower leaching temperatures, whilst higher leaching temperatures led to ink-bottle pores. This was attributed to the increase in the leaching rate with higher leaching temperatures which influences the relative speed of atomic rearrangement at the surface in comparison to the rate of Al leaching reaction. Although increased reaction rates were casually observed, this was not measured. It would be worth quantifying the change in the leaching reaction rate with respect to leaching temperature. A more detailed investigation would provide a better understanding of which parameters control the pore shape and volume created during leaching of Al.

An interesting finding of this work was that slit-shaped micro- and mesopores are more effectively used during HER in alkaline electrolysers than ink-bottled pores due to the mass transport limitations. Future work should investigate the effect of increased slit-shaped pores on the electrochemical activity of porous Ni-based electrodes. An increase in the quantity of these pores would be achieved by increasing the concentration of Al-rich phases available whilst still using a lower leaching temperature of 30 ºC without compromising too much the mechanical strength. Alternatively, other techniques could be sought to create slit-shaped pores which could also offer a control of the pore size.

The investigation of the effect of large macropores (with sizes >15 µm) showed that increasing the amount of large macropores is not advantageous to the production of electrodes for alkaline electrolysers as it results in increased electrode thickness and reduced mechanical strength with no measureable improvement in electrochemical performance. Future work should be to investigate the role of small macropores, which may be beneficial as they will not influence the mechanical strength substantially in comparison to large macropores whilst still providing an increase in the surface area. The size and shape of these small macropores should be controlled to see the effects on the electrochemical activity. Above a certain pore size, e.g. *ca.* 270 nm (for 4 M KOH electrolyte solution at 20 ºC, atmospheric operating pressure and a contact angle of 110 º) generated H_2 would leave the pores through both bubble formation and diffusion, whilst below this threshold H_2 would only diffuse away from the pore surface. The effect that this could have on electrochemical activity of porous electrodes with different pore shapes would be worth investigating.

The electrochemical performance of porous Ni-based electrodes have been examined in an alkaline electrolyser cell. Since the properties of electrolyte solution, membrane and anode were kept constant, the variation in the cell voltage was due to the change in the characteristics of the cathode material. A more detailed study in electrochemical activity could be done by using a reference electrode integrated cell. This configuration would allow measuring the electrochemical characteristics of only the cathode side while still operating under normal electrolyser cell conditions. An in-situ evaluation of electrochemical active surface during HER would be possible by using a reference electrode integrated cell.

References

1. IEA. *World Energy Outlook 2014 Executive Summary*. 2014 [cited 15th Jan 2017]; Available from: https://www.iea.org/publications/freepublications/publication/WEO_2014_ES_English_WEB.pdf.
2. IEA. *World Energy Outlook 2014 Factsheet*. 2014 [cited 15th Jan 2017].
3. Marbán, G. and T. Valdés-Solís, *Towards the hydrogen economy?* International Journal of Hydrogen Energy, 2007. **32**(12): p. 1625-1637.
4. DECC. *The UK low carbon transition plan: national strategy for climate and energy*. 2009 [cited 20th Jan 2017]; Available from: https://www.gov.uk/government/publications/the-uk-low-carbon-transition-plan-national-strategy-for-climate-and-energy.
5. EP. *Promotion of the use of energy from renewable sources*. 2009 [cited 20th Jan 2017]; Available from: http://eur-lex.europa.eu/legal-content/EN/TXT/?uri=URISERV%3Aen0009.
6. EC. *Paris Agreement*. 2017 [cited 11th Jan 2017]; Available from: https://ec.europa.eu/clima/policies/international/negotiations/paris_en.
7. Steward, D., et al., *Lifecycle cost analysis of hydrogen versus other technologies for electrical energy storage*. 2009, National Renewable Energy Laboratory (NREL), Golden, CO.
8. Chen, H., et al., *Progress in electrical energy storage system: A critical review.* Progress in Natural Science, 2009. **19**(3): p. 291-312.
9. Gupta, R.B., *Hydrogen fuel: production, transport, and storage*. 2008: Crc Press.
10. Edwards, P.P., et al., *Hydrogen and fuel cells: towards a sustainable energy future.* Energy policy, 2008. **36**(12): p. 4356-4362.
11. EIA. *International Energy Outlook 2016*. 2016 [cited 10th Jan 2017]; Available from: https://www.eia.gov/outlooks/ieo/pdf/0484(2016).pdf.
12. IEA. *CO_2 emissions from fuel combustion*. 2016 [cited 15th Jan 2017]; Available from: https://www.iea.org/publications/freepublications/publication/CO2EmissionsfromFuelCombustion_Highlights_2016.pdf.
13. Schlapbach, L. and A. Züttel, *Hydrogen-storage materials for mobile applications.* Nature, 2001. **414**(6861): p. 353-358.
14. Winter, C.-J., *Hydrogen energy—abundant, efficient, clean: a debate over the energy-system-of-change.* International journal of hydrogen energy, 2009. **34**(14): p. S1-S52.
15. Acar, C. and I. Dincer, *Comparative assessment of hydrogen production methods from renewable and non-renewable sources.* International journal of hydrogen energy, 2014. **39**(1): p. 1-12.
16. Dincer, I. and C. Acar, *Review and evaluation of hydrogen production methods for better sustainability*. International journal of hydrogen energy, 2015. **40**(34): p. 11094-11111.
17. IEA. *Hydrogen production and Storage*. 2006 [cited 25th January 2017]; Available from: https://www.iea.org/publications/freepublications/publication/hydrogen.pdf.
18. Holladay, J.D., et al., *An overview of hydrogen production technologies.* Catalysis today, 2009. **139**(4): p. 244-260.

19. Hallenbeck, P.C. and J.R. Benemann, *Biological hydrogen production; fundamentals and limiting processes.* International Journal of Hydrogen Energy, 2002. **27**(11): p. 1185-1193.
20. Ni, M., et al., *An overview of hydrogen production from biomass.* Fuel processing technology, 2006. **87**(5): p. 461-472.
21. Balat, M., *Potential importance of hydrogen as a future solution to environmental and transportation problems.* International journal of hydrogen energy, 2008. **33**(15): p. 4013-4029.
22. Hauch, A., et al., *Highly efficient high temperature electrolysis.* Journal of Materials Chemistry, 2008. **18**(20): p. 2331-2340.
23. Benemann, J., *Feasibility analysis of photobiological hydrogen production.* International journal of hydrogen energy, 1997. **22**(10): p. 979-987.
24. Mazloomi, K. and C. Gomes, *Hydrogen as an energy carrier: prospects and challenges.* Renewable and Sustainable Energy Reviews, 2012. **16**(5): p. 3024-3033.
25. Carmo, M., et al., *A comprehensive review on PEM water electrolysis.* International journal of hydrogen energy, 2013. **38**(12): p. 4901-4934.
26. Millet, P. and S. Grigoriev, *Water electrolysis technologies.* Renewable Hydrogen Technologies: Production, Purification, Storage, Applications and Safety, 2013.
27. Cerri, I., et al., *Scientific Assessment in support of the Materials Roadmap enabling Low Carbon Energy Technologies: Hydrogen and Fuel Cells*. 2012, Publications Office of the European Union.
28. Dincer, I., *Green methods for hydrogen production.* International journal of hydrogen energy, 2012. **37**(2): p. 1954-1971.
29. Zeng, K. and D. Zhang, *Recent progress in alkaline water electrolysis for hydrogen production and applications.* Progress in Energy and Combustion Science, 2010. **36**(3): p. 307-326.
30. Sigma-Aldrich. *Platinum nanopowder*. 2017 [cited 10th Jul 2017]; Available from: http://www.sigmaaldrich.com/catalog/product/aldrich/685453?lang=en&region=GB.
31. Sigma-Aldrich. *Nickel nanopowder*. 2017 [cited 10th Jul 2017]; Available from: http://www.sigmaaldrich.com/catalog/product/aldrich/577995?lang=en&region=GB.
32. Wendt, H., *Electrochemical hydrogen technologies: Electrochemical production and combustion of hydrogen*. 1990: Elsevier Science Ltd.
33. Millet, P., *Water Electrolysis for Hydrogen Generation*, in *Electrochemical Technologies for Energy Storage and Conversion: Vol. 2*, R.-S. Liu, Editor. 2012, John Wiley & Sons.
34. Nagai, N., et al., *Existence of optimum space between electrodes on hydrogen production by water electrolysis.* International journal of hydrogen energy, 2003. **28**(1): p. 35-41.
35. Ursua, A., L.M. Gandia, and P. Sanchis, *Hydrogen production from water electrolysis: current status and future trends.* Proceedings of the IEEE, 2012. **100**(2): p. 410-426.
36. Barbir, F., *PEM fuel cells: theory and practice*. 2013: Academic Press.
37. Crow, D.R., *Principles and applications of electrochemistry*. 1994: CRC Press.
38. Wendt, H. and G. Kreysa, *Electrochemical engineering: science and technology in chemical and other industries*. 1999: Springer Science & Business Media.

39. Santos, D.M., C.A. Sequeira, and J.L. Figueiredo, *Hydrogen production by alkaline water electrolysis.* Química Nova, 2013. **36**(8): p. 1176-1193.
40. Vanysek, P., *Electrochemical series.* Handbook of Chemistry and Physics, 1998. **88**.
41. Srinivasan, S., *Fuel cells: from fundamentals to applications*. 2006: Springer Science & Business media.
42. Marini, S., et al., *Advanced alkaline water electrolysis.* Electrochimica Acta, 2012. **82**: p. 384-391.
43. Zheng, Y., et al., *Advancing the Electrochemistry of the Hydrogen‐Evolution Reaction through Combining Experiment and Theory.* Angewandte Chemie International Edition, 2015. **54**(1): p. 52-65.
44. Lupi, C., A. Dell'Era, and M. Pasquali, *Nickel–cobalt electrodeposited alloys for hydrogen evolution in alkaline media.* International Journal of Hydrogen Energy, 2009. **34**(5): p. 2101-2106.
45. Imarisio, G. and A.S. Strub, *Hydrogen as an energy carrier*. Vol. 8651. 1983: Springer Science & Business Media.
46. Grdeń, M., M. Alsabet, and G. Jerkiewicz, *Surface science and electrochemical analysis of nickel foams.* ACS applied materials & interfaces, 2012. **4**(6): p. 3012-3021.
47. Guzman, R.S., J. Vilche, and A. Arvia, *The potentiodynamic behaviour of nickel in potassium hydroxide solutions.* Journal of applied electrochemistry, 1978. **8**(1): p. 67-70.
48. Divisek, J., *Determination of the kinetics of hydrogen evolution by analysis of the potential-current and potential-coverage curves.* Journal of electroanalytical chemistry and interfacial electrochemistry, 1986. **214**(1-2): p. 615-632.
49. Bockris, J.M. and E. Potter, *The mechanism of hydrogen evolution at nickel cathodes in aqueous solutions.* The Journal of Chemical Physics, 1952. **20**(4): p. 614-628.
50. Devanathan, M. and M. Selvaratnam, *Mechanism of the hydrogen-evolution reaction on nickel in alkaline solutions by the determination of the degree of coverage.* Transactions of the Faraday Society, 1960. **56**: p. 1820-1831.
51. Krstajić, N., et al., *On the kinetics of the hydrogen evolution reaction on nickel in alkaline solution: Part I. The mechanism.* Journal of Electroanalytical Chemistry, 2001. **512**(1): p. 16-26.
52. Lasia, A. and A. Rami, *Kinetics of hydrogen evolution on nickel electrodes.* Journal of electroanalytical chemistry and interfacial electrochemistry, 1990. **294**(1-2): p. 123-141.
53. Kreysa, G., B. Hakansson, and P. Ekdunge, *Kinetic and thermodynamic analysis of hydrogen evolution at nickel electrodes.* Electrochimica acta, 1988. **33**(10): p. 1351-1357.
54. Rausch, S. and H. Wendt, *Morphology and Utilization of Smooth Hydrogen‐Evolving Raney Nickel Cathode Coatings and Porous Sintered‐Nickel Cathodes.* Journal of The Electrochemical Society, 1996. **143**(9): p. 2852-2862.
55. Herraiz-Cardona, I., et al., *Assessment of the roughness factor effect and the intrinsic catalytic activity for hydrogen evolution reaction on Ni-based electrodeposits.* International Journal of Hydrogen Energy, 2011. **36**(16): p. 9428-9438.
56. Panek, J., et al., *Ni+ Ti composite layers as cathode materials for electrolytic hydrogen evolution.* International Journal of Hydrogen Energy, 2003. **28**(2): p. 169-175.

57. Elumalai, P., et al., *Kinetics of hydrogen evolution on submicron size Co, Ni, Pd and Co–Ni alloy powder electrodes by dc polarization and ac impedance studies.* Journal of applied electrochemistry, 2002. **32**(9): p. 1005-1010.
58. Dominguez-Crespo, M.A., et al., *Kinetic study of hydrogen evolution reaction on Ni 30 Mo 70, Co 30 Mo 70, Co 30 Ni 70 and Co 10 Ni 20 Mo 70 alloy electrodes.* Materials characterization, 2005. **55**(1): p. 83-91.
59. Raj, I.A. and K. Vasu, *Transition metal-based hydrogen electrodes in alkaline solution—electrocatalysis on nickel based binary alloy coatings.* Journal of applied electrochemistry, 1990. **20**(1): p. 32-38.
60. Jakšić, J., M. Vojnović, and N. Krstajić, *Kinetic analysis of hydrogen evolution at Ni–Mo alloy electrodes.* Electrochimica Acta, 2000. **45**(25): p. 4151-4158.
61. de Chialvo, M.G. and A. Chialvo, *Hydrogen evolution reaction on smooth Ni (1− x)+ Mo (x) alloys (0≤ x≤ 0.25).* Journal of Electroanalytical Chemistry, 1998. **448**(1): p. 87-93.
62. Kawashima, A., et al., *Characterization of sputter-deposited Ni-Mo and Ni-W alloy electrocatalysts for hydrogen evolution in alkaline solution.* Materials Science and Engineering: A, 1997. **226**: p. 905-909.
63. Kedzierzawski, P., D. Oleszak, and M. Janik-Czachor, *Hydrogen evolution on hot and cold consolidated Ni–Mo alloys produced by mechanical alloying.* Materials Science and Engineering: A, 2001. **300**(1): p. 105-112.
64. Divisek, J., H. Schmitz, and J. Balej, *Ni and Mo coatings as hydrogen cathodes.* Journal of applied electrochemistry, 1989. **19**(4): p. 519-530.
65. Sanches, L.S., et al., *Characterisation of electrochemically deposited Ni–Mo alloy coatings.* Electrochemistry communications, 2004. **6**(6): p. 543-548.
66. Fan, C., D. Piron, and P. Paradis, *Hydrogen evolution on electrodeposited nickel-cobalt-molybdenum in alkaline water electrolysis.* Electrochimica Acta, 1994. **39**(18): p. 2715-2722.
67. Fan, C., et al., *Study of Electrodeposited Nickel-Molybdenum, Nickel-Tungsten, Cobalt-Molybdenum, and Cobalt-Tungsten as Hydrogen Electrodes in Alkaline Water Electrolysis.* Journal of The Electrochemical Society, 1994. **141**(2): p. 382-387.
68. Stevanović, J., et al., *Hydrogen evolution at Zn-Ni alloys.* Electrochimica Acta, 1998. **43**(7): p. 705-711.
69. Krstajić, N., et al., *The determination of kinetics parameters of the hydrogen evolution on Ti□ Ni alloys by ac impedance.* Electrochimica Acta, 1997. **42**(2): p. 323-330.
70. Hu, W., *Electrocatalytic properties of new electrocatalysts for hydrogen evolution in alkaline water electrolysis.* International Journal of Hydrogen Energy, 2000. **25**(2): p. 111-118.
71. Jafarian, M., et al., *Kinetics and electrocatalytic behavior of nanocrystalline CoNiFe alloy in hydrogen evolution reaction.* International Journal of Hydrogen Energy, 2007. **32**(12): p. 1686-1693.
72. Rosalbino, F., et al., *Electrocatalytic behaviour of Co–Ni–R (R= Rare earth metal) crystalline alloys as electrode materials for hydrogen evolution reaction in alkaline medium.* International Journal of Hydrogen Energy, 2008. **33**(22): p. 6696-6703.
73. Metikoš-Huković, M. and A. Jukić, *Correlation of electronic structure and catalytic activity of Zr–Ni amorphous alloys for the hydrogen evolution reaction.* Electrochimica Acta, 2000. **45**(25): p. 4159-4170.

74. Dominguez-Crespo, M.A., et al., *Electrochemical performance of Ni–RE (RE= rare earth) as electrode material for hydrogen evolution reaction in alkaline medium.* International Journal of Hydrogen Energy, 2011. **36**(1): p. 135-151.
75. Tamura, H., C. Iwakura, and T. Kitamura, *Hydrogen evolution at LaNi 5-type alloy electrodes.* Journal of the Less Common Metals, 1983. **89**(2): p. 567-574.
76. Quaino, P., et al., *Volcano plots in hydrogen electrocatalysis–uses and abuses.* Beilstein journal of nanotechnology, 2014. **5**: p. 846.
77. Conway, B. and G. Jerkiewicz, *Relation of energies and coverages of underpotential and overpotential deposited H at Pt and other metals to the 'volcano curve'for cathodic H 2 evolution kinetics.* Electrochimica Acta, 2000. **45**(25): p. 4075-4083.
78. Sheng, W., et al., *Correlating the hydrogen evolution reaction activity in alkaline electrolytes with the hydrogen binding energy on monometallic surfaces.* Energy & Environmental Science, 2013. **6**(5): p. 1509-1512.
79. Jakšić, M.M., *Advances in electrocatalysis for hydrogen evolution in the light of the Brewer-Engel valence-bond theory.* Journal of molecular Catalysis, 1986. **38**(1): p. 161-202.
80. Conway, B. and L. Bai, *H 2 evolution kinetics at high activity Ni-Mo-Cd electrocoated cathodes and its relation to potential dependence of sorption of H.* International Journal of Hydrogen Energy, 1986. **11**(8): p. 533-540.
81. Smith, A. and D. Trimm, *THE PREPARATION OF SKELETAL CATALYSTS*.* Annu. Rev. Mater. Res., 2005. **35**: p. 127-142.
82. Fouilloux, P., *The nature of raney nickel, its adsorbed hydrogen and its catalytic activity for hydrogenation reactions (review).* Applied Catalysis, 1983. **8**(1): p. 1-42.
83. Raney, M., *Catalysts from alloys.* Industrial & Engineering Chemistry, 1940. **32**(9): p. 1199-1203.
84. Wainwright, M., *Skeletal metal catalysts.* Preparation of Solid Catalysts, 1999: p. 28-43.
85. Sane, S., et al., *Raney metal catalysts: I. comparative properties of raney nickel proceeding from Ni-Ai intermetallic phases.* Applied Catalysis, 1984. **9**(1): p. 69-83.
86. Santos, M., et al., *NiSn and porous NiZn coatings for water electrolysis.* Electrochimica Acta, 1992. **37**(1): p. 29-32.
87. Sheela, G., M. Pushpavanam, and S. Pushpavanam, *Zinc–nickel alloy electrodeposits for water electrolysis.* International Journal of Hydrogen Energy, 2002. **27**(6): p. 627-633.
88. Chen, L. and A. Lasia, *Study of the Kinetics of Hydrogen Evolution Reaction on Nickel‐Zinc Alloy Electrodes.* Journal of The Electrochemical Society, 1991. **138**(11): p. 3321-3328.
89. Ragunathan, P., S. Mitra, and M. Nayar, *Porous nickel electrodes in water electrolysis 1. Electrode preparation and polarization studies in strong alkali.* International Journal of Hydrogen Energy, 1981. **6**(5): p. 487-496.
90. Endoh, E., et al., *New Raney nickel composite-coated electrode for hydrogen evolution.* International Journal of Hydrogen Energy, 1987. **12**(7): p. 473-479.
91. Choquette, Y., H. Menard, and L. Brossard, *Hydrogen discharge on a Raney nickel composite-coated electrode.* International Journal of Hydrogen Energy, 1989. **14**(9): p. 637-642.

92. Choquette, Y., et al., *Study of the Kinetics of Hydrogen Evolution Reaction on Raney Nickel Composite-Coated Electrode by AC Impedance Technique.* Journal of The Electrochemical Society, 1990. **137**(6): p. 1723-1730.
93. Choquette, Y., et al., *Investigation of hydrogen evolution on Raney-Nickel composite-coated electrodes.* Electrochimica Acta, 1990. **35**(8): p. 1251-1256.
94. Choquette, Y., L. Brossard, and H. Ménard, *Leaching of Raney nickel composite-coated electrodes.* Journal of applied electrochemistry, 1990. **20**(5): p. 855-863.
95. Schiller, G., R. Henne, and V. Borck, *Vacuum plasma spraying of high-performance electrodes for alkaline water electrolysis.* Journal of Thermal Spray Technology, 1995. **4**(2): p. 185-194.
96. Schiller, G., et al., *High performance electrodes for an advanced intermittently operated 10-kW alkaline water electrolyzer.* International Journal of Hydrogen Energy, 1998. **23**(9): p. 761-765.
97. Birry, L. and A. Lasia, *Studies of the hydrogen evolution reaction on Raney nickel—molybdenum electrodes.* Journal of applied electrochemistry, 2004. **34**(7): p. 735-749.
98. Schiller, G. and V. Borck, *Vacuum plasma sprayed electrodes for advanced alkaline water electrolysis.* International Journal of Hydrogen Energy, 1992. **17**(4): p. 261-273.
99. Chade, D., et al., *Evaluation of Raney nickel electrodes prepared by atmospheric plasma spraying for alkaline water electrolysers.* International Journal of Hydrogen Energy, 2013. **38**(34): p. 14380-14390.
100. Tanaka, S., N. Hirose, and T. Tanaki, *Evaluation of Raney–nickel cathodes prepared with aluminum powder and tin powder.* International Journal of Hydrogen Energy, 2000. **25**(5): p. 481-485.
101. Rami, A. and A. Lasia, *Kinetics of hydrogen evolution on Ni-Al alloy electrodes.* Journal of applied electrochemistry, 1992. **22**(4): p. 376-382.
102. Martínez, W., A. Fernández, and U. Cano, *Synthesis of nickel-based skeletal catalyst for an alkaline electrolyzer.* International Journal of Hydrogen Energy, 2010. **35**(16): p. 8457-8462.
103. Los, P., A. Rami, and A. Lasia, *Hydrogen evolution reaction on Ni-Al electrodes.* Journal of applied electrochemistry, 1993. **23**(2): p. 135-140.
104. Hu, H., et al., *Kinetics of hydrogen evolution in alkali leaching of rapidly quenched Ni–Al alloy.* Applied Catalysis A: General, 2003. **252**(1): p. 173-183.
105. Chen, L. and A. Lasia, *Ni-Al Powder Electrocatalyst for Hydrogen Evolution Effect of Heat-Treatment on Morphology, Composition, and Kinetics.* Journal of The Electrochemical Society, 1993. **140**(9): p. 2464-2473.
106. Brennecke, P.W. and H.H. Ewe, *Hydrogen evolution of highly porous Raney nickel cathodes in alkaline electrolyte.* Energy Conversion and Management, 1991. **31**(6): p. 585-594.
107. Hitz, C. and A. Lasia, *Experimental study and modeling of impedance of the her on porous Ni electrodes.* Journal of Electroanalytical Chemistry, 2001. **500**(1): p. 213-222.
108. Chen, L. and A. Lasia, *Study of the Kinetics of Hydrogen Evolution Reaction on Nickel-Zinc Powder Electrodes.* Journal of The Electrochemical Society, 1992. **139**(11): p. 3214-3219.
109. Brenner, A., *Electrodeposition of alloys: principles and practice*. 2013: Elsevier.
110. Fauchais, P., *Understanding plasma spraying.* Journal of Physics D: Applied Physics, 2004. **37**(9): p. R86.

111. Smith, A.J., *Skeletal catalysts*. Surface and Nanomolecular Catalysis, 2006: p. 141-158.
112. Devred, F., et al., *The genesis of the active phase in Raney-type catalysts: the role of leaching parameters.* Applied Catalysis A: General, 2003. **244**(2): p. 291-300.
113. Frankel, G., *Pitting corrosion of metals a review of the critical factors.* Journal of the Electrochemical Society, 1998. **145**(6): p. 2186-2198.
114. Xu, W., J. Liu, and H. Zhu, *Pitting corrosion of friction stir welded aluminum alloy thick plate in alkaline chloride solution.* Electrochimica Acta, 2010. **55**(8): p. 2918-2923.
115. Landolt, D., *Corrosion and surface chemistry of metals*. 2007: CRC Press.
116. Vargel, C., *Corrosion of aluminium*. 2004: Elsevier.
117. Bardal, E., *Corrosion and protection*. 2007: Springer Science & Business Media.
118. Tanaka, S.i., et al., *Effect of Ni-Al Precursor Alloy on the Catalytic Activity for a Raney-Ni Cathode.* Journal of The Electrochemical Society, 2000. **147**(6): p. 2242-2245.
119. Lei, H., et al., *Preparation of novel Raney-Ni catalysts and characterization by XRD, SEM and XPS.* Applied Catalysis A: General, 2001. **214**(1): p. 69-76.
120. Divisek, J., H. Schmitz, and B. Steffen, *Electrocatalyst materials for hydrogen evolution.* Electrochimica Acta, 1994. **39**(11): p. 1723-1731.
121. De Giz, M., et al., *High area Ni-Zn and Ni-Co-Zn codeposits as hydrogen electrodes in alkaline solutions.* Journal of applied electrochemistry, 1992. **22**(10): p. 973-977.
122. Needes, C.R.S., *Catalytically active porous nickel electrodes*. 1978, Google Patents.
123. Wendt, H., H. Hofmann, and V. Plzak, *Materials research and development of electrocatalysts for alkaline water electrolysis.* Materials chemistry and physics, 1989. **22**(1-2): p. 27-49.
124. Upadhyaya, G., *Powder metallurgy technology*. 1997: Cambridge Int Science Publishing.
125. Angelo, P. and R. Subramanian, *Powder metallurgy: science, technology and applications*. 2008: PHI Learning Pvt. Ltd.
126. Sing, K.S. and S. Gregg, *Adsorption, surface area and porosity*. 2. ed. 1982, New York: Academic Press Inc. Ltd.
127. Lowell, S., et al., *Characterization of porous solids and powders: surface area, pore size and density*. Vol. 16. 2012: Springer Science & Business Media.
128. Sing, K.S., *Reporting physisorption data for gas/solid systems with special reference to the determination of surface area and porosity (Recommendations 1984).* Pure and applied chemistry, 1985. **57**(4): p. 603-619.
129. Thommes, M., et al., *Physisorption of gases, with special reference to the evaluation of surface area and pore size distribution (IUPAC Technical Report).* Pure and applied chemistry, 2015. **87**(9-10): p. 1051-1069.
130. Rouquerol, J., et al., *Recommendations for the characterization of porous solids (Technical Report).* Pure and applied chemistry, 1994. **66**(8): p. 1739-1758.
131. Harkins, W.D. and G. Jura, *An adsorption method for the determination of the area of a solid without the assumption of a molecular area, and the area occupied by nitrogen molecules on the surfaces of solids.* The Journal of Chemical Physics, 1943. **11**(9): p. 431-432.

132. Webb, P.A. and C. Orr, *Analytical methods in fine particle technology*. 1997: Micromeritics Instrument Corp.
133. Webb, P.A., *Volume and density determinations for particle technologists.* Micromeritics Instrument Corp, 2001. **2**(16): p. 01.
134. Shi, D., et al., *First-principles studies of Al–Ni intermetallic compounds.* Journal of solid state chemistry, 2009. **182**(10): p. 2664-2669.
135. Anovitz, L.M. and D.R. Cole, *Characterization and analysis of porosity and pore structures.* Reviews in Mineralogy and geochemistry, 2015. **80**(1): p. 61-164.
136. Dinnebier, R.E., *Powder diffraction: theory and practice*. 2008: Royal Society of Chemistry.
137. Pecharsky, V.K. and P.Y. Zavalij, *Fundamentals of powder diffraction and structural characterization of materials*. Vol. 69. 2009: Springer.
138. Toby, B.H., *R factors in Rietveld analysis: How good is good enough?* Powder diffraction, 2006. **21**(1): p. 67-70.
139. Thomas, R., *Practical guide to ICP-MS: a tutorial for beginners*. 2013: CRC press.
140. Cazes, J., *Analytical instrumentation handbook*. 2004: CRC Press.
141. Stock, S.R., *Microcomputed tomography: methodology and applications*. 2008: CRC press.
142. Storey, R.A. and I. Ymen, *Solid state characterization of pharmaceuticals*. 2011: John Wiley & Sons.
143. Allison, H.W. and H. Samelson, *Diffusion of aluminum, magnesium, silicon, and zirconium in nickel.* Journal of applied physics, 1959. **30**(9): p. 1419-1424.
144. Borg, R.J. and G.J. Dienes, *An introduction to solid state diffusion*. 2012: Elsevier.
145. Pandey, A.B., *Dispersion strengthened L12 aluminum alloys*. 2011, Google Patents.
146. Campbell, C.E. and U.R. Kattner, *A thermodynamic assessment of the Ni-Al-B system.* Journal of Phase Equilibria and Diffusion, 1999. **20**(5): p. 485.
147. Mishima, Y., S. Ochiai, and T. Suzuki, *Lattice parameters of Ni (γ), Ni 3 Al (γ') and Ni 3 Ga (γ') solid solutions with additions of transition and B-subgroup elements.* Acta metallurgica, 1985. **33**(6): p. 1161-1169.
148. Noebe, R.D., R.R. Bowman, and M.V. Nathal, *Review of the physical and mechanical properties and potential applications of the B2 compound NiAl.* 1992, DTIC Document.
149. Upadhyaya, A. and G.S. Upadhyaya, *Powder Metallurgy: Science, Technology and Materials*. 2011: Universities Press.
150. Morsi, K., *Review: reaction synthesis processing of Ni–Al intermetallic materials.* Materials Science and Engineering: A, 2001. **299**(1): p. 1-15.
151. Klein, J.C. and D.M. Hercules, *Surface analysis of Raney nickel alloys.* Analytical Chemistry, 1981. **53**(6): p. 754-758.
152. Giuranno, D., et al., *Surface Tension and Density of Al− Ni Alloys.* Journal of Chemical & Engineering Data, 2010. **55**(9): p. 3024-3028.
153. Bakker, M., D. Young, and M. Wainwright, *Selective leaching of NiAl3 and Ni2Al3 intermetallics to form Raney nickels.* Journal of materials science, 1988. **23**(11): p. 3921-3926.
154. Tanaka, S.-I., N. Hirose, and T. Tanaki, *Influence of the residual aluminum in Raney-nickel on the catalytic ability for hydrogen evolution reaction.* Denki Kagaku oyobi Kogyo Butsuri Kagaku, 1997. **65**(12): p. 1044-1048.

155. Freel, J., W. Pieters, and R. Anderson, *The structure of Raney nickel: I. Pore structure.* Journal of Catalysis, 1969. **14**(3): p. 247-256.
156. Sigma-Aldrich. *Aluminum-nickel alloy* 23.11.16]; Available from: http://www.sigmaaldrich.com/catalog/product/sial/72240?lang=en&region=GB.
157. Bhunia, A., et al., *Bubble formation in a coflow configuration in normal and reduced gravity.* AIChE journal, 1998. **44**(7): p. 1499-1509.
158. Sarkar, M.S.K.A., G. Evans, and S. Donne, *Bubble size measurement in electroflotation.* Minerals Engineering, 2010. **23**(11): p. 1058-1065.
159. Wallis, G.B., *One-dimensional two-phase flow.* 1969.
160. Matsushima, H., T. Iida, and Y. Fukunaka, *Gas bubble evolution on transparent electrode during water electrolysis in a magnetic field.* Electrochimica Acta, 2013. **100**: p. 261-264.
161. Fischer, J., et al., *Fundamental investigations and electrochemical engineering aspects concerning an advanced concept for alkaline water electrolysis.* AIChE Journal, 1980. **26**(5): p. 794-802.
162. Solaiyan, C., et al., *Preparation and characterisation of porous electrodes from nickel powder for fuel cells.* 1999.
163. Li, Z. and B.C.-Y. Lu, *Surface tension of aqueous electrolyte solutions at high concentrations—representation and prediction.* Chemical Engineering Science, 2001. **56**(8): p. 2879-2888.
164. Ohashi, M. and G.C. Paffenbarger, *Melting, flow, and thermal expansion characteristics of some dental and commercial waxes.* The Journal of the American Dental Association, 1966. **72**(5): p. 1141-1150.
165. Giesche, H., *Mercury porosimetry: a general (practical) overview.* Particle & particle systems characterization, 2006. **23**(1): p. 9-19.
166. Seuba, J., et al., *The effect of wall thickness distribution on mechanical reliability and strength in unidirectional porous ceramics.* Science and technology of advanced materials, 2016. **17**(1): p. 128-135.
167. Bekoz, N. and E. Oktay, *The role of pore wall microstructure and micropores on the mechanical properties of Cu–Ni–Mo based steel foams.* Materials Science and Engineering: A, 2014. **612**: p. 387-397.
168. Le Huec, J., et al., *Influence of porosity on the mechanical resistance of hydroxyapatite ceramics under compressive stress.* Biomaterials, 1995. **16**(2): p. 113-118.

Appendix 1. Reproducibility Results

This section reports the reproducibility results of various techniques used for the physical, chemical and electrochemical characterizations of electrodes including alkaline electrolyser cell test, Rietveld refinement, EDX, ICP-OES, He pycnometer and N_2 sorption analyses.

Table A1.1. Reproducibility results of the electrolyser cell test for an as-leached Ni60:Alloy40-B6.25 electrode sintered at 650 °C.

	Cell Voltage (V)				
Current density (A/cm^2)	Test-1	Test-2	Test-3	Average	SD*
1	1.991	1.993	2.013	1.999	0.012
0.9	1.967	1.966	1.990	1.974	0.014
0.8	1.935	1.936	1.955	1.942	0.011
0.7	1.899	1.904	1.917	1.907	0.010
0.6	1.862	1.865	1.877	1.868	0.008
0.5	1.795	1.784	1.812	1.797	0.014
0.4	1.753	1.745	1.769	1.756	0.012
0.3	1.703	1.699	1.719	1.707	0.011
0.2	1.645	1.641	1.658	1.648	0.009
0.1	1.574	1.572	1.582	1.576	0.005
0.05	1.525	1.524	1.532	1.527	0.005
0.025	1.497	1.497	1.503	1.499	0.003
0.0125	1.481	1.480	1.485	1.482	0.003
0.00625	1.466	1.467	1.470	1.468	0.002

*SD: Standard deviation

Table A1.2. Reproducibility results of the electrochemical activity of three as-leached Ni60:Alloy40-B6.25 electrodes sintered at 650 °C.

	Cell Voltage (V)				
Current density (A/cm^2)	Batch-1	Batch-2	Batch-3	Average	SD*
1	1.991	2.015	2.023	2.010	0.016
0.9	1.967	1.993	1.992	1.984	0.015
0.8	1.935	1.964	1.959	1.953	0.015
0.7	1.899	1.929	1.920	1.916	0.015
0.6	1.862	1.887	1.883	1.877	0.014
0.5	1.795	1.824	1.820	1.813	0.016
0.4	1.753	1.778	1.774	1.768	0.013
0.3	1.703	1.721	1.720	1.715	0.010
0.2	1.645	1.659	1.656	1.653	0.008
0.1	1.574	1.583	1.583	1.580	0.005
0.05	1.525	1.535	1.531	1.530	0.005
0.025	1.497	1.505	1.503	1.502	0.004
0.0125	1.481	1.485	1.485	1.484	0.003
0.00625	1.466	1.471	1.470	1.469	0.003

*SD: Standard deviation

Table A1.3. Reproducibility results of Rietveld refinement for the weight concentrations of phases and overall Al and Ni compositions in an as-leached Ni60:Alloy40-B6.25 sample sintered at 650 °C.

Measurement	AlNi (wt.%)	$AlNi_3$ (wt.%)	Ni phase (wt.%)	Al composition (wt.%)	Ni composition (wt.%)
1	28.1	28.6	43.3	12.6	87.4
2	27.6	28.8	43.6	12.5	87.5
3	28.3	28.4	43.2	12.7	87.3
Average	28.0	28.6	43.4	12.6	87.4
SD	0.4	0.2	0.2	0.1	0.1

Table A1.4. Reproducibility results of Rietveld refinement for the weights of phases present in an as-leached Ni60:Alloy40-B6.25 sample sintered at 650 °C.

Measurement	AlNi (g)	$AlNi_3$ (g)	Ni (g)
1	0.795	0.808	1.225
2	0.782	0.814	1.232
3	0.801	0.804	1.223
Average	0.793	0.809	1.226
SD	0.010	0.005	0.005

Table A1.5. Reproducibility results of Rietveld refinement for the weight concentrations of phases and overall Al and Ni compositions in three as-sintered Ni60:Alloy40-B6.25 samples, where the sintering temperature was 650 °C.

Batch	Al_3Ni_2 (wt.%)	AlNi (wt.%)	$AlNi_3$ (wt.%)	Ni (wt.%)	Al composition (wt.%)	Ni composition (wt.%)
1	30.0	19.6	16.9	33.5	20.7	79.3
2	34.2	14.7	13.5	37.6	20.4	79.6
3	31.9	17.4	16.9	33.8	20.7	79.3
Average	32.0	17.2	15.8	35.0	20.6	79.4
SD	2.1	2.5	1.9	2.3	0.2	0.2

Table A1.6. Reproducibility results of Rietveld refinement for the weights of phases present in three as-sintered Ni60:Alloy40-B6.25 samples, where the sintering temperature was 650 °C.

Batch	Al_3Ni_2 (g)	AlNi (g)	$AlNi_3$ (g)	Ni (g)	Sample weight (g)
1	0.895	0.586	0.504	1.000	2.984
2	1.023	0.439	0.405	1.125	2.992
3	0.952	0.520	0.505	1.010	2.987
Average	0.957	0.515	0.471	1.045	2.988
SD	0.064	0.074	0.057	0.070	0.004

Table A1.7. Reproducibility results of Rietveld refinement for the weight concentrations of phases and overall Al and Ni compositions in three as-leached Ni60:Alloy40-B6.25 samples sintered at 650 °C.

Batch	AlNi (wt.%)	$AlNi_3$ (wt.%)	Ni (wt.%)	Al composition (wt.%)	Ni composition (wt.%)
1	28.1	28.6	43.3	12.6	87.4
2	30.8	28.5	40.7	13.5	86.5
3	28.2	29.1	42.8	12.7	87.3
Average	29.0	28.7	42.2	13.0	87.0
SD	1.5	0.3	1.4	0.5	0.5

Table A1.8. Reproducibility results of Rietveld refinement for the weights of phases present in three as-leached Ni60:Alloy40-B6.25 samples sintered at 650 °C.

Batch	AlNi (g)	$AlNi_3$ (g)	Ni (g)	Sample weight (g)
1	0.795	0.808	1.225	2.828
2	0.876	0.811	1.157	2.845
3	0.798	0.824	1.212	2.834
Average	0.823	0.815	1.198	2.836
SD	0.046	0.009	0.036	0.009

Table A1.9. Rietveld refinement results for the commercial precursor Ni-Al alloy (Sigma-Aldrich) with a weight ratio of 50:50 and the starting metal mixture prepared by mixing Ni 255 and Ni-Al alloy with a weight ratio of 60:40 respectively.

Batch	Al_3Ni (wt.%)	Al_2Ni_3 (wt.%)	Ni (wt.%)	Al composition (wt.%)	Ni composition (wt.%)
Commercial Al-Ni alloy	51.8	48.2	-	49.7	50.3
Starting metal mixture	21.6	18.8	59.6	20.2	79.8

Table A1.10. Reproducibility results of EDX analysis for the Al concentrations on the surface and cross-section of an as-leached Ni60:Alloy40-B6.25 sample sintered at 650 °C.

Measurement	Surface Al concentration (wt.%)	Cross-section Al concentration (wt.%)
1	9.9	14.1
2	8.9	12.2
3	9.8	13.6
4	9.1	14.9
5	9.6	12.8
Average	9.5	13.5
SD	0.4	1.0

Table A1.11. Reproducibility results of EDX analysis for the Al concentrations on the surface and cross-section of three Ni60:Alloy40-B6.25 samples sintered at 650 °C.

Batch	Surface Al concentration (wt.%)*	Cross-section Al concentration (wt.%)*
1	9.5	11.1
2	9.5	14.3
3	7.5	13.5
Average	8.8	13.0
SD	1.2	1.7

*Average of 5 different scans

Table A1.12. Reproducibility results of ICP-OES analysis for normalized Al and Ni contents of three as-leached Ni60:Alloy40-B6.25 samples sintered at 650 °C.

Batch	Al composition (wt.%)	Ni composition (wt.%)
1	87.8	12.2
2	88.3	11.7
3	87.6	12.4
Average	87.9	12.1
SD	0.4	0.4

Table A1.13. ICP-OES results for the commercial precursor Ni-Al alloy (Sigma-Aldrich) with a weight ratio of 50:50.

Al composition (wt.%)	Ni composition (wt.%)
49.3	50.7

Table A1.14. Reproducibility results of He pycnometer test for an as-leached Ni60:Alloy40-B6.25 electrode sintered at 650 °C.

Measurement	Actual volume of material in the disk volume (cm^3)	% of material in the disk volume	Actual volume of closed pores in the disk volume (cm^3)	% of closed pores in the disk volume	Actual volume of open pores in the disk volume (cm^3)	% of open pores in the disk volume	Volume of open pores (cm^3/g)
1	0.376	31.2	0.092	7.6	0.740	61.2	0.259
2	0.374	31.0	0.097	8.1	0.735	60.9	0.257
3	0.374	31.0	0.104	8.6	0.728	60.4	0.255
Average	0.375	31.1	0.098	8.1	0.734	60.8	0.257
SD*	0.001	0.1	0.006	0.5	0.006	0.4	0.002

Table A1.15. The reproducibility of He pycnometer test results for three as-leached Ni60:Alloy40-B6.25 electrodes sintered at 650 °C.

Batch	Actual volume of material in the disk volume (cm^3)	% of material in the disk volume	Actual volume of closed pores in the disk volume (cm^3)	% of closed pores in the disk volume	Actual volume of open pores in the disk volume (cm^3)	% of open pores in the disk volume	Volume of open pores (cm^3/g)
1	0.374	31.0	0.092	7.6	0.740	61.4	0.259
2	0.377	31.5	0.103	8.6	0.717	59.9	0.251
3	0.374	31.0	0.111	9.2	0.721	59.8	0.252
Average	0.375	31.2	0.102	8.5	0.726	60.4	0.254
SD	0.002	0.3	0.010	0.8	0.012	0.9	0.004

Table A1.16. Reproducibility results of N_2 sorption test for an as-leached Ni60:Alloy40-B6.25 sample sintered at 650 °C.

Measurement	BET surface area (m^2/g)	Micropore area (m^2/g)	Meso- and macropore area (m^2/g)	Micropore volume (cm^3/g)	Mesopore volume (cm^3/g)
1	10.9	8.8	2.1	0.0040	0.0143
2	11.5	9.2	2.2	0.0042	0.0154
3	11.5	9.2	2.3	0.0041	0.0155
Average	11.3	9.1	2.2	0.0041	0.0151
SD	0.3	0.2	0.1	0.0001	0.0007

Table A1.17. Reproducibility results of N_2 sorption test for three as-leached Ni60:Alloy40-B6.25 samples sintered at 650 °C.

Batch	BET surface area (m^2/g)	Micropore area (m^2/g)	Meso- and macropore area (m^2/g)	Micropore volume (cm^3/g)	Mesopore volume (cm^3/g)
1	10.9	8.8	2.1	0.0040	0.014
2	7.6	6.3	1.2	0.0029	0.010
3	10.3	8.8	1.6	0.0040	0.013
Average	9.6	8.0	1.6	0.0036	0.012
SD	1.8	1.4	0.4	0.0006	0.002

Table A1.18. Reproducibility results of N_2 sorption test for three as-leached Ni60:Alloy40-B6.25 samples sintered at 900 °C.

Batch	BET surface area (m^2/g)	Micropore area (m^2/g)	Meso- and macropore area (m^2/g)	Micropore volume (cm^3/g)	Mesopore volume (cm^3/g)
1	1.15	0.98	0.18	0.00044	0.0028
2	1.20	1.02	0.18	0.00047	0.0028
3	1.20	1.01	0.19	0.00045	0.0032
Average	1.19	1.00	0.18	0.00045	0.0029
SD	0.03	0.02	0.01	0.00001	0.0003

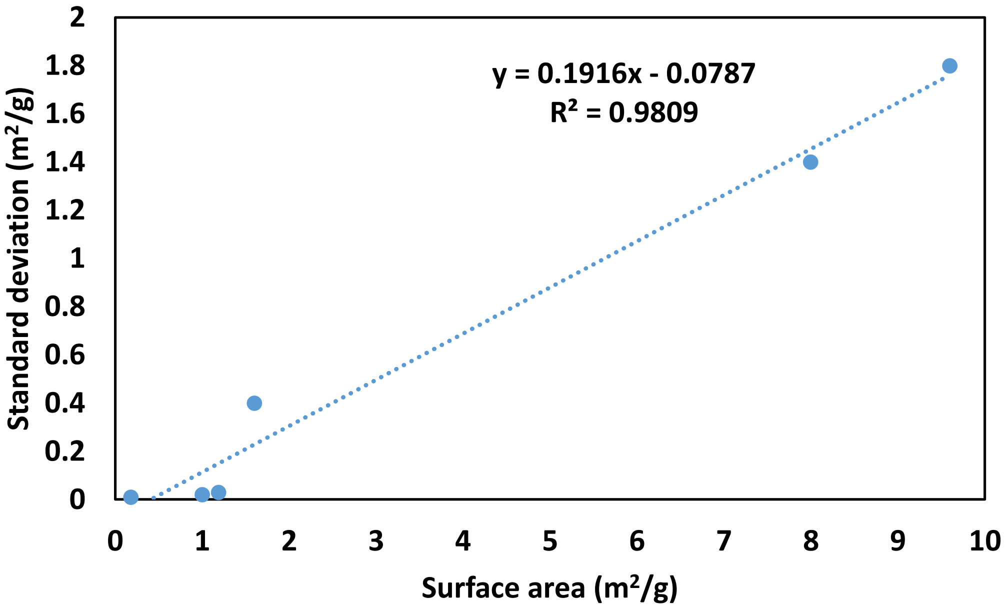

Figure A1.1. The change in the standard deviation of surface area estimated by N_2 sorption technique using BET and DA models.

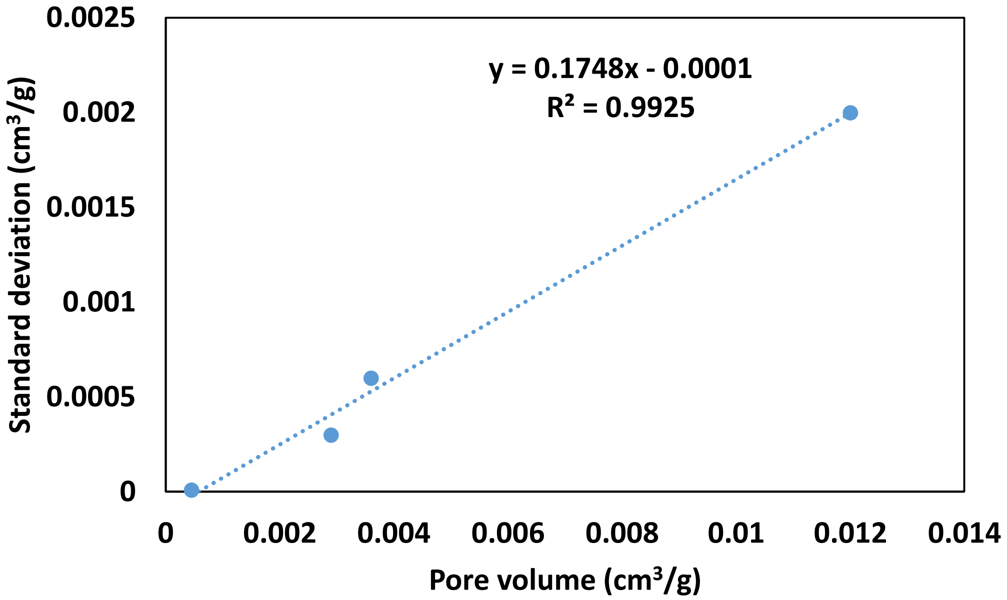

Figure A1.2. The change in the standard deviation of pore volume estimated by N_2 sorption technique using BET and DA models.

Appendix 2. Rietveld Refinement Fit

This section gives examples of Rietveld refinement fit of measured PXD patterns to theoretical data. The overall X^2 was *ca.* 2.0 for the starting alloy mixture (Al_3Ni and Al_3Ni_2), *ca.* 3.5 for as-sintered samples and *ca.* 4.5 for as-leached samples.

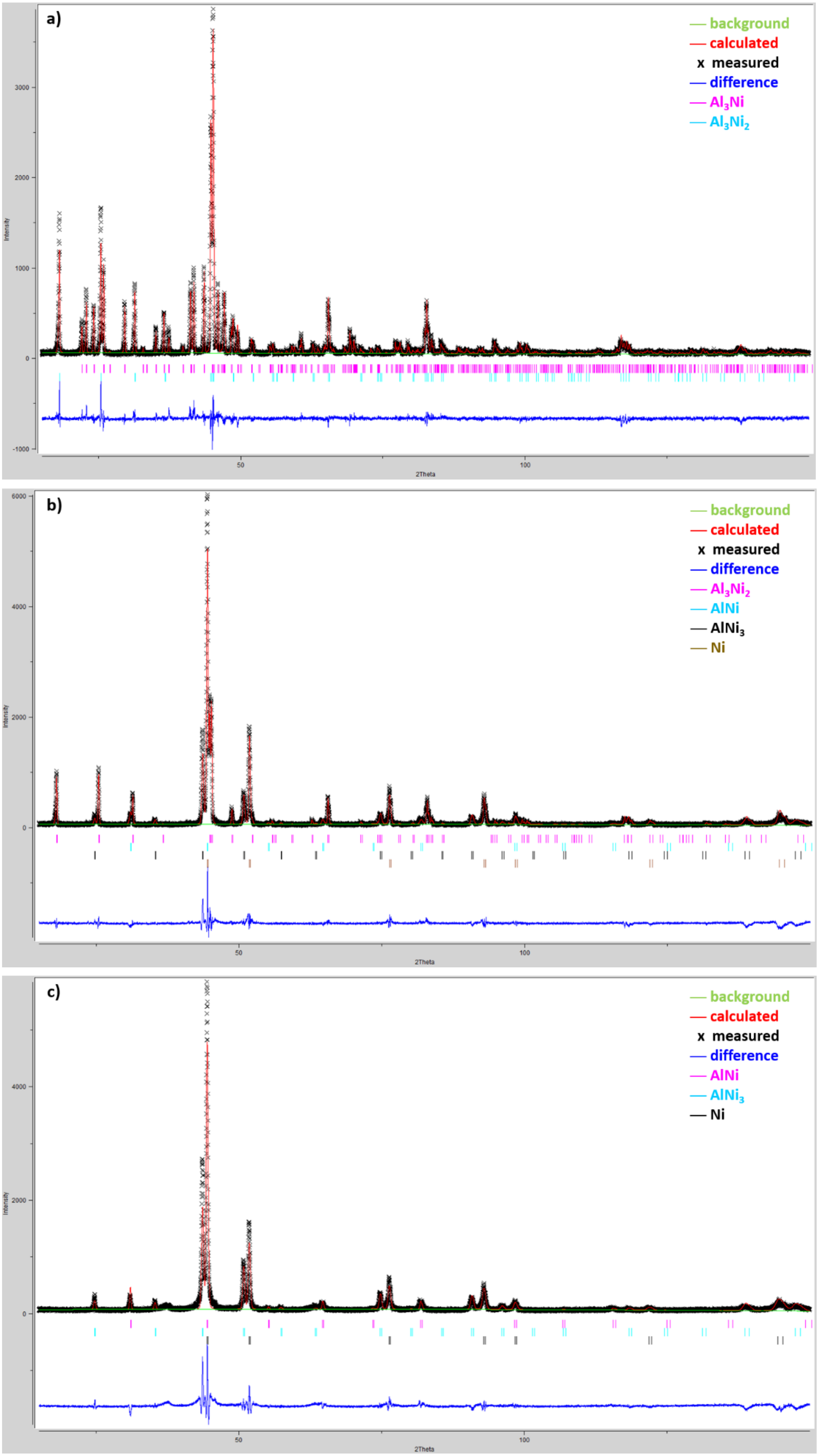

Figure A2.1. Rietveld refinement fit of the PXD data for (a) as-received starting alloy; (b) an as-sintered Ni60:Alloy40-B6.25 sample; (c) an as-leached Ni60:Alloy40-B6.25 sample.

Appendix 3. SEM Images of As-sintered Samples

This section presents higher magnification representative SEM-SE images of the surfaces of samples sintered at 650 and 900 °C.

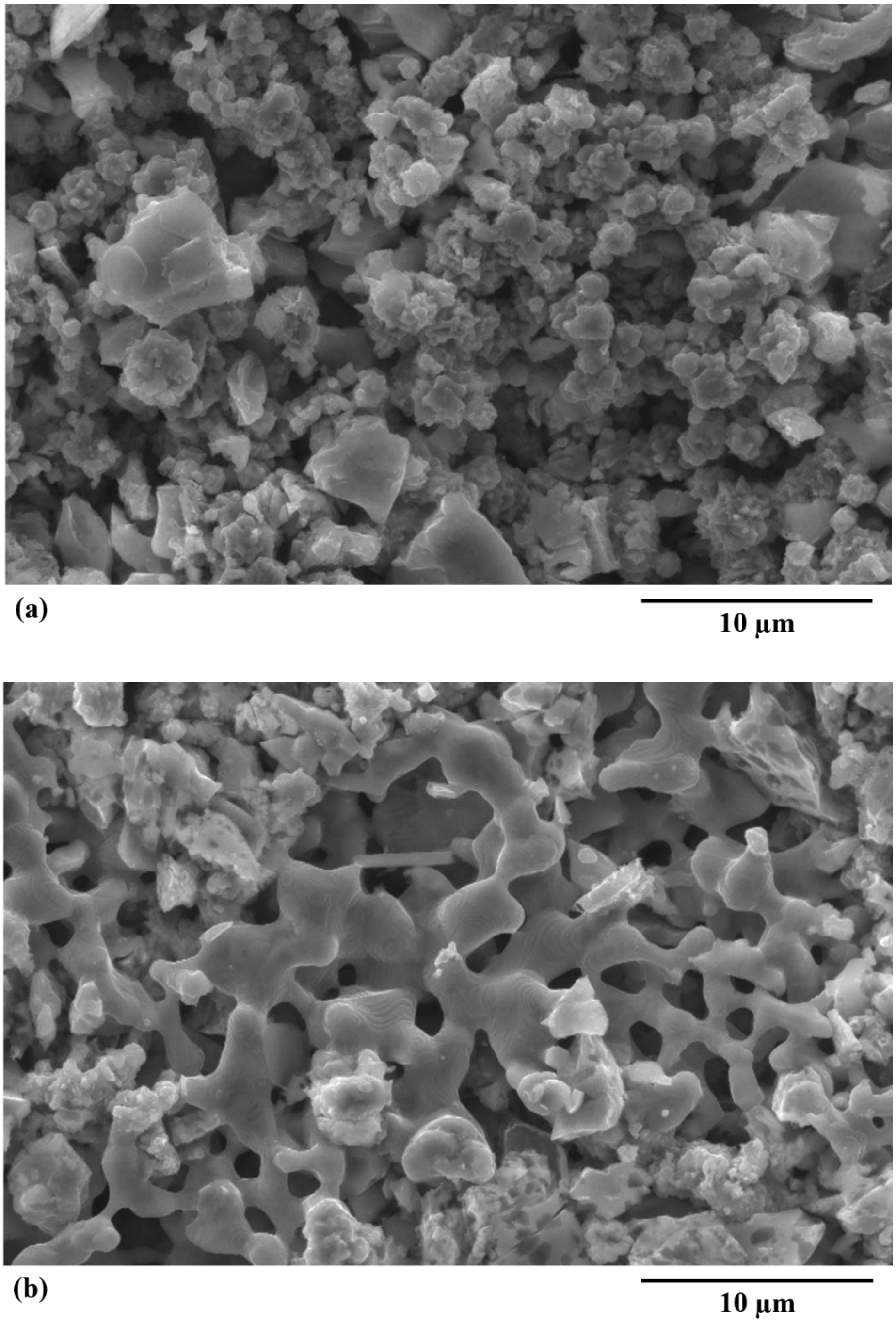

Figure A3.1. Representative SEM-SE images of the surfaces of as-sintered samples where the sintering temperature was (a) 650 °C; (b) 900 °C.

Appendix 4. SEM Images of As-leached Samples

This section gives the SEM-SE and -BSE images of the surfaces of as-leached Ni60:Alloy40-B6.25 samples sintered at different temperatures, i.e. 625, 650, 700, 750 and 900 ºC. Figure A4.1 presents lower magnification images including different constituents, while Figure A4.2 gives representative high magnification SEM-SE images of precursor alloy particles.

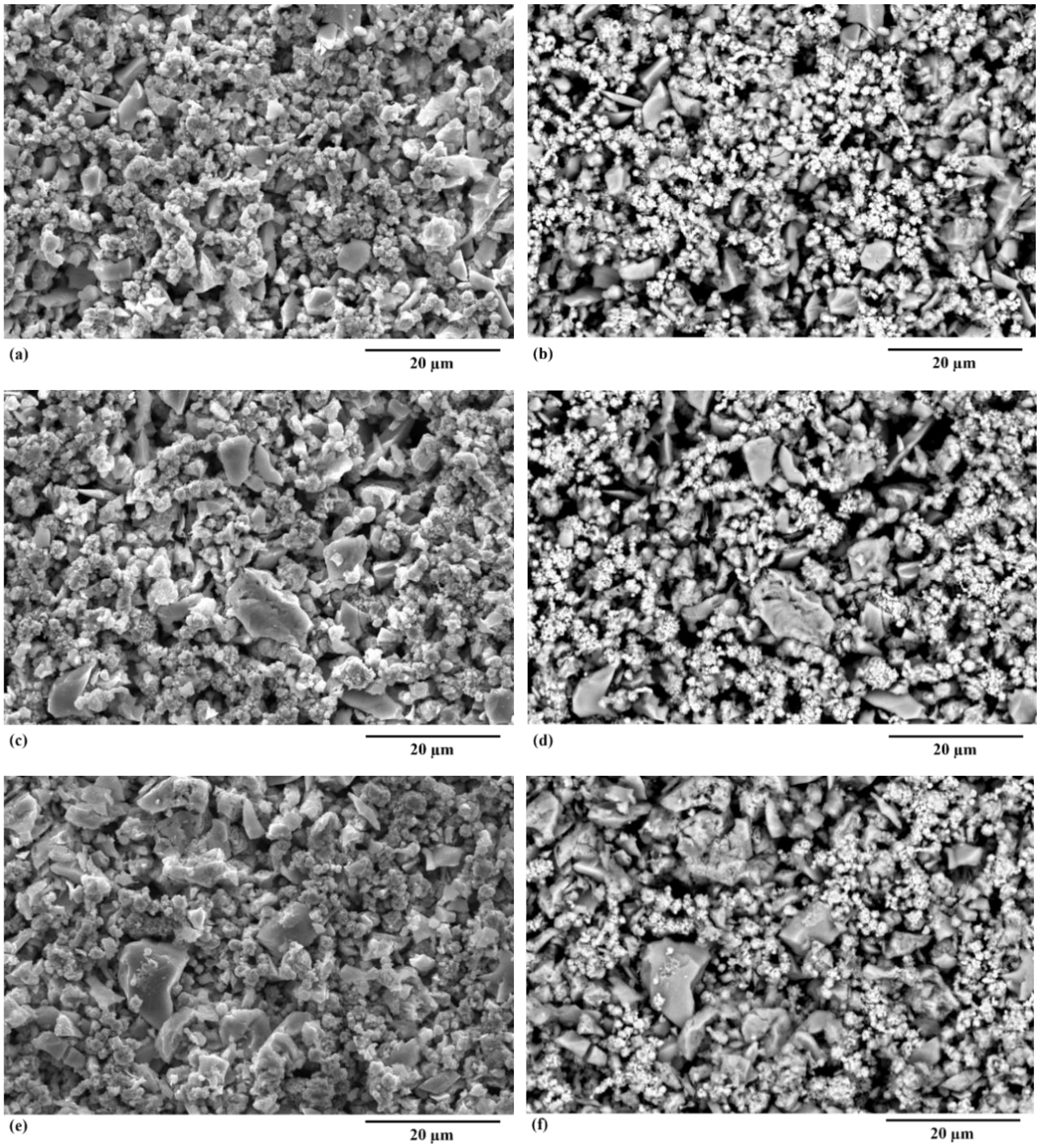

Figure A4.1. SEM SE (left) and BSE (right) images of the surfaces of as-leached Ni60:Alloy40-B6.25 samples sintered at different temperatures; (a) and (b) 625 ºC; (c) and (d) 650 ºC; (e) and (f) 700 ºC; (g) and (h) 750 ºC; (i) and (j) 900 ºC (Figure continued on next page).

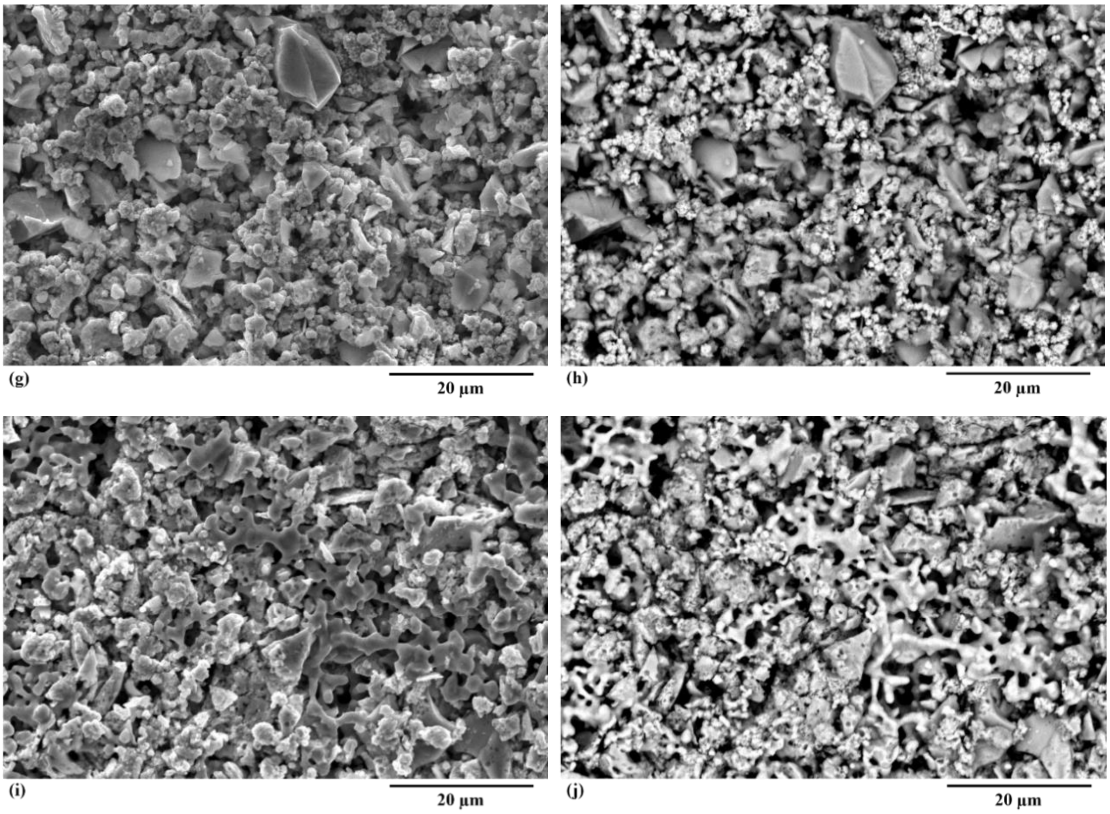

Figure A4.1. SEM SE (left) and BSE (right) images of the surfaces of as-leached Ni60:Alloy40-B6.25 samples sintered at different temperatures; (a) and (b) 625 ºC; (c) and (d) 650 ºC; (e) and (f) 700 ºC; (g) and (h) 750 ºC; (i) and (j) 900 ºC (continued from previous page).

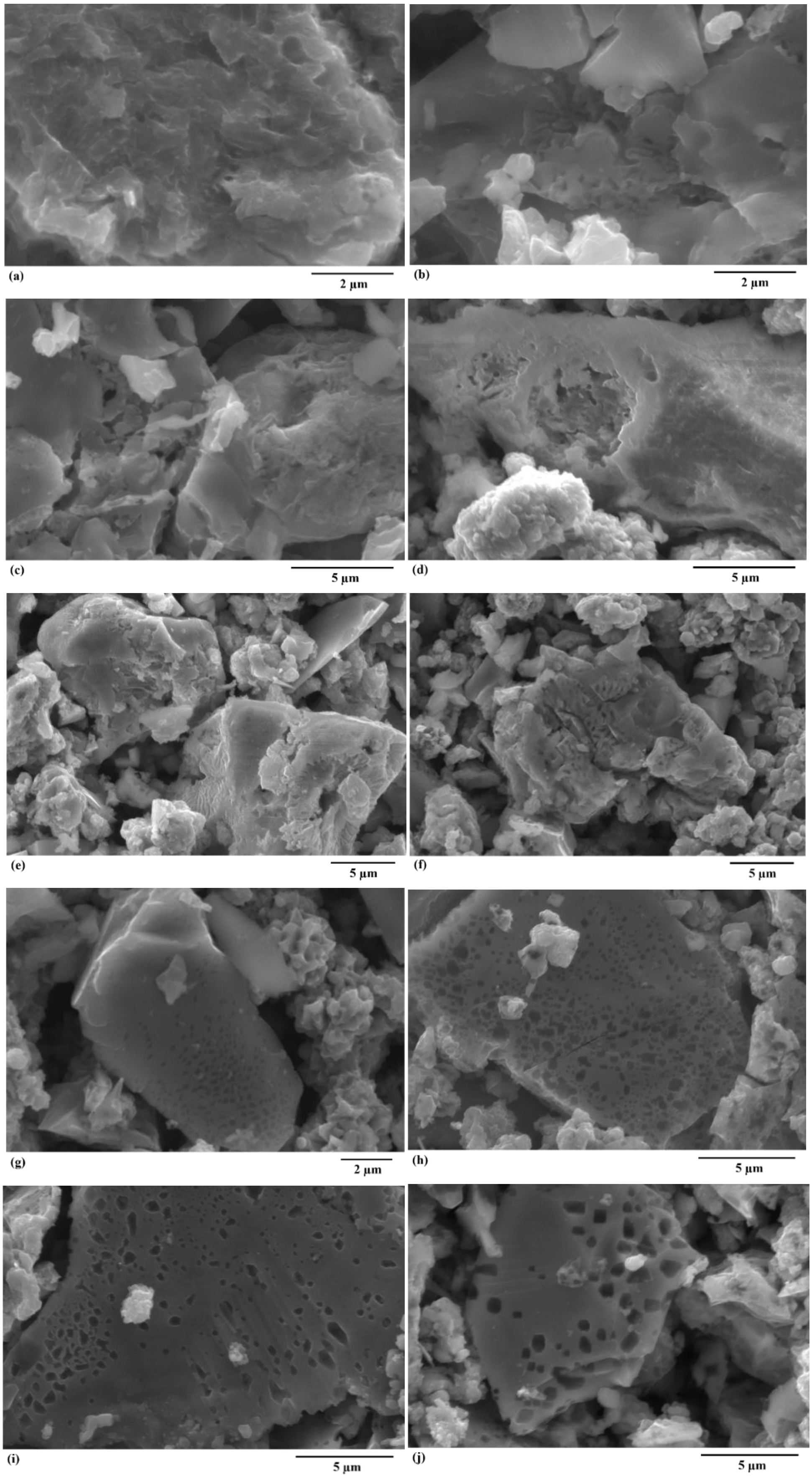

Figure A4.2. High magnification SEM-SE images of precursor alloy particles present in as-leached Ni60:Alloy40-B6.25 samples, where (a) and (b) sintered at 625 ºC; (c) and (d) sintered at 650 ºC; (e) and (f) sintered at 700 ºC; (g) and (h) sintered at 750 ºC; (i) and (j) sintered at 900 ºC.

Appendix 5. PXD Results for Starting Alloy

This section reports the PXD results of starting alloy at different stages. Figure A5.1 demonstrates the PXD patterns of as-received, as-sintered and as-leached alloy. Figure A5.2 compares the Ni peaks in the PXD patterns to that of precursor Ni 255 and an as-leached Ni60:Alloy40-B6.25 sample.

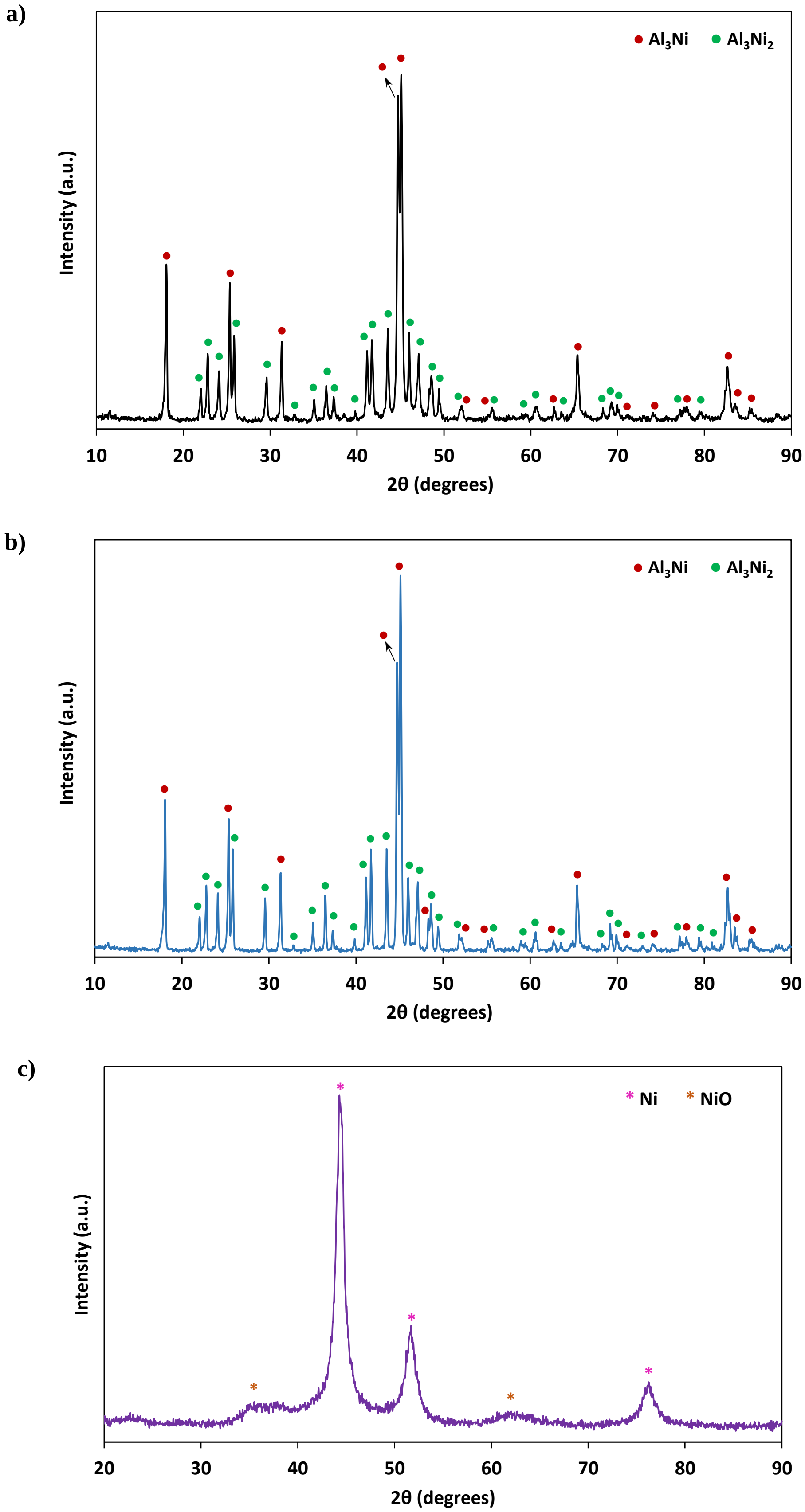

Figure A5.1. PXD patterns of (a) as-received; (b) as-sintered; (c) as-leached starting alloy, where sintering and leaching temperatures are 650 and 70 °C respectively.

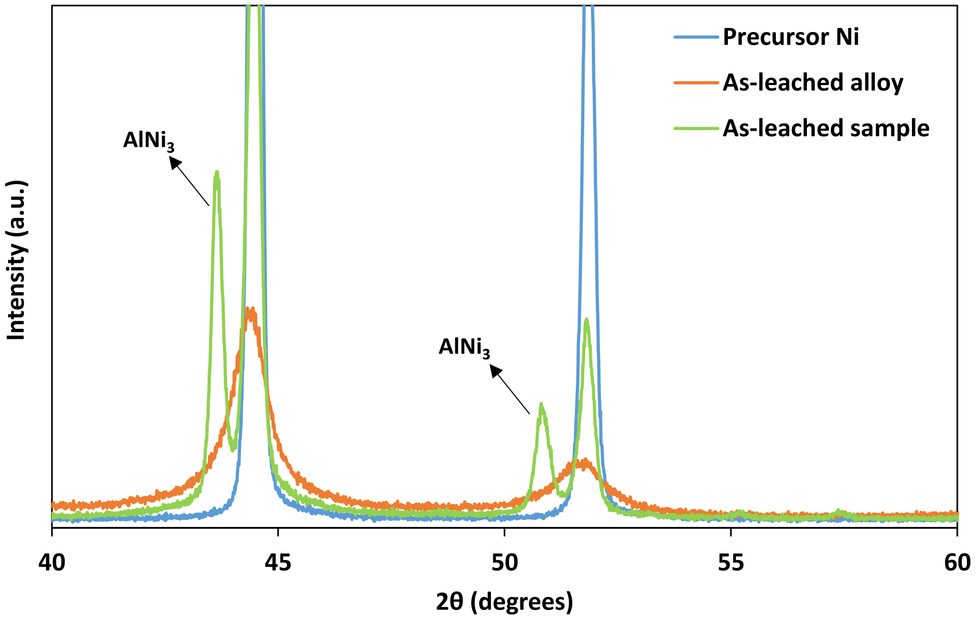

Figure A5.2. Comparison of significant Ni peaks in the PXD patterns of Ni 255, as-leached starting alloy and an as-leached Ni60:Alloy40-B6.25 sample sintered at 650 °C.

Appendix 6. ICP-MS Results

This section covers the results from ICP-MS analysis. Table A6.1 gives the ICP-MS results of Al and Ni concentrations for the blank leaching solution and leaching solutions after 18 h of leaching Ni60:Alloy40-B6.25 samples, while Table A6.2 presents calculated Al contents of these samples based on the ICP-MS results.

Table A6.1. ICP-MS results of Al and Ni concentrations for the blank leaching solution and leaching solutions sampled after 18 h of leaching Ni60:Alloy40-B6.25 samples sintered at 650 and 900 °C.

Solution analysed via the ICP-MS	Al concentration (mg/l)	Ni concentration (mg/l)
Blank leaching solution (5 M KOH solution containing 10 wt.% K-Na tartrate tetrahydrate)	5.0 ± 2.5	0.26 ± 0.03
Leaching solution after 18 h of leaching* a Ni60:Alloy40-B6.25 sintered at 650 °C.	1138.0 ± 80.5	0.24 ± 0.03
Leaching solution after 18 h of leaching* a Ni60:Alloy40-B6.25 sintered at 900 °C.	105.0 ± 3.0	0.26 ± 0.01

*Leaching was carried out at 70 °C.

Table A6.2. Al contents of Ni60:Alloy40-B6.25 samples (sintered at 650 and 900 °C) before and after leaching based on the ICP-MS analysis of leaching solutions.

Sample	Theoretical Al content before leaching (mg)	Total Al dissolved in the leaching solution measured by ICP-MS (mg)	Al composition of the sample after leaching* (wt.%)
Ni60:Alloy40-B6.25 sintered at 650 °C	600	262 ± 18	11.8 ± 0.6
Ni60:Alloy40-B6.25 sintered at 900 °C	600	24 ± 1	19.2 ± 0.1

*calculated from the ICP-MS results and dry sample weights measured after leaching.

Appendix 7. TGA Results

This section presents the TGA results for the weight loss during the sintering of Ni60:Alloy40-B6.25 samples.

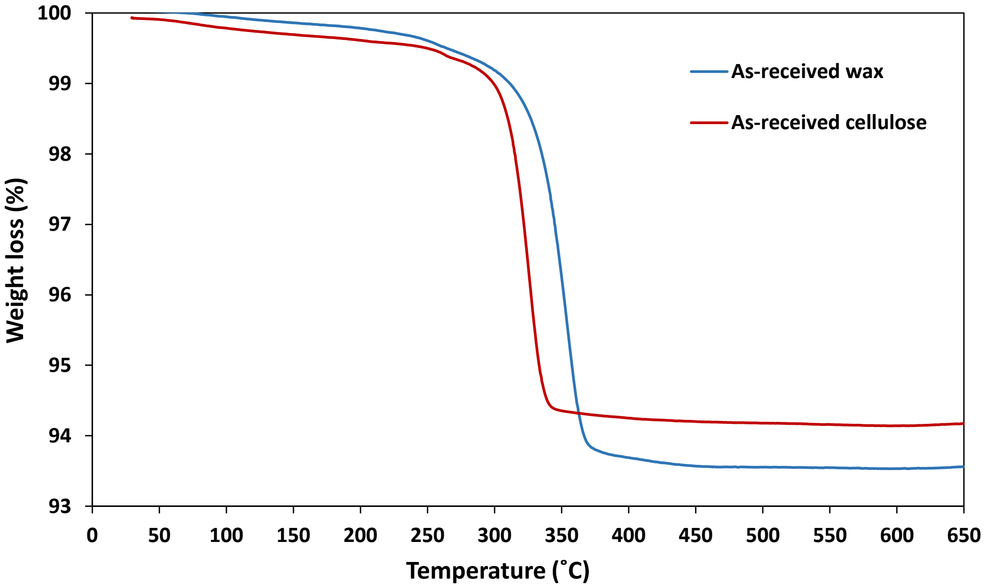

Figure A7.1. TGA results for the weight loss during the sintering of Ni60:Alloy40-B6.25 samples prepared using a binder concentration of 6.25 wt.% of the total weight.

Appendix 8. SEM Images of As-received Wax

This section gives representative SEM-SE images of as-received wax.

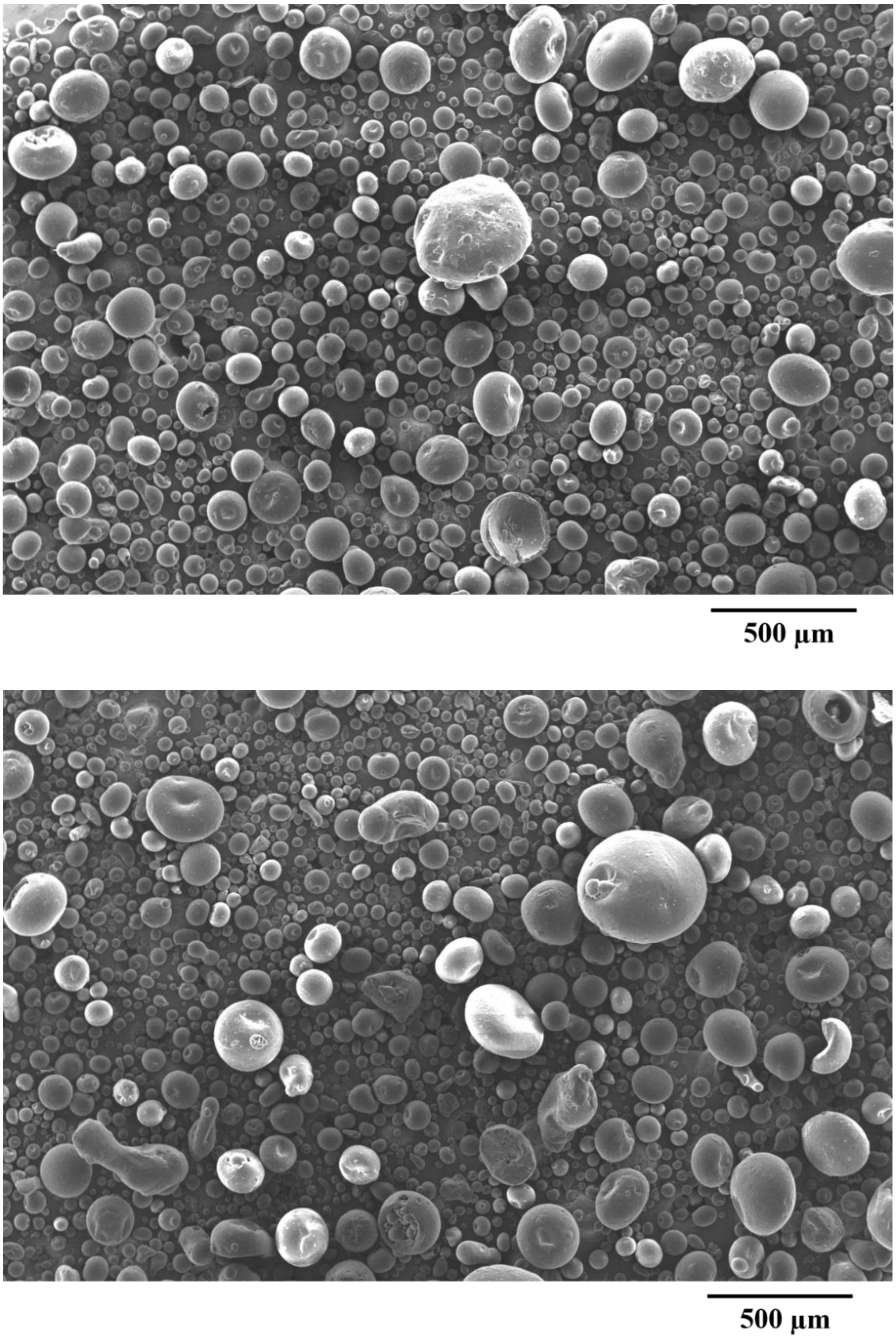

Figure A8.1. Representative SEM-SE images of as-received wax (Lonza).

Appendix 9. Laser Diffraction Results

This section gives the laser diffraction results for the particle size distribution for as-received wax binder.

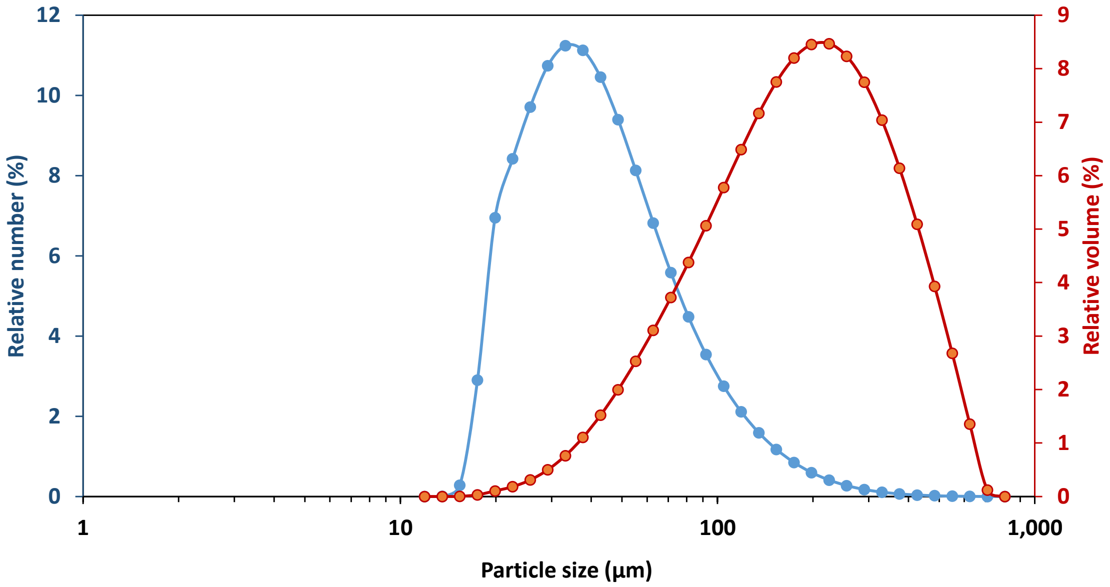

Figure A9.1. Laser diffraction results for the particle size distribution of as-received wax. The results are reported for the average of 3 measurements.

Appendix 10. Density Results of Precursor Materials

This section gives the density results for the precursor materials; i.e. Ni 255 and starting alloy powders. Loose density was measured by adding a quantity of powder to a graduated cylinder of known volume. The tap density was obtained by mechanically tapping a graduated cylinder containing the powder sample until no further change in the volume was observed. Skeletal density was measured by He pycnometer technique. The percentage of open porosity and interparticle voids were calculated using the results of tap and skeletal densities.

Table A10.1. Density characteristics of Ni 255 and starting alloy powders, where the skeletal densities were measured through the He pycnometer technique.

Powder	Loose powder density (g/ml)	Tap density (g/ml)	Skeletal density (g/ml)	Open porosity and interparticle voids (vol.%)
Ni 255	0.62	1.34	8.86	84.8
Starting alloy	0.85	1.57	4.17	62.5